

Shape & Size-Tuned Magnetic Nanostructures and Ferrofluids for Biomedical and Industrial Applications

Thesis

Submitted for the Degree of
Doctor of Philosophy (ISLM)
of
JADAVPUR UNIVERSITY

by

Srividhya, J.

Central Glass & Ceramic Research Institute



Council of Scientific and Industrial Research

196, Raja S.C. Mullick Road, Jadavpur

Kolkata-700 032

India

2017



सीएसआईआर - केन्द्रीय काँच एवं सिरामिक अनुसंधान संस्थान

196, राजा एस सी मल्लिक रोड, कोलकाता - 700 032, भारत

CSIR - CENTRAL GLASS & CERAMIC RESEARCH INSTITUTE

196, Raja S C Mullick Road, Kolkata - 700 032, India



Dr. Swapankumar Ghosh

M.Tech. (Gold Medal), PhD (DCU, Dublin), Fellow IICer

Senior Principal Scientist & Head, PMD

Professor, Engineering Sciences, AcSIR

CERTIFICATE FROM THE SUPERVISOR/S

This is to certify that the thesis entitled “**Shape & Size-Tuned Magnetic Nanostructures and Ferrofluids for Biomedical and Industrial Applications**” submitted by Ms. **Srividhya, J.**, who got her name registered on **March 27, 2013 (Index No.: FISLM/SMS&NT/P/14/01; Ref. No. D-7/E/269/14)** for the award of Ph. D. (ISLM) degree of Jadavpur University is absolutely based upon her own work under the supervision of mine and that neither her thesis nor any part of the thesis has been submitted for any degree/diploma or any other academic award anywhere before.

Date:

Kolkata

(Dr. Swapankumar Ghosh)

PhD supervisor



दूरभाष/Phone : निदेशक/Director : +91 33 2473 5829, कार्यालय/Office : 2473 3469/76/77/96; 2483 7340-46,2483 7349-50
DID Lines : 2483 8079/8082 फ़ैक्स/Fax : (033) 2473 0957,2473 6082,2483 7339,2483 8085 ई मेल/Email : dir_office@cgcri.res.in
वेब साइट/Website : www.cgcri.res.in



CERTIFICATE FROM THE SUPERVISOR/S

This is to certify that the thesis entitled “**Shape & Size-Tuned Magnetic Nanostructures and Ferrofluids for Biomedical and Industrial Applications**” submitted by **Ms. Srividhya, J.**, who got her name registered on **March 27, 2013 (Index No.: FISLM/SMS&NT/P/14/01; Ref. No. D-7/E/269/14)** for the award of Ph. D. (ISLM) degree of Jadavpur University is absolutely based upon her own work under the co-supervision of mine and that neither her thesis nor any part of the thesis has been submitted for any degree/diploma or any other academic award anywhere before.

Date:

Kolkata

(Dr. Chandan Kumar Ghosh)

PhD co-supervisor

Dedication

To my mother

Acknowledgement

I have waited eagerly to write this section and always thought that it would be the easiest part of this thesis on the contrary it is proving to be quite difficult. It has been a long trudge to accomplish my dissertation for doctoral degree, but the experience was enjoyable one during this period. This is a pleasant opportunity to acknowledge each and every individual, who have lent their expertise and cooperation nurtured my knowledge directly or indirectly in their own way to bring out this thesis would have seen possible.

On a more serious note, my heartfelt sincere gratitude goes to my advisor Dr. Swapankumar Ghosh, whom I am ever grateful for being an exceptional mentor. His instrumental expertise, insight into various experimental problems, wisdom and inspiration have allowed my research skills to develop, my innovativeness to flourish along with getting shaped as meticulous. His passion for research and broad knowledge always has been an inspiration to everyone around him. His constructive criticism and insightful thoughts, improved the quality of my work which augmented to its current form. If it weren't for his ideas, constant support, guidance, motivation and patience, none of this work would have been possible. Most importantly, he was always there whenever I needed his help, for making CGCRI 'a home far away from home' to me. I could not have wished for a better advisor. Thank you Sir, for everything you have done for me.

I am extremely indebted to Dr. Chandan Kumar Ghosh, my co-supervisor for lending his valuable time in engaging with scientific discussions regarding my work. Without his moral support and advices, it is impossible to reach this stage.

I am also obliged to the director of Central Glass & Ceramic Research Institute Dr. K. Muraleedharan for his great help in increasing the experimental facility at the Centre, which has proved to be a boon for our research work. He has provided all necessary lab facilities and made common to utilise everyone in this centre i.e., allowed the students to handle FTIR, XRD and do their own samples.

I would like to thank my dissertation committee members Dr. Kalyan K. Chattopadhyay, Dr. Gopes Chandra Das and Dr. Siddhartha Mukherjee, School of Materials and Nanotechnology, Jadavpur University, Kolkata for their time, support, suggestions and advice through the course of my thesis work. I thank Mr. Swarupnada Bhattacharya for helping me to learn Rietveld analysis.

Because of the research environment sustained by Dr. S. Ghosh, I have crossed paths with the number of Ph.D. students (Dr. V.S. Smitha, Dr. T.S. Sreeremya, Dr. Asha Krishnan, Dr. K. B. Jaimy) who have influenced and enriched my research in NIIST, Trivandrum where I joined initially. I'm extremely grateful to Dr. U.S. Hareesh allowing me to use his lab facilities and Mr. A. Peer Mohamed for extending his help any time regarding TG-DTA, BET surface area characterisation. A token of thanks are due Mr. Kiran for his TEM imaging, Dr. Manoj Raama Verma for PPMS, Thanks to Ms. Tanwistha Ghosh for her companionship during my initial days in Trivandrum and also

for her time to do FTIR measurement of few of my samples. I will never forget the hospitality rendered to me by Tanwistha Ghosh's family during my joining period as SRF.

My fellow lab friends Mr. Mathew, Dr. Somdutta Singha needs to be mentioned for their great contribution and support to my work. Dr. Jiten Ghosh for XRD, Dr. Awadesh Mallik for Raman spectroscopy, Dr. Dipten Bhattacharya for VSM, Mrs. Titir Maity for TEM, Mrs. Swati Samanta, Mrs. Moumita Kanu for various characterisation from MCID Division. I am also thankful to all those faculty members and students of the CSIR-CGCRI whose sincere cooperation and help at several instances have boosted my progress.

Special gratitude goes to Dr. R.K. Kotnala for his VSM facility and indispensable contributions to this work. My sincere thank must go to Prof. Parimal Karmakar, Department of Life Science & Biotechnology, Jadavpur University and Mr. Sujan Chatterjee for cell culture lab facility.

I gratefully acknowledge the Council of Scientific & Industrial Research (CSIR) of India for providing me a CSIR-Senior Research Fellowship. My PhD work was also financially supported by the 12Y5 network project ESC0103 and CSC0135.

Finally on a personal note, I really feel honoured for having wonderful parents, especially my mother Mrs. Usharani to whom I dedicate this thesis. She is my constant source of inspiration and provides me the strength to make my dreams come true, and my father Mr. Jagannathan for his encouragement throughout my educational endeavours. My heart bound thanks towards my younger brother Srinivasan and elder sister Sridevi for their endless love, care and support throughout my life. My special thanks to my brother directed me at right time to do PhD. During the later stage of my doctoral studies, unseen presence of my loving grandma, who would have been eternally delighted at this golden moment of my life, I believe my grandparent's heavenly blessings always there with me. A career in science would not have been possible without the great support from my family, who has always motivated me to chart my own path in life. Without their sacrifices, moral supports and blessings this thesis would not have taken its shape.

All of the above, I bow before 'Almighty' for giving me an opportunity, good health, courage and determination to achieve all personal and professional milestones in life. I believe, I could complete the course only because of the immense blessings showered over me by Almighty.

(Srividhya J.)

September, 2016

Synopsis

This thesis examines different aspects of magnetic nanocrystal fabrication, and examines a number of different synthetic protocols. A variety of morphology and size of magnetite nanoparticles are investigated, including ultrafine nanoparticles, nanocubes, nano-truncated octahedra, nanospheres and microspheres. Core-shell nanostructures, stable aqueous/non-aqueous ferrofluids were also prepared. The thesis entitled “*Shape & Size-Tuned Magnetic Nanostructures and Ferrofluids for Biomedical and Industrial Applications*” includes 6 chapters.

Chapter 1 gives the general introduction and brief review of magnetic nanomaterials, recent development of magnetic nanomaterials, crystal structure, various synthetic route, methods to stabilise the magnetic nanocrystals in aqueous and non-aqueous fluid and their practical applications.

Chapter 2 cover the materials used for fabrication of magnetite nanocrystals, various assay such as Bradford’s assay, cytotoxicity assay. The as-synthesised nanocrystals have been characterised by dynamic light scattering, XRD, TEM, SEM, TG-DTA, magnetic measurements by PPMS, VSM and spectroscopic measurements such as Mössbauer, XPS, UV-vis, FTIR, ICP-AES, and Magneto-rheological properties.

Chapter 3 Core-shell nanostructures of superparamagnetic magnetite/maghemite with tunable size were synthesised by aqueous coprecipitation method. The phase transformation of magnetic NPs subjected to temperature or laser induced oxidation were also investigated. The aqueous ferrofluid were made by proper surface functionalisation with tetramethylammonium hydroxide, starch, dextran, aminosilane etc. The magnetically switchable rheological properties of oil based ferrofluid were also prepared.

Chapter 4 Magnetite nanocrystals were precipitated in alcohol-water mixed solvents of varying dielectric constant at two different temperatures. The key colloidal properties such hydrodynamic size and surface charge of nanocrystals born in polyol-water media were thoroughly investigated by light scattering method against ageing time, temperature.

Chapter 5 Highly monodisperse sphere, cube, truncated octahedra magnetite nanocrystals of size in the range of ultra small 6.5 nm to large 135 nm were fabricated. Detailed structural, morphological and magnetic properties were studied. The cytotoxicity assay on two different cell lines: HCT-116 and MDA-MB-426 were studied after incubation with magnetic NPs

Chapter 6 summarises the important outcome of data obtained from third to fifth chapter and it describes a major findings of the whole investigations carried out throughout the thesis with the highlights of the recommendations for future scope/research.

Date:

(Srividhya J.)

Contents

	Page
Title Page	i
Certificate	ii
Dedication	iv
Acknowledgement	v
Synopsis	vii
Contents	viii
List of Publications	xiii
List of Presentations in National/International Conferences	xiv
List of Symbols and Abbreviations	xvi
Chapter One	1
Introduction	
1.1 Nanoscale materials	2
1.1.1 Generations of nanotechnology products	4
1.1.2 Types of nanomaterials and their dimension	4
1.1.3 Overview of nanomaterials in biomedical applications	5
1.2 Shape and size control of nanocrystals	5
1.3 Magnetism and magnetic materials	8
1.3.1 Magnetic classification of matter	9
1.3.2 Superparamagnetism	9
1.3.3 Magnetic anisotropy	11
1.4 Iron and iron oxides	12
1.4.1 Physical properties of Iron oxide	16
1.4.2 Occurrences of magnetite nanoparticles	16
1.4.3 Oxidation of magnetite	18
1.4.4 Surface chemistry of magnetite	18
1.5 Size- and shape-dependent magnetic properties	19
1.6 Magnetitic nanofluids/ferrofluids	20
1.6.1 Non-aqueous ferrofluids	21
1.6.2 Aqueous ferrofluids	21
1.6.3 Stabilisation of nanocrystals against aggregation	23
1.6.3.1 Electrostatic stabilisation	23
1.6.3.2 Steric / entropic stabilisation	26
1.6.4 Clustering and aggregation in aqueous suspension	29
1.7 Methods of fabricating nanostructures	30
1.8 Why surface functionalisation	34
1.8.1 Protein adsorption capacity	35

1.8.2	Biocompatibility	35
1.9	Applications of iron oxide NPs	36
1.10	Motivation and scope of the thesis	39
1.11	Objectives of the present work	40
 Chapter Two		 41
Materials and Instrumental Methods		
2.1	Materials	41
2.1.1	Fabrication of magnetite nanocrystals and ferrofluids	41
2.1.2	Cell viability assay	41
2.2	Characterisation techniques	42
2.2.1	Dynamic light scattering	42
2.2.1.1	Hydrodynamic size and its distribution	45
2.2.1.2	Surface charge or zeta potential	46
2.2.2	X-ray diffraction	47
2.2.3	Electron microscopy	50
2.2.3.1	Transmission electron microscopy	50
2.2.3.2	Field emission scanning electron microscope	53
2.2.4	Magnetic measurements	53
2.2.4.1	Magnetisation versus magnetic field	53
2.2.4.2	ZFC-FC curves	56
2.2.5	Spectroscopic measurements	58
2.2.5.1	Mössbauer spectroscopy	58
2.2.5.2	X-ray Photoelectron spectroscopy	59
2.2.5.3	Fourier transform infrared spectroscopy	60
2.2.5.4	Raman spectroscopy	60
2.2.5.5	UV–visible spectroscopy	62
2.2.5.6	ICP-Atomic emission spectroscopy	63
2.2.6	Thermogravimetry and differential thermal analysis	63
2.2.7	BET Surface area	63
2.2.8	Rheological properties: viscosity	64
 Chapter Three		 67
Aqueous coprecipitation method		
3.1	Graphical abstract	67
3.2	Introduction	69
3.3	Experimental	71

3.3.1	Aqueous coprecipitation	71
3.3.1.1	Effect of precipitation temperature	72
3.3.2	Surface functionalisation	72
3.3.2.1	Peptisation with TMAH	72
3.3.2.2	APTES modified starch/dextran coated MNPs	73
3.3.3	Magnetite calcinations at different temperatures	73
3.3.4	Phase transfer	73
3.4	Results and discussion	74
3.4.1	Aqueous coprecipitation	74
3.4.1.1	Physical/structural examination of NPs	75
3.4.1.2	Detailed X-ray diffraction analysis	77
3.4.1.3	Langevin fitting on magnetisation measurements	80
3.4.1.4	Lorentzian site analysis on Mössbauer spectra	83
3.4.1.5	XPS spectral analyses	85
3.4.2	Aqueous ferrofluid	86
3.4.2.1	Colloidal properties of functionalised MNPs	86
3.4.2.2	Stability as a function of temperature	90
3.4.2.3	Ageing study on aqueous ferrofluid stability	91
3.4.2.4	Physico-chemical measurements	94
3.4.3	Phase transformation	96
3.4.4	Non-aqueous ferrofluid	100
3.4.4.1	Heptane based ferrofluid	100
3.4.4.2	Magneto-rheology of oil based ferrofluid	100
3.4.4.2.1	Effect of shear rate on viscosity	100
3.4.4.2.2	Effect of shear rate on shear stress	103
3.4.4.2.3	Effect of cyclic magnetic field on viscosity	104
3.4.4.2.4	Effect of magnetic switching	105
3.5	Conclusions	106
Chapter Four		109
	Coprecipitation in Alcohol-Water	
4.1	Graphical abstract	109
4.2	Introduction	110
4.3	Experimental	112
4.3.1	Coprecipitation in alcohol-water mixed solvents	113
4.3.2	Effect of time	114
4.3.3	Catalytic activity	114
4.4	Results and discussion	114
4.4.1	Magnetic powder characterisation	114

4.4.1.1	TEM characterisation	114
4.4.1.2	XRD analysis	118
4.4.1.3	Magnetic property	120
4.4.1.4	BET surface area analysis	122
4.4.1.5	Surface chemistry	123
4.4.2	Colloidal properties of aqueous ferrofluid	124
4.4.2.1	Hydrodynamic size and surface charge measurement	124
4.4.2.2	pH dependent surface charge measurement	127
4.4.2.3	Temperature dependent hydrodynamic properties	128
4.4.2.3.1	PEG based colloids	128
4.4.2.3.2	DEG based colloids	129
4.4.3	Comparison of particles size from various techniques	135
4.4.4	Catalytic property of MNPs powder	136
4.5	Conclusions	137
Chapter Five		139
Shape Selective Fabrication		
5.1	Graphical abstract	139
5.2	Introduction	141
5.3	Experimental	143
5.3.1	Fabrication of magnetite sphere	143
5.3.1.1	Acid mediated collapse on microspheres	144
5.3.2	Silica precursor extraction from rice husk ash	144
5.3.3	Core-shell nanostructures	145
5.3.3.1	Magnetite microspheres@silica	145
5.3.3.2	Silver decorated magnetite nanospheres	145
5.3.4	Fabrication of magnetite cube	145
5.3.5	Fabrication of magnetite truncated octahedral	146
5.3.6	Non-specific adsorption of proteins	146
5.3.7	<i>In vitro</i> biocompatibility assessment	147
5.3.7.1	Cell culture and exposure to nanomaterials	147
5.3.7.2	Cell staining	148
5.4	Results and discussion	149
5.4.1	Solvothermal method	149
5.4.1.1	Physico-chemical characterisation of nano/microspheres	149
5.4.1.2	Core-shell nanostructures	155
5.4.1.3	Protein adsorption capacity	160

5.4.1.4	Cell culture: Dose dependent cytotoxicity assessment	160
5.4.1.5	Fluorescent microscopic examination of cells	161
5.4.2	Thermal decomposition method	162
5.4.2.1	Physico-chemical characterisation of cube/truncated octahedra	162
5.4.2.2	Lorentzian site analysis on Mössbauer spectra	167
5.4.2.3	ZFC-FC magnetic measurements	169
5.4.2.4	XPS spectra analysis	171
5.4.3	Cell culture: Dose dependent cytotoxicity of MNPs	172
5.4.3.1	Fluorescent microscopic examination of cells	173
5.5	Conclusions	175
Chapter Six		177
Overall conclusion and future prospects		
References		181
Appendices		201
Publications		

List of Publications

1. Magnetic, X-ray and Mössbauer studies on magnetite/maghemite core-shell nanostructures fabricated through an aqueous route, **Srividhya J. Iyengar**, Mathew Joy, C. K. Ghosh, S. Dey, R. K. Kotnala and Swapankumar Ghosh, *RSC Adv.*, 2014, 4(110) 64919–29.
2. Colloidal properties of water dispersible magnetite nanoparticles by photon correlation spectroscopy, **Srividhya J. Iyengar**, M. Joy, T. Maity, J. Chakraborty, R. K. Kotnala and Swapankumar Ghosh, *RSC Adv.*, 2016, 6, 14393–14402.
3. Fabrication of magnetite nanocrystals in alcohol/water mixed solvents: catalytic and colloid property evaluation, **Srividhya J. Iyengar**, M. Joy, A. P. Mohamed, S. Samanta, C. K. Ghosh and Swapankumar Ghosh, *RSC Adv.*, 2016, 6, 60845–60855.
4. Growth of hierarchical hexagonal layered double hydroxide crystals to large elongated spindle shaped particles, M. Joy, **Srividhya J. Iyengar**, J. Chakraborty and Swapankumar Ghosh, *J. Nanosci. Nanotechnol.*, 2016, 16, doi:10.1166/jnn.2016.12533.
5. Ultra-thin cerium oxide nanostructures through a facile aqueous synthetic strategy, T. S. Sreeremya, A. Krishnan, **Srividhya J. Iyengar** and Swapankumar Ghosh, *Ceram. Int.*, 2012, 38(4) 3023–28.
6. Clustering behaviour in aqueous slurry of magnetite nanoparticles at different temperatures by photon scattering, **Srividhya J. Iyengar**, M. Joy and Swapankumar Ghosh, *Trans. Ind. Ceram. Soc.*, 2017, doi: 10.1080/0371750X.2017.1299591.
7. Layered double hydroxide crystals using hydrothermal treatment: Morphology evolution, intercalation and release kinetics of diclofenac sodium, M. Joy, **Srividhya J. Iyengar**, J. Chakraborty and Swapankumar Ghosh, (Communicated to *Mater. Chem. Front.*) on Jan 28, 2017.

List of Presentations in National/International Conference

1. Fabrication and *in vitro* cytotoxicity evaluation of silver decorated magnetite nanospheres, **Srividhya J. Iyengar**, M. Joy, P. Karmakar, Swapankumar Ghosh in 79th Annual Session of **Indian Ceramic Society**, poster-48, p. 110 during Dec 13-15, 2016 held at CSIR-IICT, Hyderabad.
2. Nitrate interlayered ZnAl-LDH using hydrothermally assisted urea hydrolysis, M. Joy, **Srividhya J. Iyengar** and Swapankumar Ghosh in 79th Annual Session of **Indian Ceramic Society**, poster-14, p. 82, during Dec 13-15, 2016 held at CSIR-IICT, Hyderabad.
3. **Second best award** for the poster entitled “Ultra-stability of aqueous/non-aqueous magnetite nanofluid against temperature and ageing time: an insight through Photon Correlation Spectroscopy”, **Srividhya J. Iyengar**, Swapankumar Ghosh *et al.*, in National Conference on Nanotechnology: Materials & Applications (**NCoN:M&A**), poster-71, p. 90 during June 16-17, 2016 held in Jadavpur University, Kolkata.
4. Growth of monodispersed anisotropic magnetite nanocrystals by ‘bottom-up’ approach, **Srividhya J.**, poster presentation (PII-5) in Research Scholar’s day **4th one day workshop** abstract book Vol-4 on September 18, 2015 held in CSIR-CGCRI, Kolkata.
5. **Second best award** for the poster entitled “Size tailored monodisperse magnetite spherical nanoclusters with silica shell for biomedical applications”, **Srividhya J. Iyengar**, Swapankumar Ghosh *et al.*, in International Conference on Alumina and Other Functional Ceramics (**AOFC-2015**), poster 5, p. 89 during 11-13 March, 2015, held in CSIR-CGCRI Kolkata.
6. Fabrication of Functionalised Magnetite Nanocrystals for Biomolecule Interaction, **Srividhya J. Iyengar** and Swapankumar Ghosh *et al.* for oral presentation in 78th Annual Session of **Indian Ceramic Society**, pp. 30 held in Jamshedpur during 2-3 February, 2015.
7. A magnetic and mössbauer spectral study on growth of magnetite nanocrystals, **Srividhya J. Iyengar**, Swapankumar Ghosh *et al.* for poster presentation in 102nd **Indian Science Congress**, Poster 25, pp. 63, during 3-7 January 2015 in Mumbai.
8. Dielectric constant of the solvent allows control over the growth and surface functionalisation of nanocrystalline magnetite, **Srividhya J. Iyengar**, Swapankumar Ghosh, 7th **Bangalore India Nano**, Poster 29 during December 5-6, 2014 in Bangalore.
9. Efficient nanoceramic drug delivery matrices derived from layered double hydroxide, M. Joy, **Srividhya J.**, S. Ghosh *et al.* in International Seminar on “Emerging Materials: Characterisation & Application (**EMCA-2014**)”, during December 4-6, 2014 at CGCRI, Kolkata.

10. 'Core-shell nanostructures in pristine and aminoacid capped magnetite for health care application', **Srividhya J.**, for poster presentation (PII-21) in Research Scholar's Day **3rd Annual Workshop** abstract book Vol-3, held in CSIR-CGCRI, Kolkata on August 20, 2014.
11. "Growth Kinetics, Crystal Dimension and Lattice Strain in Size Tailored Monodisperse Magnetite Nanocrystals for Nano-Biomedicine", **Srividhya J. Iyengar**, Swapankumar Ghosh, *et al.* for oral presentation in 77th Annual Session of **Indian Ceramic Society** as P49 held in Jamshedpur during 19-21 December, 2013.
12. "Size-controlled magnetocrystalline Fe₃O₄ SPIONS by facile aqueous synthetic strategy", **Srividhya J. Iyengar**, Swapankumar Ghosh *et al* for poster presentation in Proceedings of the **NANO INDIA-2013** as P32, pp. 63 held in Trivandrum during February 19-20, 2013.
13. Synthesis and optical properties of fluorescent cerium oxide nanoparticles, A. Krishnan, T.S. Sreeremya, **Srividhya J. Iyengar**, M. Joy, S. Ghosh, **Indian Science Congress** in Section IX: Materials Science as NP12, pp. 87 during 3-7 January 2013 in Kolkata.
14. "Monodisperse superparamagnetic magnetite nanocrystals by a facile aqueous method" by **Srividhya J. Iyengar**, M. Joy, Sreeremya T.S., Asha Krishnan, Swapankumar Ghosh in a National seminar on **Smart Materials for a Smarter World** pp. IT3 in Changanassery, Kerala during September 27-28, 2012.

List of Symbols and Abbreviations

MNPs	Magnetic nanoparticles
NPs	Nanoparticles
IEP	Isoelectric point
PZC	Point of Zero Charge
DLVO	Derjaguin–Landau–Vervey–Overbeek
EG	Ethylene glycol
DEG	Diethylene glycol
EA	Ethanol
<i>n</i> PA	<i>n</i> -propanol
IPA	Isopropanol
PEG	Polyethylene glycol
XRD	X-ray diffraction
TEM	Transmission electron microscopy
TG-DTA	Thermogravimetry and differential thermal analysis
BET	Brunauer-Emmett-Teller
VSM	Vibrating sample magnetometry
JCPDS	Joint Committee on Powder Diffraction Standards
PCS	Photon correlation spectroscopy
SAED	Selected area electron diffraction
EDS	Energy dispersive spectrometry
BJH	Barrett–Joyner–Halenda
PDI	Polydispersity index
CI	Crystallinity index
M_S	Saturation magnetisation
M_R	Remanent magnetisation
H_C	Coercivity
D_{XRD}	Crystallite size
D_{TEM}	Physical size
D_{mag}	Magnetic size
D_{PCS}	Hydrodynamic size
D_{SA}	Surface area size
ζ	Zeta potential

Introduction

This thesis relates to the fabrication and characterisation of magnetic nanoparticles (MNPs), a remarkable class of material that has attracted considerable interest within the scientific community due to their interesting properties and potential applications across a range of disciplines. Iron oxides (IO) are sensitive to changing conditions such as pH, temperature and the study of their transformations is the subject of environmental mineralogy. The sizes, shapes and compositions of magnetite nanocrystals are the subject of research in several areas of mineralogy. In geophysics and geology, an important mineralogical tool is the measurement of magnetisation preserved in rock-forming magnetite crystals for the determination of the relative ages and the ancient positions of the rocks relative to Earth's magnetic field. Researchers of biomineralogy are interested in the special properties of magnetite crystals that form directly or indirectly by the activity of organisms. Materials scientists are interested in synthetic magnetite grains produced for nanotechnological applications. The scientific research of magnetite has gained significant impetus in the past decade as a result of a debate that centers on the biogenic or inorganic origin of nanocrystalline magnetite found in Martian meteorite ALH84001 (Gibson Jr *et al.*, 2001). All biomimetic synthesis processes involve a precipitation reaction in which magnetite crystals are produced from inorganic components. The chemical synthesis of NPs is an emergent and diverse area of research, driven by the need to understand the relationship between a particle's morphology and its physical properties. Understanding this enables researchers to tailor the properties of particles for a specific application, although it is often far from trivial to synthesis 'high quality' NPs with a narrow size distribution, high degree of shape selectivity and possess a uniformly crystalline. Each chapter in this thesis relates to a different aspect or approach to MNP synthesis with size tuning and/or morphology control, physico-chemical characteristics and colloidal stability of its aqueous/non-aqueous suspensions. Before discussing in more details of the present study, the importance, background, applications of magnetite NPs and the published synthetic protocols are discussed in this chapter.

1.1 Nanoscale materials

Nobel laureate Dr. Richard Feynman's prediction in his landmark speech titled "There's plenty of room at the bottom" to the American Physical Society at California Institute of Technology (Caltech) on December 29, 1959 (Feynman, 1959). Feynman is considered to be the "father of nanotechnology" because he conceptually presented, motivated, and challenged people with the desire and advantages of exploring engineered devices at the small scale in his legendary lecture. Also in the 1980s, Eric Drexler wrote several books that went beyond Feynman's vision to outline a fantastic technology that includes pumps, gears, and molecular assemblers consisting of only hundreds to thousands of atoms that, if built, promised to revolutionise almost every aspect of human endeavour.

Nanostructured or nanophase materials are made of nanometer-sized, having at least one dimension between one and a hundred nanometres, substances engineered on the atomic or molecular scale to produce either new or enhanced physical properties not exhibited by bulk solids. Research interest in nanomaterials has ballooned in recent decades, driven by their potential applications in a large number of fields. What is interesting about nanomaterials is that they often possess unique physical, chemical, optical or magnetic properties, which differ to those of their bulk counterparts of the same composition, are often shape and size dependent and can be controlled by varying the dimensions of the nanomaterials. Due to their small dimensions, the large fraction of atoms residing in the grain boundaries and interfaces of nanomaterials allow interface atomic arrangements to constitute significant volume fractions of material, and thus novel "surface" dependent materials properties [Fig. 1.1].

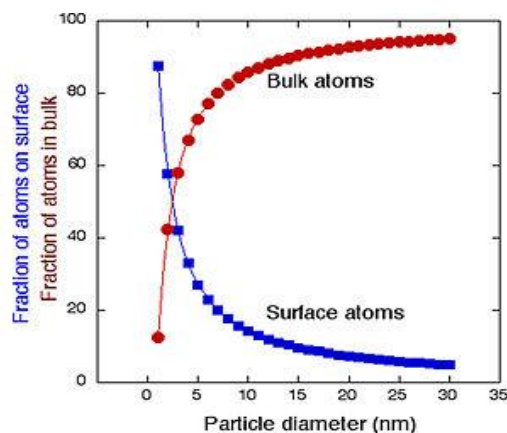


Fig. 1.1 Calculated surface to bulk ratios for solid metal particles versus size. The percentage of surface atoms increases while reducing from bulk to nanometer scale.

Most of the following properties are tuneable with size.

- Reduced melting point: Nanomaterials may have a significantly lower melting point (the difference can be as large as 1000°C) or phase transition temperature and appreciably reduced lattice constants due to a huge fraction of surface atoms in the total amount of atoms.
- Ultra hard–mechanical properties of nanomaterials may reach the theoretical strength, which are one or two orders of magnitude higher than that of single crystals in the bulk form. The enhancement in the mechanical strength is simply due to the reduced probability of defects.
- Band gap broadening: semiconductors become insulators
- Optical properties of nanomaterials such as blue shift in adsorption and emission due to an increased band gap [quantum size effects], metallic NPs changes colour in spectra due to surface plasmon resonances [Lorentz oscillator model].
- Electrical conductivity decreases with reduced dimension due to increased surface scattering. Electrical conductivity increases due to the better ordering and ballistic transport.
- Magnetic properties of nanostructured materials are distinctly different from that of bulk materials. Ferromagnetism disappears and transfers to superparamagnetism in the nanometer scale due to single domain.
- Self-purification is an intrinsic thermodynamic property of nanostructures and nanomaterials due to enhanced diffusion of impurities/defects/dislocations to the nearby surface.
- Exhibit enhanced catalytic properties (e.g., nano Au, Ag, ceria, iron oxide particles)

In order to explore novel physical properties/phenomena and realise potential applications, the ability to fabricate and process the nanomaterials and nanostructures is the first corner stone in nanotechnology.

The emergence of improved characterisation techniques (such as the advances made to transmission electron microscopy) have allowed researchers to probe the precise nature of nanomaterials, enabling the relationships between size, shape, elemental composition and physical properties of a material to be investigated. As such, the ability to develop ‘tunable’ nanomaterial syntheses (which can produce a high-quality nanomaterial product with properties pre-determined for a particular application) has emerged as a major research goal for scientists. The last decade alone has seen a dramatic rise in the

number of published reports relating to nanoscale science, from 18,000 in 2000 to ~155,000 in 2016 (Web). Within nanoscale research a number of distinct research branches have emerged, each relating to the study of a particular type of nanomaterial and its applications. It is therefore prudent to first provide an overview of the different types of nanomaterial that can currently be produced, so the work contained within this thesis can be appreciated within the context of nanomaterial synthesis in general.

1.1.1 Generations of nanotechnology products

There are hundreds of commercially available products using nanotechnology currently in the market including cosmetics, sunscreens, textiles and sport items, veterinary medicines etc. Roco predicted four overlapping generations of nanotechnology products from 2000 to 2020 (Roco, 2006). The first generation involved the simple components of NPs, nanotubes, nanolayers and nanocoatings. The second generation (after 2005) involves active nanostructures that change their properties (morphology, shape, magnetic, biological, etc.) during operation. Examples are targeted drugs and chemicals, energy storage devices, transistors and so on. In the third generation (after 2010) includes nanosystems that might self-assemble or self-organise. Examples are artificial organs and electronic devices. The fourth generation (after 2015-2020) includes molecular nanosystems, where each molecule in the nanosystem has a specific structure and plays a different role.

1.1.2 Types of nanomaterials and their dimension

The nanomaterials are usually classified according to their morphologies (see Fig. 1.2).

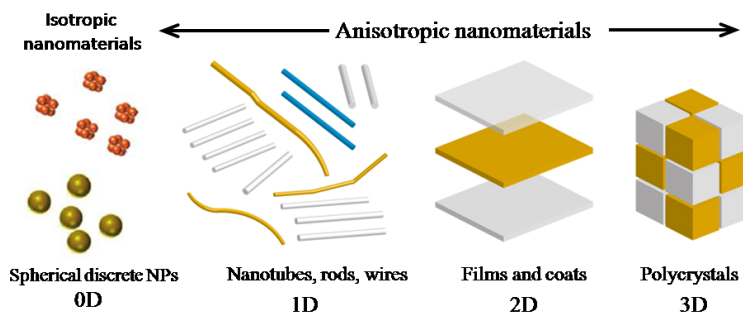


Fig. 1.2 Different types of nanomaterial a) spherical discrete nanoparticle, b) high aspect ratio nanowire, c) hollow nanotube and d) thin film of material, provided thickness (t) is less than 100 nm.

Nanozymes are nanomaterials with enzyme-like characteristics (Wei and Wang, 2013). They are an emerging type of artificial enzyme, which have been used for wide

applications in such as biosensing, bioimaging, tumour diagnosis and therapy, antibiofouling, etc.

1.1.3 Overview of nanomaterials in biomedical applications

Recently, the integration of nanotechnology with molecular biology and genomics has set into motion to the extensive development of an emerging research area, which offers exciting and abundant opportunities for discovering new processes, phenomena, and results in science, especially in biology and medicine. Nanoscale materials have now been exploited in many biological applications, such as biosensor, biological separation, molecular imaging, and anticancer therapy (Table 1.1).

Table 1.1 Typical inorganic NPs and their biomedical applications

Category	Examples	Intrinsic properties	Biomedical applications
Metallic NPs (Qiu <i>et al.</i> , 2016)	Au, Ag	Surface plasmon resonance, Surface reactivity, Catalysis	Chemical/biochemical sensing, disease diagnostics; optical imaging, Raman probe; photothermal cancer therapy; drug delivery; antimicrobial agents.
Semiconduct NPs or Quantum dots (Kumar and Nann, 2006)	CdSe, CdS, CdTe	Fluorescence, Luminescence	Cellular imaging; long-term cell trafficking; diagnostics and sensing based on energy transfer techniques.
Metal oxide NPs (Ghosh <i>et al.</i> , 2010)	Fe ₃ O ₄ , Fe ₂ O ₃ , Ferrite	Superparamagnetic, Large magnetic moments in a magnetic field	MRI, magnetic hyperthermia, separation area, theranostics; diagnosis and monitoring, target delivery of drugs / genes

1.2 Shape and size control of nanocrystals

Nano magnetite exhibits unique and tunable fundamental size- and shape-dependent magnetic, optical, and other properties (Iyengar *et al.*, 2014). The unique chemical and physical properties of nanocrystals are determined not only by the large portion of surface atoms but also by the crystallographic structures of the particle surface. The former is determined by the size of the particles and the latter relies on the particle shape. Shapes occur either in order to minimize the surface energy of the particles or because of the kinetics of the growth. If kinetics controlled process dominates, the shape is determined by the rate at which the different crystal faces grow. If the particles are formed in thermal equilibrium, their shape or crystal habit results from minimising the surface energy. In the later case, the surfaces are determined by performing a Wulff construction (Kumar and Nann, 2006). Surface energies associated with different crystallographic planes of *fcc*

crystals follow the sequence $\gamma\{111\} < \gamma\{100\} < \gamma\{110\}$ (Wang *et al.*, 2012). The difference in growth rates between crystal facets can be determined by consideration of the free energies of each facet. The free energy γ of each facet can be calculated by considering the number of broken bonds on the surface, the bond strength and the density of surface atoms, given by

$$\gamma = \frac{1}{2}N_b\varepsilon P_a \quad (1.1)$$

where N_b is the number of broken bonds, ε is the bond strength, and P_a is the density of surface atoms (Douglas, 2012).

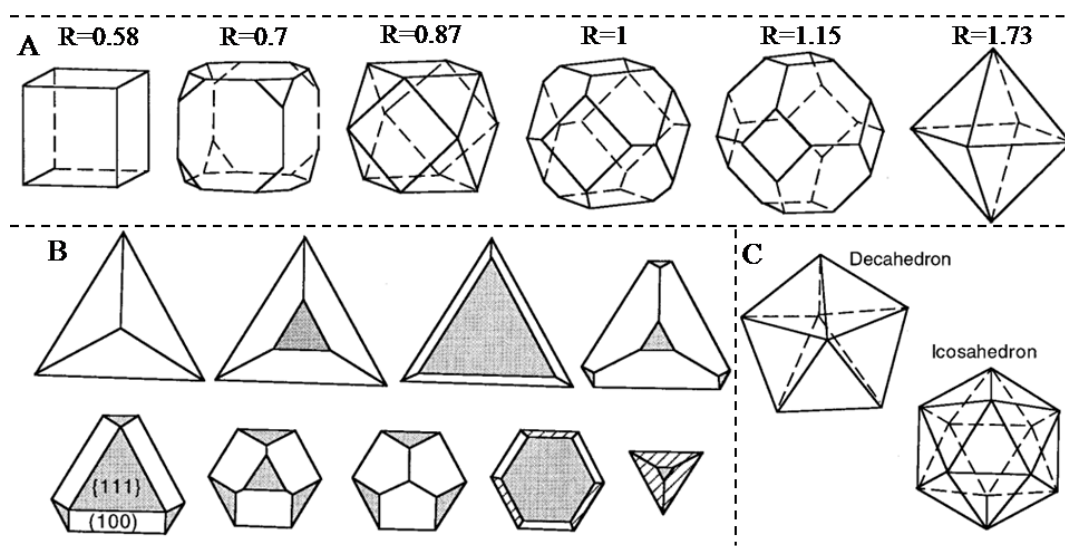


Fig. 1.3 (A) Geometrical shapes of cubooctahedral nanocrystals as a function of the ratio, R , of the growth rate along the (100) / (111) . (B) Evolution in shapes of a series of $\{111\}$ based nanocrystals as the ratio of $\{111\}$ to $\{100\}$ increases. The beginning crystal is bounded by three $\{100\}$ facets and a $\{111\}$ base, while the final one is a $\{111\}$ bounded tetrahedron. (C) Geometrical shapes of multiply twinned decahedral and icosahedral crystals.

Fig. 1.3A shows a group of cubooctahedral shapes as a function of the ratio, R , of the growth rate in the (100) to that of the (111) . The longest direction in a cube is the (111) diagonal, the longest direction in the octahedron is the (100) diagonal, and the longest direction in the cubooctahedron ($R=0.87$) is the (110) direction. The crystals with $0.87 < R < 1.73$ have the $\{100\}$ and $\{111\}$ facets, called as truncated octahedra. The other group of particles has a fixed (111) base with exposed $\{111\}$ and $\{100\}$ facets (Fig. 1.3B). An increase in the area ratio of $\{111\}$ to $\{100\}$ results in the evolution of crystal shapes from a triangle-based pyramid to a tetrahedron. For a spherical single-crystalline particle, its surface must contain high-index crystallography planes, which possibly result in a higher surface energy. Facets tend to form on the crystal surface to increase the portion of

the low-index planes. As a result, for crystals smaller than ~20 nm, the surface is a polyhedron. Both the octahedral and tetrahedral morphologies have larger surface area to volume ratios than a cube of the same volume however, single crystal NPs exist as truncated octahedra which are enclosed by a mixture of {111} and {100} facets, as shown in Fig. 1.3A. The truncated octahedra has a nearly spherical profile and a low surface area to volume ratio, meaning the overall free surface energy is lower than for the octahedral or tetrahedral shapes.

One can tune the crystal size and shape via controlling the growth rate of different facets in a delicate balance either by utilizing the inherent crystal structure property or by external factors such as application of adsorbed species (surfactant molecules or ions) different solvent, temperature, heating rate, time, etc. The adsorbed species are usually ‘molecular capping agents’ that can selectively bind onto specific crystal facets during crystal growth which causes a reduction in growth at this facet. Those facets where adsorbed species are weakly bound will experience increased growth. The degree to which binding occurs at any given site is determined by the surface energies of each facet, and by the affinity of the capping agent used for a particular material. The length of the hydrocarbon backbone of surfactants can also control particle shape and size by determining the packing of surfactants on a particle surface. The long chain surfactants enables them to spontaneously form lamellar species, similar to liquid crystals, can act as nano-reactors in which constrained or anisotropic growth of NPs can occur (Chen *et al.*, 2007). Shorter surfactant molecules will not be able to separate particles in solution as efficiently as longer molecules, meaning that aggregation among particles is more likely to occur, leading to larger particles. An *et al.* reported that increasing the surfactant chain length from decanoic acid (C₉H₁₉COOH) to behenic acid (C₂₁H₄₃COOH) resulted in the size of MnO NPs reducing from 13 nm to 3 nm (An *et al.*, 2012). Kovalenko and co-workers could tune the morphology by changing the stabilisers; sodium oleate could lead to nanocubes, potassium oleate generated a mixture of nanocubes with bipyramidal morphologies while OA and dibutylammonium oleate gave spherical shape (Kovalenko *et al.*, 2007).

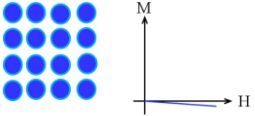
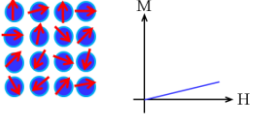
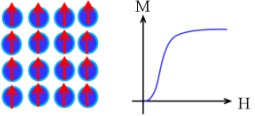
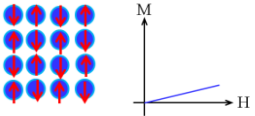
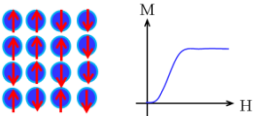
The above discussions highlight the considerable number of underlying processes that can contribute to NP formation. It is clear that understanding the complexities of NP synthesis requires thorough and systematic study across a large number of variables, and there is still much work to be done before the nature and role of the species involved in the nucleation and growth processes is fully understood. As this thesis is concerned with the

fabrication of magnetite NPs, some discussion of magnetism, size effects (superparamagnetism), crystal structure, physical/ magnetic properties, different synthetic methodology, factors concern about aqueous as well as non-aqueous ferrofluids and the potential applications of MNPs are required and are given in the following sections.

1.3 Magnetism and magnetic materials

Magnetic materials are classified by virtue of their response to an externally applied magnetic field. The orientations of the magnetic moments in a material help to identify different forms of magnetism observed in nature.

Table 1.2 Summary of the different types of magnetic behaviour with suitable examples

Magnetism	Example	Atomic/magnetic behavior	
Dia	Inert gases, Many metals i.e., Au, Cu, Hg, non-metallic elements i.e., B, Si, P, S, many ions i.e., Na ⁺ , Cl ⁻ & their salts, diatomic molecules i.e., H ₂ , N ₂ , H ₂ O, most organic compounds	Atoms have no magnetic moment. Susceptibility is small & negative, 10 ⁻⁶ to 10 ⁻⁵	
Para	Some metals, i.e., Al; Some diatomic gases, i.e., O ₂ , NO; ions of transition metals and rare earth metals and their salts, rare earth oxides	Atoms have randomly oriented magnetic moments. Susceptibility is small & positive, +10 ⁻⁵ to +10 ⁻³	
Ferro	Transition metals Fe, H, Co, Ni; rare earths with 64 ≤ Z ≤ 69; alloys of ferromagnetic elements; some alloys of Mn, i.e., MnBi, Cu ₂ MnAl.	Atoms have parallel aligned magnetic moments. Susceptibility is large (below T _C)	
Aniferro	Transition metals Mn, Cr & many of their compound, i.e., MnO, CoO, NiO, Cr ₂ O ₃ , MnS, MnSe, CuC ₁₂ .	Atoms have antiparallel aligned magnetic moments. Susceptibility is small & positive, +10 ⁻⁵ to +10 ⁻³	
Ferri	Fe ₃ O ₄ , γ-Fe ₂ O ₃ , mixed oxides of iron and other elements such as Sr ferrites	Atoms have mixed parallel and anti parallel aligned magnetic moments. Susceptibility is large (below T _C)	

If a magnetic field H induces magnetism M in a material, the material is said to possess a magnetic susceptibility

$$M = K H \quad (1.2)$$

$$\text{or } M = \chi H / V$$

where K is the susceptibility, which is dimensionless, or χ is the volume susceptibility, units $\text{m}^3 \cdot \text{kg}^{-1}$. In the SI system M and H are measured in units of Am^{-1} , where $1 \text{ Am}^{-1} = 4\pi/10^3 \text{ Oe}$. On a microscopic level the magnetism arises due to the presence of magnetic moments, a single unpaired electron has a moment of $1 \mu_B$, a Bohr magneton, where $1 \mu_B = 9.27402 \times 10^{-24} \text{ Am}^2$ and $1 \text{ Am}^2 \cdot \text{kg}^{-1} = 1 \text{ emu} \cdot \text{g}^{-1}$.

1.3.1 Magnetic classification of matter

Magnetic materials can be classified into few categories based on magnetic behaviour (Table 1.2). For example, materials having no magnetic moment in the absence of magnetic field are said to diamagnetic material. Paramagnetic material having magnetic moment in the absence of magnetic field exhibits zero magnetisation due to thermal energy induced randomization of their magnetic moment. Materials having mutually interactive magnetic moment possess net magnetization in the absence of magnetic field. An antiferromagnetic material contains two-sub magnetic lattice structure of antiparallel magnetic moment and gives zero magnetisation in the absence of magnetic field. If the magnetic of two sub-lattices is not equal, then they are said to be ferrimagnetic material. A complete discussion of the theories behind the different classes of magnetism materials is beyond the scope of this dissertation. But some appropriate fundamentals will be provided to address the magnetisation in ferrimagnetic NPs and their dispersions.

1.3.2 Superparamagnetism

It has been realised in the case of ferromagnetic materials that they exhibit domains where all moments are oriented parallel and the whole system consists of large number of such domains. Magnetisation differs from domain to domain. This happens due to minimizing the magnetostatic energy of the material. Size-dependent coercivity of magnetic materials and superparamagnetism was summarised by a double potential well diagram given in Fig. 1.4. For every ferromagnetic material, there exist critical diameter (R_{sd}) of the domain, expressed by the following equation

$$R_{sd} = \frac{36\sqrt{AK}}{\mu_0 M_s^2} \quad (1.4)$$

where A is the exchange constant, K is the effective anisotropy constant and M_s is the saturation magnetisation (Cornell and Schwertmann, 1996). For the majority of magnetic nanomaterials, R_{sd} will be in the range of 10-100 nm, though for materials with a high magnetic anisotropy (large K value) this value can be higher. For a single domain particle,

the amount of energy required to reverse the magnetisation over the energy barrier from one stable magnetic configuration to the other is proportional to $KV/k_B T$, where k_B is Boltzmann's constant, V is the particle volume and T is temperature (Lefebure *et al.*, 1998). If the ambient thermal energy is enough to overcome the anisotropy energy barrier, the magnetisation will no longer be stable and the NP is said to be superparamagnetic.

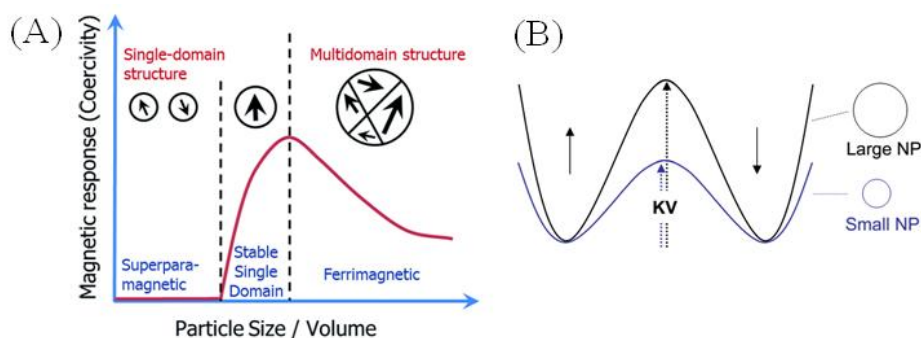


Fig. 1.4 Schematic illustration on (A) behaviour of size-dependent coercivity of magnetic particles and (B) potential well diagrams for small and large superparamagnetic particles. The energy barrier separating the two spin states is given by KV , with K the anisotropy constant and V the particle volume (Douglas, 2012).

In a superparamagnetic regime the magnetisation of the NPs can easily be saturated in the presence of an external magnetic field. Once the field is removed however, the ambient thermal energy is enough to randomise the magnetic moments of the particles, giving a zero net magnetisation –i.e., M_R (the remnant magnetisation) and H_C (the field required to bring the net magnetisation back to zero, known as the coercivity) are both zero. This can be visualised in the hysteresis loops given in Fig. 1.5, comparing the magnetic characteristics of a bulk ferromagnetic material with those of a single-domain superparamagnetic nanoparticulate material.

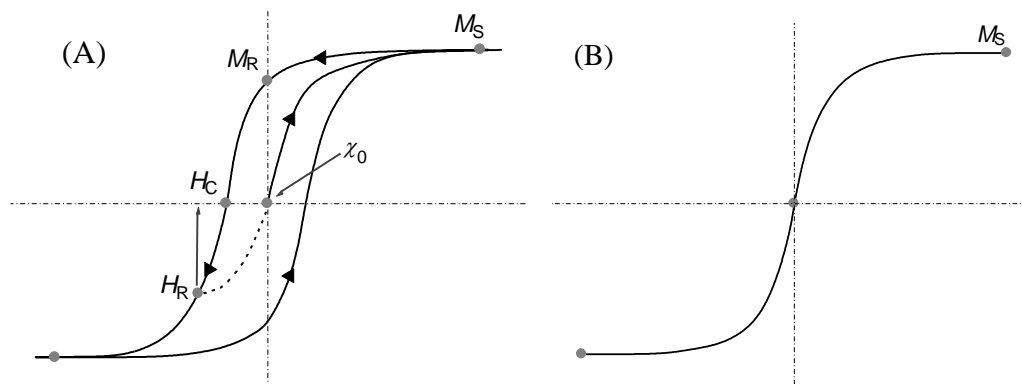


Fig. 1.5 Hysteresis loops for (A) a ferromagnetic and (B) a superparamagnetic nanomaterials

The M_S value of IONPs decreases with the particle size which is detrimental for the efficiency (relaxivity) of the NPs. This reduction of M_S has been attributed to surface effects (spin surface disorders, spin canting) (Corot *et al.*, 2006). The magnetic properties of superparamagnetic NPs lend them well to certain applications, more so than others. For example, the poor magnetic stability of such particles under ambient conditions has been a constant barrier in developing high density magnetic data storage devices. As such, developing procedures to synthesise NPs with high anisotropy constants that can counteract the thermal fluctuations that are apparent at small particle volumes is currently a high interest area of research. It is interesting to note that much of the earlier MNPs literature was carried out by IBM, as part of their search for high density data storage technologies (Sun *et al.*, 2000).

1.3.3 Magnetic anisotropy

Magnetic materials are very often anisotropic, in that there is a preference for the magnetisation to point along one direction as opposed to others. In a single domain particle, all the individual (atomic) magnetic moment are ferro or ferrimagnetically coupled in the whole volume, so that the magnetisation of the entire particle can be described by one magnetic moment. The anisotropy energy, E_a , may be defined by

$$E_a = KV \sin^2 \theta \quad (1.3)$$

where K is the magnetic anisotropy (volumic) density, V the particle volume and θ the angle between the easy axis and the magnetic moment directions. K is also sometimes called anisotropy constant which varies drastically with temperature (Ghosh, 2006).

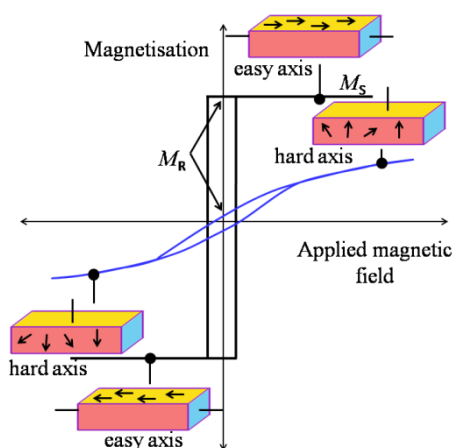


Fig. 1.6 The hysteresis loop where magnetisation (M) in the sample is shown against the external magnetic field strength (H) with easy and hard axes of magnetisation.

The difference between the response of a material along an easy axis and along a hard axis is illustrated in the hysteresis loop shown in Fig. 1.6. In the curve shown in black, a low applied field is required. It is “easy”, to drive all of the moments to point along a particular direction. Upon reducing the field to zero, the magnetisation remains constant since the moments are quite content to point along this axis. The blue curve shows that it is “hard” to saturate the moments along the direction perpendicular to easy axis. At a relatively large applied field, it is still the case that not all of the moments have been forced to align. Unlike the behaviour observed along the easy axis, the magnetisation decreases quite significantly as the applied field is reduced to zero. It is energetically less favourable for the moments to point along the direction in which the field was applied. The horizontal segments of the black hysteresis loop correspond to situations in which every moment in the sample has been forced to point to the left or to the right, as shown in the small drawings in the Fig. 1.6. When all of the moments in a magnetic sample are forced to point in the same direction, it is said that the sample has reached its M_s . Above this field no further magnetisation can be acquired. The remanence is much smaller in the case of the hard axis loop than it is when the field is applied along the easy axis.

1.4 Iron and iron oxides

Iron and its compounds are widespread in nature and readily synthesised in the laboratory. Iron compounds present in the hydrosphere, the lithosphere and (as pollutants) in the atmosphere. Iron is a biogenic element, present in all biota, but some iron compounds can cause harmful effects to humans, animals, and environment (Cornell and Schwertmann, 2003; Gurzau *et al.*, 2003). In occupational exposure of humans, iron and iron oxide (IO) are known to produce benign siderosis. Analyses of urban air samples showed that the probable sources of iron compounds are the iron and steel industry (Gurzau *et al.*, 2003) and urban transport such as underground railways (Luhar and Hurley, 2003). Tunnel dust—generated by interaction of brakes, wheels and rails—contains about 90% iron, 1–2% quartz and the remnants of other metals in the underground rail system (Luhar and Hurley, 2003).

IO are a class of compounds that are composed of iron, oxygen and/or hydroxide ions and are subject of study in many disciplines from environmental and industrial chemistry to biology and corrosion science. There are 16 important IO oxy-hydroxide polymorphs are hematite (α - Fe_2O_3), maghemite (γ - Fe_2O_3) and magnetite (Fe_3O_4); the less commonly found are the Fe_{1-x}O (wüstite), β - and ε - Fe_2O_3 phases and the low-temperature

rhombohedral structure of magnetite. In most of these compounds, iron is in the trivalent state, but FeO and Fe₃O₄ contain Fe(II) (Cornell and Schwertmann, 2003). The IO polymorph exists in a rich variety of structures and occurs in a great variety of settings, from geological to nanoscale technological applications and display a wide range of properties and behaviour. Iron oxides are very fascinating magnetic materials due to their crystal chemistry and oxygen stoichiometry dependent inter convertible magnetic properties and have attracted increasing attention in recent years.

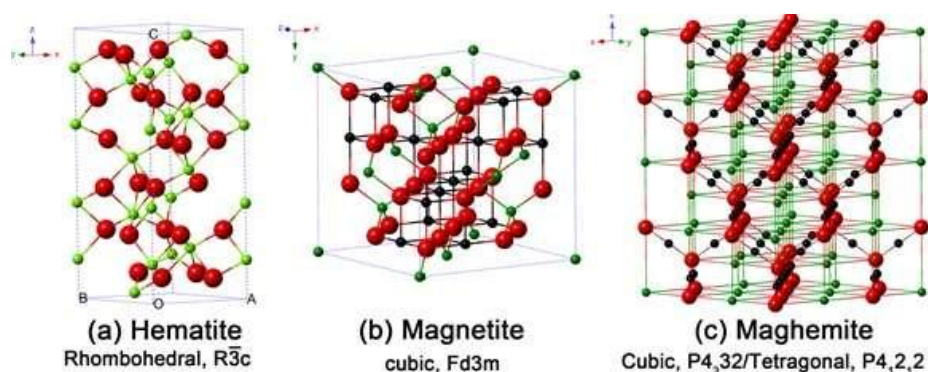


Fig. 1.7 Crystal structures of hematite, magnetite and maghemite (black: Fe²⁺, green: Fe³⁺, red: O²⁻) (Wu *et al.*, 2015).

Ferromagnetic Fe₃O₄ can be transformed into antiferromagnetic α -Fe₂O₃ via the controlled oxidation (Hou *et al.*, 2007), or vice versa in a reducing atmosphere (Jia *et al.*, 2007). Similarly, ferromagnetic spinels are converted to superparamagnetic particles by reducing crystal size down to nanoscale (Tian *et al.*, 2011). Among these, Fe₃O₄ is the most studied member owing to its excellent magnetic properties and its non-toxic, biocompatible nature.

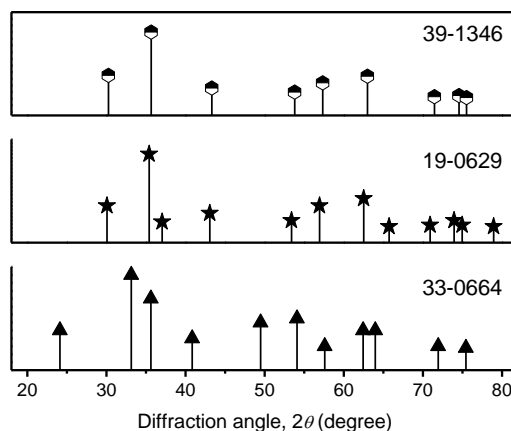


Fig. 1.8 XRD peak lines from standard powder diffraction files of α -Fe₂O₃, Fe₃O₄ and γ -Fe₂O₃

Hematite (α -Fe₂O₃)

Hematite has a hexagonal close-packed unit cell in which two-thirds of the octahedral sites occupied by Fe³⁺ ions (corundum structure) as shown in Fig. 1.7 (a). It is an *n*-type semiconductor ($E_g = 2.1$ eV), where the conduction band is composed of empty *d*-orbitals of Fe³⁺ and the valence band consists of occupied 3*d* crystal field orbitals of Fe³⁺ with some admixture from the O 2*p* non-bonding orbitals (Zhang *et al.*, 1993) as well as an interesting anode material. As the most stable IO under ambient conditions, hematite is widely used in catalysts, pigments and gas sensors due to its low cost and high resistance to corrosion/oxidative change. Generally α -Fe₂O₃ has weak ferromagnetism at room temperature, while the M_S is often smaller than 1 emu.g⁻¹ (Wu *et al.*, 2015). Figure 1.8 shows the X-ray diffraction peaks from the standard powder diffraction files of α -Fe₂O₃ (ICDD 33–0664), Fe₃O₄ (19–0629) and γ -Fe₂O₃ (39–1346), and it can be found that γ -Fe₂O₃ has a crystal structure similar to that of Fe₃O₄ with peak shift towards slightly higher angles.

Maghemite (γ -Fe₂O₃)

The structure of γ -Fe₂O₃ is cubic; each unit contains 32 O²⁻ ions, 21 $\frac{1}{3}$ Fe³⁺ ions and 2 $\frac{1}{3}$ vacancies (Fig. 1.7c). Oxygen anions give rise to a cubic close-packed array while ferric ions are distributed over tetrahedral sites (8 Fe ions per unit cell) and octahedral sites (the remaining Fe ions and vacancies). Therefore, the maghemite can be considered as fully oxidised magnetite, and it is an *n*-type semiconductor with a band gap of 2.0 eV. It exhibit ferrimagnetism at 300 K, with the M_S reaching to 78 emu.g⁻¹ (Corot *et al.*, 2006).

Magnetite (Fe₃O₄)

Magnetite ((Fe²⁺O)(Fe³⁺₂O₃); ferroferric oxide) is one of the oldest ferromagnetic materials known to mankind (around 2000 BC), named for an ancient region of Greece where metal production was prominent. It crystallises in face centred cubic inverse spinel (Fe₃O₄) structure of type AB₂O₄ where A signifies a divalent, and B a trivalent iron. It is more conveniently expressed in the formula FeO.Fe₂O₃, with a cubic close packed oxygen anion array, and iron (cation) in both fourfold (tetrahedral sites) and sixfold (octahedral sites) coordination. The unit cell is composed of 56 atoms, 32 O²⁻ anions, 16 Fe³⁺ cations and 8 Fe²⁺ cations. The moments on the Fe²⁺ and Fe³⁺ sites (of inverse spinel structure) are opposite and unequal. Indeed, magnetite was considered a ferromagnet until the 1940's, when Néel provided the theoretical framework for understanding ferrimagnetism. When

the particle size decreases, the oxygen content in the sample will correspondingly decrease, which consequently lead to lowering of the valence state of the cations.

Figure 1.9 shows the lattice parameters a in the (001) plane and c in the direction perpendicular to it are identical under equilibrium conditions but differ for tetragonal systems. The lower symmetry in this case also leads to the distinction between axial O^{ax} and equatorial O^{eq} atoms, $u > 0$ (Friak *et al.*, 2007).

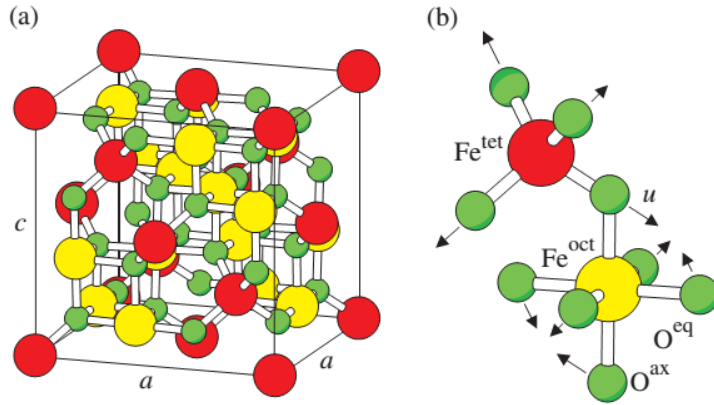


Fig. 1.9 Schematic representation of (a) partial unit cell ($1/4^{\text{th}}$) magnetite crystalline structure, (b) magnification of one tetrahedron and one adjacent octahedron sharing an oxygen atom. Large spheres labelled by Fe^{tet} and Fe^{oct} represent iron atoms on tetrahedrally and octahedrally coordinated sublattices, respectively surrounded by oxygen (Friak *et al.*, 2007).

The magnetic moment arises due to the Fe^{2+} cations only. Each Fe^{2+} is high spin so it contributes 4 unpaired electrons. The moment, and as a result the easy axis of the resulting magnetite crystal, is aligned along the cube edge. The saturation magnetisation can be calculated from

$$M_s = (n_B \mu_B) / V \quad (1.5)$$

where n_B is the number of Bohr magnetons per unit cell = 32, $\mu_B = 9.2704 \times 10^{-24}$ Am²/Bohr magneton, and V is the volume of the unit cell, 5.906×10^{-28} m³. Thus $M_s = 5.0 \times 10^5$ Am⁻¹. By dividing by the density ($\rho = 5207.42$ kg.m⁻³), the mass magnetisation can be obtained, $\sigma (Fe_3O_4) = 96$ Am².kg⁻¹ = 96 emu.g⁻¹ values which can be verified for bulk magnetite (Table 1.3). The M_s value for pure bulk Fe is 218 emu.g⁻¹, which is as expected because of the presence of oxide shells (Guo *et al.*, 2007). The spins of 3d electrons in the two interpenetrating sublattices in the octahedrally coordinated Fe^{3+} and Fe^{2+} “are coupled ferromagnetically via a double-exchange mechanism associated with inter-ion electron transfer”. In other words, the electrons can hop between Fe^{2+} and Fe^{3+} ions in the octahedral sites at room temperature, rendering magnetite a unique class of half to a quarter of their pure metal counterparts. In stoichiometric magnetite $Fe^{3+}:Fe^{2+} = 2:1$,

and the divalent irons may be partly or fully replaced by other divalent ions (Co, Mn, Zn, etc). Thus, Fe_3O_4 can be both an *n*- and *p*-type semiconductor. However, Fe_3O_4 has the lowest resistivity among iron oxides due to its small band gap (0.1 eV) (Boxall *et al.*, 1996).

1.4.1 Physical properties of Iron oxide

Table 1.3 Magnetic and mineralogical data of few selected forms of Iron oxide

Property	Value (Unit)		
Crystal name	Magnetite	Maghemite	Hematite
Formula	$\text{Fe}^{2+}\text{Fe}^{3+}_2\text{O}_4$	$\gamma\text{-Fe}^{3+}_2\text{O}_3$	$\alpha\text{-Fe}^{3+}_2\text{O}_3$
Crystal system	FCC, inverse spinel	Cubic/ Tetragonal	Trigonal
Lattice parameter (nm)	$a=0.839$	$a=0.834$	$a=0.5032$ $c=1.3737$
Molar mass ($\text{g}\cdot\text{mol}^{-1}$)	231.54	159.69	159.69
Appearance	Black	Brown	Brick red
Density ($\text{g}\cdot\text{cm}^3$)	5.18	4.87	5.27
M_s ($\text{emu}\cdot\text{g}^{-1}$)	90-98	76-81	0.4
Curie temp (K)	848-858	820-986	948
Band gap (eV)	0.1	2	2.1
Refractive index	$n_D = 2.42$		$n_o = 3.150\text{--}3.220$, $n_e = 2.870\text{--}2.940$

1.4.2 Occurrences of magnetite nanoparticles

In nature, magnetite is present virtually everywhere (in soil, rocks, lakes and streams, in marine sediments, in air and in organisms), in most cases as nanocrystals that have a large specific surface areas and are thus good adsorbents.

Magnetite in Human life a Recent Discovery

In 1992, “the presence of biogenic magnetite in human brain tissue” was discovered by Dr. Joseph Kirschvink, a geologist and professor at the California Institute of Technology who said at the time that the discovery was sure to astound most scientists but what it's doing there remains a mystery. It exists in the cerebral cortex, cerebellum, and in the lining surrounding the brain and spinal cord and consists of five million magnetite crystals (4 ng) in each g of brain tissue. Several studies suggested that levels of biogenic magnetite

in human brain tissue may be elevated in subjects with Alzheimer disease or associated with aging (Strbak *et al.*, 2011). Magnetite interacts over a million times more strongly with external magnetic fields than any other biological material including the iron in red blood cells.

Geogenic magnetite

Small grains of magnetite occur in almost all crystalline rocks as well as many sedimentary rocks. With an iron content of about 70%, magnetite is a valuable source of iron ore and, consequently, was explored for the production of iron metal since ancient times. Its mineral hardness is 5.5 to 6.5 and it has a density of 5.2 g.cm^{-3} and dissolves slowly in hydrochloric acid.

Biogenic magnetite

Crystals of magnetite have also been found in some bacteria, *Magnetospirillum Magnetotacticum*, brains of bees, termites, some birds, pigeon, and even of humans. These crystals are thought to be involved in magnetoreception, the ability to sense the polarity or the inclination of the earth's magnetic field, and to be involved in navigation. Snails have teeth made of magnetite on their radula, making them unique among animals, means they have an exceptionally abrasive tongue with which they scrape food from rocks (Majewski and Thierry, 2007). Magnetite crystals produced by living systems have unique features that distinguish them from geologically produced crystals. These involve (i) single domain size, (ii) chemical purity, (iii) crystallographic perfection, (iv) participation in chain structure, (v) unusual morphology and (vi) [111] elongation. These properties serve to maximise the net magnetic moment which affects the migratory and homing abilities of animal species in Earth's magnetic field.

Synthetic magnetite

Several studies trying to address the properties of magnetite formed by biogenic or inorganic processes, in order to determine whether it is possible to synthesise magnetite nanocrystals with specific properties such as narrow size distributions and unique morphologies, similar to the crystals that form in biogenic processes. Such crystals would have special applications because they might have interesting and controlled magnetic properties.

1.4.3 Oxidation of magnetite

Oxidation is a common phenomenon observed in Fe²⁺ ion containing materials like magnetite. Conversion of magnetite to maghemite involves a reduction in the number of Fe atoms per unit cell, from 24 in magnetite to 21⅓ in maghemite. The inverse spinel structure is maintained during oxidation and therefore the oxygen arrangement does not change. These facts favour the diffusion of Fe outward over the diffusion of oxygen inward. Moreover, an oxygen ion is almost twice as big as Fe ion and this would make the oxygen diffusion much harder compared to iron diffusion. Studies on the cation self-diffusion of magnetite revealed that the Fe²⁺ ions are mainly responsible for diffusion (Dieckmann *et al.*, 1978).

The diffusion mechanism predicts that the oxidation time will be strongly dependent on the size of the crystal; in small crystals the diffusion lengths are short. The temperatures needed for the oxidation of NPs to occur in a few hours are much lower than those used in studies of larger particles, which are usually above 150°C. At room temperature, the oxidation rate of the nanocrystals is much faster than that of the bigger particles. Murad *et al.* reported that it took years for the fine magnetite crystals (100–300 nm) to change to maghemite at room temperature (Sidhu *et al.*, 1977; Murad and Schwertmann, 1993). Experiment showed that for 9 nm nanocrystals at 24°C in water, oxidation is detectable after a few hours and completed in about three months (Tang *et al.*, 2003).

1.4.4 Surface chemistry of magnetite

The aqueous chemistry of metal cations is extremely complex and diverse and it is possible to control many characteristics of oxide NPs in particular the crystalline structure and its surface characteristics including particle size and shape (Jolivet, 2000). The surface iron atoms which are not chemically bound to oxygen atoms act as Lewis acids and therefore coordinate with molecules that donate electrons, Lewis bases. In aqueous suspensions, surface iron atoms coordinate with water which leaves hydroxyl groups and thus surface is hydrophilic (Cornell and Schwertmann, 1996) which reacts with both acids and bases. It is well known that the surface charge in oxides is largely dependent on the pH of the suspension, and thus, the surface is amphoteric in nature. The pH of zero surface charge, pH_{pzc}, or isoelectric point, is at pH 6.8 for magnetite. Iron cations form hexa coordinated aquo-complexes, [Fe(H₂O)₆]²⁺ in water in which the polarisation of coordinated water molecules is strongly dependent on the formal charge (oxidation state)

and size of the iron cation. This makes the ferric aquo-complexes more acidic than ferrous complexes. The hydroxylation of the cations occurs in very distinct ranges of pH (at pH \geq 1 for the ferric and pH~6 for the ferrous polycation) (Jolivet *et al.*, 2004). Hydroxylated complexes condense mainly via olation mechanism, with the elimination of water and formation of hydroxo bridges. During precipitation, the aquo hydroxo zero-charge complex forms which is the precursor of the solid (Jolivet, 2000).

1.5 Size- and shape-dependent magnetic properties

A key property of magnetite nanocrystals produced for technological applications is their controlled and uniform sizes and shape. Understanding the correlation between the magnetic properties and the size and shape of MNPs is a prerequisite for widespread applications of magnetism in different areas. It is also strongly dependent on the synthesis route as well as on their non-magnetic matrix or substrate. Moreover, for a given synthesis route the resulting magnetic properties of nanosized magnetite appears to strongly depend on nanosized changes in the crystal morphology, like antiphase boundaries, and crystal structure such as oxygen deficiency and local ionic disorder. Bulk magnetite has cubic magnetic anisotropy, with the {111} and {100} directions' being the easy and hard axes of magnetisation, respectively (Majewski and Thierry, 2007).

Levy *et al.* studied the magnetic properties of IONPs from 6 to 18 nm, the results revealed that magnetic disorder was particularly evident for 13–18 nm IONPs due to a drastic loss of their hyperthermia performance (Levy *et al.*, 2011). Guardia *et al.* reported that pseudospherical and faceted IONPs with a narrow size distribution (4–20 nm) and a high saturation magnetisation ($M_S \approx 80\text{--}85 \text{ emu.g}^{-1}$ at 5 K) were obtained by thermal decomposition using oleic acid as a surfactant. In contrast, decanoic acid yields much larger pseudocubic IONPs (45 nm) with a broader size distribution and a larger saturation magnetisation ($M_S = 92 \text{ emu.g}^{-1}$ at 5 K), which is close to the expected value for bulk magnetite (Corot *et al.*, 2006). One-dimensional IO nanostructures are very appealing, owing to their many unique physicochemical properties based on high intrinsic anisotropy and surface activity. Wu *et al.* showed a comparative study of the magnetic behaviour of single and tubular clustered Fe_3O_4 NPs. The results revealed that the competition of the demagnetisation energy of shape and the magnetocrystalline anisotropy energy of small IONPs would increase the coercivity, and the magnetic properties are strongly influenced by the morphology of the Fe_3O_4 NPs (Wu *et al.*, 2012).

Nanofluids

Nanofluids (*nanoparticle fluid* suspensions) is the term coined by Choi (1995) to describe this new class of nanotechnology-based heat transfer fluids that exhibit thermal properties superior to those of their host fluids or conventional particle fluid suspensions. Nanofluids are engineered by dispersing solid NPs (in the range of 1–100 nm) in traditional heat transfer fluids such as water, oil, and ethylene glycol. The nanofluids have the potential to be next-generation coolants such as smart coolants for computers and safe coolants for nuclear reactors. As a result, the research topic of nanofluids has been receiving increased attention worldwide. The recent growth of work in this rapidly emerging area of nanofluids is most evident from the exponentially increasing number of patents/publications.

1.6 Magnetitic nanofluids/ferrofluids

A ferrofluid is a colloidal suspension of sub-domain magnetic particles in a liquid carrier (aqueous or non-aqueous) whose rheological behaviour can be controlled by means of a magnetic field (Iyengar *et al.*, 2016). These particles are typically magnetite particles and the like, are suspended as extremely finely divided form with the help of dispersing aids, anti-agglomeration agents. The stability of the NPs suspension in the required base liquid for any desired application need the optimum particle size, the proper surface stabilisation and the suitable choice of the suspending medium. For certain applications, e.g., magnetic domain detection, water is a more desirable liquid carrier than non-aqueous solvents. The dispersions should satisfy the conditions of narrow size distribution and high stability without aggregation. Interparticle forces play a pivotal role in determining the rheology and light-scattering behaviour of NP dispersions. For example, concentrated NP dispersions can be transformed from an easily pourable liquid to a stiff paste by changing the interparticle forces from repulsive to attractive. Flocculation or aggregation will induce the formation of large clusters or aggregates that will scatter light. The ability to control and manipulate the sign of particle interactions represents a first step towards optimised NP processing.

The particles in a ferrofluid primarily consist of NPs which remain suspended by Brownian motion and generally will not settle under normal gravitational forces. Magneto rheological fluid primarily consist of micrometre-scale particles (that are 1–3 orders of magnitude larger than those of ferrofluids) which are too heavy for Brownian motion to keep them suspended, and thus will settle over time because of the inherent density

difference between the particle and its carrier fluid. These two fluids have very different applications as a result.

1.6.1 Non-aqueous ferrofluids

Stable dispersions of magnetic nanoparticle clusters (MNPCs) have been prepared using various dispersion media containing hydrocarbons like oil, heptanes, toluene, hexane etc. NPs synthesised by aqueous coprecipitation methods cannot be dispersed in non-aqueous solvent as the surface of NPs will have hydroxyl ions attached to it. Such NPs can be transformed into a stable fluid by the application of a fatty acid. The superhydrophobic and superoleophilic nanofluids, with selective absorbance property, can collect contaminant oil while completely repelling the water molecules and can be used as an efficient tool to remove the oil contaminant. It can maintain good dispersion stability even under the influence of external fields, such as centrifugal and magnetic (Rashin *et al.*, 2014). Fluids for heat transport are of great importance to many industrial fields, including electronics, heating, ventilating and air conditioning (HVAC), and transportation. The thermal conductivity of these fluids plays a vital role in the development of energy-efficient heat transfer equipment.

1.6.2 Aqueous ferrofluids

Among various dispersions, aqueous ferrofluids have been used in biomedical as well as industrial applications. MNPs have found application in medical diagnostics such as MRI and therapies such as cancer treatment. For such applications as either MNPs or their clusters (MNPCs), the constituent particles must be highly magnetic, biocompatible and fully dispersible in biological media without aggregation with minimal surface passivation (Ninjabdar and Brougham, 2011). It is imperative to have a biocompatible solvent such as water at optimum pH for possible bio-ingestion.

Brownian motion of the NPs improves with reduced particle size fortifies the stability of a magnetic fluid forming the colloidal system avoiding agglomeration and precipitation. Under the normal gravitational forces ~ 10 nm particles will remain dispersed, as it should not sediment due to random thermal motions, and should not aggregate due to van der Waals (vdW) interactions in suspension. However, coagulation due to magnetic dipolar attraction is still possible. So, the dispersion relies on the balancing of the gravitational, magnetic, and vdW forces. The classical approach applied in Derjaguin–Landau–Verwey–Overbeek (DLVO) theory is a way to forecast the net

interaction energy implicating vdW, steric and electrostatic forces in dilute dispersions (Iyengar *et al.*, 2016). The attractive magnetic energy between two magnetic dipoles is a function of the dipole moments μ_1 and μ_2 and the distance between the particles given by equation

$$E_A^{Mag} = \frac{1}{4\pi\mu_0 r^3} [\bar{\mu}_1 \bar{\mu}_2 - 3(\bar{\mu}_1 \cdot \bar{r}/r)(\bar{\mu}_2 \cdot \bar{r}/r)] \quad (1.6)$$

where r is the vector between the centres of the two dipoles and μ_0 is the permeability of space (Smit and Wijn, 1959). The magnetic dipole of a single domain particle is $\mu = I_0 V$ where I_0 is the magnetisation per unit volume of the particle and V is the volume of the particle. The interaction energy increases as the distance between the particles decreases and aggregation may occur unless prevented by a repulsive force. The attraction energy can also be expressed in the following form;

$$E_d = -\frac{\pi M_S^2 d^3}{9\mu_0 (1+2)^3} \quad (1.7)$$

where M_S is the saturation magnetisation and μ_0 is the magnetic permeability, s is the distance between the spherical surfaces, d is the diameter of the particles and $l = 2s/d$. The magnetic energy of the system is small when the particles are superparamagnetic, as the energy is proportional to volume, and so is overcome by thermal fluctuations resulting in colloidal stability. The factor l expresses the importance of the volume fraction in determining stability.

The relative importance of the gravitational force can be accessed from the ratio of the gravitational energy to the attractive magnetic energy, which is given by;

$$\frac{\text{Gravitational Energy}}{\text{Magnetic Energy}} = \frac{\Delta\rho g L}{\mu_0 M H} \quad (1.8)$$

where $\Delta\rho$ is the difference in density of the solid and the liquid, L is the height of the suspension and g is the gravitational constant. Using common values for the parameters it is found that the gravitational effect on NP stability for typical magnetite fluids is insignificant. The vdW forces are the result of spontaneously induced polarisability of fluctuating electric dipole-dipole forces and are a relatively weak distance dependent interaction. The energy due to the vdW force, which arises due to fluctuating dipole energies for equal sized sphere is given by the Hamaker expression.

$$E_i = -\frac{A}{6} \left(\frac{2}{l^2+4l} + \frac{2}{(l+2)^2} + \ln \frac{l^2+4l}{(l+2)^2} \right) \quad (1.9)$$

where A is the Hamaker constant (approximately 10^{-19} N.m for Fe_3O_4 , $\gamma\text{-Fe}_2\text{O}_3$ and Fe) (Ghosh, 2006). So the interaction energy increases as two particles come closer. The vdW

attractive forces are a significant factor and must be countered with a repulsive force to maintain a stable colloidal suspension. To control the colloidal stability of ferrofluids, the steric or electrostatic (due to the electric double layer) repulsive forces must be more than the vdW, and magnetic dipolar attractive interactions (Iyengar *et al.*, 2016). Hence, the particles are coated with surfactants to provide stability due to steric and/or electrostatic stabilisation.

1.6.3 Stabilisation of nanocrystals against aggregation

Electrostatic and steric repulsions are two forces which balance the attractive forces among the colloidal particles. In a stable system, the maximum attractive interparticle energy should be sufficiently small, in the order of $1-2 k_B T$, to allow thermal motion or agitation to readily break all particle–particle bonds. Aggregation due to attractive forces associated with MNPs can be prevented by applying an electrostatic double layer at the solid–liquid interface or by use of polymers or surfactant functioning as a steric stabiliser (Cornell and Schwertmann, 1996). Ionic surfactants prevent agglomeration due to the repulsive forces originating from the proximity of like charged particles approaching each other.

1.6.3.1 Electrostatic stabilisation

Electrostatic stabilisation is a pH sensitive method since it is induced by charge. Close to the pH_{PZC} the net surface charge density is zero and the interparticle electrostatic repulsions are not sufficient to prevent the particles vdW attractive forces causing flocculation. The isoelectric point of magnetite can be shifted to pH 2-4 by applying a silica coating on magnetite and thus coated MNPs are stable in suspension above pH 4. Phosphate and carboxylate functional groups are known to bind to the surface of magnetite (Ghosh, 2006). Weakly polarising, positively charged ions, such as the $\text{N}(\text{CH}_3)^{4+}$ ion of tetramethylammonium hydroxide (TMAH) are also known to stabilise the particles (Iyengar *et al.*, 2016). NPs with large surface energy and vdW interaction combine together form aggregates under gravity or grow to form larger particles. They are also protected by electrostatic charges at the surfaces to remain stable in suspensions. The NP in its dispersion possesses a surface charge which might have developed through one or more of the following mechanisms:

- (i) Preferential adsorption of ions
- (ii) Dissociation of surface charged species

- (iii) Isomorphic substitution of ions
- (iv) Accumulation or depletion of electrons at the surface
- (v) Physical adsorption of charged species onto the surface

The surface charge in oxides is mainly derived from preferential dissolution or deposition of ions. In the oxide systems, typical charge determining ions are H^+ and OH^- groups and as their concentration varies, the surface charge density changes from positive to negative or vice versa. When a surface charge density of a solid surface is established, there will be an electrostatic force between the NP surface and the charged species in the proximity to segregate positive and negatively charged species towards it (see Fig. 1.10). As a result a layer of oppositely charged ions called counter ions is introduced over the NP. This firm layer of counter ions is called a stern layer. At the same time, a layer of counter ions diffuse over the medium towards the stern layer which is only loosely attracted to the colloidal surface. This diffused layer of loosely bound ions in between stern layer and bulk is called Gouy-Chapman layer (Goetze *et al.*, 2002).

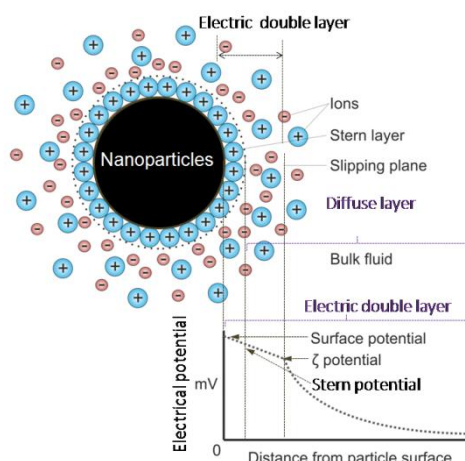


Fig. 1.10 Illustration of the principle of electrostatic stabilisation by varying the zeta potential upon adjusting the pH.

As the ions are farther from the NP, the electrostatic influence goes on decreasing and the bulk solution is usually neutral. This creates the formation of an ‘electrical double layer’ in the colloidal dispersion. Subsequently, potential difference arises across the double layer usually termed as the ‘zeta-potential’. The thickness of the double layer is also another crucial factor influencing the stability. The stability can be well understood by measuring the zeta potential of the dispersion. Highly stable dispersions possess a zeta potential of absolute value between 25 and 30 mV (Iyengar *et al.*, 2016). As the thickness of the double layer proportionally increases the zeta potential and the consequent stability,

addition of charged ions e.g., an acid or a base is expected to boost the stability of the dispersion. The particles repel each other when they go closer than a certain distance. Electrical double layer interactions originate from the accumulation of counter ions near a charged surface. A net charge may build up on the surfaces of NPs in liquids through various mechanisms such as the dissociation of surface groups, the specific adsorption or dissolution of ions, and the presence of crystalline defects (Bertrand *et al.*, 1994).

Magnetite in aqueous media preferably adsorbs hydroxyl ions and so it possesses a negative surface in the absence of any surface modification. In order to stabilise magnetite particle in aqueous media, it is desirable to increase the positive ion concentration in the phase, owing to its negative surface. Thus magnetite is usually electrostatically stabilised at slightly lower pH which creates an electric double layer which results in a Coulombic repulsion force between individual NPs. The dissociation of surface hydroxyl groups is the main charging-up mechanism for metal oxide surfaces in water and depends on the pH: the corresponding surface reactions may be expressed as

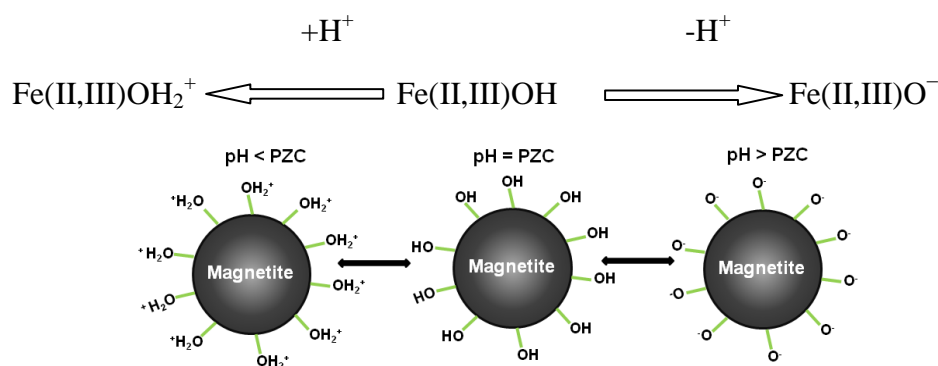


Fig. 1.11 Surface chemistry of magnetite in acidic and in alkaline environment

The resulting aqueous dispersions were stable in basic conditions. In acidic pH, the dominating surface species is tentatively Fe(II,III)OH_2^+ , implying positive zeta potentials. With increasing pH, the ζ decreases and Fe(II,III)OH becomes dominating species around pH_{PZC} . At alkaline pH, the surface species Fe(II,III)O^- is mainly responsible for the negative ζ (Iyengar *et al.*, 2014). The pH at which the net surface charge is neutral is called the isoelectric point (IEP), and is typically close to pH 6 for synthetic magnetite (Iyengar *et al.*, 2016). The adsorption of charged molecules with a high affinity for the surface can also be used to increase the surface charge. The range of these interactions is defined by the Debye length κ^{-1} and strongly decreases with increasing ionic strength I:

$$\kappa^{-1} = \sqrt{\frac{\epsilon_r \epsilon_0 k_B T}{2N_A e^2 I^2}} \quad (1.10)$$

where ϵ_r is the dielectric constant of the solvent, ϵ_0 the permittivity of vacuum, k_B the Boltzmann constant, T the temperature, N_A Avogadro's number and e the elementary charge. A high concentration of free ions will screen the repulsive double layer interactions and decrease their range. Electrical double layer interactions can also be used to stabilise particles suspended in low-polar solvent ($\epsilon_r < 11$) (Van Der Hoeven and Lyklema, 1992).

1.6.3.2 Steric / entropic stabilisation

The stabilisation provided by the steric bulky layer of materials i.e., polymer or surfactant surrounded by NPs metal core is referred as 'steric stabilisation'. This is achieved by the incorporation of a suitable surfactant molecule to the particle surface as a part of the synthetic pathway. The surfactant molecules in general are mutually unreactive as well as repulsive and have a long chain amphiphilic structure with a polar head group and non-polar tail of saturated or unsaturated hydrocarbon. If the head group forms a positive ion in a solution it is referred to as a cationic surfactant, and in the case of forming a negative ion it is called an anionic surfactant. Usually surfactant molecules have long amphiphilic (fatty) chains with a polar head group which binds onto the magnetite surface either chemically or physicochemically. Particles stabilised in this way can be dispersed in non-polar hydrocarbon solvents, such as hexane, with the readily solvated hydrophobic hydrocarbon chains extending from the particle surface (Shen *et al.*, 1999). The surfactant thickness must be such that the sum of the energy of vdW (E_i , eqn 1.9) and magnetic attractive forces (E_d , eqn 1.7) is less than or equal to the thermal energy or Brownian motion of the particle system (eqn 1.11) (Fertman, 1990).

$$|E_i + E_d| \leq kT \quad (1.11)$$

The stabilisation mechanism can be explained in two ways. When two particles each containing an adsorbed surfactant layer of thickness δ approach to a distance of separation h , where $h \leq 2\delta$, repulsion occurs as a result of two main effects: (i) unfavourable mixing of the stabilising chains of the adsorbed layers. (ii) When the particles approach one another the surfactant tails interpenetrate creating an osmotic pressure and a repulsive force because of an increase in configurational entropy as the surfactant chains begin to compress one another. This is referred to as elastic (entropic) interaction.

Mackor proposed a model for particle-particle collisions where the surfactant tails compress and repel one another. Rosenswieg *et al.* modified the Mackor expression for the

repulsive forces based on a flat surface model to an integrated expression for two approaching nanospheres (Tadmor *et al.*, 2000).

$$\frac{E_r}{kT} 2\pi d^2 \xi \left[2 - \frac{l+2}{t} \ln \left(\frac{1+t}{1+l/2} \right) - \frac{l}{t} \right] \quad (1.12)$$

where ξ is the concentration of adsorbed surfactant molecules, and $l=2s/d$, $t=2\delta/d$, k is Boltzmann's constant, T is the absolute temperature.

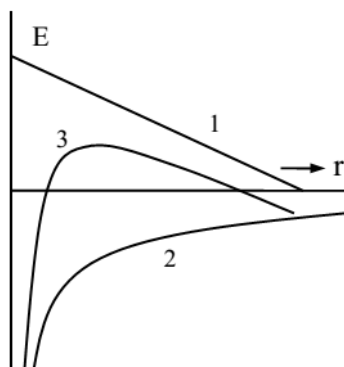


Fig. 1.12 The potential energy diagram for steric stabilisation where 1 represents repulsive force due to surfactant, 2 attractive energies of magnetite NPs and 3 net energy.

The surfactant coated NPs will not agglomerate as long as the net energy is positive. A long carboxylic acid chain creates a potential barrier of $\sim 25 k_B T$ that is an order of magnitude greater than the thermal energy for each particle and under this condition it is unlikely the particles will coalesce (Tadmor *et al.*, 2000). The steric stabilisation of fatty acid coated MNPs in non-polar and aqueous carrier liquid by monodentate (shown schematically in Fig. 1.13) or chelating bidentate fashion (Zhang *et al.*, 2006), where the interaction between the COO^- group and the Fe atom was covalent. The carboxylic head group of the primary fatty acid layer is chemisorbed onto the magnetite (see Fig. 1.14).

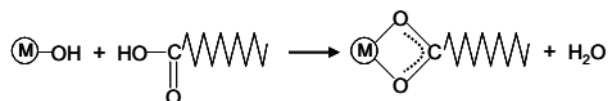


Fig. 1.13 Chemisorbed carboxylic acid group on magnetite particle, M (Ghosh, 2006).

It is indicated by the small circles at the surface of the magnetite in Fig. 1.14 (b and c) and the hydrophobic non-polar tail of the surfactant, extends out into the non-polar solvent in Fig. 1.14b as a curved line. Hence, along with steric stabilisation, the surface passivation also allows the particles to be dispersible in non-polar solvents like heptane, toluene etc. Such specific adsorption controls the crystal growth by sterically hindering the interaction between the particles and allows them to remain separated in dispersion.

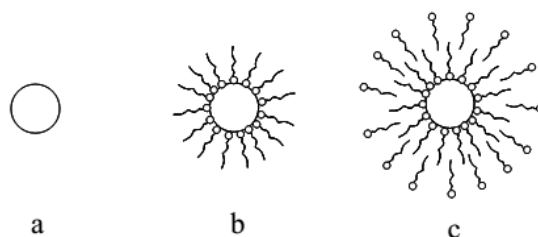


Fig. 1.14 Schematic diagram of a) bare Fe_3O_4 particle, b) monolayer surfactant coated in non-polar solvent and c) bilayer stabilised in aqueous suspension.

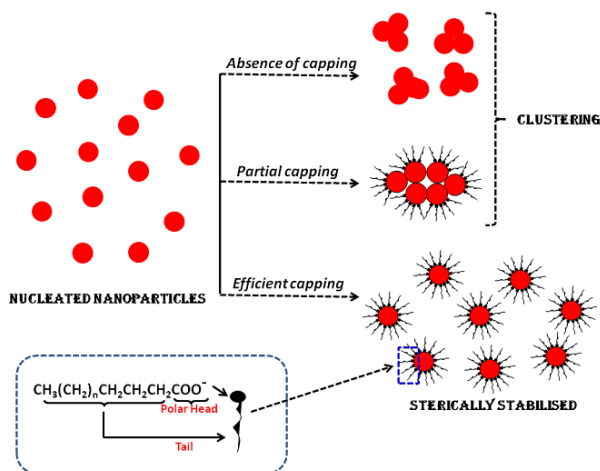


Fig. 1.15 Schematic representation of the steric stabilisation provided by surfactant over the NP surface

The amount of surfactant to NPs ratio also determines the fate of this dispersion. Eventually, the particles will be prevented from agglomeration, thus facilitating the stability of the dispersion and the principle is depicted in Fig. 1.15.

Figure 1.14 shows the sterically stabilised NPs with hydrophilic surface which can be engineered via two approaches. In the first method, the hydrophobic surface of the stabilised NPs can be renovated to hydrophilic by chemical modifications in which a second layer of similar surfactant is grafted over the primary layer in a reversed fashion of attachment (Liu and Snee, 2010) as shown in. This mode of surface passivation is initiated by Shimoiizaka *et al.* on iron oxide NPs in the early 1980s (Shimoiizaka *et al.*, 1980). Secondly, surfactants possessing polarity on both sides can be used as surface modifier. For example, polyethylene glycol (PEG) is an amphiphilic molecule which is capable chelating the NPs by covalent bonding with oxygen. This particular manner of attachment lead to the outcrop of polar $-\text{OH}$ groups over the NP surface, thus rendering it hydrophilic.

Colloidal stability in blood is a major concern when designing a NP system for drug delivery. Preventing aggregation is keen since any particle over 200 nm will be readily cleared by the spleen (Gref *et al.*, 1995). Once the NPs enter the vasculature, they will

encounter cells, plasma proteins, and various electrolytes. Considering this environment, electrostatic repulsion stabilisers would be rendered relatively helpless. The ionic concentration from the electrolytes would screen the electrostatic double layer reducing its potential as a barrier (He *et al.*, 2008; Golas *et al.*, 2010). An additional concern of electrostatic repulsion stabilisers is the increased detection by macrophages leading to reticuloendothelial system readily engulfed by macrophages (Xiao *et al.*, 2011).

1.6.4 Clustering and aggregation in aqueous suspension

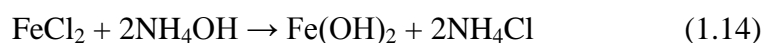
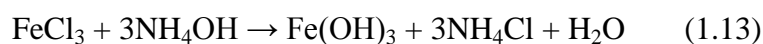
It has been reported recently that water-based magnetic fluids consist of a considerable fraction of non-superparamagnetic particles at room temperature (Shinoda *et al.*, 2002). The presence of a large number of inherent clusters in the range of 200 nm in the water-based fluids, as compared to hydrocarbon based or ionic fluids, is probably due to the differences in the preparation technique, which assists the formation of aggregates. It was reported that at zero field, the formation of rings was favoured over chains for all clusters large enough to contain more than three particles due to the strong dipole–dipole interaction between particles in the aqueous system.

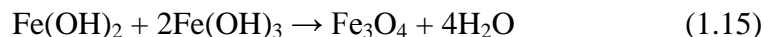
It is a common observation that monodispersed NPs as evidenced by electron microscopy techniques often show polydispersity in aqueous suspensions due to clustering. Dynamic light scattering techniques has been used to provide useful insights into the nature of the aggregates formed in hydrous ferric oxide flocks in suspension. The assembly of particle appears to exhibit fractal properties over a significant size and its concentration range. The aggregates tend to break easily by agitation resulting in break up and/or restructuring to denser assemblages (Lo and Waite, 2000). Commercial ferrofluids e.g., Nanomags®-D-spio, FluidMAG-DX are also reported to form aggregates of variable size averaging a ~100 nm though the crystallite size is 8.4 nm and are classified under “cluster type” and “multi domain cores” as a result of equilibrating magnetic, gravitational and electrostatic forces (Sakellari *et al.*, 2015). The uniformity of MNP aggregates in aqueous suspensions helps tune the heating efficiency in hyperthermia applications. In MRI, the NMR signals in the relaxivity profile are modulated by the presence of MNP clusters of different sizes, thus making the efficacy of MNP based contrast agents magnetic field and size dependent. However, to the best of our knowledge there is no detailed study on the colloidal stability of aqueous suspensions of magnetite NPs and the effect of its concentration, temperature and ageing time on clustering which is extremely important for predicting its application.

1.7 Methods of fabricating nanostructures

Present day material science requires the expertise to organise materials with controlled morphology, low dimensionality and functionality. The synthesis of magnetic nanomaterials with the desired property and stability is rather challenging. The size, its distribution, morphology and dimensionality of the nanocrystals and their distribution greatly modify the physical, chemical, mechanical and magnetic properties that their synthesis requires careful manipulation. Fabrication of various magnetic nanostructures with different morphologies including spheres, cubes, octahedra, wires, and rods to date by employing traditional wet chemical methods (co-precipitation, thermal decomposition, hydrothermal and solvothermal syntheses, sol–gel synthesis, microemulsion, ultrasound irradiation and biological synthesis) to more exotic techniques such as laser pyrolysis or chemical vapour deposition (Corot *et al.*, 2006). These methods can be broadly divided into aqueous and non-aqueous routes. Aqueous approaches are attractive in terms of their low cost and sustainability. However, there is a generic challenge in directly obtaining water-soluble monodisperse magnetic NPs without size selection. Non-aqueous routes generally produce NPs which are dispersible only in non-polar solvents. Magnetic behaviour is an important parameter in design and synthesising of superparamagnetic iron oxide NPs (SPIONs) in order to maximally facilitate their imaging and therapeutic efficacy as these applications require high magnetisation values.

Chemical coprecipitation is a relatively faster and simpler way to fabricate magnetic oxides. It is the most widely employed and easiest method, typically involves the precipitation of Fe^{3+} and Fe^{2+} salts in the ratio 2:1 in an aqueous medium using a strong base such as NaOH or KOH under inert conditions at low temperatures $\sim 90^\circ\text{C}$ over a hot plate magnetic stirrer while continuous stirring. The nucleation of the Fe_3O_4 is easier when the solution $\text{pH} < 11$, while the growth of the Fe_3O_4 nucleus is easier when the solution $\text{pH} > 11$ (Wu *et al.*, 2015). Shen *et al.* synthesised a hydrophobic magnetite NPs using oleylamine and oleic acid surfactant by coprecipitation method (Shen *et al.*, 1999). Pinheiro *et al.* precipitated a 80 nm magnetite cube using ferrous sulphate in a solution of KOH and KNO_3 (Pinheiro *et al.*, 2013). The sequence of magnetite formation from the ferrous and ferric chlorides via hydrated ferrous and ferric oxides during alkali precipitation may be given as





Recently, the growth rate of the magnetite NPs was measured in real-time during the precipitation by an integrated AC magnetic susceptometer within the mixing zone of the reactant (Strom *et al.*, 2010). Coprecipitation was widely studied in preparing Fe₃O₄ NPs in gram-scale production.

Polyol process refers to a poly-alcohol that acts not only as a solvent, but also as a mild reducing agent and when coupled with a base, it serves as a perfect medium for the reduction of metal salt precursors. In this process, a solid inorganic precursor is decomposed in a liquid polyol by heating to its boiling point. The reduction to metal can be achieved in various polyols such as ethylene glycol, propylene glycol, diethylene glycol, polyethylene glycol (Fig. 1.16).

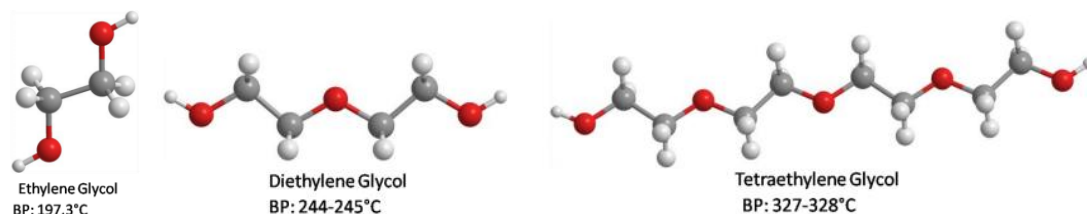


Fig. 1.16 Various polyols used for the reduction of metal salt precursors. Varying the hydroxyl sites has an effect on the overall reduction potential of the polyol along with a boiling point change.

The reduction of metals in a liquid polyol medium occurs by dissolution of the metal salt precursor, reduction of the dissolved species by the polyol, and nucleation and growth of the metal particles from the solution.

High-temperature thermal decomposition of an alkaline organometallic iron species such as Fe(acac)₃ or iron pentacarbonyl in high boiling organic solvents containing organic surfactants produce significantly smaller size NPs. Gao *et al.* obtained 5 nm magnetite particles via the reaction of Fe(acac)₃ with 2-pyrrolidone (Li *et al.*, 2004). Guardia *et al.* developed 5 nm and ~30 nm cubic shaped magnetite via decomposition of Fe(acac)₃ in dibenzyl ether in the presence of decanoic acid and to further expand the particle size to 50 nm by adjusting the final synthesis temperature (Guardia *et al.*, 2010). Pinna *et al.* prepared magnetite nanocrystals through solvothermal reactions of Fe(acac)₃ and benzyl alcohol or benzylamine at 175–200°C (Pinna *et al.*, 2005). This also developed chitosan oligosaccharide-stabilised ~30 nm ferrimagnetic iron oxide nanocubes, as an effective heat nanomediator for cancer hyperthermia, using Fe(acac)₃, 4-biphenylcarboxylic acid, oleic

acid and benzyl ether. Chito-FIONs also exhibited superior magnetic heating ability with a high specific loss power value (2614 W.g^{-1}) compared with commercial superparamagnetic Feridex NPs (83 W.g^{-1}) (Bae *et al.*, 2012).

Hydrothermal reactions generally performed using autoclaves or high-pressure reactors under aqueous conditions at high temperatures, offer good size and morphological control over the products. Magnetite octahedrons obtained by aspartic acid assisted aqueous hydrothermal route (Qu *et al.*, 2010). The template free hematite ($\alpha\text{-Fe}_2\text{O}_3$) single nanotubes were prepared by the hydrothermal treatment of iron(III) chloride with sulphate and phosphate additives at 220°C . Different morphologies of $\alpha\text{-Fe}_2\text{O}_3$ are reported by adjusting the reaction time, ferric ion concentration, and phosphate and sulphate additive concentrations (Wu *et al.*, 2010).

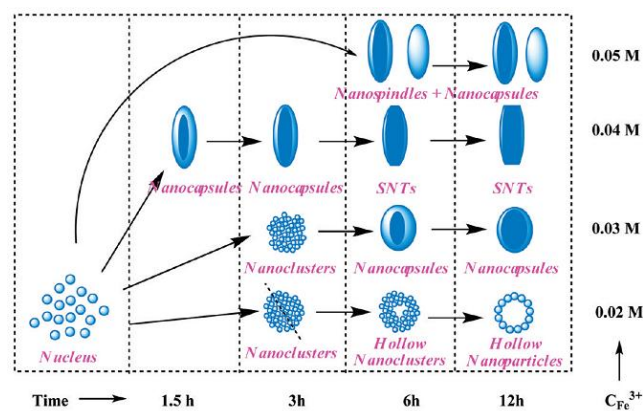


Fig. 1.17 Schematic illustration of the shape evolution for hematite nanostructures at different reaction times and different ferric concentrations under hydrothermal treatment (Wu *et al.*, 2010).

Solvothermal reactions involve hydrolysis of ferric salts in ethylene glycol in the presence of sodium acetate as reducing and surface modifier produced 200, 400 and 800 nm ferrite MFe_2O_4 ($\text{M} = \text{Fe}, \text{Mn}, \text{Zn}, \text{Co}$) microspheres at 200°C for 8, 48 and 72 h reaction time respectively (Deng *et al.*, 2005). Luo *et al.* synthesised hollow microspheres by replacing sodium acetate with ammonium acetate in the above said experiment (Luo *et al.*, 2010). A solution containing $\text{Fe}(\text{acac})_3$, diphenyl ether and 1,6-hexanedi-ol produced hollow magnetite submicrosphere at 220°C by solvothermal treatment (Wang *et al.*, 2010).

Biosynthesis method is a green chemical and eco-friendly route, and the obtained products exhibit good biocompatibility. In traditional biosynthesis, magnetotactic bacteria and iron reducing bacteria such as *Geobacter metallireducens*, *M. Gryphiswaldense*, are used under anaerobic conditions. Significant recent advancement, Bharde and coworkers have

reported that the bacterium *Actinobacter* sp. is capable of synthesising superparamagnetic maghemite NPs under aerobic conditions when reacted with a ferric chloride precursor (Bharde *et al.*, 2008). Recently, Sundaram *et al.* reported the ability of *Bacillus subtilis* strains isolated from rhizosphere soil to produce magnetite NPs (Sundaram *et al.*, 2012). However, the size and shape control of magnetic NPs during biosynthesis processes, and the elucidation of the exact mechanism of NPs production using living organisms, require much more experimentation.

It is understood from the Table 1.4, fabrication processes that are relatively cheap and fast result in broad size distributions and shape selectivity. However, the nanotechnological applications need particles with strictly controlled size and shape, and composites that are produced by the combination of magnetite NPs with organic materials.

Table 1.4 Summary and comparison of the synthetic methods for producing magnetic NPs.

Methods	Reaction conditions	and	Reaction temp (°C)	Reaction period	Size distribution	Shape control	Yield
Co-Precipitation	Very ambient	simple,	20-150	Minutes	Relatively narrow	Not good	High/scalable
Thermal decomposition	Complicated, insert atm.		100-350	Hours-days	Very narrow	Very good	High/scalable
Hydro- or Solvothermal synthesis	simple, pressure	high	150-220	Hours-days	Very narrow	Very good	High/scalable
Sol-gel and Poly-ol method	Complicated, ambient		25-200	Hours	Narrow	Good	Medium
Microemulsion	Complicated, ambient		20-80	Hours	Narrow	Good	Low
Sonolysis or sonochemical method	Very ambient	simple,	20-50	Minutes	Narrow	Bad	Medium
Microwave-assisted synthesis	Very ambient	simple,	100-200	Minutes	Medium	Good	Medium
Biosynthesis	Complicated, ambient		RT	Hours-days	Broad	Bad	Low
Electrochemical methods	Complicated, ambient		RT	Hours-days	Medium	Medium	Medium
Aerosol/vapour methods	Complicated, insert atm.		>100	Minutes-hours	Relatively narrow	Medium	High/scalable

Such materials can be produced using biomimetic synthesis. The main goal of this research is to understand how reaction conditions affect the sizes and shapes of magnetite nanocrystals precipitated from solutions that contained only inorganic or both inorganic and organic components.

1.8 Why surface functionalisation

Surface modification plays an essential role in determining the successful application of NPs in biomedical fields; several concerns remain to be addressed. The primary concern probably is the stability of NPs in water as already discussed, since most biochemical process occurs in aqueous environment. However, generally used methods usually provide NPs with hydrophobic ligands, meaning they are unstable in aqueous solution. Another important concern is the potential health and safety issues while exploring nanomaterials to human body and environment. The determinants of particle toxicity are known to be the large surface area and chemical reactivity in relation to small size (and thus the ability to generate reactive oxygen species) and the capability to penetrate tissues and cells (Nel *et al.*, 2006). Thus, particles in nanoscale are likely to be more hazardous than their bulk compartments, and bare particles are more toxic than functionalised ones (Cavaliere-Jaricot *et al.*, 2008). One of the examples to be considered is the potential cytotoxicity of QDs, because the heavy metals core toxicity, and particularly at high concentrations they could cause harmful effects on embryo development and cell viability and function (Chen, 2014).

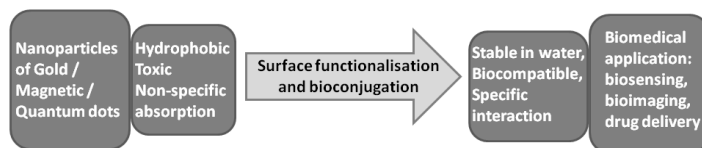


Fig. 1.18 Strategy for bridging the unique feature of NPs to biomedical applications

Lastly, a NP must be conjugated to a well-defined biological molecule such as antibody, receptor, enzyme or nucleic acid, for targeting application. Hence, there exists a gap between the nature of NPs and their uses in biomedicine. One method to bridge such a gap is the surface functionalisation of NPs (Fig. 1.18). A proper surface coating can stabilise particles and thus may increase (i) the sensitivity of NPs based sensor, (ii) enables the NPs specifically to biological species and avoids non-specific interactions with components in the complex matrix, (iii) preventing the dissolution and release of core materials that may cause toxicity to biological system. Furthermore, the steric hindrance of coating can affect (i) the fate of NPs in biological system, such as cellular uptake and accumulation, circulation and clearance from the body, (ii) the maintenance of the intrinsic nanocrystal properties such as fluorescence and magnetic behaviour. Core-shell architectures allow researchers to combine multiple functionalities on a single NP. During the surface

modification particles size distribution especially for MNPs should be narrow enough to be applied in many areas. Moreover, appropriate surface functionality is the prerequisite for conjugating biomolecules to NPs for biomedical applications (Chen, 2014).

1.8.1 Protein adsorption capacity

If NPs are injected intravenously, immediate interaction with plasma proteins occurs, known as opsonisation (Armstrong *et al.*, 1997). The amount of adsorbed proteins is based on the size, charge and hydrophobicity of the particle surface. With increasing size, charge and hydrophobicity of the particles, the capacity of protein adsorption increases (Müller *et al.*, 1997). The dehydration of hydrophobic areas results in entropy gain which facilitates protein adsorption. The adsorbed protein components play an important role in the biodistribution, degradation and elimination of the NPs (Müller *et al.*, 1997).

1.8.2 Biocompatibility of as-synthesised nanomaterials

Biocompatibility is a broad term which has come to define an engineered system able to fulfill its intended application while minimising unwanted interactions with the body. Toxicology is the study of adverse effects of chemical and physical agents on living organisms and the environment. The basic assumption of toxicology is that there is a relationship between the dose, the concentration at the affected site, and the resulting adverse effects. The physician Theophrast von Hohenheim (Paracelsus, 1493-1541) was the first one to discover the relationship between dose and effect of substances; he is often called the “father of toxicology”.

In the case of NP systems, toxicity is typically the critical factor in defining their biocompatibility (Lewinski *et al.*, 2008) and if intended for use in humans and animals, requires extensive testing for toxic side effects. Apart from acute toxicity, the toxicity of degradation products, stimulation of cells with subsequent release of inflammatory mediators (Maaßen *et al.*, 1993), and toxic effects through the particulate system have to be seriously considered. A first indication about the toxicity can be obtained by studying tissues from cell cultures histologically after incubation with NPs.

Yang *et al.* found both particle composition and shape were key factors in determining the toxicity of nanomaterials (Yang *et al.*, 2009). They utilized methyl thiazolyl tetrazolium (MTT) and water-soluble tetrazolium (WST) assays to evaluate the cytotoxicity of four types of NPs: carbon black (CB), SWCNT, silicon dioxide (SiO₂) and zinc oxide (ZnO). ZnO was found to be much more toxic than the non-metal NPs. Their

further measurements on glutathione depletion, malondialdehyde production, superoxide dismutase inhibition, and reactive oxygen species generation indicated that oxidative stress could play an important role in causing toxic effects. Although carbon nanotubes were less cytotoxic, comet assay showed that they induced more DNA damage. In comparison, CB and SiO₂ were found relatively non-toxic.

As the building blocks and functional unit of any living organisms, cells are at the center of examining the interactions of living systems and nanomaterials. Historically research of the nano-safety community has been focused on eukaryotic cells, especially mammalian cells. With that consideration we review the state with the framework of mammalian systems; the different cytotoxicities induced by nanomaterials in mammalian cells will be discussed in chapter 5.

1.9 Applications of iron oxide NPs

Iron oxides are of great interest to a variety of scientific disciplines for various applications that range from opto-electronics, medicine, environmental remediation, pigments, corrosion protection, gas sensing, electronic packaging, mechanical engineering, aerospace and bioengineering, among others. A key property of magnetite nanocrystals essential for technological applications is their controlled and uniform sizes. Due to their interesting stimulus responsive properties, magnetic materials have been employed in such as magneto-optical wave filters (Philip *et al.*, 2003)/ switches, sensors, modulators, optical circulators, and optical isolators (Li *et al.*, 2013), nonlinear optics (Huang and Yu, 2005; Pu *et al.*, 2005), high-density information storage (Zhang *et al.*, 2015), to control fluids in space (Jeong *et al.*, 2007), and defect sensors (Mahendran and Philip, 2012). Major attention has also been directed toward the development of MNPs as sustainable nanocatalysts for specific chemical transformations having both economic and environmental significance in applications such as deodorising (Usami *et al.*, 2007), solid propellants (Rudy *et al.*, 1989), exhaust gases of internal combustion engines (Rudy *et al.*, 1989) and degradation of organic pollutants in waste water (Amutha *et al.*, 2011); the MNPs can easily be separated from the reaction mixture by an external magnetic field. Recently, exploration of novel uses of magnetic particles in the separations area has increased significantly, i.e., as magnetic adsorbents for anionic dye removal from waste water (Yan *et al.*, 2015). Outstanding magneto-electrical properties have also been reported in strain induced magnetite (Vaz *et al.*, 2009).

Biomedical application

Recent technological advances in smart multifunctional nano-bio-magnetic platforms offer exciting opportunities in personalised medicine for more accurate early prognosis, monitoring and treatment of various diseases without jeopardising healthy tissues by identifying unique biochemical markers of disease before the appearance of symptoms obviates the need. Stable aqueous ferrofluids of Fe_3O_4 , Fe_2O_3 , or ferrites have been successfully used in extensive applications such as magnetic resonance imaging (MRI) for imaging the brain and the central nervous system (Kim *et al.*, 2003; Piao *et al.*, 2008; Yang *et al.*, 2010), for assessing cardiac function (Aviles *et al.*, 2008), as a drug delivery/gene-delivery platform (Corot *et al.*, 2006), ferro-fluids, MICR ink (Lee *et al.*, 2002), cell targeting (Uchida *et al.*, 2006), magnetic force based tissue engineering (Shimizu *et al.*, 2007), magnetically controllable catheters, glucose sensing (Rossi *et al.*, 2004), sensing tumor by magnetoimpedance (Shinkai, 2002), and magnetic separation of biological materials.

MRI imaging contrast agents

The work of Paul C. Lauterbur (Lauterbur, 1973) in 1972 demonstrated image formation by reconstruction from a number of NMR measurements, each taken in the presence of a linear field gradient applied in different directions. This was the real foundation of a new non-invasive technique MRI, which produces images of the body in thin slices. Paramagnetic species called “contrast agents” can be administered to the subject to improve the image quality/ contrast of a particular anatomical or functional region. Contrast agents can considerably reduce the spin-lattice relaxation time T_1 , the spin-spin relaxation time T_2 as well as T_2^* , the dephasing time in the presence of field inhomogeneities (Bonnemain, 1998). With applications, such as bowel contrast agents (i.e., Lumiren[®] and Gastromark[®]) and liver/spleen imaging (i.e., Endorem[®] and Feridex IV[®]) (Jeong *et al.*, 2007; Zhang *et al.*, 2015), already on the market, SPIOs have led the way for MNPs into the clinic. Several forms of ultrasmall SPIOs have undergone clinical trials with one of the most notable being Combidex[®] which is in late stage clinical trials for use in the detection of lymph node metastases (Harisinghani *et al.*, 2003).

Magnetic hyperthermia

Magnetic NPs have the unique physical property of being able to remotely heat when exposed to an alternating magnetic field due to the absorption of energy from the magnetic

field and conversion into heat primarily through Brownian relaxation and Neel relaxation (Rosensweig, 2002).

Magnetic theranostics

As therapeutic tools, MNPs have been evaluated extensively for targeted delivery of pharmaceuticals through magnetic drug targeting and by active targeting through the attachment of high affinity ligands. In the spirit of Ehrlich's "Magic Bullet" (Winau *et al.*, 2004), MNPs have the potential to overcome limitations associated with systemic distribution of conventional chemotherapies. With the ability to utilize magnetic attraction and/or specific targeting of disease biomarkers, MNPs offer an attractive means of remotely directing therapeutic agents specifically to a disease site, while simultaneously reducing dosage and the deleterious side effects associated with non-specific uptake of cytotoxic drugs by healthy tissue.

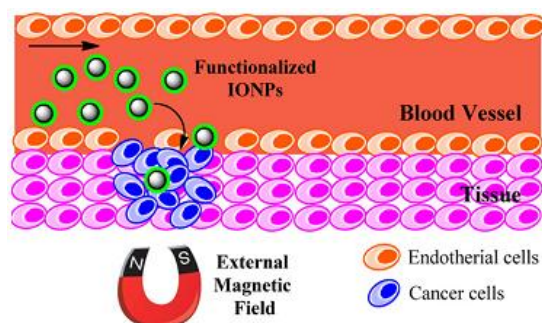


Fig. 1.19 Schematic of MNP based drug delivery system: drug-loaded IONPs are guided *in vivo* to the targeted tumour site using a high-gradient magnetic field (Wu *et al.*, 2015).

Also referred to as magnetic targeted carriers, colloidal IO particles in early clinical trials have demonstrated some degree of success with the technique and shown satisfactory toleration by patients. Furthermore, the use of MNPs as carriers in multifunctional nanoplateforms as a means of real-time monitoring of drug delivery is an area of intense interest (Sun *et al.*, 2008).

Nanocryosurgery is a procedure that uses freezing to destroy undesired tissues. Although, it cannot be regarded as a routine method for cancer treatment, cryosurgery is becoming a popular alternative to traditional therapies because of its important clinical advantages. According to simulations performed by Yan and Liu, intentional loading of NPs with high thermal conductivity into the target tissues can reduce the final temperature, increase the maximum freezing rate, and enlarge the ice volume obtained in the absence of NPs (Yan and Liu, 2008). Also, introduction of NP enhanced freezing could also make conventional

cryosurgery more flexible in many aspects such as artificially interfering in the size, shape, image and direction of ice ball formation. The concepts of nanocryosurgery may offer new opportunities for future tumour treatment. Magnetite and diamond are perhaps the most popular and appropriate choice for enhancing freezing because of their good biological compatibility.

1.10 Motivation and scope of the thesis

Magnetite based nanoparticles are subjects of considerable scientific interest world-wide for its high saturation magnetisation and biocompatibility, but also for vast techno-commercial value for applications as seen above. Its unique magnetic properties made its own place among other magnetic materials and is really appreciated both by engineering and biomedical fields. Ferrofluids find their industrial applications in dynamic seals, dampers, thermal management, shock absorbers, sensors and actuators owing to their magneto controllability. The drastic enhancement in the thermal conductivity in ferrofluids with applied magnetic field has made them promising for externally controllable coolants and could especially be applied in space systems, nuclear power plants and automotive industry. Though nanoscaling has improved activity of its bulk property, in comparison with other metal oxide nanosystems, the morphology dependent functional property is less explored for magnetite. Synthesis of MNPs and especially its colloidal stabilisation in water with reasonable shelf life are quite challenging since one needs control over the size, its distribution and shape. Among the varieties of synthesis techniques, wet chemical route with *in situ* surface modification is preferred due to its economic and simplicity. Every method has its own pros and cons and for best results one has to optimise the parameters involved in the chemical reaction. As pointed out, the need to explore and understand the structure-property functional correlation in these nanomaterials is inevitable for the wide scale commercial applications. One of the major stumbling blocks towards this goal is the difficulty in obtaining stable aqueous ferrofluids. On such background, the present thesis aims at studying the colloidal properties of ultra stable aqueous ferrofluids against temperature, time and magnetic field. Over all, the present thesis is an attempt to study the concealed and unexplored aspects of magnetite in order to broaden its importance so as to compete with other inorganic nanocrystals of its own kind. Thus, the main objective of the present work are summarised as follows.

1.11 Objectives of the present work

1. Monodisperse size controlled superparamagnetic nanocrystals through aqueous coprecipitation method by varying the precipitation temperature and development of ultrastable aqueous, non-aqueous and oil based ferrofluids by introducing proper surface acting moieties.
2. The dispersibility of the as-synthesised nanocrystals in aqueous media, its hydrodynamic size and surface charge has been tested systematically to demonstrate its long-term stability. The temperature dependent kinetics study in which hydrodynamic size was measured during due course of time.
3. The magnetic field dependent tunable rheological properties of non-aqueous ferrofluids were examined by magnetic sweep cycle experiments as well as on-off switch operation which are aimed for practical applications in nanodevices.
4. Role of dielectric constant of the reaction media on which magnetite crystals born can be elucidated by thorough investigation of its colloidal and catalytic properties such as combustion of soot carbon.
5. Size and morphology tuned magnetite nanoparticles, nano-, microspheres, nanocube, nano- truncated octahedra etc. have been fabricated by high temperature process.
6. The as-synthesised nanocrystals have been tested for MTT assay and WST cytotoxicity assay on two different cell lines.

The thesis, has been designed on the above objectives, epitomises facile coprecipitation, solvothermal, thermal decomposition approach for fabricating magnetic nanostructures and its ferrofluids for the novel applications in biomedical and industries. The results obtained have been discussed and correlations have been derived between the experimental parameters and the properties in the following sections.

Materials and instrumental Methods

In this chapter, the experimental techniques which are applied throughout the thesis will be described with a special emphasis on photon correlation spectroscopy (PCS), transmission electron microscopy (TEM), as the application of these tools are undoubtedly central to nanoparticle research. As our synthesised particles (magnetite) are magnetic in nature, the magnetic properties and iron stoichiometry is evaluated by advanced techniques such as VSM, PPMS, Mössbeaur spectroscopy, X-ray photoelectron spectroscopy etc.

2.1 Materials

2.1.1 Fabrication of magnetite nanocrystals

All chemicals were of reagent grade and used without further purifications. Ferric chloride hexahydrate ($\text{FeCl}_3 \cdot 6\text{H}_2\text{O}$ >99%), Ferrous chloride tetrahydrate ($\text{FeCl}_2 \cdot 4\text{H}_2\text{O}$ >98%), iron (III) acetylacetonate ($\text{Fe}(\text{acac})_3$, 97%), (3-Aminopropyl) triethoxysilane, 25% tetramethylammonium hydroxide aqueous solution, benzyl ether (98%) and oleylamine were procured from Sigma Aldrich, India. Absolute ethanol (99.9%), and *n*-Propanol (AR) were purchased from S.d. FINE-CHEM Ltd, India. Ammonia solution (25%, EMPARTA), trisodium citrate dehydrate, Dextran (*Leuconostoc* sp.), sodium acetate trihydrate crystal (guaranteed reagent, GR), ammonium acetate (EMPARTA), ethylene glycol (EG, GR), diethylene glycol (DEG for synthesis), PEG-400, acetone (GR), isopropyl alcohol (IPA, GR), methanol (GR), sodium hydroxide (GR), potato starch soluble (GR), acetone (GR) and 35% hydrochloric acid (EMPLURA) were from procured from Merck, India. Oleic acid (90%) purchased from Alfa aesar, India. Sesame oil, Rice Hull Ash (RHA) collected from IFB Agro industries Ltd, Noorpur, West Bengal, India.

2.1.2 Cell viability assay

Human colorectal cancer line HCT 116 (ATCC[®] CCL-247TM) was obtained from the (ATCC, Manassas, VA). Human breast cancer cell line (MDA-MB-468) was procured from National centre for cell sciences, Pune. WST-1 [2-(4-iodophenyl)-3-(4-nitrophenyl)-5-(2,4-disulfophenyl)-2H-tetrazolium] reagent procured from Roche Life Science. MTT

[3-(4,5-dimethylthiazol-2-yl)-2,5-diphenyltetrazolium bromide] reagent, PEN-STREP, 0.1% Fungizone, N,N-dimethylformamide (DMF) were purchased from Sigma-Aldrich, India. Bovine serum albumin, Coomassie brilliant blue (CBG-25) purchased from S.d. FINE-CHEM Ltd, India, 85% orthophosphoric acid, Sodium chloride, potassium chloride, Disodium hydrogen phosphate, Potassium dihydrogen phosphate purchased from Merck, India. Dulbecco's Modified Eagle's Medium (DMEM), fetal bovine serum (FBS) were obtained from Invitrogen, India. All chemicals utilised in this study were of analytical grade and needed no further purification. Millipore water is used for the reactions, washings and dilutions etc.

2.2 Characterisation techniques

2.2.1 Dynamic Light Scattering (DLS)

DLS also referred to as Photoelectron Correlation Spectroscopy (PCS) is used for particle size, size distribution, charge etc., in NP suspensions. The technique measures time-dependent fluctuations in the intensity of light scattered by colloidal particles in suspension. A low intensity laser beam is scattered by particles in suspension. The diffusion of particles causes rapid fluctuations in backscattered intensity around a mean value at a certain angle. The instrument determines the particle size by measuring the rate of fluctuations in the scattered laser light. The timescale of the fluctuations depends on the particle size (Pecora, 1985). The experimental scattering time autocorrelation function is directly obtained from the measurement. The size of a particle is calculated from the translational diffusion coefficient by using the Stokes-Einstein equation;

$$D_{PCS} = \frac{kT}{3\pi\eta D} \quad (2.1)$$

where D_{PCS} is the hydrodynamic diameter of the NPs, k is Boltzmann's constant, T is the absolute temperature (K), η is the viscosity (mPa.s) and D represents the translational diffusion coefficient ($\text{m}^2.\text{s}^{-1}$). The Z_{av} size and the polydispersity index (PDI) were obtained from the correlograms by Cumulants analysis method as defined in ISO13321 and described by Koppel and Kaszuba *et al.* (Stolarczyk *et al.*, 2009). Briefly, the logarithm of the correlation function of the scattered intensity is fitted to the polynomial function

$$\ln(g_1(t)) = a + bt + ct^2 + dt^3 + \dots \quad (2.2)$$

A second-order cumulant analysis was performed. The true hydrodynamic diameter (Z_{av}) was determined from the first cumulant, represents the Z-average diffusion coefficient according to the Stokes-Einstein equation. The PDI, which estimates the width of the distribution, was determined from the second cumulant divided by the square of the first cumulant ($2c/b^2$) (Iyengar *et al.*, 2016). Values close to zero (i.e., a small contribution of the second order cumulant, corresponding to variance) indicate a monodisperse suspension, larger values (>0.3) are indicative of very broad and/or polydisperse distributions. The intensity size distributions are also fits obtained, in this case, from analysis of the correlation functions using the General Purpose algorithm based upon a non-negative least squares fit using Dispersion Technology Software (v. 7.11, Malvern Instruments; Worcestershire UK).

The advantages are that PCS is a non-destructive method and it can measure *in situ* average particle size in a range between 0.4 and 8630 nm. Despite its practical success, standard PCS techniques are limited to very dilute (single scattering) samples. All reliable methods for interpreting the experimental time autocorrelation function are based on the assumption that the particles under consideration are spherical and are based on the established data on the interaction between the spherical particles and its surroundings, i.e., the particle is assumed to tumble freely in suspension without interacting with other particles. For non-spherical particles, the technique does not provide any information about the actual particle shape but rather indicates the “equivalent spherical diameter”, the diameter of an imaginary sphere of the same volume (Ghosh, 2006). There are some models for dealing with PCS data from anisotropic particles such as rods and disks, non-spherical or even cluster-like particles (Comberg and Wriedt, 1999). The results obtained are invariably very sensitive to the shape information built into the model.

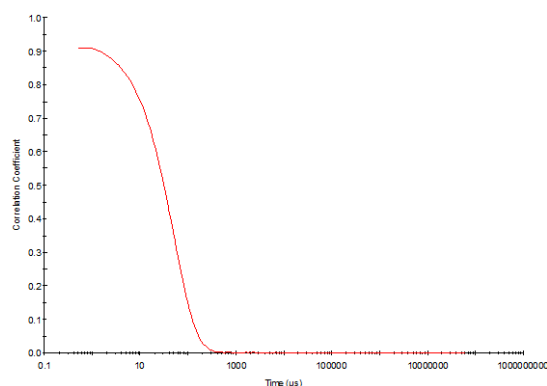


Fig. 2.1 The intensity auto correlation coefficient of aqueous (~10 nm) magnetite nanofluid.

Shape information can more reliably be obtained from static light scattering approaches (Wriedt, 1998), where the intensity is measured as a function of the scattering angle. However limitations remain and the static scattering techniques are not suitable for particles of size close to or below 100 nm. A correlation function can be used to determine the correlation or relationship between the measurements of a fluctuating signal. An example of the intensity autocorrelation function due to the diffusional motion is shown in Fig. 2.1. The electric field correlation function, $g_1(t)$ which is directly related to the dynamics of the scatterer may be defined as;

$$g_1(t) = \langle I(t)I(t + \tau) \rangle \quad (2.3)$$

where I is the intensity, τ is delay time, the angle brackets denote the time averaging. The normalised intensity autocorrelation function $g_2(t)$ is related to the field correlation function by the relation (Pecora, 1985).

$$g_2(t) = 1 + \sigma |g_1(t)|^2 \quad (2.4)$$

where σ is an instrumental coherence factor mainly determined by the number of coherence areas exposed on the detector. The coherence area is defined by

$$A_{coherence} = \frac{\lambda^2 R^2}{\pi a^2} \quad (2.5)$$

where R is the distance between the detector and the scattering volume of radius a , λ being the wavelength of the incident light. The optics of the PCS spectrometer is designed so that σ is close to the ideal value of one. Since the fluctuation of the intensity signal is caused by the motion of particles, those particles that diffuse more quickly are characterised by a smaller fluctuation time. As seen in eqn 2.1, the diffusion coefficient is inversely proportional to the size of the particles, and, consequently, the smaller the particle, the shorter the fluctuation time. For a monodisperse suspension the autocorrelation function is a single exponential and may be expressed as;

$$g_1(t) = \exp(-t/\tau) \quad (2.6)$$

where $1/\tau$ is the characteristic time constant of the correlation function. It is related to the diffusion coefficient by $\Gamma = Dq^2$, and the scattering vector, q , is given by

$$q = \frac{4\pi n}{\lambda_0} \sin\left(\frac{\theta}{2}\right) \quad (2.7)$$

in which n is the index of refraction of the liquid medium, θ is the scattering angle and λ_0 is the laser wavelength in air. Geometrically, the scattering vector is defined as the

difference between the scattered wave vector and the incident wave vector. By combining eqn (2.1) and the equation for the line width, Γ , an equation for the radius of the scattering particle is obtained as

$$r = k_B T q^2 / 6\pi\eta\Gamma \quad (2.8)$$

Using equation (2.8) the size of the scattering particles can then be determined if the temperature and viscosity are known. When the logarithm of the autocorrelation function is graphed versus time, the slope of the resulting line is the line width, Γ .

2.2.1.1 Hydrodynamic size and its distribution

The colloidal stability in terms of size and charge of the synthesised magnetite based aqueous nanofluids were determined by light scattering technique using a Zetasizer Nano-ZS (Malvern Instruments, Malvern, UK) at 25 °C. Aqueous samples were taken in standard (12.5 × 12.5 × 45 mm) disposable polystyrene cuvettes and loaded in the press-fit sample chamber in the machine. For non-aqueous suspensions, glass cuvettes were used. The instrument uses a 4 mW He–Ne laser ($\lambda = 632.6$ nm) to illuminate the sample and measures the time dependent fluctuation in the intensity of light scattered from particles in suspension at a fixed scattering angle of 173°. The scattered light is detected using a sensitive avalanche photodiode detector and the signal is then converted into digital pulses by a pulse amplifier discriminator.

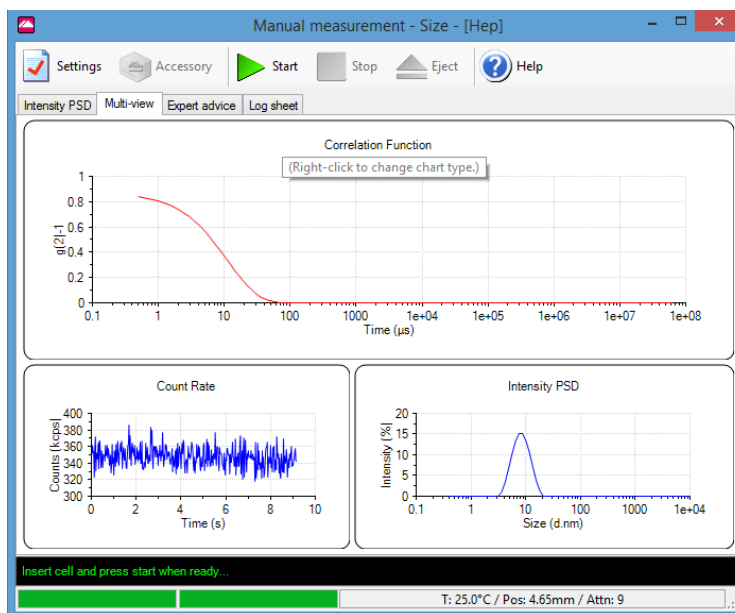


Fig. 2.2 The PCS results window indicating the Z_{av} , count rate, correlation function for the same ~ 10 nm superparamagnetic aqueous ferrofluids.

The output, a stream of digital pulses, is then fed to the correlator which calculates the normalised autocorrelation function of the incoming pulses, i.e. the detected intensity. The laser power is automatically attenuated so that the count rate from the sample, especially high scattering samples, is within acceptable limits. An attenuation index of 11 denotes no attenuation (full laser power), while 0 denotes full attenuation (total laser block). The measurement position within the cuvette was automatically determined by the software to allow a large range of sample concentrations to be measured. Lower range of numbers indicates that the measurement position is closer to the cuvette wall (when sample is turbid).

The results of the measurement are available based either on intensity, volume or number. This is the true size to use if a number is required for quality control purposes. It will only be comparable with other techniques if the sample is monomodal (i.e. only one peak in the size distribution), spherical and monodisperse (i.e. there is no width to the distribution), and the sample is prepared in the correct dispersant. The temperature kinetics study were performed by selected highly stable ferrofluid of different concentrations in a thermostatic sample chamber were exposed between 20 and 65°C in interval of 5°C and the hydrodynamic sizes of suspension were recorded with an accuracy of $\pm 0.1^\circ\text{C}$. For temperature dependent measurements, the samples were equilibrated for at least 10 min at each temperature before the measurements. Each measurement made over a period of 3 min at least triplicate to check the accuracy and reproducibility of experimental findings.

2.2.1.2 The surface charge or zeta potential of particles and molecules is determined by measuring their velocity while they are moving due to electrophoresis. Particles and molecules that have a zeta potential will migrate towards an electrode if a field is applied. The speed they move is proportional to the field strength and their zeta potential. If we know the field strength, we simply measure the speed of movement, using laser Doppler electrophoresis, and then apply established theories to calculate the zeta potential. To improve the sensitivity and accuracy of the measurements we use a technique called M3-PALS (phase analysis light scattering) multi-frequency measurement which determines the mean and distribution during the same measurement.

The surface charge was estimated by measuring the zeta potential converted from electrophoretic mobilities of their dispersion in water at 25°C using the Smoluchowski formula using Malvern Zetasizer Software v.7.11. The designated air-tight polystyrene

cuvette of the Zetasizer instrument was filled with the required volume of bubble-free nanofluid and the tests were carried out at 25°C. The results were obtained with theoretical refractive index of magnetite 2.42 (Cornell and Schwertmann, 1996). In order to find out the point of zero charge (PZC), the pH of the dispersion was adjusted either with aqueous 10^{-3} M NaOH or H₂SO₄. The pH of well dispersed magnetite fluids was checked just before each ζ -potential measurement.

2.2.2 X-ray diffraction (XRD) is a non-destructive analytic tool for deriving the detailed information about the crystallographic structure, phases, in polycrystalline samples and other structural parameters such as average crystallite size, lattice constants, strain, crystallinity, crystal defects, chemical composition. The term XRD is a bit generic as there are several types such as single crystal, powder, thin film, reflexivity and X-ray rocking curve analysis. Since all the NP samples synthesised in this research are in powder form, the technique employed is powdered XRD. Powder XRD must be used with either multicrystalline samples or a sample which has been ground to a fine powder. This allows all of the possible crystal orientations to be accessed simultaneously. In the case of NPs there is no need to further powder the samples since they are already in a fine power form. There is no reason to believe that there is any correlation of the crystallographic orientation from particle to particle in a pressed NP sample. This means that XRD is a valid method for determining the degree of crystallinity of a sample as well as the crystal structure that exists. The spacing of the various peaks also gives the information for determining the crystal structure lattice parameters.

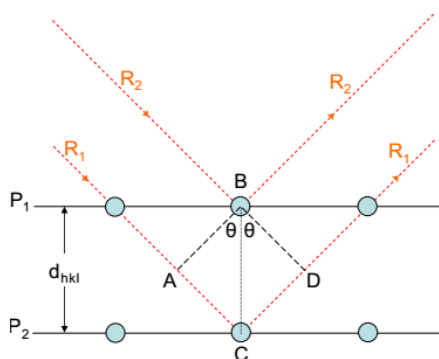


Fig. 2.3 A simplified view of the interaction of X-ray radiation and crystal planes to demonstrate Bragg's law

In XRD a collimated beam of X-ray with a wavelength of 1.5406 Å is incident on a specimen and is diffracted by the crystal planes in the specimen according to the Bragg's law illustrated in Fig. 2.3. P₁ and P₂ indicates a set of parallel planes with Miller indices

hkl and interplanar spacing d_{hkl} , θ is known as diffraction angle. The two incident beams R_1 and R_2 are shown being scattered by atoms C and B respectively. Simple geometry shows that

$$AC = CD = d_{hkl} \sin \theta \quad (2.9)$$

It can clearly be seen that ray R_1 travels a distance $AC + CD$ greater than R_2 , therefore

$$\text{path difference} = AC + CD = 2d_{hkl} \sin \theta \quad (2.10)$$

If the path difference is an integer ($AC + CD = n\lambda$), then constructive interference of the rays will occur, and the reflection is observed. A non-integer value causes destructive interference between the scattered rays and the reflection is not observed. Equation 2.10 can be simplified to give Bragg's law, which states the angles for allowed scattering from a crystal lattice.

$$n\lambda = 2d \sin \theta \quad (2.11)$$

where λ is the wave length of the X-ray radiation, n is an integer. The intensity of the diffracted X-rays is measured and plotted as a function of diffraction angle 2θ . From the 2θ values of the peaks, the lattice spacing (d) values are calculated using the eqn (2.12). We have for any plane with index (hkl)

$$d_{hkl} = \frac{1}{\sqrt{\frac{h^2}{a^2} + \frac{k^2}{b^2} + \frac{l^2}{c^2}}} \quad (2.12)$$

$$\text{when } a=b=c, \quad d_{hkl} = \frac{a}{\sqrt{h^2 + k^2 + l^2}} \quad (2.13)$$

Sample identification can be easily done by comparing the experimental pattern to that in JCPDS file. The powder XRD patterns of as-synthesised magnetite nanocrystals were recorded with Bruker D8 Advanced diffractometer equipped with source $CuK\alpha_1$ radiation ($\lambda=1.5406 \text{ \AA}$) with a step size of $0.05^\circ 2\theta$ and a scan speed of 4° min^{-1} . In the infinite crystal approximation and monochromatic X-ray approximation the peaks would be infinitely narrow. Except for single crystalline particles, the randomly oriented crystals in NPs cause broadening of the diffraction patterns. The effect becomes more pronounced, when the crystallite size is of the order of few nanometers. The simplest and most widely used method for estimating crystallite size is from the half the maximum intensity (FWHM) of a diffraction peak by Debye-Scherrer formula,

$$D_{XRD} = \frac{0.9\lambda}{\beta_{2\theta} \cos \theta} \quad (2.14)$$

where λ is the X-ray wavelength, $\beta_{2\theta}$ is the line broadening at FWHM in radians, and θ is the Bragg angle, D_{XRD} is the mean size of the ordered (crystalline) domains. Debye–Scherrer formula, though widely been used to estimate crystal sizes, underestimates the grain size as it ignores the line broadening due to microstrain in the lattice as a result packing defects/dislocation structures etc (Tjong and Chen, 2004). The mean crystallite size and microstrain involved in as-synthesised nano magneto-crystalline samples were estimated by the Cauchy–Cauchy (CC) approach also known as Williamson–Hall (Cushing *et al.*, 2004) plot from the linear dependence line-profiling of prominent X-ray diffraction peaks of $\beta_{2\theta} \cos\theta$ versus $\sin\theta$ as described in eqn (2.15):

$$\beta_{2\theta} \cos \theta = 2\varepsilon \sin \theta + 0.9 \lambda/D \quad (2.15)$$

where D is the crystal size, ε is the maximum micro deformation of a lattice, $\beta_{2\theta}$ is the integral width of the diffraction peaks at angle θ by the eqn (2.16):

$$\beta_{2\theta} = I/I_{\text{Max}} \quad (2.16)$$

Strain is estimated from the slope (2ε) and the average crystal size (D) from the intercept ($0.9\lambda/D$) of the linear regression assuming the particles are spherical. W-H analysis is sometimes used as a complementary method to confirm TEM values and to make them more robust from the statistical point of view. Rietveld powder structure refinement analysis of X-ray powder diffraction step scan data was done using the JAVA based MAUD program to obtain the structural and microstructural refinement parameters through a least-square method (Rietveld, 1966). The experimental profiles are fitted with the most suitable pseudo-Voigt (pV) analytical function with asymmetry and the background of each pattern is fitted with a fourth order polynomial function. Standard Harris analysis (Krishnan *et al.*, 2013) was performed on X-ray data of magnetite powders to estimate preferred orientation of specific crystal planes and is expressed as texture coefficient $C(h_i k_i l_i)$, following the equation given eqn (2.17),

$$C(h_i k_i l_i) = \frac{I(h_i k_i l_i)}{I_o(h_i k_i l_i)} \left[\frac{1}{n} \sum \frac{I(h_i k_i l_i)}{I_o(h_i k_i l_i)} \right]^{-1} \quad (2.17)$$

where, $I(h_i k_i l_i)$ is the diffraction intensity of the $(h_i k_i l_i)$ plane of the particular sample under investigation, $I_o(h_i k_i l_i)$ is the intensity of the $(h_i k_i l_i)$ plane from the standard JCPDS powder diffraction pattern for the corresponding peak i , and n is the number of reflections taken in to account. Activation energy for the growth of magnetite crystals during syntheses at different temperatures are shown in eqn (2.18)

$$D_{\text{XRD}} = k.e^{-\left(\frac{E}{RT}\right)} \quad (2.18)$$

where, D_{XRD} is the crystallite size, R the universal gas constant, T the reaction temperature, E is the activation energy and k is a constant which may depend on the initial value of crystal size.

2.2.3 Electron microscopy

2.2.3.1 Transmission Electron Microscopy (TEM) is a straight forward technique to determine the size, morphologies of the nanostructured materials as well as to obtain crystal structural information. We have used FEI Tecnai 30 G² S-Twin High Resolution-TEM (HRTEM) operated at 300 kV equipped with a Gatan CCD camera. Here, electrons are accelerated to 300 keV projected on to a thin specimen by means of a condenser lens system, and penetrate in to the sample. TEM uses transmitted and diffracted electrons which generates a two dimensional projection of the sample. The principal contrast in this projection or image is provided by diffracted electrons. In bright field images the transmitted electrons generate bright regions while the diffracted electrons produce dark regions. In dark field image the diffracted electrons preferentially form the image. In TEM, one can switch between imaging the sample and viewing its diffraction pattern by changing the strength of the intermediate lens. The greatest advantages that TEM offers are the high magnification ranging from 50 to 10⁶ and its ability to provide both image and diffraction information from a single sample. The high magnification or resolution of TEM is given by

$$\lambda = \frac{h}{\sqrt{2mqV}} \quad (2.19)$$

where m and q are the electron mass and charge, h the Planck's constant and V is the potential difference through which the electrons are accelerated. This can be approximated to

$$\lambda = \frac{1.22}{\sqrt{E}} \quad (2.20)$$

with E in electron volts (eV) and λ in nm (Williams and Carter, 2009). From eqn (2.20) it can be shown that for a 300 keV electron, $\lambda \approx 0.0022$ nm, which is far smaller than the diameter of an atom. This limit represents the theoretical maximum resolution obtainable for an electron at 300 keV, though in practice this resolution is not achieved due to limitations with electron lenses.

Figure 2.4 is the schematic illustration of TEM. From top down, it has an emission source, a tungsten filament or a lanthanum hexaboride (LaB₆) source. Typically a TEM consists of three stages of lenses (i) condenser, (ii) objective, and (iii) projector lenses. The condenser lenses are responsible for primary beam formation, whilst the objective lenses focus the beam down onto the sample itself. The projector lenses are used to expand the beam onto the phosphor screen or other imaging device such as film. The magnification of the TEM is due to the ratio of the distances between the specimen and the objective lens image plane imaging systems in a TEM consist of a phosphor screen, which may be made of fine (10-100 μm) particulate zinc sulphide, for direct observation by the operator. Optionally, an image recording system such as film based or doped YAG screen coupled CCD's. To record the image, the phosphorescent screen is removed and an appropriate piece of photographic film is put in its place.

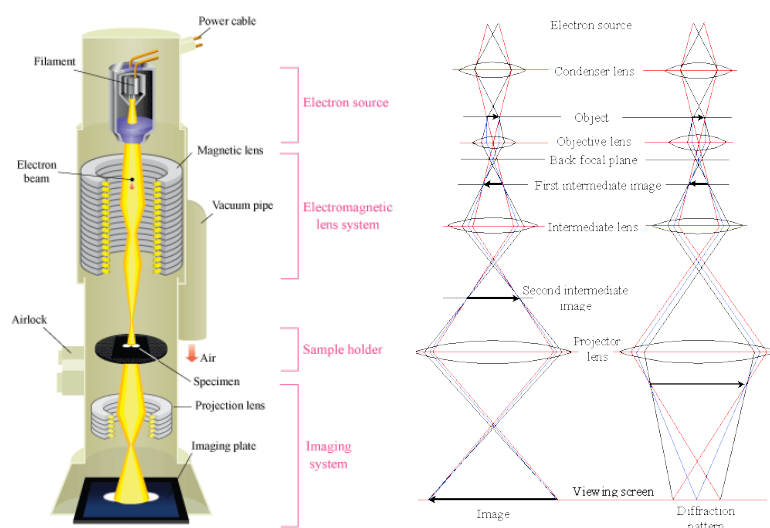


Fig 2.4 Schematic diagram of transmission electron microscope

The energy of the electrons expose the film in much the same way that light does for conventional photography. Specially coated digital cameras can also be employed to capture the images. The primary form of TEM measurement is bright field imaging in which the contrast is produced by direct occlusion of the electron beam, either by absorption or by scattering. The resulting image is a projection of electron transparency.

Image analysis

The size distribution is calculated from the careful inspection on bright field micrographs containing few hundreds of NPs. The standard deviation of size was calculated using the formula eqn (2.21),

$$\sigma = \sqrt{\frac{1}{N} \sum_{i=1}^N (x_i - \bar{x})^2} \quad (2.21)$$

where N is sampling number, x_i is random variable, \bar{x} is mean size and the size distribution is calculated using probability density eqn (2.22), based on a log-normal function

$$p(D) = \frac{1}{D\sigma_1\sqrt{2\pi}} \exp\left\{-\frac{[\ln(D/D_0)]^2}{2\sigma_1^2}\right\} \quad (2.22)$$

where σ is standard deviation, D is size, and D_0 is the mean size. HRTEM can generate lattice images of the crystalline material allowing the direct characterisation of the specimen's atomic structure. Fourier filtering is used to extract the lattice fringe information. The resolution of the HRTEM is 1 nm or smaller.

Sample preparation

Samples are typically prepared from a dilute solution of nanoparticles in suspension. The TEM grids were prepared by drop casting (15 μ l) the nanopowder dispersions onto 400 mesh amorphous-carbon coated copper grids and allowing the solvent to evaporate. The desired result is a single layer of nanoparticles.

Selected area electron diffraction pattern (SAED) offers a unique capability to determine the crystal structure of individual nanomaterials and the crystal structure of the different parts of a sample. A small area of the specimen can be selected and its electron diffraction pattern (rings or spots) produced on the screen of the microscope by making appropriate arrangement in the lenses of TEM. This is an optional arrangement in HRTEM. The SAED allows the researcher to determine lattice constant of the crystalline material which can help in species identification. Basically diffraction patterns are distinguishable as spot patterns resulting from single crystal diffraction zones or ring patterns from the randomly oriented crystal aggregates (polycrystallites). For nanocrystallites or less crystalline materials, the diffraction patterns will be a diffused ring. The ' d ' spacing between lattice planes can be estimated from the formula

$$d = \lambda L/R \quad (2.23)$$

where λ is wavelength of electron wave, L is camera length, R is radius of diffraction ring. The estimation of d -values enables us to describe the crystal structure of the crystalline specimen.

Energy Dispersive X-ray Spectroscopy (EDS) attached to the TEM equipped with high-angle annular dark-field detector with beam scanning capability (Fischione Instruments,

Inc., USA) with TIA analysis software, used to determine the chemical composition on several crystal grains. Upon exposing the samples to high energy electron beams the various atoms present in the sample emit characteristic X-rays which can be observed as several distinct peaks on an energy scale. The intensities of the peaks can be compared with the peaks of a standard sample to obtain the relative amounts of each atomic species, whereby accurate composition of the sample can be determined. The use of EDS has been demonstrated in oxide nanoparticle research in a number of reports (Iyengar *et al.*, 2014).

2.2.3.2 Field emission scanning electron microscope (FESEM) provides the image of the morphology and microstructures of the bulk and nanostructured materials. In this SEM, Field Emission Gun provides the electron beam and the resolution is as high as 1 nm and the instrument operates in the range of 20-30,000 \times . It scans a focused beam of electrons over the sample and detects the yield of secondary and backscattered electrons according to the position of the primary beam. The removal of electrons is the result of secondary low energy electron generation, a process in which the primary high energy electron (back scattered) beam knocks multiple lower energy electrons from atoms in a sample. The secondary electrons which are responsible for the topological contrast provide mainly information about the surface morphology. The backscattered electrons which are responsible for the atomic number contrast carry information on the samples composition (Watt, 1997). The sample typically has to be coated by gold and well grounded to prevent charging the material. FESEM, Supra 35 VP, Carl Zeiss, Germany, 30 kV, image resolution 1.5 nm, energy resolution \sim 133 eV and Zigma, Carl Zeiss, Germany, 30 kV, image resolution 1.3 nm, energy resolution \sim 127 eV were used in this study.

2.2.4 Magnetic measurements

2.2.4.1 Magnetisation versus magnetic field

Vibrating Sample Magnetometer (VSM) operates on Faraday's Law of induction, which tells us that a changing magnetic field will produce an electric field. This electric field can be measured and provides us information about the changing magnetic field. It was invented more than 50 years ago and was a breakthrough in magnetic materials research. Fig. 2.5 is the schematic of a VSM used to measure the magnetic behaviour of magnetic materials. Using VSM the hysteresis, loop parameters namely saturation magnetisation, coercive field and remanence can be derived. A VSM can be installed in an electromagnet

as well as in a superconducting magnet. Consequently it can be operated over a broad temperature range. It is always a magnetically open system, which means the sample geometry has to be considered. The main improvement is that here a different magnetisation measuring principle is used. The sample vibrates periodically at the magnet gap or bore. As vibrating device a motor, a loudspeaker or a piezoelectric transducer can be used. Consequently a periodic induction voltage is generated in the pick-up coil (Grössinger, 2008). This allows the use of a lock-in amplifier with an enhanced signal to noise ratio (Fig. 2.5).

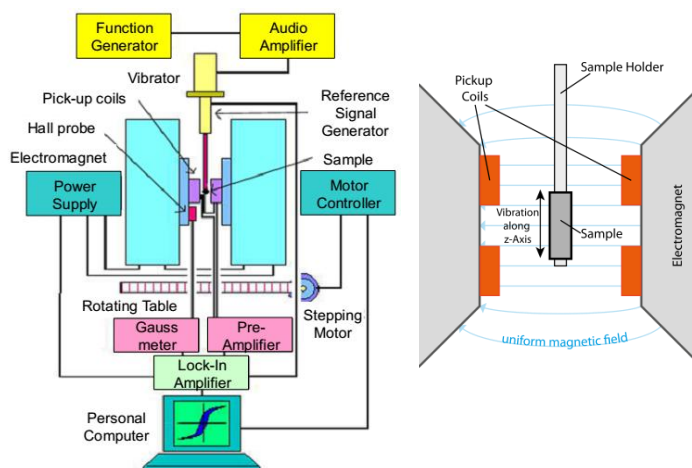


Fig. 2.5 Schematic diagram of vibrating sample magnetometer.

In a VSM, the sample to be studied is placed in a constant magnetic field. If the sample is magnetic, this constant magnetic field will magnetise the sample by aligning the magnetic domains or the individual magnetic spins, with the field. The stronger the constant field, the larger the magnetisation. The magnetic dipole moment of the sample will create a magnetic field around the sample, sometimes called the magnetic stray field. As the sample is moved up and down, this magnetic stray field change as a function of time and can be sensed by a set of pick up coils. A transducer converts a sinusoidal ac drive signal provided by a circuit located in the console into a sinusoidal vertical vibration of the sample rod and the sample is thus made to undergo a sinusoidal motion in a uniform magnetic field. Coils mounted on the pole pieces of the magnet pick up the signal resulting from the sample motion.

The alternating magnetic field will cause an electric field in the pickup coil as according to Faradays law of induction, the current will be proportional to the magnetisation of the sample. The greater the magnetisation, larger is the induced current. The induction current is amplified by a transimpedance amplifier and a lock in amplifier.

The various components are interfaced via a computer. Controlling and monitoring software, the system can tell you how much the sample is magnetised and how magnetisation depends on the strength of the constant magnetic field. For particular field strength, the corresponding signal received from the probe is translated into a value of magnetic moment of the sample. When the constant field varies over a given range, a plot of magnetisation versus magnetic field strength is generated.

The dipole moment is induced in the sample when it is placed in a uniform magnetic field M . Then the amount of magnetic flux linked to the coil placed in the vicinity of this magnetic field is given by

$$\phi = \mu_0 n \alpha M \quad (2.24)$$

where μ_0 is the permeability of free space, n the number of turns per unit length of coil and α represents the geometric moment decided by position of moment with respect to coil as well as shape of coil. A harmonic oscillator of the type,

$$Z = Z_0 + A \exp(j\omega t) \quad (2.25)$$

induces an emf in the stationary detection coil. The induced emf is given by

$$V = -\frac{d\phi}{dt} = -j\omega\mu_0 n M A \left(\frac{\partial\alpha}{\partial z}\right) e^{j\omega t} \quad (2.26)$$

If amplitude of vibration (A), frequency ω and $\frac{\partial\alpha}{\partial z}$ are constant over the sample zone then induced voltage is proportional to the magnetic moment of the sample. A cryogenic setup attached to the sample permits low temperature measurements. This is the basic idea behind VSM (Krishnan and Banerjee, 1999). The magnetisation measurements (hysteresis loop) were carried out employing a Lakeshore 7305, US VSM at 300 K. The slope of an M-H curve at any given point is the differential susceptibility, χ_v of the material and is given by:

$$\chi_v = \frac{M}{H} \quad (2.27)$$

where M is magnetisation, and H is applied field. χ_v is the susceptibility a small amplitude low frequency ac field would see at a given dc field. It should be noted that in a complete treatment, susceptibility should be a tensor as it is possible that magnetisation occurs in a direction not aligned with the applied field. As the strength of the magnetic field is increased, the slope begins to approach zero. This is the result of the fact that nearly all spins are aligned with the magnetic field so increasing the strength of the magnetic fields has no effect. The magnetisation at this point is called the saturation magnetisation (M_s),

from this point the field strength is reduced. In a ferromagnetic material the curve will not trace back upon itself. This property is known as hysteresis since the history of the sample determines its current behaviour. When the field is reduced back to zero, a net magnetisation remains. This is known as the remanent magnetisation (M_R) and it is an important property of applied magnetic materials because it determines how “strong” a magnet is. From here the field direction is reversed, reducing the magnetisation eventually back to zero. The field at which the magnetisation goes back to zero is known as the coercivity (H_C). The coercivity can be thought of as how difficult the material is to demagnetise. In a typical ferromagnet, the bottom half of the curve is identical to the top half. If the material is brought from saturation to saturation the curve never returns to the initial curve.

Crystal dimensions can also be estimated from the magnetisation curves based on the theory of superparamagnetism as proposed by Bean and co-workers (Bean and Livingston, 1959). To fit the magnetisation curves, we assume that individual grains are single crystals without mutual interaction and each particle has an inner single-domain core with the spontaneous magnetisation. The magnetisation of N number of ideal non-interaction superparamagnetic NPs, each with identical magnetic moment μ , at constant temperature T in magnetic field H is given by Langevin function eqn (2.28),

$$M(H) = N\mu \left\{ \frac{e^{\left(\frac{\mu H}{k_B T}\right)} - 1}{e^{\left(\frac{\mu H}{k_B T}\right)} + 1} - \frac{k_B T}{\mu H} \right\} \quad (2.28)$$

where k_B and $N\mu$ are the Boltzmann constant and M_S of the synthesised sample.

The magnetisation curve was fitted using a non-linear-least squares routine to obtain two parameters: the log-mean single particle moment, μ , and M_S . The size, called “magnetic size”, is significantly smaller than the physical size obtained from TEM.

2.2.4.2 ZFC-FC curves

Field-cooled (FC) and zero-field cooled (ZFC) magnetic measurements were taken using a Physical Property Measurement System (PPMS) from Quantum Design (San Diego, CA). The system used for the temperature range of 2 to 350 K and uses a liquid helium cooled superconducting magnet that can attain magnetic fields of up to 7 Tesla. FC-ZFC curves are extremely useful for studying magnetic nanoparticulate systems. In ZFC measurements, sample is cooled to liquid helium temperatures under zero applied

magnetic fields, while it is above its paramagnetic or superparamagnetic transition temperature. Then small uniform external field is applied and the net magnetisation is measured while heating the sample at a constant rate. For small magnetic particles, this curve has a characteristic shape. As the particle cools in a zero applied magnetic field, they will tend to magnetise along the preferred crystal directions in the lattice, thus minimising the magneto-crystalline energy. Since the orientation of each crystallite varies, the net moment of the systems will be zero. Even when a small external field is applied the moments will remain locked into the preferred crystal directions, as seen in the low temperature portion of the ZFC curve.

As the temperature increases more thermal energy is available to disturb the system. Therefore more moments will align with the external field direction in order to minimise the Zeeman energy term. In other words, thermal vibration is providing the activation energy required for the Zeeman interaction. Eventually the net moment of the system reaches a maximum where the greatest population of moments has aligned with the external field. The peak temperature is called blocking temperature T_B which depends on particle volume. As temperature rises above T_B , thermal vibrations become strong enough to overcome the Zeeman interaction and thus randomise the moments (Denardin *et al.*, 2002).

Field cooled measurements proceed in a similar manner to ZFC except that the constant external field is applied while cooling and heating. The net moment is usually measured while heating. In order for the curves to be useful as a pair they must be measured with the same field strength. When the two graphs are plotted on top of each other there is a temperature at which they merge. This temperature is known as the irreversibility temperature. However, the FC curve will diverge from the ZFC curve at a point near the T_B . This divergence occurs because the spins from each particle will tend to align with the easy crystalline axis that is closest to the applied field direction and remain frozen in that direction at low temperature. The temperature at which the peak magnetisation in the ZFC graph occurs is the T_B . At this point the thermal energy ($k_B T$) overcomes the anisotropy barrier. At any temperature above this, the thermal energy decreases the magnetisation by randomising the spin orientations. This leads to a familiar Curie-Weiss law behaviour where T_C

$$M \propto \frac{1}{T - T_C} \quad (2.29)$$

T_C is normally the Curie temperature. It is important to note that ZFC, FC are non-equilibrium measurements (Roy *et al.*, 2006). Care must be taken to ensure the same heating rate is used during the measurements in order to properly compare the measurements.

2.2.5 Spectroscopic measurements

2.2.5.1 Mössbauer spectroscopy is a technique based on the Mössbauer effect. This effect, discovered by Rudolf Mössbauer in 1958, consists in the nearly recoil-free, resonant absorption and emission of γ -rays in solids. Like NMR spectroscopy, Mössbauer spectroscopy probes tiny changes in the energy levels of an atomic nucleus in response to its environment. Typically, three types of nuclear interactions may be observed

- (a) an isomeric shift, also known as a chemical shift
- (b) quadrupole splitting and
- (c) magnetic/hyperfine splitting, also known as the Zeeman effect.

Due to the high energy and extremely narrow line widths of γ -rays, Mössbauer spectroscopy is a very sensitive technique in terms of energy resolution, capable of detecting change in just a few parts per 10^{11} .

Just as a gun recoils when a bullet is fired, conservation of momentum requires a nucleus (such as in a gas) to recoil during emission or absorption of a γ -ray. If a nucleus at rest emits a γ -ray, the energy of the γ -ray is slightly less than the natural energy of the transition, but in order for a nucleus at rest to absorb a γ -ray, the γ -ray's energy must be slightly greater than the natural energy, because in both cases energy is lost to recoil. This means that nuclear resonance is unobservable with free nuclei, because the shift in energy is too great and the emission and absorption spectra have no significant overlap. The recoil fraction of the Mössbauer absorption is analysed by nuclear resonance vibrational spectroscopy. Nuclei in a solid crystal, however, are not free to recoil because they are bound in place in the crystal lattice. When a nucleus in a solid emits or absorbs a gamma ray, some energy can still be lost as recoil energy, but in this case it always occurs in discrete packets called phonons (quantised vibrations of the crystal lattice). Any whole number of phonons can be emitted, including zero, which is known as a "recoil-free" event. In this case conservation of momentum is satisfied by the momentum of the crystal as a whole, so practically no energy is lost.

Mössbauer found that a significant fraction of emission and absorption events will be recoil-free, which is quantified using the Lamb–Mössbauer factor. This fact is what makes Mössbauer spectroscopy possible, because it means gamma rays emitted by one nucleus can be resonantly absorbed by a sample containing nuclei of the same isotope, and this absorption can be measured. ^{57}Fe Mössbauer spectra of the selected magnetite specimens were recorded at room temperature by means of a standard constant acceleration transmission mode with a ~ 50 mCi ^{57}Co diffused in rhodium matrix using a α -Fe foil for calibration. The experimental profiles were fitted to Lorentzian site analysis using Recoil program.

2.2.5.2 X-ray Photoelectron Spectroscopy (XPS) is a surface-sensitive quantitative spectroscopic technique, which measures the elemental composition at the parts per thousand ranges. The spectrum is obtained by irradiating the sample with a beam of X-rays while simultaneously measuring the kinetic energy and number of electrons that escape from the top. The kinetic energy is measured by an electron energy analyser which further determines the binding energy of the corresponding photoelectrons. From the binding energy and intensity of a photoelectron peak, the elemental identity, chemical state, and quantity of an element are determined. XPS can also provide information on the oxidation state and local bonding environment of atoms within a surface. Due to the high elemental sensitivity and tuneable spatial resolution of XPS, changes in oxide chemistry can be monitored over relatively large (few hundred μm) or more localised (tens of μm) areas. The ability of XPS to differentiate between atoms of the same oxidation state having different bonding arrangements allows for the quantitative analysis of surfaces containing mixed oxide phases. This is of particular importance when studying the iron oxide products especially, magnetite fabricated in aqueous environments (Iyengar *et al.*, 2014).

XPS spectra of the magnetic samples were recorded on XPS system (PHI 5000 Versa Probe II, ULVAC-PHI, INC., USA), maintaining a base pressure of the analysis chamber in the range of $3\text{--}6 \times 10^{-10}$ Torr, using a monochromatic Al $K\alpha$ X-ray source (1486.6 eV). Selected spectra, especially N 1s and valence band spectra were recorded to eliminate the overlap between different Auger and/or core levels. Binding energy (BE) calibration was performed with Au $4f_{7/2}$ core level at 83.9 eV. The spectrum was recorded using a Peltier cooled CCD detector with an acquisition time of 10 s using a $5\times$ objective. The XPS data was deconvoluted with XPS PEAK 4.1 software which produced stable and

almost super imposable baselines, confirming the stability of the fits and helping to validate the interpretation.

2.2.5.3 Fourier transform infrared (FTIR) spectroscopy is a useful technique for characterising materials and obtaining information on the molecular structure, dynamics and environment of a compound by making use of the energy involved in different bond vibrations in the materials. Vibrational motion of chemical bonds occurs in the infrared region of the energy beam. The FTIR spectroscopy exploits this phenomenon. When a material is exposed to IR energy this energy couples with the energy of the sample. If the impinging IR energy is in resonance with the vibration of the chemical bond in the sample the intensity of the beam is measured before and after it interacts with the sample. The incident radiation can be detected in transmission or reflection mode. The intensity is plotted as a function of the frequency in the IR spectrum (Smith, 1999). When electromagnetic radiations representing the IR region with the wavenumber range $400\text{--}4000\text{ cm}^{-1}$ are transmitted through the sample, it is absorbed by the functional groups present in the specimen for bond vibrations. In an infrared spectrum, the absorption or transmittance peaks correspond to the frequencies of vibrations between the bonds of the atoms making up the material. As the frequency of energy absorbed depends on the masses, chemical environment of the atoms and the type of vibration, the resulting spectrum can easily convey the particular groups present in the sample. This aspect makes infrared spectroscopy quite useful in material characterisation. FTIR spectra of the as prepared products were recorded at room temperature using the KBr (Sigma Aldrich, ~ 99%) pellet method on a Perkin-Elmer Spectrum (100 as well as Two series) spectrophotometer ranging from $400\text{ to }4000\text{ cm}^{-1}$ with average of 50 scans.

2.2.5.4 Raman spectroscopy is a technique making use of the vibrational, rotational and other low-frequency energy transitions in a system. Raman spectroscopy is used to identify different molecules and even functional groups within larger molecules. The bonds formed between atoms have specific vibrational frequencies that correspond to the atom's masses and the strength of the bond between them. Complex molecules therefore exhibit many peaks and can be readily identified by the pattern or “finger print” created by those peaks. As such, there are many uses for micro Raman spectrometers as they can non-destructively identify microscopic samples or microscopic areas of larger samples. When an intense monochromatic light beam impinges on the sample, the electric field of the incident radiation distorts the electron clouds that make up the chemical bonds in the

sample, storing some energy. When the field reverses as the wave passes, the distorted electron clouds relax and the stored energy is reradiated. Although, the incident beam may be polarised so that the electric field is oriented in a specific direction with respect to the sample, the scattered beam is reradiated in all directions, making possible a variety of scattering geometries. Most of the stored energy is reradiated at the same frequency as that of the incident exciting light. This component is known as the Rayleigh scattering and gives a strong central line in the scattering spectrum.

However, a small portion of the stored energy is transferred to the sample itself, exciting the vibrational modes. The vibrational energies are deducted from the energy of the incident beam and weak side bands appear in the spectrum at frequencies less than that of the incident beam. These are the Raman lines. Their separation from the Rayleigh line is a direct measure of the vibrational frequencies of the sample. It relies on the inelastic scattering of monochromatic light, usually from a laser source in the visible, near infrared, or near ultraviolet range. The laser light interacts with molecular vibrations, phonons or other excitations in the system and as a result, the energy of the laser photons will be either shifted up or down commonly called as ‘Raman effect’. This shift in energy provides information about the vibrational modes in the system, which in turn serves as a fingerprint of the molecules under study. Typically, the sample is illuminated with a laser beam and the radiations from the illuminated spot are collected with lenses which are being sent through a monochromator. Elastic scattered radiations corresponding to the wavelength of the laser line is filtered out and the rest of the collected light is dispersed onto a detector by either a notch filter or a band pass filter.

Raman spectra of the powder specimens in the present study were recorded at room temperature using by 514.5 nm radiation from an argon ion laser (Stellar Pro, 50 mW) on Princeton instruments Acton SP2500. Raman spectrometer is equipped with an optical microscope (Olympus Confocal Raman Optics micrometer), thermoelectrically cooled ($-60\text{ }^{\circ}\text{C}$) charge-coupled device (CCD) detector, a CCD camera (resolution 1340×1100) that can provide a good laser beam. Samples were compacted into a 1 mm cavity held on an anodised aluminium plate. The laser beam was focused on the sample by a $\times 50$ lens to a spot size of ca. 5–6 μm . Coaxial backscatter geometry was employed for signal collection with spectral resolution of $\sim 1\text{ cm}^{-1}$. The Raman shifts were calibrated using the 520 cm^{-1} line of a silicon wafer. The spectra were collected using 2.5 mW laser power over the range $1000\text{--}200\text{ cm}^{-1}$ and accumulation over 10 scans, each with an exposure time of 10 s to further reduce noise.

2.2.5.5 UV-visible spectroscopy refers to the absorbance or reflectance spectroscopy in the ultraviolet-visible spectral region between 190 to 800 nm which is divided into the ultraviolet (UV, 190–400 nm) and visible (Vis, 400–800 nm) regions. Molecules on irradiation with the UV-visible radiations undergo electronic transitions on absorbing the corresponding energy, the amount of energy absorbed being dependent on the structure of the compound. Therefore the absorbance spectrum of a molecule often serves as source of identification of its electronic state. As a molecule absorbs energy, an electron is promoted from an occupied molecular orbital, usually a non-bonding n or bonding π orbital to an unoccupied anti-bonding molecular orbital, π^* or σ^* . In short, the molecule may undergo several energy transitions which is given in the increasing order of energy as n to $\pi^* < n$ to $\sigma^* < \pi$ to $\pi^* < \sigma$ to $\pi^* < \sigma$ to σ^* . Since all these transitions require fixed amount of energy, the UV-visible spectrum of a compound would consist of one or more well defined peaks, each corresponding to the transfer of an electron from one electronic level to another. The intensity of absorption is in accordance with Beer's and Lambert's Law which states that the fraction of incident radiation absorbed is proportional to the number of absorbing molecules in its path. Thus UV-Visible spectroscopy is a powerful analytical tool for the qualitative as well as quantitative assessment of molecules. The measurements are usually carried out in very dilute solutions and the most important criterion in the choice of solvent is that it must be transparent within the wavelength range being examined. For preparing stock solutions, the sample is accurately weighed and made up to volume in volumetric flask. Aliquots are removed from this solution and appropriate dilutions are made to make solutions of desired concentration.

For recording the spectrum 1 cm square quartz cell is commonly used which requires ~1 ml of solution. The quartz cell containing solution is placed in the path of light beam and spectrum is recorded by varying the wavelength of incident light. The spectrum can also be deduced from well powered solid samples which use special sample holders. In the present study, the absorbance spectra of the samples were obtained using a UV-visible V-730 JASCO spectrophotometer (Japan) in the wavelength range of 200–800 nm. The absorbances of surface modified samples were conducted in their corresponding dispersions, water and toluene being the dispersion media for hydrophilic and hydrophobic samples respectively. For bulk and uncoated samples, the measurements were done on powdered samples.

2.2.5.6 Inductively coupled plasma-Atomic emission spectroscopy (ICP-AES) is a type of emission spectroscopy that uses the inductively coupled plasma to produce excited atoms and ions that emit electromagnetic radiation at wavelengths characteristic of a particular element. It is a flame technique with a flame temperature in a range from 6000 to 10000 K. The intensity of this emission is indicative of the concentration of the element within the sample. ICP-AES, Spectro CIROS Vision, Spectro Analytical Instruments, Germany was used in this study to estimate total iron concentration in the acidified dispersions of the magnetite NPs. Samples were prepared for analysis as follows. Concentrated HCl (0.5 ml) and 1 ml Milli-Q H₂O was added to a small aliquot of the NP suspension. The mixture was heated until only 1-2 drops of liquid remained, at which time 20 ml deionised water was added. The solution was heated to boiling, then immediately removed from heat and allowed to cool to room temperature. The suspension was then diluted to obtain exactly 50 ml volume.

2.2.6 Thermogravimetry (TG) and differential thermal analysis (DTA) was used to investigate the physico-chemical changes in the synthesised nanocrystals as a function of temperature under ultrapure nitrogen purge. In this method, the sample is placed on a high-precision balance and subsequently heated following a given temperature program. During the heating process, sample loses weight due to its decomposition on supply of heat which is monitored by a precision balance. The thermogravimetric profile is obtained as the plot of sample weight against temperature from which the thermal stability of the components can be interpreted. In DTA, the material under study and an inert reference are made to undergo identical thermal cycles, while recording any temperature difference between sample and reference. Changes in the sample, either exothermic or endothermic, can be detected relative to the inert reference. i.e., DTA provides data on the transformations that have occurred, such as glass transitions, crystallisation, melting and sublimation. The area under a DTA peak is the enthalpy change and is not affected by the heat capacity of the sample. In the present study, TG-DTA has been carried out on powder samples using a simultaneous thermal analyser (STA 6000, Perkin Elmer, US as well as STA 449 C, NETZSCH, Germany) in nitrogen/air atmosphere heated at a constant rate of 10 °C min⁻¹ under nitrogen purge.

2.2.7 BET Surface area The specific surface area and pore size distribution of the magnetite powders were calculated from the N₂ adsorption data following the *Brunauer–*

Emmett–Teller (BET) technique at 77 K. Two different models of surface area analyser (TriStar II 3020 Version 3.02) and (Quantachrome Instruments version 10.01) have been used. Surface area (SA) analyses were conducted on powder samples after degassing them at 200 °C for 3 h.

$$D_{SA} = \frac{6000}{\rho \cdot SA} \quad (2.30)$$

Particle size (D_{SA}) was also calculated from the BET surface area using eqn (2.30) with an assumption that all the particles are spherical and unclustered using $\rho = 5.18 \text{ g cm}^{-3}$ for magnetite.

2.2.8 Rheological properties: Viscosity

Rheological properties play a very important role in fluid flow. During application of nanofluids they are likely to flow either by forced or natural convection and hence, the flow properties such as viscosity are therefore essential in the study of suspensions containing nano sized particles. All materials that show flow behaviour are referred to as fluids. In all fluids, there are frictional forces between the molecules and, therefore, they display a certain flow resistance which can be measured as viscosity (Buyevich, 1999). Viscosity is a transport property which refers to the resistance of a material to flow. When dealing with nanofluids, one is often tempted to consider the dispersed medium under question as a homogeneous fluid characterised by properties such as density and viscosity which in turn will only require a single set of mass and momentum conservation equations. However, such a simple picture will not provide useful explanations for cases where the fluid is unsteady and non-uniform.

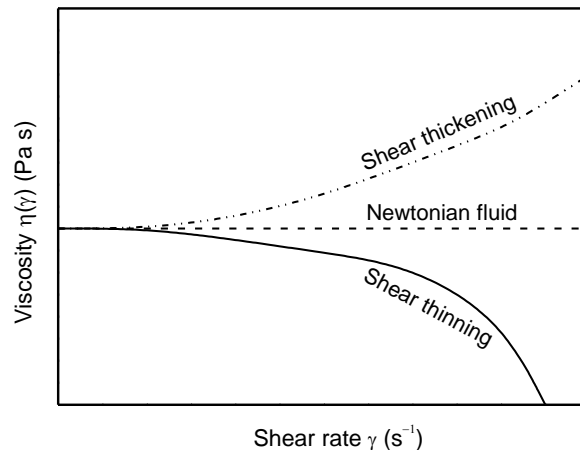


Fig. 2.6 Viscosity of Newtonian, shear thickening and shear thinning fluids as a function of shear rate

(a) Newtonian flow behaviour: Isaac Newton found that the shear force acting on a liquid is proportional to the resulting flow velocity (Buyevich, 1999). Hence, a fluid is said to be Newtonian if the viscosity remains constant with an increase in shear rate as depicted in Fig 2.6. Newtonian flow behaviour is observed in low molecular liquids such as water, mineral oils (without polymer additives) and solvents. However, more complex flow behaviour is expected for fluids containing suspended particles.

(b) Non-Newtonian flow behaviour: Fluids, whose viscosity changes with an increase in shear rate, are referred to as Non-Newtonian. These fluids could be further classified according to their flow behaviour. Shear-thinning and shear-thickening flow behaviour is discussed in the following sections.

(i) Shear-thinning flow behaviour

For samples that display shear-thinning behaviour, the shear viscosity is dependent on the degree of shear load. Thus, the viscosity decreases with an increase in shear stress (fig. 2.6). In dispersions, shearing can cause the particles to orient in the flow direction and in the direction of the flow gradient. This can lead to disintegration of agglomerates or change in particle form. The interaction forces between particles may decrease during the process and cause a lowering in the flow resistance. Examples of shear-thinning materials include shampoos, paints and polymer solutions.

(ii) Shear-thickening flow behaviour

Similar to shear thinning fluids, the shear viscosity of samples displaying shear thickening behaviour is also dependent on the degree of shear load. However, the viscosity increases with an increase in shear stress (fig. 2.6). With highly concentrated suspensions, the probability of particle interaction is much higher and may result in particles becoming wedged together and thus increase the flow resistance. Particle shape plays an important role since during the shear process, particles rotate as they move. Cube-shape particles take up more volume when rotating than spherical particles and hence less free volume is available for the liquid between the particles. Compared to shear thinning materials, shear thickening materials are much less common in industrial practice. Examples of shear-thickening materials include dispersions with a high concentration of solids or polymers such as ceramic suspensions.

(iii) The yield point

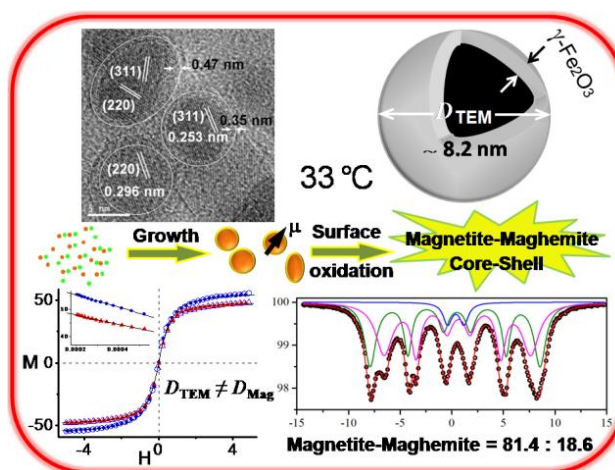
The yield point or yield stress refers to the external force required before a material will start to flow. A typical example is toothpaste; a certain amount of force must be applied before the tooth paste starts to flow. Materials with yield points tend to flow inhomogeneously.

Viscosity measurements were performed using Anton Paar-Physica MCR 301 Rheometer (Cape Peninsula University of Technology (CPUT), Cape Town) at 25 °C, and application of magnetic field using magnet-physik FH-54 Gauss/Telometer.

Aqueous coprecipitation

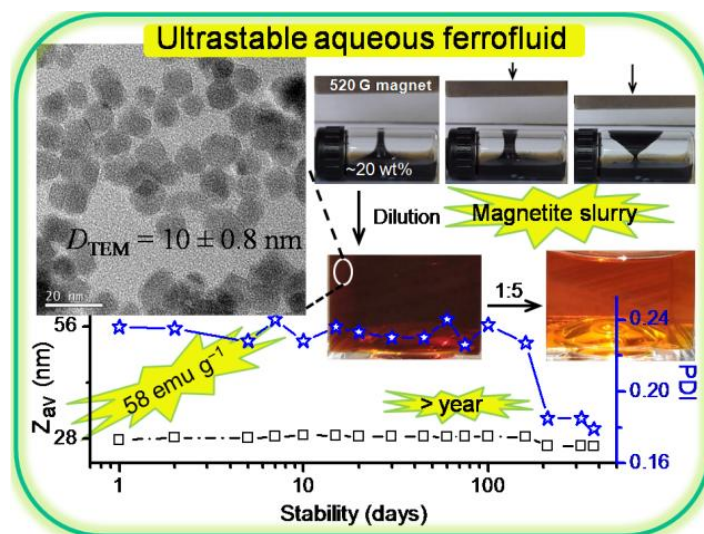
3.1 Graphical abstract

Uniform 8-13 nm sized 0D superparamagnetic Fe_3O_4 nanocrystals were synthesised by an aqueous ‘co-precipitation’ route under the N_2 atmosphere at different precipitation temperatures to understand the growth kinetics. We also report development of ultra-stable aqueous colloidal dispersion of magnetite nanocrystals, magnetitic nanofluids, in the presence of tetramethyl ammonium hydroxide (TMAH). The synthesised nanocrystals were characterised by XRD, TG–DTA, XPS and TEM for evaluating the phase, crystal structure and morphology. FTIR spectroscopy was used to shed light onto the nature of the interaction between TMAH and Fe_3O_4 NPs. The magnetic characteristics of as-synthesised nanocrystals were characterised by VSM, PPMS and Mössbauer spectroscopy.



TEM investigation revealed highly crystalline spherical magnetite particles in the 8.2–12.5 nm size range. The kinetically controlled, as grown NPs were found to possess a preferential (311) orientation of the cubic phase, with highest magnetic susceptibility of $\sim 57 \text{ emu.g}^{-1}$ for aqueous medium whereas 64.68 and 57.92 emu.g^{-1} at room temperature before and after peptisation in physiological saline. Williamson–Hall technique was employed to evaluate the mean crystallite size and microstrain involved in the as-synthesised nanocrystals from the X-ray peak broadening. In addition to FTIR and Raman spectra, Rietveld structural refinement of XRD confirms the magnetite phase with 5-20% maghemite in the sample. VSM and Mössbauer spectral data allowed us to fit the magnetite/maghemite content to a core-shell model where the shell is 0.2–0.3 nm thick

maghemite over 7.8 nm magnetite core. The small activation energy of $\sim 10 \text{ kJ.mol}^{-1}$ calculated from Arrhenius plot for the complex process of nucleation and growth by diffusion during synthesis shows the significance of the precipitation temperature in the size controlled fabrication processes of nanocrystals. With a view to establish the temperature and Raman laser power relationship, evolution of different iron oxide phases due to the oxidation under heat treatment as well as Raman from the laser spot with increasing power also investigated. The key colloidal properties such as charge, hydrodynamic size, photon counts, dispersion stability and surface chemistry have been analysed and compared with a dispersion of aqueous precipitated magnetite. The TMA suspensions are stable over a year without any loss due to precipitation.



Photon scattering experiments have indicated the presence of very small NP clusters of 28 nm in aqueous suspensions. The lower extent of agglomeration in TMA promotes the one-shell clusters of primary nanoparticles, a fact which can forecast the stability of the ferrofluid. BET results reveal a mesoporous structure and a large surface area of $124 \text{ m}^2.\text{g}^{-1}$. Magnetic measurement shows that the particles are superparamagnetic in nature. The change in surface charge of the magnetic fluid from -44 to $+49 \text{ mV}$ while varying the pH indicated the PZC at pH 5.98. The dynamic processes were investigated during the photon scattering experiment against time, temperature and concentration. The stability of the ferrofluid against time, temperature and concentration indicates the great potentials in biotechnology, selective catalysis and other industrial applications.

3.2 Introduction

Magnetite nanoparticles (MNPs) in the form of powder or slurry have been attracting increasing interest worldwide for their size and shape-dependent novel magnetic, optical, and other unique properties (Li *et al.*, 2010). Another interesting property that arises from finite size and surface effects is the existence of superparamagnetism at room temperatures, magnetising strongly under an applied field, but retaining no permanent magnetism once the field is removed (Iyengar *et al.*, 2014). Magnetite is the only FDA approved magnetic materials for use in humans since IONPs are generally well-tolerated *in vivo* (Garcia-Jimeno and Estelrich, 2013). In the future, patients are more likely to be exposed to pharmaceutical products containing such particles (Mahmoudi *et al.*, 2010). Néel relaxation of superparamagnetic Fe_3O_4 is an effective way to heat up the nanocrystals and the surrounding tissue by transferring energy from the external magnetic field in therapeutic hyperthermia and, more recently, in the development of theranostic technologies (Daou *et al.*, 2006; Ghosh *et al.*, 2010).

Large surface area to volume ratio for NPs provides enormous driving force for diffusion, especially at elevated temperatures (Ghosh *et al.*, 2010). Colombo *et al.* calculated the activation energy for the reduction of iron oxides (hematite, maghemite and magnetite) at 150° to 400°C under reductive atmosphere (Colombo *et al.*, 1967). Brus *et al.* reported the diffusion controlled aqueous oxidation kinetics of magnetite NPs (Tang *et al.*, 2003). Although magnetite nanocrystals prepared by the precipitation technique have been extensively studied, to the best of our knowledge, seldom efforts have been devoted on its growth kinetics during crystallisation. Magnetite NPs are susceptible to undergo surface oxidation in air to $\gamma\text{-Fe}_2\text{O}_3$, and hence the control of magnetic properties at these very small sizes still remains a challenge. Average size estimation by TEM is by analysing rather a limited number of NPs (typically 100–300) compared to $>10^{12}$ NPs investigated by XRD and VSM (Frison *et al.*, 2013). Debye-Scherrer formula, though widely been used to estimate crystal sizes, underestimates the grain size as it ignores the line broadening due to microstrain in the lattice as a result packing defects / dislocation structures etc (Tjong and Chen, 2004). Application of Williamson–Hall method on X-ray profiles not only estimate the crystallite sizes but also isolates the peak broadening due to internal lattice strain (Dorofeev *et al.*, 2012).

Over the past couple of decades numerous techniques have been proposed to synthesise nano-sized Fe_3O_4 particles. The aqueous coprecipitation of Fe^{2+} and Fe^{3+} salts

using an alkali remains the most intensively studied, modified and improved method to find economic and environmental friendly pathways for fabrication of controlled metal oxide nanostructures. Most of the industrial applications of magnetite demand highly magnetic NPs with precise knowledge of size, lattice strain/defects and minimal surface passivation. Crystal dimension of nanomaterials affect key colloid properties such as rheology, film gloss, catalytic activity, chemical sensing etc (Masala and Seshadri, 2004). Very often increasing mismatch of magnetic NP size and its M_S values (and as a result increasing magnetic anisotropy) is reported with decreasing size in magnetite NPs. This is due to the presence of a magnetically dead layer of oxidised 15-30% amorphous component (with a thickness varying between 0.3 and 1.0 nm) over the maghemite shell of magnetite–maghemite core–shell structure (Frison *et al.*, 2013). We show that there are size-dependent changes in the local structure and oxidation state of the oxide shell, the relative fraction of maghemite increasing at the expense of magnetite as the core dimensions decrease. This size/structure correlation has been explained in terms of morphological and structural disorder arguments (Iyengar *et al.*, 2014).

It is more difficult to maintain the stability of MNPC dispersions because thermal energy does not prevent coagulation produced by the vdW forces that induce strong short-range isotropic interactions (Garcia-Jimeno and Estelrich, 2013), and the inter-particle magnetic dipolar attraction from single domain MNPs (Ramimoghadam *et al.*, 2015). It is a common observation that monodispersed NPs as observed by electron microscopy techniques often show polydispersity in aqueous suspensions due to clustering. Therefore, the development of magnetite powder dispersion having superior stability as well as good biocompatibility is desirable. The least hydrodynamic sizes reported so far are 4-8 times the TEM sizes for magnetite NPs, surface functionalised with PEG (Garcia-Jimeno and Estelrich, 2013; Ramimoghadam *et al.*, 2015), citrate (Ramimoghadam *et al.*, 2015), dehydroascorbic acid (vitamin-C) (Xiao *et al.*, 2011), diethylene glycol and N-methyldiethanolamine (Lartigue *et al.*, 2012), and PEG-1000 and PVP K-30 (Tu *et al.*, 2013). Majority of these reports used photon scattering technique just to derive size data for comparison as a part of routine characterisation. However, to the best of our knowledge there is no detailed study on the colloidal stability of aqueous suspensions of magnetite NPs and the effect of its concentration temperature and ageing time on clustering which is extremely important for predicting its application.

In this chapter, we report the estimation of the crystal dimensions of magnetite synthesised through surfactant free aqueous coprecipitation route from the TEM, XRD, and magnetisation profiles fitted by Langevin eqn (2.28). The maghemite content in magnetite was determined from the Mossbauer spectral fitting. The magnetite phase was confirmed from the X-ray, TEM, Raman and FTIR spectroscopy. The magnetic powder was thoroughly characterised by thermal analyses (TG-DTA), surface area analysis, and hydrodynamic size and zeta (ζ) potential measurements. The XRD data were analysed by Rietveld refinements. The activation energy for growth of size tailored magnetite crystals was calculated employing Arrhenius equation. The crystal dimensions were carefully correlated in terms of maghemite layer content over magnetite core in a core-shell model. In this chapter, we report the preparation of an ultrastable aqueous colloidal suspension of magnetite, peptised by TMAH. The stability and the coagulation kinetics of the ferrofluids have been studied against the slurry concentration, temperature as well as time by PCS. We demonstrated, for the first time, the simple way one can control the uniformity of magnetic one-shell clusters in aqueous solution. The ζ -potential of magnetite ferrofluids was examined as a function of pH. The enhanced stability of peptised magnetite suspension has been correlated to the zeta potential and other colloidal properties, this places understanding of the colloidal behaviour on a strong physical basis and shows pathways for achieving such ultrastable stability even in aqueous suspensions. Experiment on magnetoviscous effect and yield stress of phase transferred non-aqueous oil based ferrofluids has been carried out for different magnetic field strengths using stress controlled rheometer. The formation and destruction of magnetically induced structures and the interactions of NPs and aggregation are also discussed. Furthermore, reversibly switchable stimuli response properties of fluids are demonstrated and may find applications in miniature devices such as micro- and nano-electromechanical systems.

3.3 Experimental

3.3.1 Aqueous coprecipitation

The procedure adopted here is a modification of the method of Shen *et al.* (Shen *et al.*, 1999) To elucidate the formation process of Fe_3O_4 nanocrystals in a size tailored manner, 4.2 mmol $\text{FeCl}_2 \cdot 4\text{H}_2\text{O}$ and 8.4 mmol $\text{FeCl}_3 \cdot 6\text{H}_2\text{O}$ (such that $\text{Fe}^{3+} / \text{Fe}^{2+} = 2$) were dissolved in 35 ml deionized water previously deaerated by purging nitrogen gas in a 100 ml three-neck round bottom flask whose central neck was connected to a water-cooled condenser.

A thermometer and a glass pipette for N₂ gas purge were connected through thermometer pockets to the other two necks. The reaction mixture was heated slowly to 90°C over a hot plate magnetic stirrer while continuous stirring. The clear off-yellow colour of the suspension turned to muddy orange at ~80°C indicating the complete hydrolysis of ferrous and ferric chlorides. After heating the reaction mixture for ~30 min at 90°C, ~7 ml NH₃ solution was added while vigorous stirring. The orange coloured suspension immediately turned black indicating the formation of magnetite crystals. At this point the net Fe²⁺ concentration was 100 mM. The temperature was maintained at 90°C for further 30 min to allow crystal growth. The suspension was cooled naturally to ambient temperature. The resultant pH of the reaction mixture was ~11. The entire experiment was carried out carefully under a closed nitrogen atmosphere. The precipitated black solid was collected by magnetic decantation with a help of permanent neodymium iron boron magnet (520 G strength), and washed five times with 1:1 acetone and methanol mixture. This magnetite is designated as T90.

3.3.1.1 Effect of precipitation temperature

Similarly, magnetites (~1 g) were produced using the same precursor concentrations at temperatures 33°, 45°, 60°, and 75°C under identical conditions and were named as T33, T45, T60, and T75. After the final washing, the precipitates were collected and dried at room temperature in a vacuum oven.

3.3.2 Surface functionalisation

For a batch of ~1 g magnetite, 4.5 mmol FeCl₂.4H₂O and 9 mmol FeCl₃.6H₂O were dissolved in 300 ml of physiological saline instead of water, such that Fe²⁺/Fe³⁺ was 1:2 in a 500 ml three-necked flask. Biopolymer (0.2 g of either starch or dextran) was dissolved in iron solution and labeled as ‘Sta’, ‘Dex’ respectively. The magnetite precipitated at 45 °C after precursor iron chloride salts hydrolysis at 80°C. The magnetite crystallized in physiological saline was labelled as ‘PS’.

3.3.2.1 Peptisation with TMAH

About 4 ml of commercial 25% TMAH solution was added to the wet PS magnetite cake and peptised homogeneously which was labelled as TMA. The TMA powder was re-dispersed in deaerated water and the resultant product was a stable nanofluid without any precipitation over a year. A TMA fluid of ~25% solid content was placed in a vial, and

was subsequently subjected to a static magnetic field of several hundred Gauss. The particles remained dispersed in the fluid even in the presence of the external field indicating the formation of a stable colloidal dispersion.

3.3.2.2 APTES modified starch/dextran coated magnetite NPs

A suspension of ~1 g 'PS' in 150 ml ethanol/water (volume ratio, 1:1) was transferred into a three-necked flask connected to a water-cooled condenser. The silanisation was performed by addition of APTES into the Fe_3O_4 suspension in the molar ratio of 4:1, refluxed at 81°C for 5 h under vigorous stirring. The pH of the above suspension was ~11. The black solid mass was collected with the help of a strong bar magnet after the silanisation process, labelled as 'APT', washed with ethanol, followed by deionised water for three to four times. Similarly, the silanisation of starch or dextran coated magnetite was carried out by the addition of APTES into the respective Fe_3O_4 suspension and labelled as 'SAPT', 'DAPT' respectively

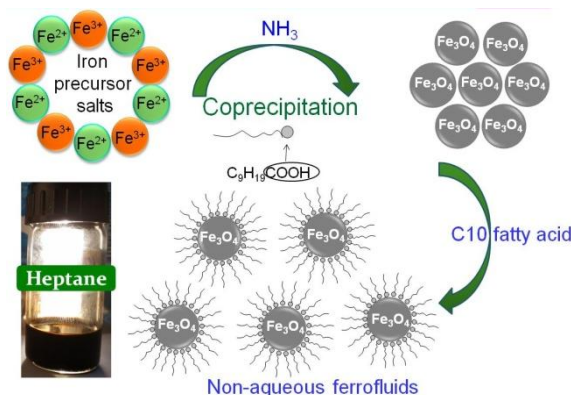
3.3.3 Magnetite calcinations at different temperatures

Samples of 'T45' dry powder were ground, placed in ceramic crucibles and calcined at different temperatures: 45° (C1), 225° (C2), 300° (C3), 400° (C4) and 450°C (C5). The crucible was placed in the furnace, heated to the desired calcination temperature in air for 1 h. The sample was allowed to cool down to room temperature in the furnace. The reddish powder obtained was kept in a desiccator over silica gel and the same has been characterised.

3.3.4 Phase transfer

For a batch of ~1 g magnetite, 8.7 mmol $\text{FeCl}_2 \cdot 4\text{H}_2\text{O}$ and 4.32 mmol $\text{FeCl}_3 \cdot 6\text{H}_2\text{O}$ were dissolved in 150 ml of deaerated Millipore water. The solution was heated slowly to 80°C with very strong magnetic stirring while purging with N_2 gas and maintained for 30 minute at 80°C. One fifth of the total of 25 mmol of decanoic acid was added to the solution followed by immediate addition of the required volume 50 ml of 25% ammonia. The remaining surfactant was then added to the mixture in five parts over five minutes; stirring was continued for another 30 min at 80°C. The suspension was then cooled naturally to room temperature and precipitated by the sequential addition of equal volumes of acetone and methanol. A black precipitate was separated by using a strong bar magnet to hold the solids and washing them alternately with acetone and methanol (polar organic

solvents) five times to remove all surfactants, except that part directly bonded to the particle surface. Such washed particles disperse readily in non-polar organic solvents such as heptane or oil (sesame oil) to produce concentrated dispersions.



Scheme 3.1 Phase transfer of aqueous synthesised magnetite to non-polar organic solvents

Please refer chapter two for the chemicals used and the details of characterisation techniques adopted here.

3.4 Results and discussion

3.4.1 Aqueous coprecipitation

Magnetite nanoparticles were synthesised by the economic, non-toxic aqueous coprecipitation method at different reaction temperatures in the range 33° to 90°C . The synthesised iron oxide powders (T33 to T90) were typically black in colour and were strongly attracted by the NdFeB bar magnet indicating the presence of magnetite as the dominant phase, although ancillary $\gamma\text{-Fe}_2\text{O}_3$ may not be completely excluded in the case uncoated nanocrystals.

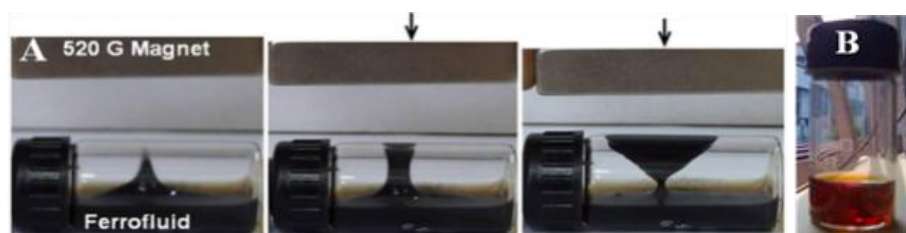


Fig. 3.1 (A) Frames from a video of a ~20 wt% TMA-based ferrofluid in a 15 ml glass vial being manipulated with a ~500 G strength bar magnet, and (B) dilute suspension of TMA in water.

The TMA suspension kept their colloidal characteristics over a year with no visible sedimentation. Contrarily, the PS suspension was sedimented completely after ~1 h, evidencing the larger and/or aggregated nature of PS particles. Fig. 3.1 shows the video

frames of thick slurry of TMA in presence of a strong bar magnet. The black slurry on ~50 times dilution turned in to a translucent wine-red solution (panel B).

3.4.1.1 Physical/structural examination of NPs

The bright field HR-TEM images for selected samples T90, T75, T60 and T33 are shown in Fig. 3.2 TEM images show spherical, crystalline and well resolved particles with narrow size distribution in 8–13 nm range. Apparently the particles have less interaction among them in TMA than that in bare NPs at room temperature, which will be further investigated by the magnetization and light scattering measurements in later sections (Fig. 3.9 and 3.10).

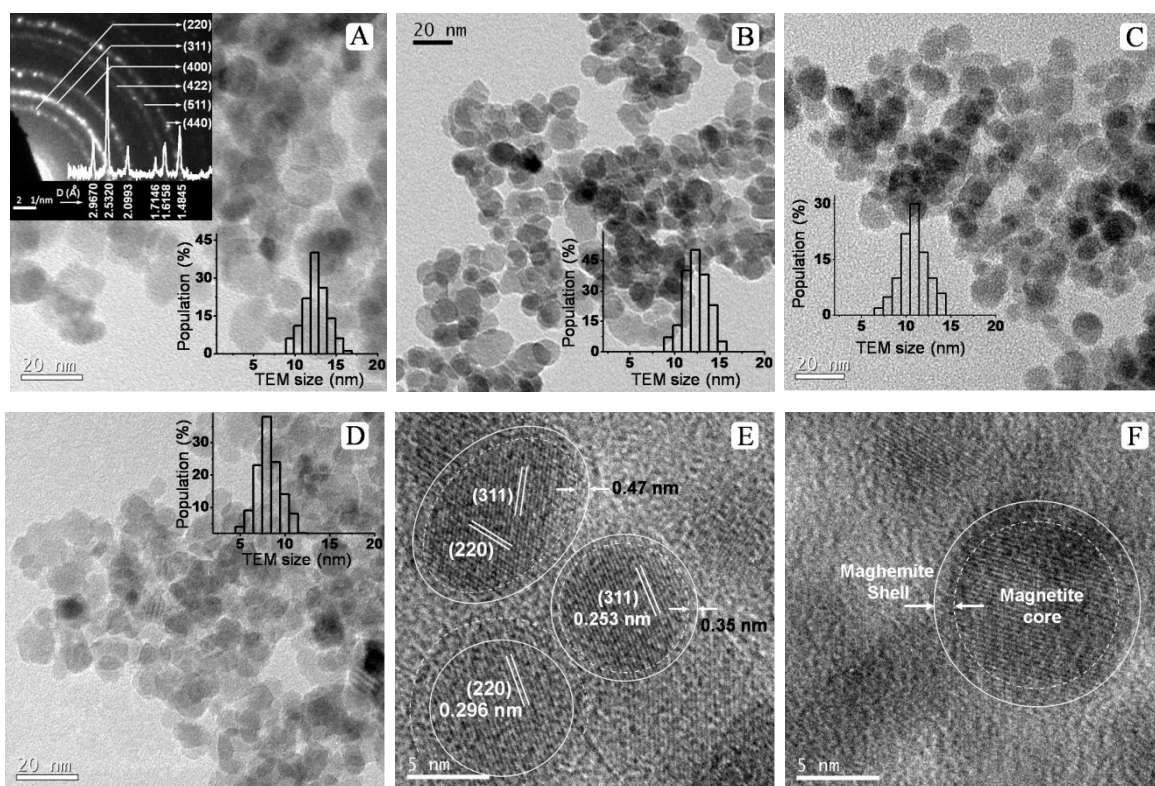


Fig. 3.2 Bright-field TEM images of as synthesised magnetite nanoparticles (A) T90 with its SAED pattern (inset), (B) T75, (C) T60, (D) T33, HR-TEM of (E) T33 and (F) T90 (indicating clear crystalline core surrounded by amorphous shell (marked with white line)). The size distribution histograms of the corresponding nanocrystals for all the images are presented as inset to each image.

The TEM results shown in Fig. 3.2 reveal that the precipitation temperature increases the average particle size of T33 from 7.8 ± 1.9 nm to 10.8 ± 2.0 nm in T60, while 75°C reaction temperature further increases the size to 12.3 ± 1.6 nm. On the other hand, the magnetite synthesised at 90°C doesn't improve the equilibrium size much but most particles fall in relatively wider 12.4 ± 1.9 nm size range. Few BF, HR-TEM images of the magnetite

crystals precipitated in physiological saline followed by surface functionalisation with TMAH are shown in Fig. 3.3. The large individual as aggregated grains with sizes in the range 8-15 nm with an average of 11.6 ± 1.9 nm was observed in PS. The TMA ferrofluid has more uniformly distributed sized NPs in the 8.5 to 11 nm range with average 10.3 ± 0.8 nm of narrow size distribution. This was actually expected, as TMAH acts as a surface-active agent favouring the dispersion of NPs. The mean size of the particles/aggregates is larger in the case of PS sample.

Careful examination of the HR images (3.2E, 3.3C) indicates that all the NPs are indeed single crystals and fringes belonging to predominant (111), (220) and (311) planes with corresponding d -spacings 0.48, 0.29 and 0.25 nm could be identified.

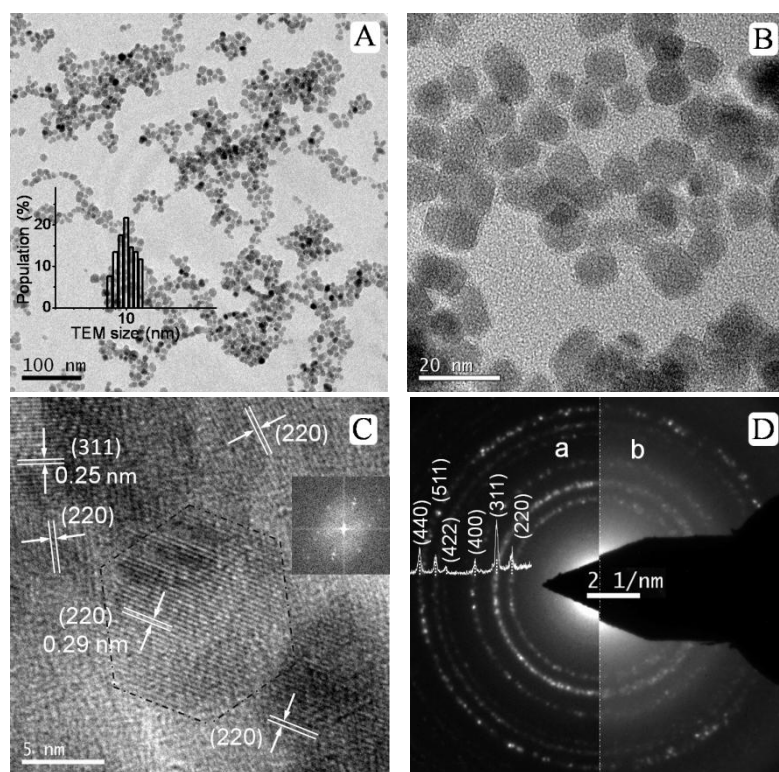


Fig. 3.3 BF-TEM images of peptised TMA (A, B, C) suspensions at (A) low, (B) higher magnifications, (C) HR-TEM images and its fast Fourier transforms is shown as inset and (D) electron diffraction pattern of (a) bare PS and (b) TMA matched with X-ray diffraction pattern with their (hkl) planes marked. Inset in A is the histogram representing size distribution.

Fourier filtering was used to extract the lattice fringe information. SAED patterns of bare and coated magnetite given in Fig. 3.3D show clear Debye–Scherrer rings for (220), (311), (400), (422), (511) and (440) planes with corresponding interplanar spacings 0.2967, 0.2532, 0.2099, 0.1715, 0.1616 and 0.1485 nm respectively matching the XRD pattern of

cubic inverse spinel magnetite (JCPDS card no. 19-0629). In addition, the bright diffraction spot in the rings indicate that the NPs are well crystallised.

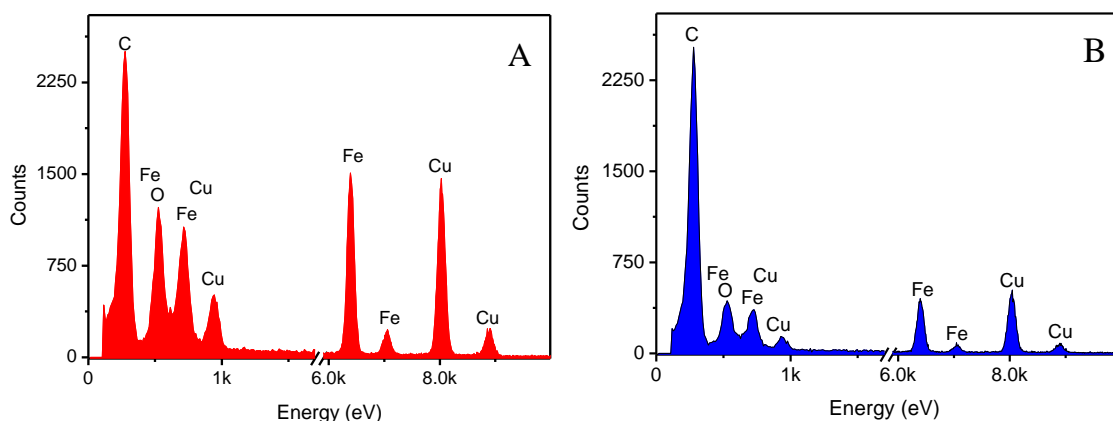


Fig. 3.4 Energy dispersive spectra of synthetic magnetite A) PS as well as B) coated sample TMA over the TEM grid.

The EDS spectra of PS and TMA specimens show the presence of Fe and O in the samples which also confirms that the NPs have no detectable impurities: the signal corresponding to C and Cu was due to the carbon film over the copper TEM grid and as well as C from TMAH.

3.4.1.2 Detailed X-ray diffraction analysis

The X-ray diffraction patterns of Fe_3O_4 synthesised at different temperatures and texture coefficient on the XRD patterns are shown in Fig. 3.5.

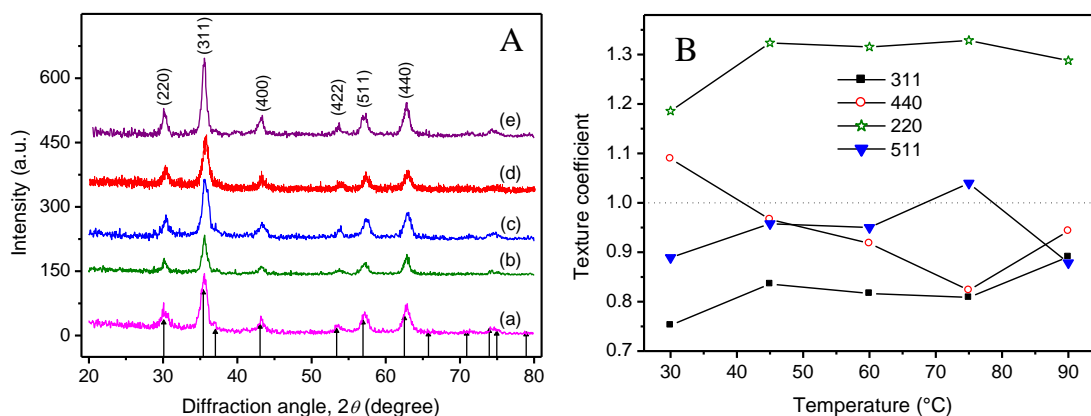


Fig. 3.5 (A) X-ray diffraction patterns of magnetites (a) T33, (b) T45, (b) T60, (d) T75, and (e) T90. The vertical drop lines in (A) are the theoretical Bragg positions for inverse spinel magnetite phase following JCPDS Card No. 19-0629. (B) The texture coefficient of magnetite nanocrystals, calculated from their powder XRD patterns (JCPDS card No. 19-0629 is used as reference for the calculations) as a function of synthesis temperature.

All Bragg's planes, including PS and TMA (data not provided here), could be indexed to face centred cubic inverse spinel magnetite of $Fd\bar{3}m$, #227 space group with lattice constant a in the range 0.8340-0.8366 nm whereas the same for bulk magnetite is 0.8396 nm (JCPDS card No. 19-0629). Broad diffraction peaks (Fig. 3.5A) indicate the nanocrystalline nature of the particles. When the reaction temperature was increased in steps from 33° to 90°C, a slight progressive narrowing of the X-ray diffraction peaks occurred as a result of crystal growth and reduction of microstrain in the lattice originating from defects. The preferential orientation of the crystallites along different crystal planes (hkl), texture coefficients, $C(hkl)$ in the Fe_3O_4 nanocrystals (Fig. 3.5B) shows preferentially grown {110} planes to texture coefficient value of 1.323 in T45 because of the growth confinement of (311), (440) and (511) crystal facets and reduced slightly further to 1.288 in T90 (synthesised at 90°C). Fe_3O_4 with predominant active (220) planes (T45 to T90) is of great potential in catalytic applications. A $C(hkl)$ value of 1 indicates a particle with randomly oriented crystallites, while a larger value indicates an abundance of crystallites oriented to that (hkl) plane (Sreeremya *et al.*, 2012). The high-index planes usually have higher surface energy. The energy for different crystal planes is in the order $\gamma(111) < \gamma(100) < \gamma(110) < \gamma(220)$ for the face-centered-cubic magnetite phase (Yang *et al.*, 2011).

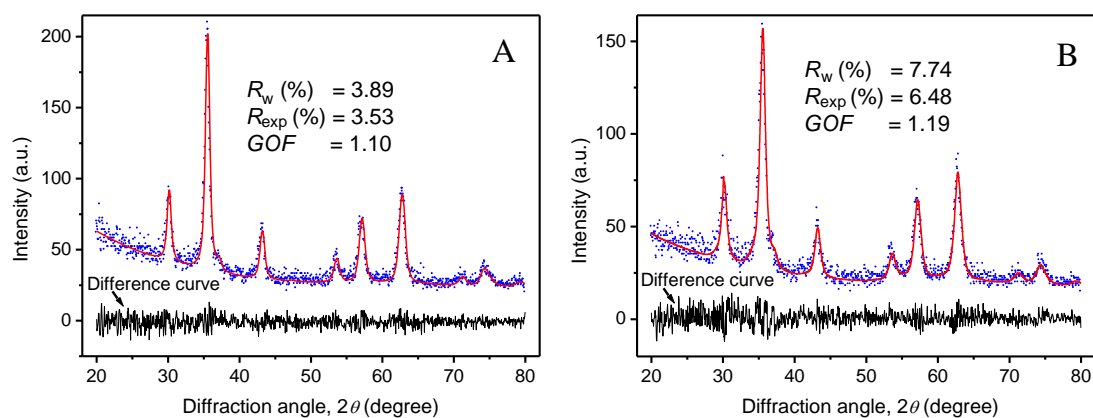


Fig. 3.6 Typical Rietveld fit (solid line) for (A) T90 and (B) T33 over the corresponding raw XRD data (dots). The black layer at the bottom of A and B is the difference curve between XRD and Rietveld simulation.

The match of the X-ray pattern with its Rietveld fit and the resultant almost spikeless difference pattern indicates the quality of fit in magnetite-maghemite mixed phases in the synthesised sample. The Rietveld analyses of X-ray patterns of T33 and T90 (Fig. 3.6) allowed us to estimate the relative concentrations of magnetite phase as 89.2 and 87.3%

respectively which is compatible with a core-shell model where the shell is 0.2–0.3 nm thick in a $D_{\text{TEM}}=8.2$ and 12.5 nm particles in T33 and T90 respectively. The core-shell structures were also observed from HR-TEM images (Fig. 3.2). The fit parameters are consistent with reported data in the literature (Yathindranath *et al.*, 2011).

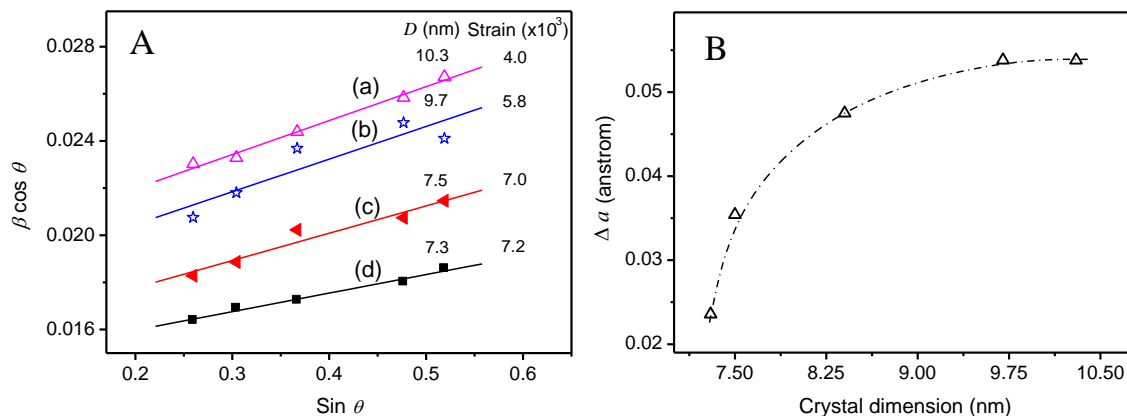


Fig. 3.7 (A) Williamson-Hall plot of $\beta \cos \theta$ versus $\sin \theta$ for the reasonably well-resolved Bragg lines of Fe_3O_4 nanocrystals (a) T33, (b) T45, (c) T75, and (d) T90 synthesised at different temperatures. The straight lines are the fits to the data. The calculated crystal dimensions and lattice strains evaluated from the linear fits are shown with corresponding data layers. (B) Change in lattice parameter (Δa) calculated from their powder X-ray diffraction patterns (reference JCPDS card No. 19-0629 is used for the calculations).

The grain sizes obtained from the Williamson-Hall plots (eqn 2.15) showed almost linear increase with increasing precipitation temperature indicating crystal growth during precipitation (Fig. 3.7). A steady increase in the lattice strain was observed (in the range $4.0\text{--}7.2 \times 10^{-3}$) with decrease in the particle size (Fig. 3.7B) (Narayanan *et al.*, 2008). It is interesting to note that the estimated D_{XRD} from the W-H technique for all the nanocrystals are within $D_{\text{TEM}} - 2.5$ nm as the shell of amorphous layer has not contributed to the X-ray diffraction. The deviation is more in the crystals synthesised at higher temperatures. Atoms at the surface and edges are under-coordinated with the presence of broken bonds. As the crystal dimension decreases, the surface area-to-volume ratio increases resulting in an increased broken bond density at the surface causing the remaining bonds to contract spontaneously with an associated increase in bond strength, which in turn produces localized strain (Sun, 2010). A decrease in the lattice parameter to 8.3596 \AA was observed when the particle size increased from 7.3 to 8.4 nm as a result of possible higher surface oxidation of magnetite crystals to $\gamma\text{-Fe}_2\text{O}_3$. The cell constant decreased slightly further to $\sim 8.3544 \text{ \AA}$ on increasing size to 9.7 nm and remained almost constant thereafter. Williamson-Hall analysis of X-ray data confirmed that the lattice parameter and crystal lattice strains in magnetite NPs is primarily dependant on the crystal sizes.

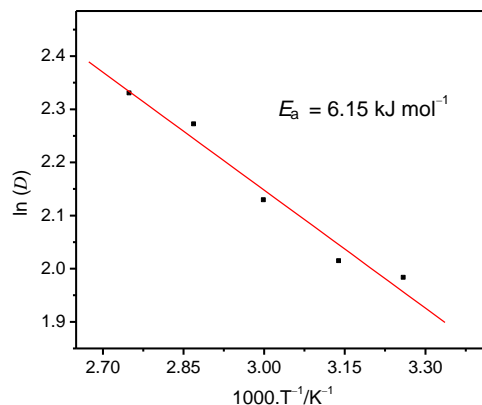


Fig. 3.8 Arrhenius plot of change in crystallite size as a function of reaction temperatures for ammonia precipitated magnetite samples.

Arrhenius plot for the samples prepared at temperatures in the range 33–90°C (Fig. 3.8) gave the activation energy from the gradient of the linear regression as 6.15 kJ.Mol⁻¹ under the condition of homogeneous growth of nanocrystallites. This energy is responsible for initiating the complex process of nucleation and growth by diffusion as well as secondary growth by Ostwald ripening. In the case of ammonia precipitated magnetite crystals, the activation energy is relatively small as the nanocrystals have large surface area and its poor crystallinity. The growth process involves a dissolution–crystallisation mechanism allowing a decrease of the free enthalpy of the system by reduction of the surface area (Bean and Livingston, 1959).

3.4.1.3 Langevin fitting on magnetisation measurements

Figures 3.9 and 3.10 show the field dependent magnetic properties of the synthesised Fe₃O₄ samples, measured by VSM at room temperature and magnetisation at higher field resolution using PPMS at different temperatures. The hysteresis loops apparently pass through the origin which indicates zero coercivity and zero remanence (Fig. 3.9A), signifying that the samples are in the superparamagnetic state with unstable magnetisation at this temperature (Xu *et al.*, 2010) and the samples possess higher magnetisation at 250 K due to reduced thermal energy (Fig. 3.9B). In contrast to M_S of ferromagnetic Fe₃O₄ NPs, measured by Tian *et al.*, (Tian *et al.*, 2011), we observed unsaturated magnetic behaviour in our synthesised nanoparticles that confirms the superparamagnetic nature. On careful examination of the high resolution magnetisation data (Fig. 3.9B) it is observed that both T33 and T90 display coercivities to the extent of mere 21 and 16 Oe respectively. Appearance of the coercivity may be attributed to the long range magnetic dipolar interactions.

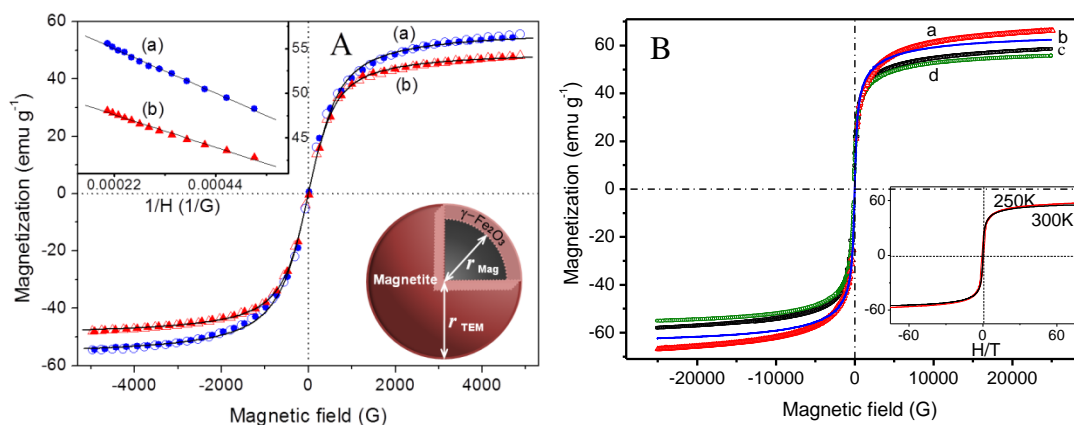


Fig. 3.9 Magnetisation versus applied magnetic field data (A) with low field resolution for selected magnetite (a) T33 and (b) T90 specimens and (B) higher field resolution from PPMS at temperatures 250 and 300 K and its inset representing the magnetisation data as a function of H/T for T90. Typical Langevin fits are represented by solid black lines in (A).

The magnetisation profiles as a function of H/T (inset of Fig. 3.9B) are very much close to each other suggesting non-interactive nature of the particle. However, small deviation between the curves in the high field region and presence of coercive field indicate that the mutual interaction is not absolutely zero i.e., weak interaction exists among them (Respaud, 1999). Due to the asymptotic increase of magnetisation for high fields, the saturation magnetisation value can be obtained from the fitting of the M_S vs. $1/H$ curves, extrapolating the magnetisation value to $1/H = 0$ (Liu and Zhang, 2001). According to inset of Fig. 3.9A, the observed magnetisation for T90 and T33 are 48.44 and 56.11 emu respectively. The curves were fitted with Langevin function in order to get M_S of samples and the obtained fitting parameters are summarised in Table 3.1.

Table 3.1 The detailed analysis from the Langevin fit of the magnetite samples

Sample	$Exp M_S$ (emu.g ⁻¹)	$Cal M_S$ (emu.g ⁻¹)	μ (emu per NP)	R^2	Standard error	D_{mag} (nm)
W	64.68	65.14	1.28E-16	0.9989	±1.8	8.98
TMA	57.92	58.30	1.16E-16	0.9988	±1.7	9.02
APT	64.46	64.63	1.44E-16	0.9992	±1.6	9.38
SAPT	57.24	58.05	1.51E-16	0.9996	±1.0	9.85
DAPT	51.85	52.12	1.03E-16	0.9990	±1.3	9.02

It is noteworthy to mention that the M_S of our synthesised samples is greater than that of Fe_3O_4 nanocubes of size ~ 10 nm and nanorods of length > 100 nm and diameter of ~ 10 nm (Shi *et al.*, 2014), but is quite less than the bulk Fe_3O_4 (92 emu.g⁻¹) (Cao *et al.*, 2008) and the reduction of M_S may be attributed to the disordered surface spin or spin

canting behaviour at the surface of the nanoparticles and change in degree of inversion. It is worthy to mention that M_s of T33 is higher than that of T90 i.e., bigger particle has lower value of M_s . The magnetic sizes of T90 ($D_{\text{mag}}=10.83$ nm) from our computations are smaller than the physical size measured by TEM ($D_{\text{TEM}}=12.42$ nm). It is reasonable to assume that the difference may be attributed to the presence of magnetically inactive outer layer that is responsible for suppression of magnetisation in our synthesised samples (Kodama *et al.*, 1999; Liu and Zhang, 2001). As it is well known that Fe_3O_4 having inverse spinel structure in bulk possesses mixed spinel structure in nano-phase and the degree of inversion decreases with increase in particle size. Since T90 has larger size than T33, the reduction of magnetisation in case of T90 may be ascribed to the reduction of the degree of inversion. Interestingly, it has been observed that D_{TEM} for T33 (8.2 nm) is smaller than D_{mag} (9.86 nm) i.e., magnetic size is overestimated by approximately 10% in comparison to TEM size. Such over estimation was previously observed by few researchers and can be explained on the basis of perturbation in the Langevin function caused by interparticle interactions that was ignored during fitting (Pascal *et al.*, 1999) or the consideration of single size distribution of the particles.

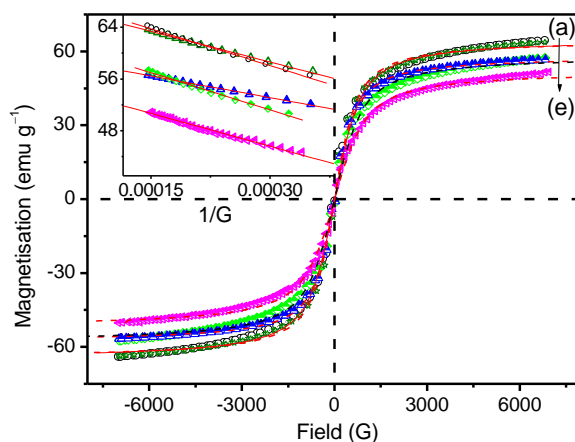


Fig. 3.10 Magnetisation versus applied magnetic field profiles with typical Langevin fits represented by solid red lines with the magnetisation data as a function of $1/H$ for (a) PS (b) APT (c) TMA (d) SAPT and (e) DAPT.

In order to get better information, the magnetic sizes (D_{mag}) were also calculated by using eqn (3.1) (Ozkaya *et al.*, 2009; Yu and Kwak, 2011),

$$D_{\text{mag}} = \left(\frac{18kT}{\pi} \frac{\chi}{\rho M_s^2} \right)^{\frac{1}{3}} \quad (3.1)$$

where χ and ρ represent susceptibility $\left(\frac{dM}{dH} \right)_{H \rightarrow 0}$ and density of the material respectively.

Eqn (3.1) gives D_{mag} as 6.6 nm for T33 and remove the discrepancy that emerged from the

Langevin curve analysis. The mean diameter of the superparamagnetic TMA particles is estimated to be ~ 9.02 nm, which is smaller than the average physical size of ~ 10.3 nm (magnetic core + non-magnetic outer shell) as determined from TEM measurements.

3.4.1.4 Lorentzian site analysis of Mössbauer spectra

^{57}Fe Mössbauer spectra of T33 and T90 samples shown in Fig. 3.11 consist of two sextets and a single doublet pattern depending on the size and crystallinity of the particles. The outer sextet of smaller area corresponds to Fe^{3+} in tetrahedral (A) sites while the inner sextet with larger area corresponds to Fe^{3+} and Fe^{2+} in octahedral (B) sites. However, the weak doublet peak signifies the presence of some particles lying below the critical size for superparamagnetic relaxation at the measurement time-scale. The average hyperfine magnetic field (HMF) decreased in the magnetic powder specimens from T33 synthesised at 33°C to T90 prepared at 90°C (Table 3.2). This drop may be attributed to the lower net magnetic moment per unit formula for T90 as determined by the Fe^{3+} ion concentration at octahedral site in comparatively larger particles. The relative area ratio of two Fe^{3+} sextets for both the samples reveals that the concentration of Fe^{3+} ions at the octahedral (B) site is lower than that at the tetrahedral (A) site.

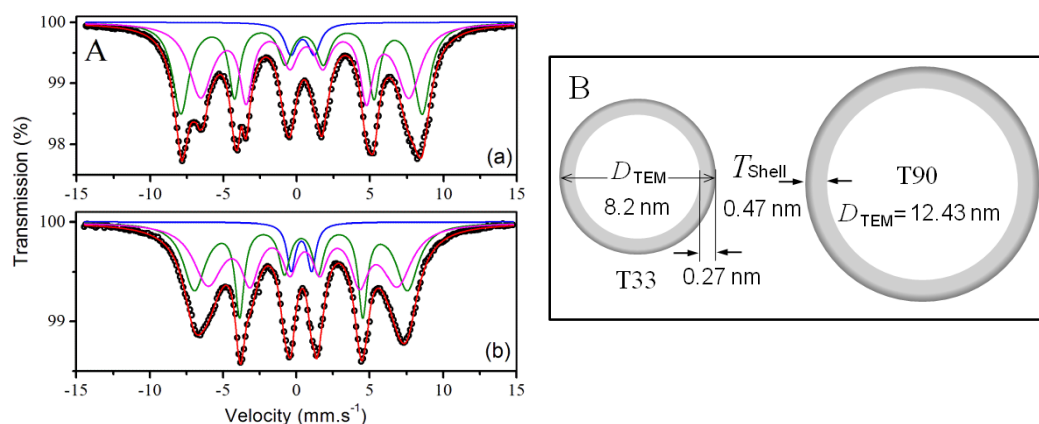


Fig. 3.11 (A) ^{57}Fe transmission Mössbauer spectra of (a) T33 and (b) T90 recorded at room temperature. Symbols represent the experimental data and the continuous lines correspond to the NORMOS fits and (B) schematic representation of core-shell frameworks in T33 and T90.

The isomer shift (IS; δ) values corresponding to tetrahedral (δ_A) and octahedral (δ_B) sites of the magnetite specimens (Table 3.2) illustrate that the s-electron density at the Mössbauer active nuclear site is significantly affected by the rise in precipitation temperature. Nevertheless, the value of the isomer shift of Fe^{3+} in the A site is higher than

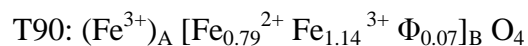
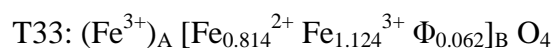
that generally reported for the micrometric bulk magnetite (Daou *et al.*, 2006), indicating a possible charge transfers in the A site also.

Table 3.2 Values of room temperature ^{57}Fe Mössbauer parameters by Lorentzian site analysis using Recoil program.

Sample	Site	IS, δ^a (mm.s $^{-1}$)	QS, ΔE_Q^a (mm.s $^{-1}$)	Average HMF, B_{hf}^b (Tesla)	Width a (mm.s $^{-1}$)	Area c (%)
T33	Doublet	0.40	1.60	-	0.45	4.7
	Sextet (A)	0.42	-0.08	51.0	0.55	42.5
	Sextet [B]	0.60	-0.06	44.0	0.65	52.8
T90	Doublet	0.35	1.40	-	0.35	6.2
	Sextet (A)	0.32	-0.02	45.1	0.45	43.1
	Sextet [B]	0.52	-0.08	40.0	0.60	50.7

a SD ± 0.03 ; b SD ± 0.4 ; c SD ± 0.2

Negative quadrupole shift (QS) for both the samples may be attributed to the oblate charge distribution of Fe. The ferric character of the Fe ion is also manifested by the magnitude of the magnetic hyperfine fields and is proportional to the spin of the ferric ion (Tian *et al.*, 2011). The sextet area leading to a $\text{Fe}^{3+}_{\text{tetra}}/\text{Fe}^{3+,2+}_{\text{octa}}$ ratio of T33 and T90 is found to be 0.80 (42.5/52.8) and 0.85 respectively, in contrast to the theoretical ratio 0.50. Such intensity ratios exceeds 0.50 are called super stoichiometry in oxygen or cationic vacancies (Daou *et al.*, 2006). It is likely that the low concentration of elementary iron is the reason that it does not show up in Mossbauer spectra. In contrast to relative intensity ratio 1:2 corresponding to Fe between A and B sites in bulk inverse spinel magnetite, $(\text{Fe}^{3+})_{\text{A}} [\text{Fe}^{2+} \text{Fe}^{3+}]_{\text{B}} \text{O}_4$, we observed the global composition of T33 and T90 as,



where Φ represents the cation vacancy at the B-site. The stoichiometry implies that the Fe_3O_4 content in T33 sample was 81.4% and the rest being Fe_2O_3 . T90 contains slightly lower amount of magnetite at 79%. The relatively larger fraction of oxidised Fe^{3+} (maghemite) in T90 may be attributed to the dominating effect of higher precipitation temperature though T33 has a larger fraction of surface atoms. The Φ -value clearly indicates the formation of non-stoichiometric magnetite with some Fe^{2+} deficient lattice sites. If we assume the overall shape of the magnetic nanocrystals are spherical and the oxidised $\gamma\text{-Fe}_2\text{O}_3$ phase exists as shell of uniform thickness over magnetite in a core-shell

model, one can easily compute the 18.6% maghemite in 8.2 nm crystal to ~0.27 nm thick shell as shown in Fig. 3.11. Similarly, 79% magnetite content in 12.4 nm T90 is compatible with 11.6 nm core/0.47 nm shell. The thickness of maghemite shell obtained from magnetisation studies are close match to the same observed from TEM micrography. The formation process of maghemite shell over magnetite core begins by dissociative oxygenation of Fe^{2+} cations at the surface. This phenomenon generates surface Fe^{3+} cations along with cation vacancies. The Fe^{2+} ions diffuse out from the inner oxide core to the surface to attain the Fe^{3+} state. During this process, the outer oxide layer thickens and a radial compositional gradient is established producing a core-shell structure, with maghemite being more abundant in proximity to the surface of the particles forming shell. In order to observe superparamagnetism, as shown in Fig. 3.9, the time-scale of the measurement t_m should exceed the superparamagnetic relaxation time (τ), which is usually in the order of 10^{-9} – 10^{-10} s (Lai *et al.*, 2012). The critical size D_C of the particles to be superparamagnetic may be calculated empirically from the equation $D_C = (\ln t_m/\tau)^{1/3}$. In the measurement of magnetisation, the observation time $t_m \sim 1$ s, and hence the superparamagnetic relaxation can be observed in particles with of size 10^1 – 10^2 nm. In a Mössbauer study the measurement time is much shorter ($t_m \sim 10^{-8}$ s), and therefore manifestation of superparamagnetism is expected in particles of much finer sizes (Lukashova *et al.*, 2013).

3.4.1.5 XPS spectral analyses

XPS spectrum of TMA powder shown in Fig. 3.12 was used to study the valence states of Fe in the as-prepared NPs after functionalisation. The XPS wide spectrum shows the peaks attributed to the core levels of O (A), Fe (A), Fe 2p and 3p, O 1s, C 1s where the Fe 2p electron core level is characterised by $2p_{1/2}$ and $2p_{3/2}$ series peaks. Fe $2p_{3/2}$ and Fe $2p_{1/2}$ double peaks correspond to the binding energies of 709 and 722 eV respectively (Fig. 3.12B). The double peaks in high resolution Fe 2p scan are broadened due to the appearance of Fe^{2+} ($2p_{3/2}$) and Fe^{2+} ($2p_{1/2}$) in magnetite which is in agreement with the reported literature (Lai *et al.*, 2010). The relative peak areas of Fe^{2+} and Fe^{3+} in the high resolution 2p scan were calculated as 0.33:0.61, close to that of the stoichiometric Fe_3O_4 , which could also be shown as $\text{FeO}\cdot\text{Fe}_2\text{O}_3$. The predominant peak at 528.3 eV is attributed to O 1s (Li *et al.*, 2011), which can be deconvoluted to the binding energies of 528.3 and 529.6 eV belonging to the lattice oxygen in Fe_3O_4 .

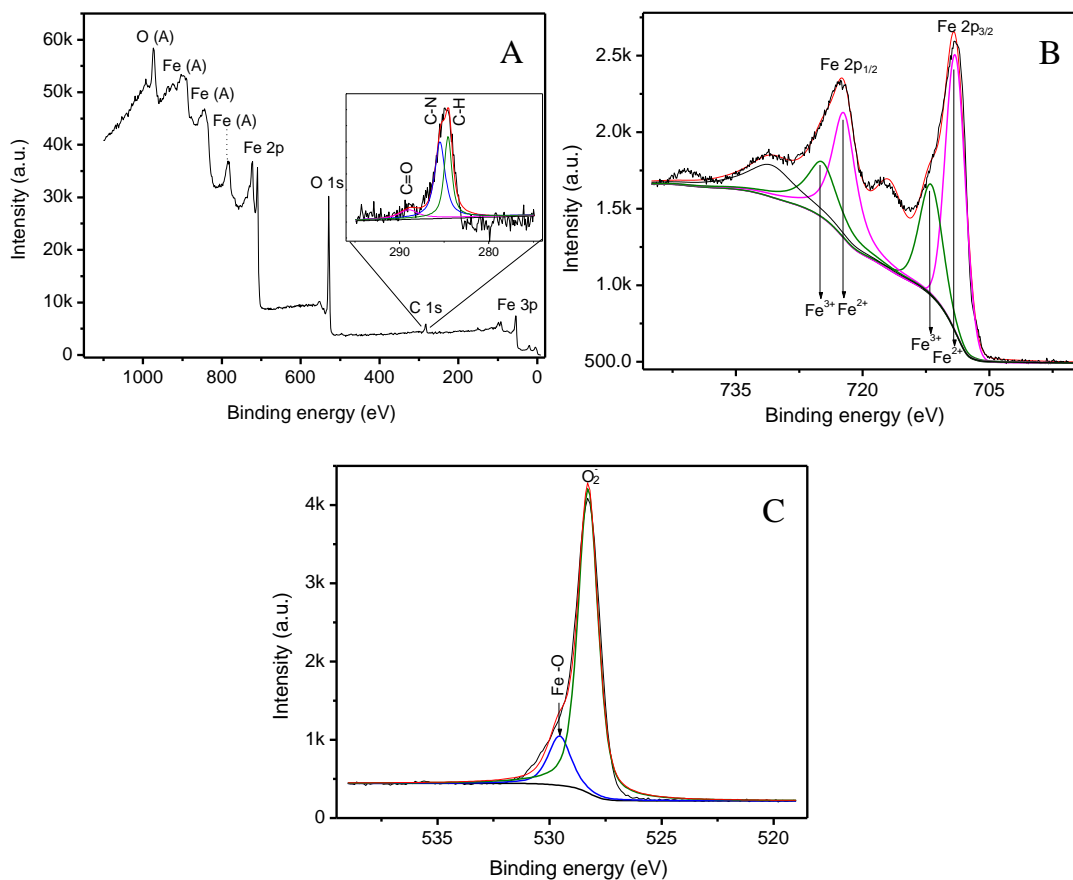


Fig. 3.12 (A) Survey spectrum and high resolution XPS, (B) Fe 2P, and (C) O 1S spectra of TMA sample. The solid red line over a raw data is a typical fit by XPS software.

The lower intensity of the C 1s peaks compared to that of Fe and O proves that the organic layer around MNPs is substantially thinner. The asymmetric C 1s peak is deconvoluted into three peaks at 284.6, 285.5 and 290 eV (see inset Fig. 3.12A). The main peak at 284.6 eV is assigned to C–H bonds in methyl group (Jha *et al.*, 2013), and the second peak centred at 285.5 eV can be attributed to C–N bonds (Wang *et al.*, 2008). The first two peaks of C 1s belonging to TMA attached electrostatically to the surface hydroxyls and the third very weak peak at 289 eV is ascribed to trace amount of CO₂ adsorbed onto the fine NPs surface. The amount of residual TMAH in the dried TMA NPs was too little, so that the N 1s signal obtained by the XPS detector was very weak and almost absent.

3.4.2 Aqueous ferrofluid

3.4.2.1 Colloidal properties of functionalised MNPs

The variations in the zeta potential of uncoated and TMA peptised magnetite as a function of the pH and their phase plots are shown in Fig. 3.13. The zeta potential is the electrical potential measured at the shear plane, and represents the portion of the charge that can exert electrostatic attraction and repulsion forces on neighbouring particles in suspension.

The magnitude of the ζ -potential is proportional to the amount of charge on the NPs surface. The ζ -potential values of PS and TMA suspensions at their natural pH and the suspension stability are shown in Table 3.3. Our experiments were performed at the natural pH of the PS suspension where no electrostatic repulsion is expected. Bare MNP surfaces are slightly positively charged (pH 6.7) and the small electrostatic repulsive forces among particles is not able to prevent particle–particle contact and consequent clustering as was indicated by the zeta potential of 4.9 mV (Table 3.3).

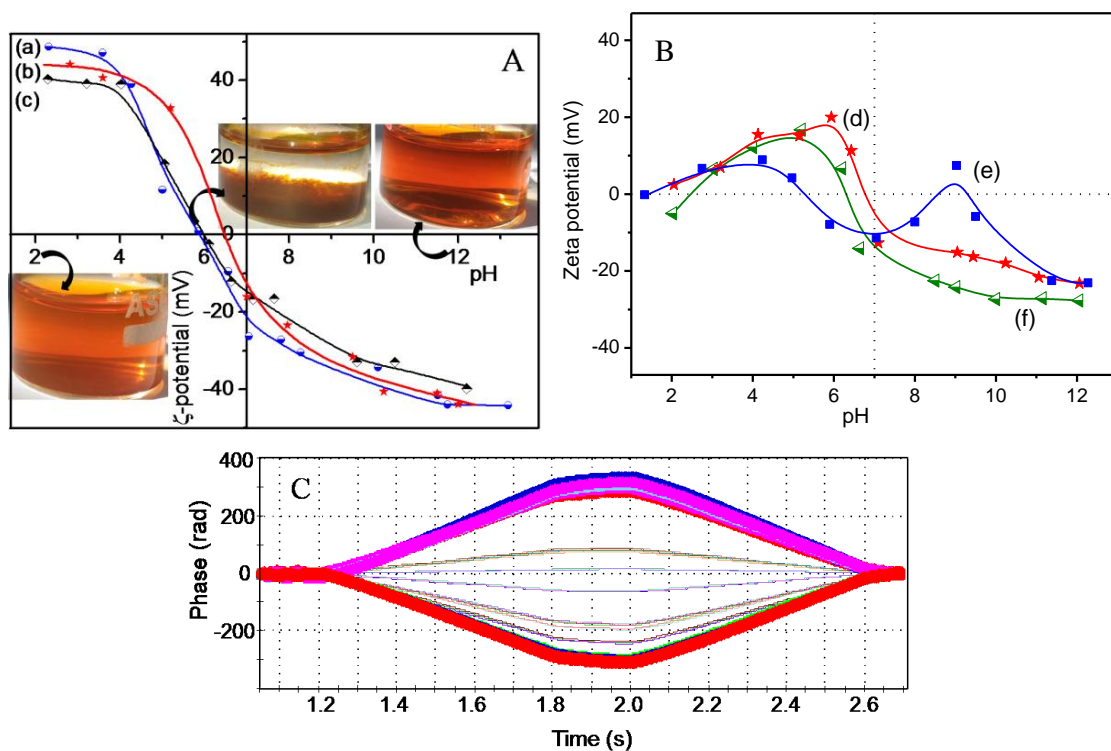


Fig. 3.13 (A) Variations in the zeta potentials of (a) TMA and (b) T60 (c) PS, (B) biopolymer treated samples (d) APT (e) SAPT (f) DAPT magnetite suspended in Millipore water as a function of the fluid pH. (C) The associated phase changes from negative to positive with zeta potential of magnetite nanocrystals suspension while varying the pH of surrounding medium from 13-2.

TMA suspension peptised with strong organic base TMAH shows very high zeta potential of -44 mV in spite of dilution ($\sim 1:5$) and exhibited ultra stability over 1 year without any apparent precipitation. The ${}^+\text{N}(\text{CH}_3)_4$ cations of TMAH interact electrostatically with the OH groups attached to the bare magnetic NPs surface. This surface structure creates electrostatic interparticle repulsion that can overcome the coagulation forces of magnetic interaction and van der Waals attraction forces among NPs in water. Zeta potentials of the NPs are pH dependent and was observed to flip on both sides of the isoelectric point from positive surface charge (+ve ζ -potential) in acidic pH to negatively charged surfaces as

reflected in the negative zeta potential at basic pH. As pointed out in Fig. 3.13, the PZC slightly moved from 5.88 for unmodified NPs to higher pH values 5.98 for TMA and ~6.45 for T60. Pristine magnetite PS dispersion exhibited ζ -values in the range of +40.3 to -39.8 mV whereas +44.1 to -43.9 mV for T60 dispersion in the 2 to 13.1 pH range. Adsorption of $[(\text{CH}_3)_4\text{N}]^+$ ions tend to increase the negative charge of the magnetite further to -44.2 mV at alkaline pH and increases positive charge to 48.7 mV in the acidic range. The TMA coated magnetite was extremely stable in both acidic and alkaline pH except for the pH close to their PZC between 5 and 7. The higher clustering tendency of NPs in PS can be explained by the bigger particle sizes and as a result higher crystallinity. In larger particles of well-crystallised magnetite, the bulk properties supersede surface properties, and they are expected to magnetically attract more strongly each other (Hosono *et al.*, 2009).

Table 3.3 Zeta potential of magnetite dispersion at their natural pH and its suspension stability

Sample	Zeta (mV)	pH	Stability
PS	+4.9	6.7	1 h
TMA	-44	11.75	> 1 year

Results presented in Fig. 3.13B show that the pH values corresponding to the PZC of the APT, SAPT and DAPT samples were found to be about 6.77, 5.27 and 6.27, respectively. Moreover, the role of the ionic strength on the particle size also is largely dependent on the nature of the coating material or electrolyte. The smallest cations being the best screening ions, their influence on the surface charge is highest. Therefore, the TMA ferrofluid was stable above the $\text{pH} > 7$ and below $\text{pH} < 5$. The phase plot obtained with TMA sample is excellent in quality in all the pH ranges and flipped from negative to positive zeta while varying the pH from 13 to 2 shown in Fig 3.13A. The hydrodynamic diameter (Z-average size, Z_{av}) and the corresponding correlation function against time are depicted in Fig. 3.14. The overall yield of Fe_3O_4 into aqueous dispersed MNPs was >95% for TMA. The Z_{av} size was estimated by running the experiment in dynamic auto-mode using Zetasizer Nano ZS in which the machine optimizes all machine parameters to derive the best and reproducible size data. Aqueous dispersion of PS showed NPs in 33–825 nm size range with Z_{av} size of 129 nm with PDI 0.358 indicating polydisperse nature of the distribution. The calculated number distribution, N_{av} is 43 nm. This is further consolidated by the poor fit to the correlation function (panel A in Fig. 3.14). The signal correlation due

to the random thermal motion of NPs reduced to ~ 0.74 after $100 \mu\text{s}$ in TMA where as the correlation of the signal takes a long time to decay and remained almost unchanged at ~ 1.0 at the same point of time ($100 \mu\text{s}$) in case of PS containing slow moving larger particles.

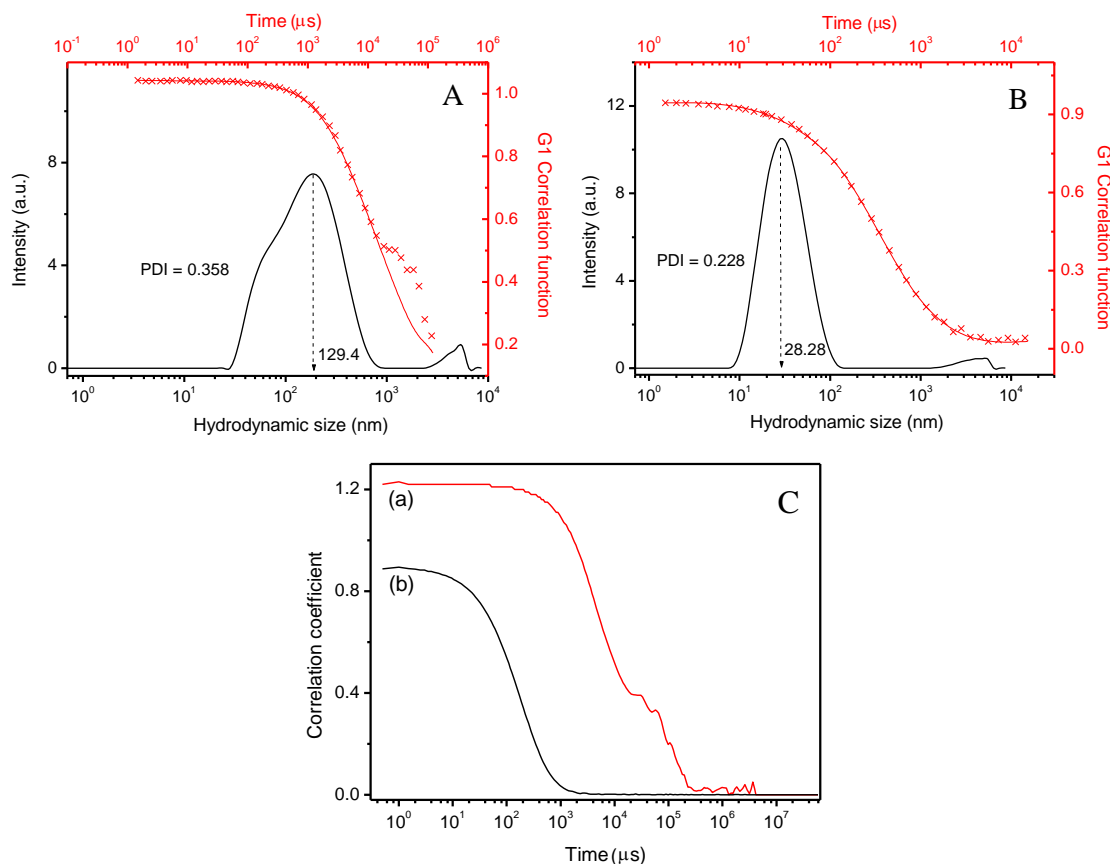


Fig. 3.14 Hydrodynamic size (Z_{av}) of (A) pure as well as (B) peptised synthetic magnetite. The correlation function of the same is plotted against time. (C) Raw correlation data of (a) pure and (b) TMA coated magnetite nanofluid.

The Z_{av} size for TMA is 28 nm with the presence of particles in the $8.7\text{--}91 \text{ nm}$ size range which is ~ 2 times larger than D_{TEM} size of 10.3 nm (Fig. 3.3). The D_{PCS} of $\sim 28 \text{ nm}$ could be due to tetrahedrally arranged close-packed clusters of a total of maximum 4 particles with average hydrodynamic diameter of $\sim 2 \times D_{TEM} = 26 \text{ nm}$ which is very close to 28 nm . The algorithm in the Malvern size measurement software converts the intensity of photon signal to size by Cumulants analysis. Photon scattering techniques rely on the fact that the intensity of scattered light increases by about a million times if the size of particles responsible for photon scattering increases by one order of magnitude (Meledandri *et al.*, 2008). In other words, TMA suspension contains more than 99% 13 nm particles with $<0.01\%$ of 28 nm clusters. The PDI (0.228) indicates the complete absence of any larger aggregates as supported by good fit to the correlation data also.

3.4.2.2 Stability as a function of temperature

To understand the clustering kinetics, hydrodynamic size, PDI, mean photon count in TMA slurry was recorded as a function of NP concentration, temperature and time and is provided in Fig. 3.15 and 3.16. The measurement has been carried out under static mode when, ideally, the number of photons scattered is proportional to the Z_{av} of the scattering NPs. When the concentration of NPs was 25 mM (neat) as well as its 1:1 dilution, the dispersion exhibited the smallest reproducible Z_{av} size ca. 28 nm which confirmed the excellent colloidal stability of TMA where as its N_{av} (13 nm), calculated from the intensity distribution, is close to the primary particle size as observed from TEM (10.3 nm).

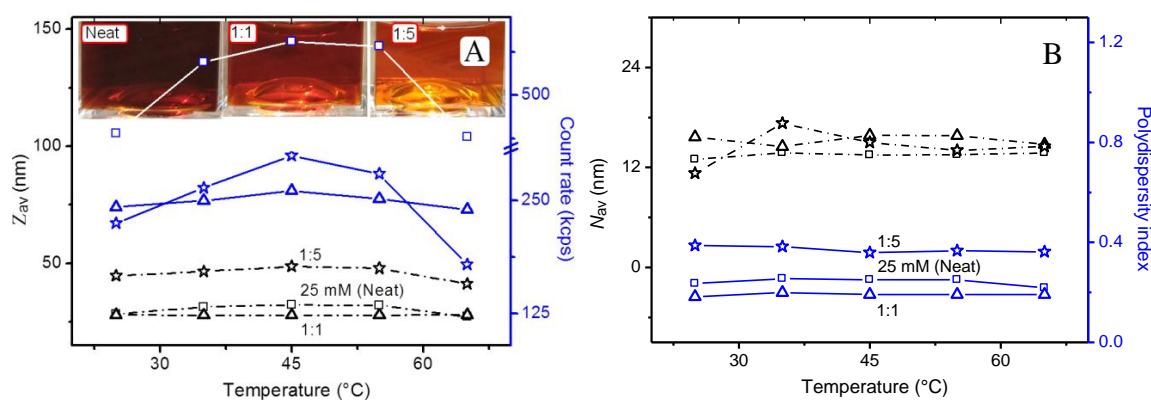


Fig. 3.15 Hydrodynamic size and the colloidal stability as a function of temperature for MNPs suspension examined at various concentrations, the mean particle size (A) Z_{av} (dotted line) plotted against mean count rate (solid line) and (B) N_{av} (dotted line) plotted against polydispersity index (solid layer) with different concentrations neat (square box), 1:1 (triangle), 1:5 (star) dilutions.

The Z_{av} size increased from 28 to 46 nm when NP concentration was decreased from an initial 25 mM to 4.2 mM with a concomitant decrease in the mean photon count rate from 450 to 260 kcps. However, the TMA suspension was always stable irrespective of MNPs concentrations in water. When temperature for 25 mM slurry was increased from 25 to 45°C, the hydrodynamic size 28.3 nm grew to 32.3 nm and decreased down to 27.3 nm when the temperature was further increased from 45° to 65°C. The increase in size and mean photon counts till 45°C may be due to the transformation of cluster structure from initial tetrahedral ($2 \times D_{TEM}$) to one-shell hexagonal close-packed ($3 \times D_{TEM}$) and back to the tetrahedral at ~65°C. In the process, the count rate changed by ~22% from initial of 450 kcps in 25 mM suspension. No obvious change in the Z_{av} size (~28 nm) was observed with ageing time extended even upto 4 months (Fig. 3.15).

3.4.2.3 Ageing study on aqueous ferrofluid stability

We observed that the ferrofluids are stable on ageing at room temperature over a year even after the temperature treatment, with no evidence of flocculation or settling and there was no change in the hydrodynamic size. These results show that monodispersed nanoscale magnetite crystals have been synthesised in aqueous medium which retained its magnetic properties, with very good water dispersibility. This makes them suitable as a candidate for biomedical applications.

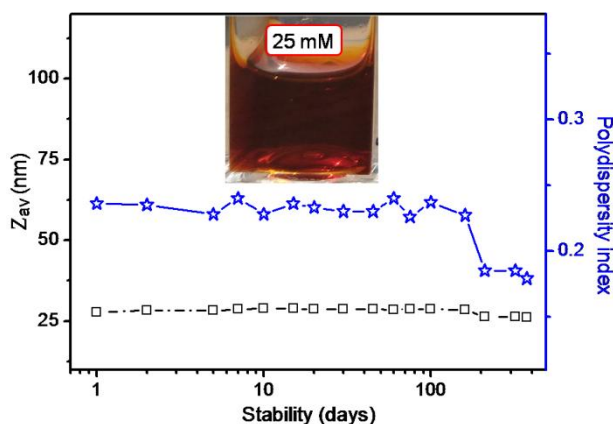


Fig. 3.16 Z_{av} and PDI of magnetite dispersion plotted as function of time. The TMA suspension used in the experiments is shown in the inset.

On ageing, the hydrodynamic size (Z_{av}) is reduced from 28.5 to ~26 nm but PDI improves from 0.227 to 0.185. The bimodal distribution of TMA improving to monomodal in the last three data points (Fig. 3.16) resulted the decrease.

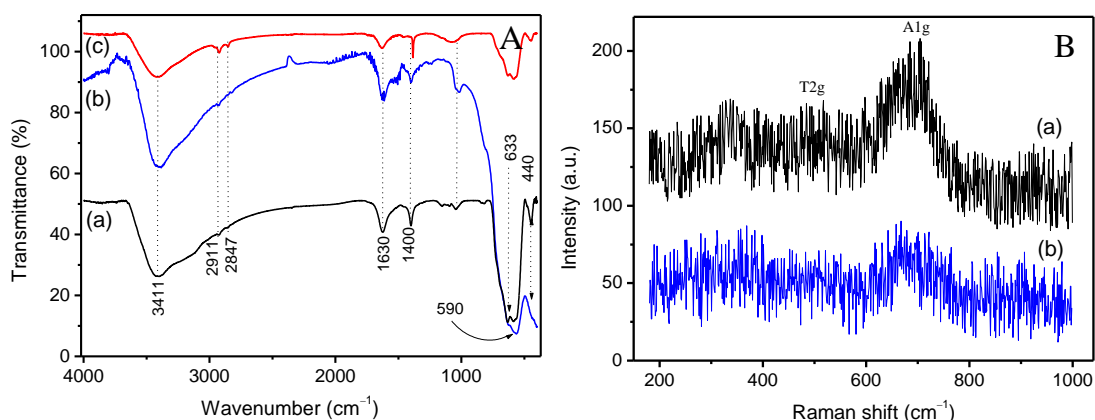


Fig. 3.17 (A) FTIR spectra of the as-obtained (a) T33, (b) T90 and (c) TMA magnetite nanocrystals and (B) typical Raman spectra of (a) T75 and (b) T90 recorded after exposure for 60 s to 2.5 mW laser powers.

FTIR and Raman spectra on selected magnetite specimens conducted in air are shown in Fig. 3.17. The IR absorption bands in the 630–550 cm^{-1} range is attributed to the

vibrations of Fe–O bonds in tetrahedral and octahedral sites (Andrade *et al.*, 2009) and must have been resulted from the split of the ν_1 band at $\sim 570\text{ cm}^{-1}$ (Marinescu *et al.*, 2006). The band at $\sim 440\text{ cm}^{-1}$ in T90 is due to the octahedral Fe only and corresponds to the ν_2 band of Fe–O of bulk magnetite ($\sim 370\text{ cm}^{-1}$) shifted to a higher wavenumber. FTIR spectra also confirm the presence of *fcc* magnetite in the materials as was previously confirmed from the TEM and XRD data (Fig. 3.1 and 2). The intensity reduction of the band at $\sim 590\text{ cm}^{-1}$ from T90 to T33 is probably due to part of the Fe_3O_4 being reduced to elementary iron (Dong *et al.*, 2013). The presence of O–H stretching vibration at $\sim 3411\text{ cm}^{-1}$ and O–H deformed vibration (bending modes) at 1630 cm^{-1} are attributed to the presence of coordinated OH groups or water molecules with the unsaturated surface Fe atoms (Ebrahimezhad *et al.*, 2012). C–O stretching vibrations of CO_3^- anion at 1400 cm^{-1} (ν_3) in both the samples are due to atmospheric CO_2 (Chen *et al.*, 2011). Small absorption bands at 2918 and 2847 cm^{-1} are due to the ν_{as} (C–H) and ν_{s} ($-\text{CH}_3$) vibrations of tetramethyl group in TMA sample. The very small hump at $\sim 2918\text{ cm}^{-1}$ in bare NPs might have come from some remaining oil impurities from the IR mould. The presence of which was confirmed by XPS also. Raman spectra presented in Fig. 3.17B have also indicated the presence of predominantly magnetite with small amount of maghemite ($\gamma\text{-Fe}_2\text{O}_3$) as impurity in the black magnetic products (T75 and T90). The Raman spectra taken with relatively low intensity laser power of 2.5 mW on magnetite crystals of T75 and T90 shows the co-existence of the two phases at the illuminated point. The specimen produced characteristic vibrations as broad peak at $\sim 600\text{ cm}^{-1}$ extending up to 785 cm^{-1} which could be assigned to the A_{1g} mode, due to phonon confinement effects in the nanocrystals. A_{1g} mode is related with symmetric stretch of oxygen atoms along Fe–O bonds (Shebanova and Lazor, 2003). The peak due to the A_{1g} mode of vibration is relatively less intense in T90 and this could be due to dimensional effects or stress in the nanocrystals. The characteristic bands at 667 and 536 cm^{-1} can be assigned to the A_{1g} and T_{2g} transitions of magnetite, respectively, which are consistent with the values reported in the literature (Li *et al.*, 2012). The characteristic vibration bands belonging to magnetite can easily be distinguished from that of $\gamma\text{-Fe}_2\text{O}_3$ at 720 , 500 , and 350 cm^{-1} . Furthermore, no obvious bands of other impurities such as hematite (390 , 280 , 220 cm^{-1}) or akaganeite (1110 , 880 cm^{-1}) can be detected. This further confirms that the black product is predominantly magnetite with small amount of maghemite as impurity phase (Qu *et al.*, 2010).

BET surface area

The pore structure and the BET surface area of the pure T90, T33, PS and peptised TMA samples were investigated by nitrogen isothermal adsorption shown in Fig. 3.18. The complete analyses of the isotherms are provided in Table 3.4. The isothermal gas adsorption-desorption exhibits a type IV profile according to the IUPAC nomenclature of mesoporous materials where the lower curve represents the adsorption of N₂ gas on the surfaces of the NPs, while the upper curve represents the progressive withdrawal; desorption of the adsorbed N₂ (Liebau, 2003). Surface area was estimated from the desorption branch of the isothermal gas-adsorption isotherm which indicated that there is no apparent changes in the pore structure on peptisation.

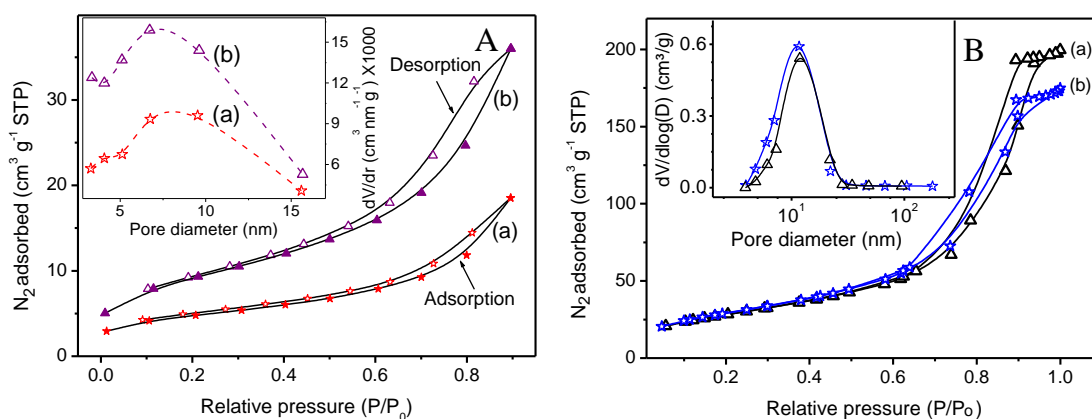


Fig. 3.18 (A) Volume N₂ adsorbed versus relative pressure for Fe₃O₄ nanocrystals at 77K for the powder samples (a) T90 and (b) T33. Inset shows the plot of pore size distribution derived from the BJH analysis. (B) Nitrogen isotherms and their pore size distribution profiles for magnetite nanocrystals (a) before and (b) after peptisation with TMA.

The plot of dv/dr versus pore size determined by the Barrett–Joyner–Halenda (BJH) method shows that the pores (inset of Fig. 3.18A) are in the mesoporous range (5–10 nm) and is attributed to the interspaces of the constituent particles. It is obvious that the surface area of magnetite powders decreased with increase in size while increasing the precipitation temperature (Table 3.4). The particle size (D_{SA}) measured by nitrogen adsorption is somewhat larger than the size estimated from TEM analysis (Fig. 3.2 and 3.3). This discrepancy can possibly be explained by agglomeration of smaller particles to form larger ones, thereby effectively reducing the collective surface area. The problem of agglomeration in dried NPs was particularly aggravated by the possible magnetic interactions and strong hydrogen bonding among them. The BET surface area of 106 m².g⁻¹ in TMA with a pore volume of 0.3051 cm³.g⁻¹, is comparable to that of PS (102 m².g⁻¹, pore volume 0.3426 cm³.g⁻¹).

Table 3.4 Surface area, total pore volume, pore diameter and size of as synthesised magnetite in different temperatures

Sample	BJH pore distribution desorption				BET surface area (m ² .g ⁻¹)	Size, D _{SA} (nm)
	Surface area (m ² .g ⁻¹)	Pore volume (cm ³ .g ⁻¹)	Pore diameter (nm)	Total pore volume (cm ³ .g ⁻¹)		
T90	51	0.106	9.531	0.1197	68	17.0
T75	76	0.145	6.782	0.1586	91	12.7
T60	90	0.174	5.141	0.1889	105	11.0
T45	85	0.165	6.720	0.1836	108	10.7
T33	106	0.195	6.729	0.2113	124	9.4

From the isothermal gas desorption, based on the BJH method, a monodal pore size distribution of ~12 nm was estimated in both the magnetites (TMA and PS). The BET SA in TMA (106 m².g⁻¹) can be equated to D_{SA} of 10.9 nm which is slightly more than the D_{TEM} (10.3 nm) probably because of presence of surface coatings (Iyengar *et al.*, 2014). The D_{SA} size of 11.4 nm calculated from 102 m².g⁻¹ SA in PS, which is very close to the D_{TEM} of 11.6 nm. Probably the creation of SA due to the presence of interparticulate pores just counter balanced the loss in SA due to clustering.

3.4.2.4 Physico-chemical measurements

Figure 3.19 shows the TG profiles of pristine (T90, PS), TMA, APT as well as biopolymer treated magnetite. The total weight loss ranging from 3.8, 3.15% (for T90 and PS) to 19.6% for SAPT as shown in panel B of Fig. 3.19. The TMA shows 4.22% weight loss with similar patterns of three-step decomposition in the temperature range 30-1000°C.

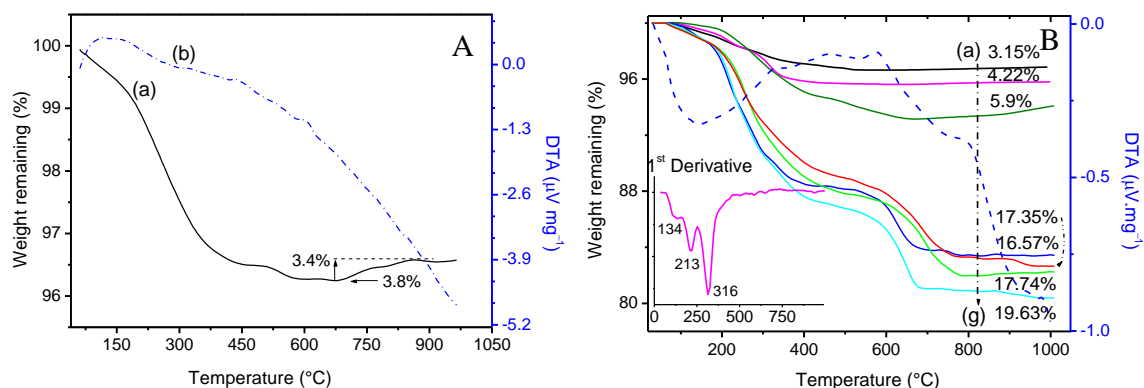


Fig. 3.19 Thermogravimetric and DTA profile of (A) T90 and (B) Surface treated (a) PS, (b) TMA, (C) APT, (d) Dex, (e) DAPT, (f) SAPT and (g) Sta magnetite. Inset in B is the first derivative of TG spectrum of TMA representing the effects of thermal treatment on T90 in pure nitrogen atmosphere.

The peak centred at $\sim 130^\circ\text{C}$ is responsible for the removal of molecular water confined in the pores and or chemisorbed on the crystal lattice. The next exothermic peak at $\sim 213^\circ\text{C}$ for the removal of crystalline water and unwashed chlorides from the material followed by the last peak for a huge loss nearly 4% at $\sim 310^\circ\text{C}$ is due to burning of carbon products from the decomposition of tetramethylammonium group attached to the nanocrystals surfaces in the case of TMA sample. The weight loss continued till $\sim 565^\circ\text{C}$ and it could be attributed to the removal of multi-layers of water of hydration from the surface of the NPs as well as dehydration of iron oxyhydroxide (FeOOH) formed in the ambient moisture. A small weight gain of $\sim 0.4\%$, observed in the temperature range $685\text{-}860^\circ\text{C}$ for T90 $\sim 0.2\%$ was observed after 640°C for PS, 0.21% after 668°C onwards for TMA sample which is due to oxidation of magnetite to $\gamma\text{-Fe}_2\text{O}_3$, though the experiment was conducted under continuous nitrogen purge. The TMAH content in TMA magnetite can easily be calculated as 1.1% . When this is applied to the M_S value of PS, one can expect a value of 63.97 emu.g^{-1} for TMA instead of actual 57.92 emu.g^{-1} .

Table 3.5 Crystal sizes obtained from different techniques TEM, XRD, magnetisation curve, PCS and surface area on magnetite

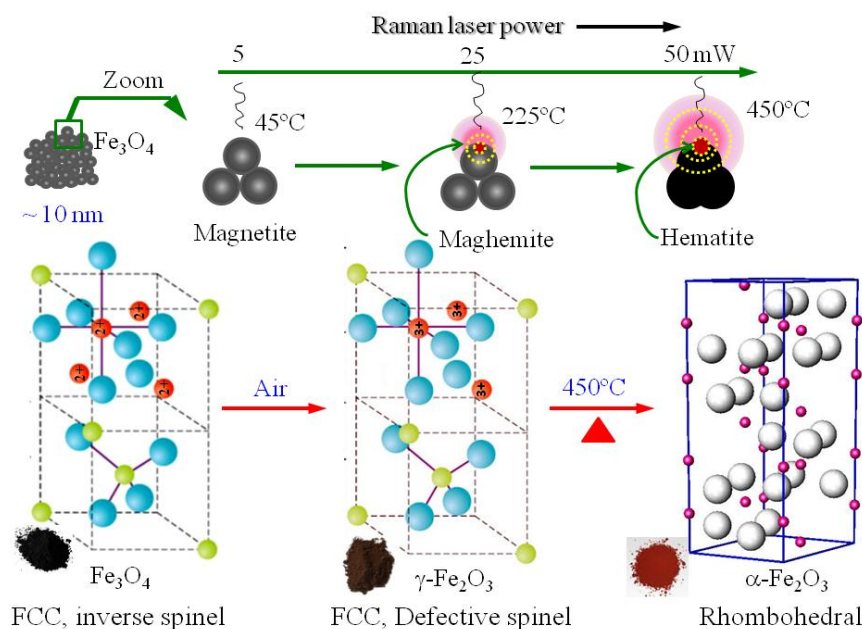
Sample	D_{TEM} (nm)	D_{XRD} (nm)	D_{mag} (nm)	D_{PCS} (nm)	D_{SA} (nm)
PS	11.6	8.7	8.98	43	11.4
APT	12.12	9.29	9.38	-	9.6
SAPT	-	9.75	9.85	-	15.6
DAPT	-	9.5	9.02	-	-
TMA	10.3	10.7	9.02	13	10.9

We now conclude that nearly 9% reduction in the M_S value of TMA is due to its reduced crystal dimension of 10.3 nm compared to that (11.6 nm) in PS in addition to $\sim 1\%$ reduction due to the non-magnetic chemical surrounding in TMA. The magnetite nanocrystal dimensions, determined by TEM, XRD, Langevin fitting magnetisation curve, PCS and BET surface area techniques are summarised in Table 3.5. A very close observation is that the dry NPs characterised by BET, TEM, XRD, Magnetisation curve, proven the mesoporous single crystalline uniform size distributed, superparamagnetic behaviour of magnetite characteristic of FCC inverse spinel crystal system. Size measurement based on the light scattering method is one of the most important techniques by which one can have in the *in-situ* information on the state of clustering and extent of

hydration of NPs in suspensions where there are many counteracting forces operating. The situation becomes more complicated when NPs are dispersed in water. The temperature, concentration and time dependent kinetics of growth of hydrodynamic size confirmed their stability of TMA suspension in this study.

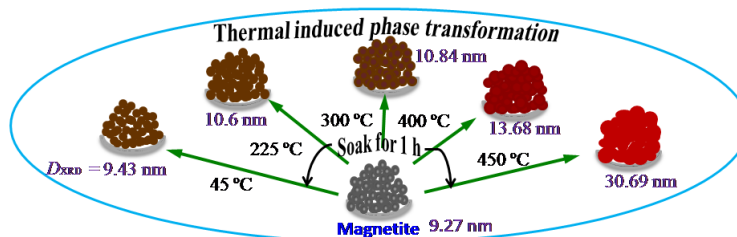
3.4.3 Phase transformation

As per the reported literature, Raman laser power intensity of 5, 25, 50 mW produces local heating (Shebanova and Lazor, 2003) to the tune of 45, 225 and 450°C which transforms the magnetite to thermodynamically more stable phase.



Scheme 3.2 Relationship of Raman laser power and local heating on magnetite nanoparticles.

For magnetite NPs of size ~9 nm easily undergo surface oxidation of Fe²⁺ to Fe³⁺ leads to a cation-deficient spinel, maghemite even at low temperature (45 °C) in air presumably due to their similar crystal structures and heating to 450°C for 1 h is sufficient to phase transform entirely to hematite as their crystal structures are completely different (Scheme 3.2). The thermal effect of a laser beam results from its absorption by a sample. With a view to establish the temperature and Raman laser power relationship, evolution of different phases due to the oxidation under heat treatment as well as Raman from the laser spot with increasing power (5, 25, 50 mW). The controlled oxidation of magnetite in air from 45–450°C leads to the change of physical appearance from black (magnetite) to brown, red-brown, brick red colour which indicates the phase transformation.



Scheme 3.3 Phase transitions of magnetite upon annealing at different temperature

The crystallite size calculated by applying Scherrer equation has grown into 30 nm from 9 nm in as-synthesised powder which is shown in scheme 3.3. The effect of the calcination temperature on the crystallinity and phase of the samples was investigated by Rietveld analysis on XRD techniques.

Raman spectroscopy

Figure 3.21 shows the Raman spectra recorded on magnetite with increasing laser power and also on heat treated samples with low laser power (2.5 mW) to avoid further laser induced phase transformation. The peak due to the A_{1g} mode of vibration is relatively less intense in NPs (panel ‘a’ of Fig. 3.21A) compared to C1 (panel ‘a’ of Fig. 3.21B).

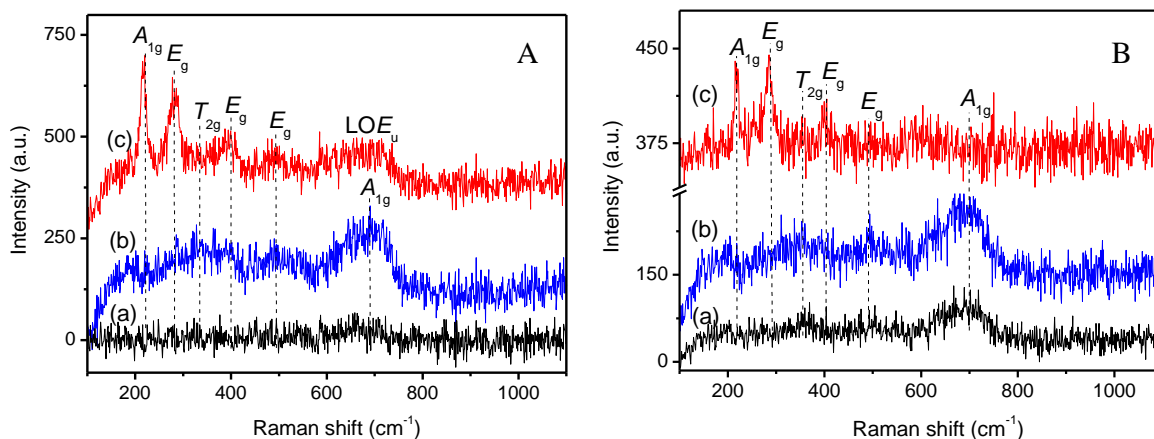


Fig. 3.21 Typical Raman spectra of (A) as-synthesised ~ 9 nm Fe_3O_4 recorded by different laser intensity (a) 5, (b) 25, and (c) 50 mW and (B) annealed magnetite (a) 45° , (b) 225° , (c) 450°C recorded by 2.5 mW laser.

It is well known that the Raman modes of magnetite are unusually broad (typical full width half maximum $\sim 40\text{--}50\text{ cm}^{-1}$). The origin of this phenomenon has been attributed to the strong electron–phonon interaction in this compound. On the other hand, the typical line widths of the Raman modes of hematite are only $10\text{--}20\text{ cm}^{-1}$ (Shebanova and Lazor, 2003). An increased laser power of 25 mW results new features beginning to appear in the spectrum in addition to the bands of magnetite (layer b). The phonon bands observed at

692, 487 and 399 cm^{-1} could be assigned as A_{1g} , T_{2g} , E_g modes characteristic of maghemite ($\gamma\text{-Fe}_2\text{O}_3$) (Bersani *et al.*, 1999). E_g and T_{2g} modes are corresponding to symmetric and asymmetric bending of Fe–O, respectively in FeO_4 tetrahedron (Shebanova and Lazor, 2003). This could be an incomplete phase transformation to metastable maghemite by laser induced heating. Exposure of the powder specimen to highest laser power 50 mW causes the new bands grow in intensity with the decrease in bandwidths of the vibrational modes (layer c). The phonon bands observed at 700, 500, 380, 273 and 215 cm^{-1} could be assigned as LOE_u , E_g , E_g , E_g , A_{1g} modes characteristic of hematite ($\alpha\text{-Fe}_2\text{O}_3$) (Bersani *et al.*, 1999). The 450°C annealed sample shows the similar spectrum to that of 50 mW laser recorded T45 sample.

Rietveld analysis

The Rietveld analysis also supports the phase composition at different temperature. The semiconducting nature of magnetite is explained by the fast electron hopping between iron cations on the octahedral sites. It is not unlikely that the laser-assisted electron transfer, along with the thermal effects, may play a major role in the oxidation of this inverse spinel. Moreover, a realistic view of the oxidation of magnetite has to consider also a possible catalytic effect of hydroxyl groups adsorbed on the surface. Their inevitable occurrence results from the dissociation of water molecules interacting with the surface of magnetite (Shebanova and Lazor, 2003). It was indistinguishable from the diffractogram of the as-synthesised T45 and annealed at 225 °C samples (Fig 3.22A). This was expected because both magnetite and maghemite have the same crystal structure with only slightly different d -spacing. Any difference was obscured by the peak broadening due to small crystal size. After close examination by Rietveld method, the presence of maghemite phase (space group P4132 (213); JCPDS No. 39-1346) and the composition is thought to consist of a defect magnetite structure with $a = 8.34 \pm 0.001 \text{ \AA}$ lattice parameter. This study indicating that the complete oxidation of Fe_3O_4 under O_2 leads to $\gamma\text{-Fe}_2\text{O}_3$. Fig. 3.22B consists of maghemite characteristics along with additional weak diffraction peaks of (104), (024) and (300) that are characteristic of rhombohedral structure of $\alpha\text{-Fe}_2\text{O}_3$ ($R\bar{3}c$; JCPDS No. 33-0664) with lattice constant $a=5.04 \text{ \AA}$, $c =13.74 \text{ \AA}$. After oxidation of magnetite under air at 450°C for 1 h, the black assembly is transformed to a brick red one having ~30 nm crystallite size calculated by applying the Scherrer equation to the most intense peak (104).

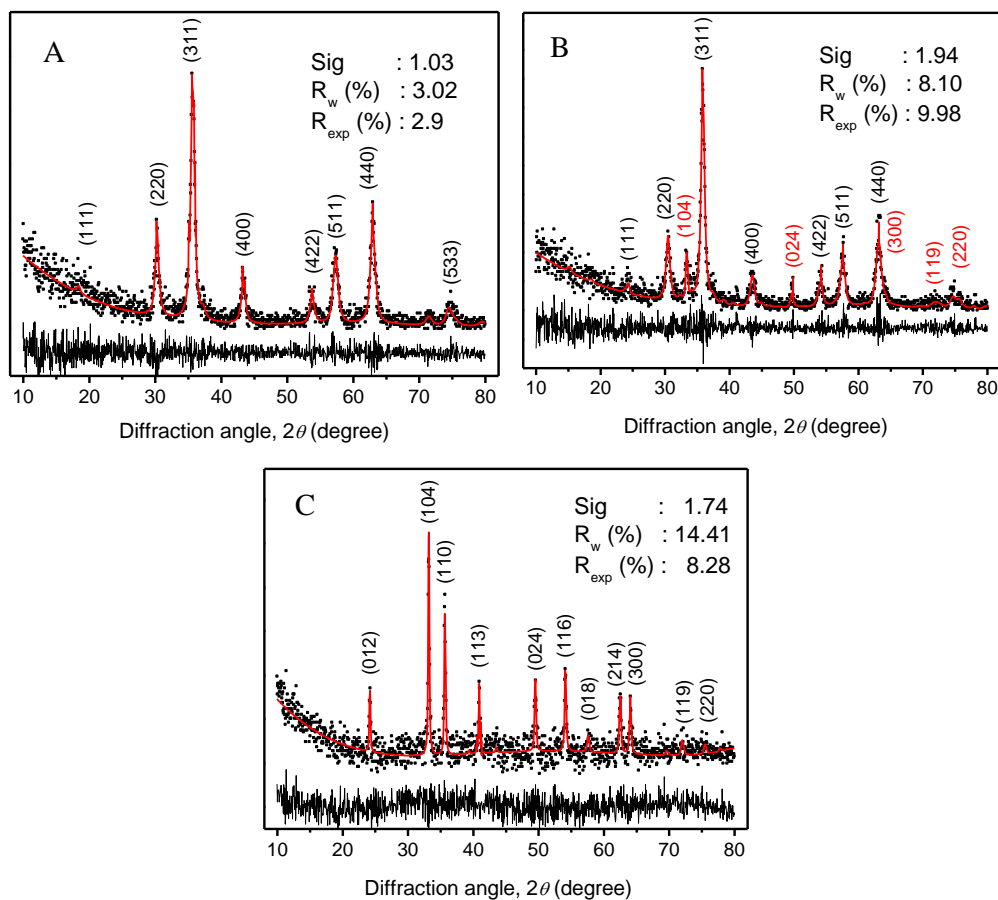


Fig. 3.22 Rietveld analysis on XRD patterns for Fe_3O_4 annealed at (A) 225° , (B) 400° and (C) 450°C . The solid lines are Rietveld fit over the dotted raw data. The crystal planes marked based on JCPDS card.

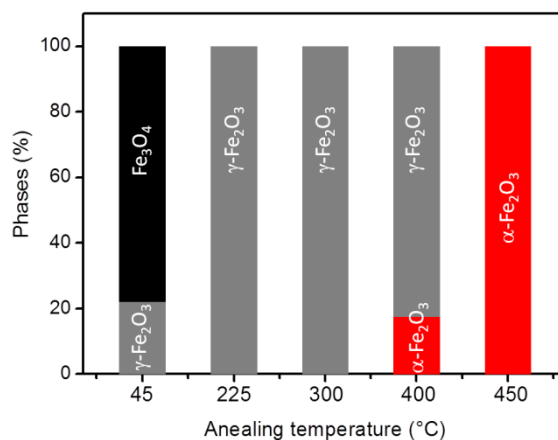


Fig. 3.23 The percent IO phases calculated from Rietveld analyses on respective XRD patterns of thermally annealed magnetite samples for 1 h

Fig. 3.22C shows typical reflection patterns, indexed as the (012), (104), (110), (113), (024), (116), (122), (214) and (030) crystal planes belonging to the rhombohedral structure of $\alpha\text{-Fe}_2\text{O}_3$, indicating the complete transformation of Fe_3O_4 into $\alpha\text{-Fe}_2\text{O}_3$ at this temperature. Fig. 3.23 shows the overall iron oxide phase content in annealed magnetite

sample at various temperatures. About ~21% magnetite NPs transformed into maghemite at 45°C for an hour, complete transformation takes place at 225°C, and retains the maghemite phase even at 300°C but crystallite size were grown. The hematite transformation begins at 400°C and completed by ~450°C. Jubb *et al.* (Jubb and Allen, 2010) found that heating for 4 h at 575°C is suitable for transforming the initial Fe films completely to hematite, also documented in the literature.

3.4.4 Non-aqueous ferrofluids

3.4.4.1 Heptane based ferrofluid

The non-aqueous ferrofluid was prepared by an aqueous precipitated magnetite has been successfully phase transferred to non-aqueous solvent heptane. The morphological and hydrodynamic size of magnetite is presented in Fig. 3.24.

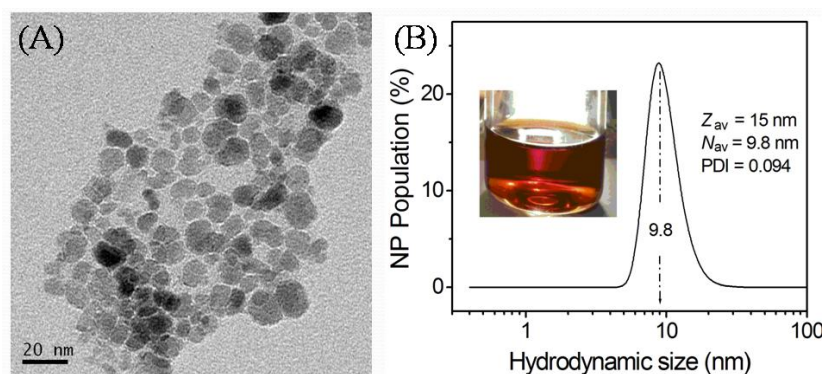


Fig. 3.24 (A) BF-TEM image and (B) PCS study on magnetite dispersed in heptane

The PDI very close to zero shows the monodispersity of NPs and the hydrodynamic size (D_{PCS}) is 9.8 nm which is larger than the physical size ($D_{TEM} \sim 8.2$ nm) due to the C10 surfactant chain length (Hrianca *et al.*, 2002).

3.4.4.2 Magneto-rheology on oil based ferrofluid

The rheological measurements conducted on two different (10 and 20%) magnetite loading of sesame oil based ferrofluids at 25°C under the controlled shear rate (100–1000 s^{-1}) measurements. This part focused primarily on viscosity of ferrofluids while varying shear rate, cyclic and switchable applications of external magnetic field.

3.4.4.1 Effect of shear rate on viscosity

The flow behaviour of magnetite based ferrofluid systems was measured as change in viscosity against shear rate in the range 100–1000 s^{-1} . At zero magnetic fields, the

viscosity of ferrofluid is greater than that of the base fluid oil, shear thinning behaviour. This is due to particles being loaded in the oil offer resistance to flow. MNPs gets align along the direction of the magnetic field when a magnetic field is applied, forming of chain like structure, thus increase in viscosity. Under low shear flow, some of the chains might break, but not all of them. As the shear rate increases more chains begin to break, since these chains affect the viscosity, it is easy to observe that as the chains break one should see the viscosity decreases and these phenomena is schematically represented in Fig. 3.25.

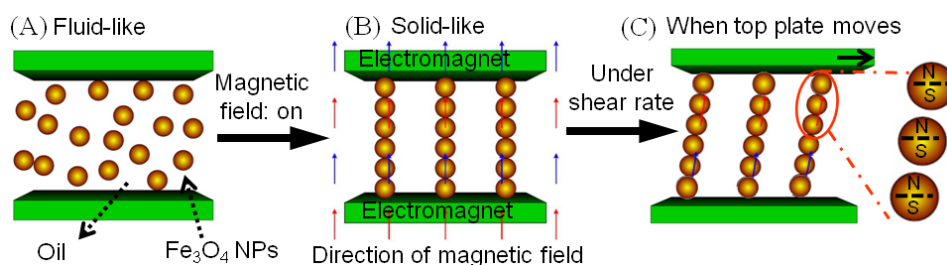


Fig. 3.25 Schematic illustration of ferrofluid (A) fluid-like behaviour, (B) chain formation of polarised MNPs under applied magnetic field and (C) chain moving towards shearing direction under magnetic field

Figure 3.26 shows the dependency of viscosity on shear rate at an increasing magnitude of four different magnetic field strengths. It is expected that for oil the viscosity is independent of shear rate indicating Newtonian flow behaviour.

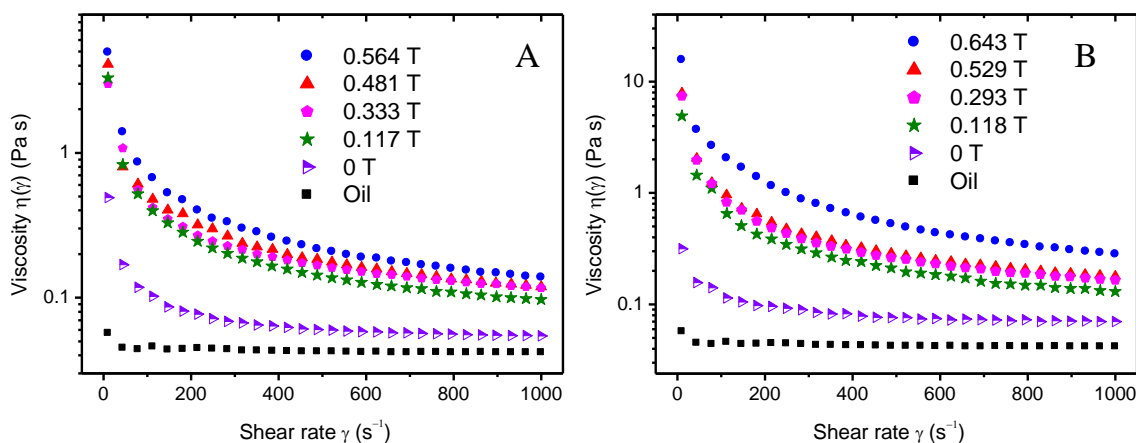


Fig. 3.26 Variation in viscosity of (A) 10 and (B) 20% oil based ferrofluid and oil as a function of shear rate at different magnetic field strength.

The flow curves of ferrofluid under the influence of magnetic field exhibit a shear thinning non-Newtonian behaviour. The non-linearity observed in the flow curves for 10 and 20% of the ferrofluid depict the pseudo-plastic behaviour of the system. It is evident

from Fig. 3.26 that with the increase in the magnitude of the magnetic field offer more resistance to flow and subsequently the viscosity increases. Thus, the magnetic field exhibits a strong influence on the flow behaviour of the ferrofluid. At relatively higher concentration (20%), it is plausible that this sudden application of magnetic field causes instantaneous cluster formation which results in huge increase in viscosity of the ferrofluids. However, such an effect is less predominant in 10% due to less number of NPs (Fig. 3.26) and thus the main difference between them is that the magnitude of the viscosity. It is pertinent to mention that the increase in viscosity takes place only in the low shear rate region while shear thinning occurs for the remaining applied shear rates.

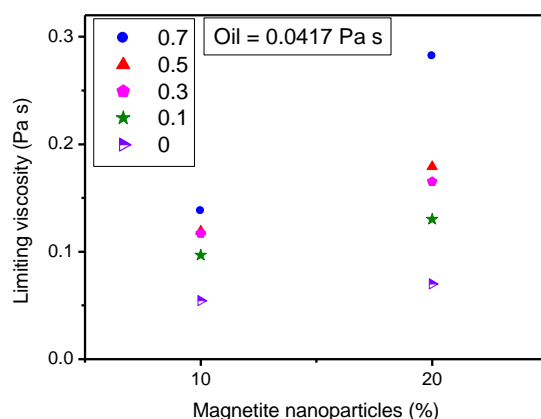


Fig. 3.27 Limiting viscosity of ferrofluid as a function of NP loading at different applied magnetic fields.

The applied magnetic field causes a strong interaction among MNPs and leads to the formation of magnetic structures. But with the increase in shearing rate, the agglomerated structures tend to break down and NPs arrange themselves go along the shearing direction. This leads to decrease in the fluid viscosity at high shear rates. The viscosity of the ferrofluids at highest shear rates is called the high shear limiting viscosity. Fig. 3.26 shows the high shear limiting viscosity of 10 and 20% NPs dispersions at different magnetic fields. It is observed that the limiting viscosity increases with the increase in the NP concentration and magnetic field. This implies that these formed structures are not completely destroyed even at high shear rates which inflict a strong effect on the limiting viscosity. Similar shear thinning behaviour with enhanced viscosity under the influence of magnetic field has been earlier reported (Nowak *et al.*, 2014), but the order of enhancement observed in this study is much higher as compared to others.

3.4.4.2 Effect of shear rate on shear stress

Figure 3.28 shows the variation of shear stress with shear rate under the application of different magnetic fields for 10 and 20% NP dispersions. The shear stress is observed to increase non-linearly with shear rate and also with the increase in magnetic field strength. The dependence of the yield stress on the magnetic field strength was investigated. The yield stress was estimated from a controlled shear rate measurement on the shear stress. Each stress curve data was fitted by Herschel-Bulkley (Cvek *et al.*, 2016) model given by

$$\tau = \tau_y + k\dot{\gamma}^n \quad (3.2)$$

where τ_y , k , $\dot{\gamma}$ ($=d\gamma/dt$) and n are the yield stress, consistency parameter, shear rate and power law index respectively. The calculated values of τ_y , k and n for different field for both the samples are shown in Table 3.6.

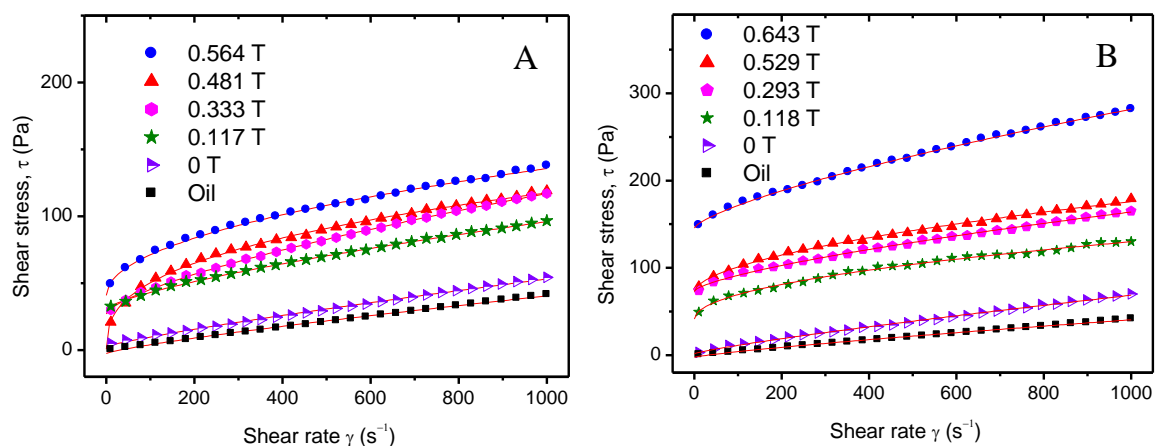


Fig. 3.28 Changes in shear stress on (A) 10 and (B) 20% oil based ferrofluid as a function of shear rate at different applied magnetic fields. Solid lines represent the Herschel-Bulkley model predictions fitted to the experimental data.

The ferrofluid requires a force greater than that of the yield stress to cause the fluid to flow freely. It is evident from Fig. 3.28 that the magnitude of the yield stress becomes higher with the increase in the applied field strength and also with NPs concentration. It may be noted that yield stress increases with increases in magnetic field and concentration of NPs. Concentrated ferrofluids contains more particle–particle as well as dipole–dipole interaction give rise to more chain formation results in a yield stress. As the concentration of the NPs increase, the magnetostatic interaction among polarised particles increase under the influence of magnetic field require much higher force to break and make the ferrofluid free flowing and hence the yield stress is high and a more pronounced shear thinning behaviour.

Table 3.6 Rheometric parameters estimated by fitting eqn (3.2) to the shear stress variation with shear rate, τ

NPs (%)	Fit results	No field (B=0)		Applied magnetic field, B (T)			
		Oil	FF	0.1	0.3	0.5	0.7
10	Yield stress	2.401	2.519	27.12	30.42	40.98	74
	Consistency parameter	0.1449	0.493	0.7536	0.4707	3.099	0.8965
	Power law index	0.8237	0.8435	0.6922	0.7146	0.495	0.3716
20	Yield stress	2.401	1.865	41.49	72.7	73.56	145.6
	Consistency parameter	0.1449	0.1893	2.783	2.168	0.7072	0.9345
	Power law index	0.8237	0.849	0.5007	0.5592	0.7023	0.721

It is pertinent that $n < 1$ for all magnetite ferrofluid subjected to different magnetic fields which indicate shear thinning of the fluids. Also, the n -values vary in a close range suggesting parallel viscosity curves which is evident from Fig. 3.27.

3.4.4.3 Effect of cyclic magnetic field on viscosity

This part is aimed to explore the effect of magnetic fields on the magneto-rheological performance of 10 and 20% magnetite loaded ferrofluids. Data contained in Fig. 3.29 were obtained by gradually increasing and withdrawing (decay) the magnetic field intensity (0 to 0.7 T) in a ferrofluid under constant shear rate of 100 s^{-1} and the same was continued for three consecutive cycles. While increasing the magnetic field (rise), the interaction among MNPs and the flow resistance increases leading to an increase in the viscosity. During the decay period, the viscosity value drops but relatively at lower rate than the rise period exhibiting a substantial hysteresis. This may be attributed to the fact that the relaxation time of structures might be longer than the measurement time (each data point interval is 10 s) allowed and hence the structures cannot completely relax. Such observed hysteresis in viscosity profiles during application and withdrawal of magnetic field has been reported earlier (Shima and Philip, 2011). After one complete cycle, the viscosity values increase further during the next two cycles of magnetic sweep. Though the field is completely withdrawn, the viscosity remains similar to that in the beginning of the cycle suggesting the absence of hard aggregation. But during the next cycle of magnetic sweep, the magnetic moment of the MNPs align themselves relatively faster as compared to the previous cycle.

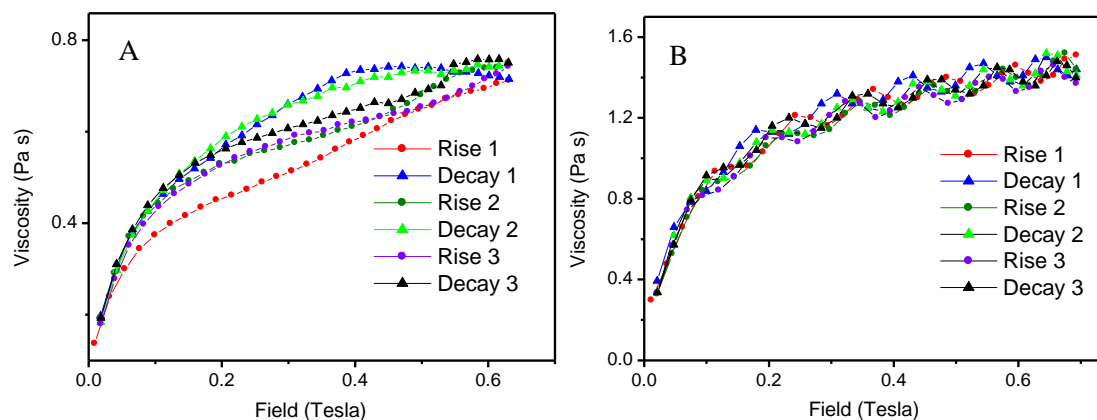


Fig. 3.29 Viscosity as a function of applied magnetic field strengths (during rise and decay) for (A) 10 and (B) 20% MNPs containing ferrofluids at a shear rate of 100 s^{-1}

This leads to the increased viscosity during the consecutive magnetic sweeps. However, the trend is not so much pronounced as the concentration of the dispersed NPs (20%) in the nanofluid is increased. The viscosity increase and decrease path during the magnetic sweep cycle is followed repeatedly within acceptable error limits.

3.4.4.4 Effect of magnetic switching

This part has focused on the stimuli response properties of ferrofluids. Viscosity tests were carried out in the absence (off) and presence (on) of magnetic fields. The shearing rate has been kept constant over the entire time for each experiment while it has been varied across different iterations. While increasing/decreasing the shearing rate by orders of magnitude, the viscosity increases/decreases by orders of magnitude. The steady viscosity with time for a given magnetic field indicates that the magnetic structures/chains are not broken by shear rate.

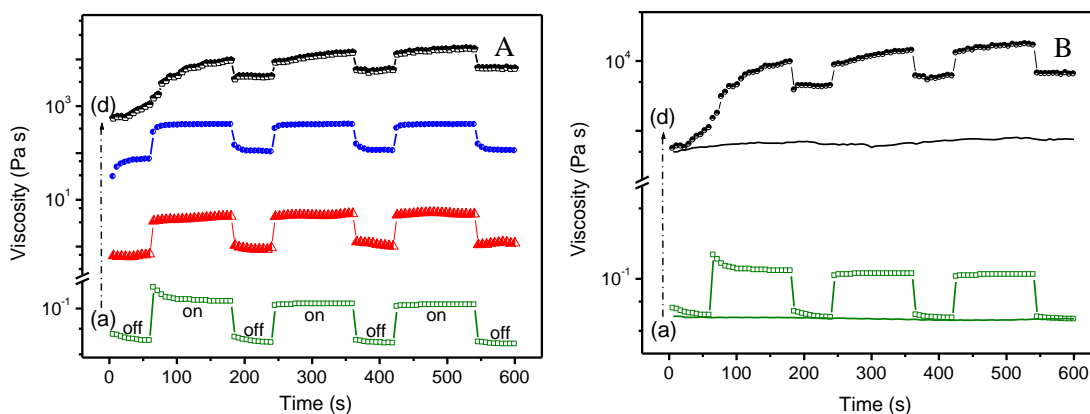


Fig. 3.30 (A) Variation in viscosity of ferrofluid with time during field ($B=0.3 \text{ T}$) on and off state under (a) 0.001, (b) 0.01, (c) 100, (d) 1000 shearing rates and (B) comparison of viscosity for periodically applied field as well as no field under shearing rate 0.001 and 1000 s^{-1}

To understand the typical nature of the ferrofluid, the viscosity is measured under no external magnetic field shown in Fig. 3.30 B. It is evident at 0.001 and 1000 s⁻¹, the baseline viscosity without external magnetic field is independent of time. This time dependent viscosity of ferrofluids at low shear rates is due to the thixotropic behaviour of fluid where the weak bonds are formed over time due to inter-particle interaction. At constant high shear rate (1000 s⁻¹), the interaction significantly leads to the increase in viscosity of the resultant fluid due to formation of magnetic structures even without magnetic field. It is clear from the number of on-off switching cycles; an equilibrium value is achieved more quickly. Upon turning off the magnetic field, the viscosity values drops to baseline viscosity immediately, results stepped curves for viscosity are observed due to pulsed magnetic field. This shows the perfect reversibility of the observed phenomena. This offers interesting possibilities of using these ferrofluids in reversibly switchable microfluidic devices, electro mechanical devices such as NEMS, MEMS etc.

3.5 Conclusions

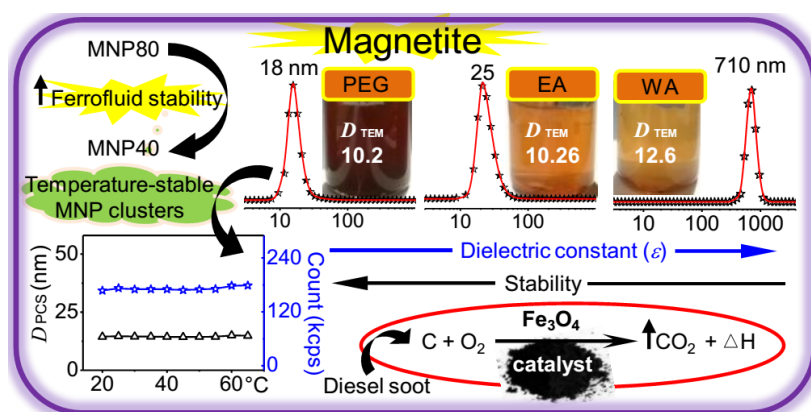
Monodisperse magnetite NPs with size in the range 6–13 nm were successfully synthesised by ammonia precipitation technique in the temperature range 33–90°C. The nanocrystalline magnetite, used in highly stable TMA nanofluid, has been synthesised by ammonia coprecipitation in physiological saline and had a BET surface area of 106 m².g⁻¹. The XRD and the Rietveld refinement confirm the inverse spinel structure of cubic magnetite as dominant phase. The activation energy for the growth for nanocrystallites during relatively higher temperature of precipitation was estimated to be ~6.15 kJ.mol⁻¹ which is responsible for initiating the complex process of nucleation and growth by diffusion. W-H technique indicated crystal dimensions within D_{TEM} 2.5 nm as the shell of amorphous layer has not contributed to the XRD. The lattice strains calculated were relatively high and in the range 5.5-8.9×10⁻³ with very small variations for samples T33 to T90. The D_{mag} derived from the Langevin computations were slightly smaller than the physical sizes from TEM analysis due to the supposedly presence of a magnetically “dead” layer of atoms over magnetite shell at the surface. The reduced M_S value of 58 emu.g⁻¹ in TMA specimen is due to its reduced crystal dimension along with small contribution of the presence of non-magnetic TMAH. TG-DTA, EDAX, as well as XPS and FTIR spectra confirmed the presence of surface coordinated tetramethyl group in TMA. TGDTA as well as EDAX also confirmed the successful coating of TMAH on NPs in TMA. The size of the magnetite one-shell nanoclusters was controlled within 28.3–32.3

nm range in a wide temperature range. The novelty of this work is that this is a successful attempt to correlate the stability of ultra-stable colloidal suspension of the superparamagnetic NPs against time and temperature by simple photon correlation spectroscopy in conjunction with colloid surface properties. The monodispersity of these MNPs containing aqueous ferrofluid have no effect on heating which has great potential in hyperthermia and may find suitable in various biomedical and industrial applications. The oil based ferrofluid exhibit a dramatic reorganisation when subjected to an applied magnetic field and the particles aggregate to form chain-like structures along the direction of the applied magnetic field. More pronounced non-Newtonian shear-thinning behaviour of viscosity can be observed a low shear rate region under the influence of magnetic field. It should be noted that the synthesis strategy may be extended to the preparation of complex functional structures with controlled physicochemical properties for a variety of applications.

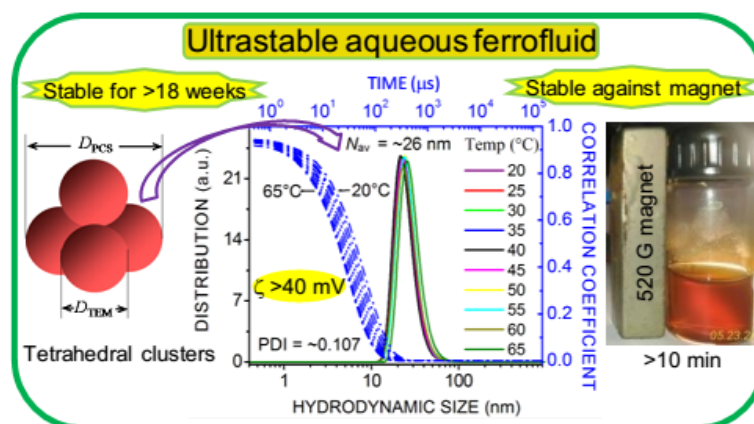
Alcohol-water mixed solvent

4.1 Graphical abstract

In this chapter, the Fe_3O_4 nanocrystals have been synthesised by homogeneous precipitation in different alcohol/water (1:1) mixed solvents at two different temperatures to elucidate the role of dielectric constant (ϵ) of the reaction medium. The effects of different solvents on the properties of precipitated NPs including its catalytic activity in carbon combustion reaction were examined. HRTEM images, SAED and XRD confirmed pure *fcc* inverse spinel Fe_3O_4 phase with narrow size distribution and the crystals are completely dispersible in water. The morphological features such as surface termination and shape of the Fe_3O_4 NPs were analysed by HR-TEM.



As the ϵ decreases, the crystal size decreases for mono-ol systems compared to ~ 13 nm size in water whereas ethylene glycol/water yields finer ~ 8.2 nm crystals though it has highest ϵ among mono-/poly-ols.



Soot combustion study demonstrates that the catalytic activity is mainly due to available surface area along with exposure of active crystallographic facets.

The thermal analysis as well as FTIR data indicated the presence of organic content in the material. An insight into the colloids by light scattering shows that the alcohol mediated process produces 16-33 nm MNP clusters composed of 2-3 particles in highly stable aqueous magnetic fluids. The relatively high temperature process favours higher crystallinity and particle size with reduced colloidal stability in aqueous phase. We also demonstrated the potential for obtaining ferrofluids and its colloidal stability has been studied at different temperatures over months by observing hydrodynamic size and surface charge by photon correlation spectroscopy. Outer shell of surface active DEG used in the present study not only produced stable “one-shell cluster” dispersion, which was found to be unaffected by heating and magnetic field, but also may be highly useful for biomedical applications due to their known bio-compatibility. The nanocrystalline powders and the dispersed colloids may also find their great applicable potentials as ferrofluids, selective catalysis etc.

4.2 Introduction

Magnetite nanocrystals can easily be synthesised by aqueous precipitation method (Iyengar *et al.*, 2014), though it has the disadvantage of agglomeration of fine particles, which imposes a major challenge to realisation of the full potential of its nanocrystalline powders. In the precipitation process, low dielectric constant solvents, e.g., alcohols, can alter the nucleation kinetics which results in reduction of the size and distribution of the resulting particles (Hamada and Matijević, 1981; Chen and Chang, 2004; Wang *et al.*, 2010). Mono- or polyol type of alcohols in a water-alcohol mixed solvent act as surfactants also and suppress the growth of nanocrystals while alkali precipitation of metal oxide nanocrystals (Remani and Ghosh, 2009; Garcia-Jimeno and Estelrich, 2013). Guo and Xiao reported that the crystallite size and crystallinity of the particles decreased with the increasing IPA addition in hydrothermal reactions (Guo and Xiao, 2006). Ghosh *et al.* demonstrated that the radius (r) of nanocrystals produced in a precipitation reaction decreases with decrease in the ε of the alcohol-water mixed solvents (Remani and Ghosh, 2009; Sreeremya *et al.*, 2012) following the eqn (4.1):

$$\frac{1}{r} = \frac{kT\rho}{2m\gamma} \ln C + \frac{\rho z_+ z_- e^2}{8\pi m \gamma \varepsilon \varepsilon_0 (r_+ + r_-)} \quad (4.1)$$

where ε_0 is the permittivity in vacuum, r_+ and r_- are the radii of charged z_+ and z_- ions respectively, and e represents the charge of electron (1.602×10^{-19} C). The solubility can be modulated by varying the composition of mixed solvent. Formation (precipitation) of particles is strongly dependent upon the supersaturation of solute following classical nucleation theory. Supersaturation can be achieved by lowering of temperature, solvent evaporation, pH change, chemical reaction, alteration in solvent composition, etc. and is defined as the ratio of solute concentration (C) and saturation concentration, m is the molecular weight of the solute and γ is the interfacial energy between solute and solution phases.

The effect of solvent can change the particle morphology specially pronounced at higher concentrations of Fe-precursors (>0.5 M) (Chowdhury *et al.*, 2014). Chowdhury *et al.* evaluated the effect of alcohol-water mixed solvents with alcohols such as butanol, propanol, ethanol and methanol on the β -FeOOH nanorod under hydrothermal conditions (Chowdhury *et al.*, 2014). Zhang *et al.* synthesised 15–300 nm magnetite crystals with controllably variable morphologies including nanospheres to nano-octahedra/ nano-hexaprism in EG-water mixed solvent (Zhang *et al.*, 2011). Wang *et al.* fabricated well-defined micrometer sized magnetite crystals with star-shaped hexapods, octahedrons, concave octahedrons, and octahedral frameworks in IPA-water by solvothermal approach. Estelrich *et al.* reported high molecular weight (2–10 kDa) PEG coated magnetite ferrofluids with a dipole–cation binding between the ether group of PEG and the +vely charged NP core with suspension stability over two years (Garcia-Jimeno and Estelrich, 2013). Metal oxides become charged by the adsorption of hydrogen (H^+) or hydroxyl ions (OH^-) in aqueous suspensions, while remaining neutral at a specific pH called as PZC (Erdemoglu and Sarikaya, 2006). The stability of nanofluids and the clustering can easily be predicted from the zeta potential measurements. To avoid undesirable errors of using mathematical equations or Henry formula to relate electrophoretic mobility to ζ -potential of NPs, the surface charges of suspended particles are reported in terms of ζ -potential (Masoudi *et al.*, 2012). Though precipitation of metal oxides e.g., TiO_2 , ZrO_2 , CeO_2 , and SiO_2 in alcohol/water mixed solvents were already been reported (Gao *et al.*, 1999; Chen and Chang, 2004; Sreeremya *et al.*, 2012), there is no systematic study on the effect of solvents of variable dielectric constant and precipitation temperatures on magnetic nanocrystals and to the best of our knowledge, there is no study on the effect of

solvents/precipitation temperatures on the catalytic and colloidal properties/ stability of aqueous suspensions of magnetite NPs.

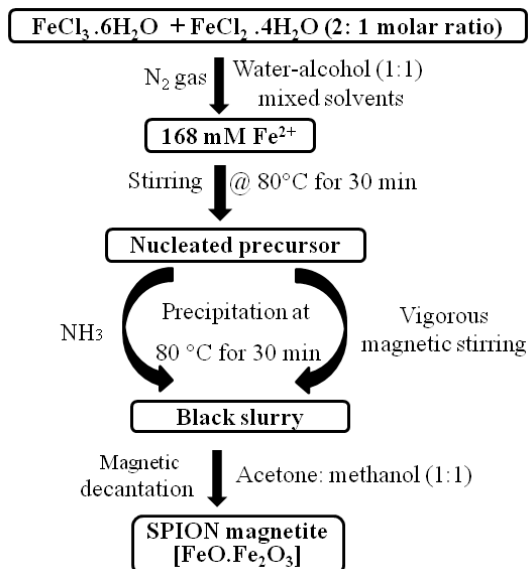
In this section, the effect of various alcohols of different polarities on the size, colloidal stability, reactivity, and other related properties of magnetite nanocrystals by ammonia precipitation is presented. Six alcohols have been employed with decreasing ϵ value in the order ethylene glycol (EG)>diethylene glycol (DEG)>ethanol (EA)>*n*-propanol (*n*PA)>isopropanol (IPA)>polyethylene glycol (PEG). Mixed solvents of 1:1 water-alcohol produced small Fe₃O₄ NPs in the size range 8–13 nm. The powders as well as nanofluids have been characterised thoroughly by various techniques. The crystal structure and magnetic properties of the resultant colloidal particles have been investigated by XRD, TEM, TG-DTA, VSM. The hydrodynamic size as well as zeta potential was evaluated by PCS. To evaluate the colloidal stability, extensive zeta potential measurements have been carried out. Plausible mechanism of the clustering phenomena in aqueous suspension has been proposed. The catalytic activity of the crystals investigated by diesel soot combustion have been explained in terms of its texture coefficient of different crystal planes, size and BET surface area. This study lays a strong foundation to relate the activity on a physical basis for future nanomaterial development which will pave the way to potential biomedical applications.

4.3 Experimental

4.3.1 Coprecipitation in alcohol-water mixed solvents

To fabricate magnetite nanocrystals as shown in Scheme 4.1, a 8.4 mmol portion of FeCl₂.4H₂O and 16.8 mmol FeCl₃.6H₂O (such that Fe³⁺/Fe²⁺= 2) were dissolved in 35 ml 1:1 water-alcohol mixed solvent deaerated by purging nitrogen gas through it for 30 min in a 100 ml three-neck round bottom flask. Several alcohols ca. EA, *n*PA, IPA, EG, DEG and PEG-400 were used in this study. The reaction mixture was heated to 80°C by a hot-plate magnetic stirrer and was maintained at this temperature for ~30 min while continuous stirring and nitrogen purging in a closed set up. Subsequently, the reactor was cooled naturally to 40°C and was kept constant. About 15 ml NH₃ solution was added to the homogeneous mixture in one shot when the reaction mixture turned black (pH~11). Vigorous stirring and the temperature (40°C) were maintained for further 30 min and then allowed to cool down to ambient temperature. At this point the net Fe²⁺ concentration was 168 mM. The settled black precipitate was subjected to repeated alternating magnetic

decantation and washing with water to remove impurities; the final washing step was done with methanol to break down hard agglomerates.



Scheme 4.1 The flow chart representing the step by step magnetite synthetic strategy by coprecipitation technique

The fine powder form of magnetite was obtained by drying the resulted black slurry in vacuum oven at 60°C and preserved in a dessicator for further characterisation which are labelled with the corresponding alcohol abbreviations.

Table 4.1 The sample details such as sample designations, reaction media, dielectric constants of solvent, precipitation temperatures

Solvents used with water (1:1)	ϵ (Furniss <i>et al.</i> , 1978)	Sample ID at different precipitation temperatures	
		40°C	80°C
Water	80.2	WA	WA80
Ethyl alcohol	52.4	EA	EA80
<i>n</i> -propyl alcohol	50.25	<i>n</i> PA	<i>n</i> PA80
Isopropyl alcohol	50.05	IPA	IPA80
Ethylene glycol	58.95	EG	EG80
Diethylene glycol	55.95	DEG	DEG80
Polyethylene glycol	46.3	PEG	PEG80

Magnetite precipitated in water medium at 40°C is designated as WA. Magnetite was also precipitated at 80°C to study the effect of temperature and labelled as alcohol abbreviation followed by numeric (precipitation temperature), e.g., EG80 stands for magnetite in ethylene glycol-water solvent at 80°C. The samples were designated based on the reaction

media and precipitation temperature, respective dielectric constants of the reaction media were also tabulated in Table 4.1 for a clear idea of the samples synthesized.

4.3.2 Effect of time

About 8.4 mmol portion of $\text{FeCl}_2 \cdot 4\text{H}_2\text{O}$ and 16.8 mmol $\text{FeCl}_3 \cdot 6\text{H}_2\text{O}$ were dissolved in 35 ml 1:1 water–DEG mixed solvent deaerated by purging with nitrogen gas for 30 min in a 100 ml three-neck round bottom flask. The reaction procedure followed similar way as mentioned above except that the precipitation time was maintained for 40 min. The sample is designated as MDG.

4.3.3 Catalytic activity

The reactivity of magnetite NPs in catalysing combustion of carbon was investigated by controlled combustion of a 4 mg mixture of Fe_3O_4 catalyst, carbon soot (collected by burning diesel), and α -alumina under dry air atmosphere. The measurements were carried out applying a sample with a ramp of $10^\circ\text{C min}^{-1}$ in $50\text{--}700^\circ\text{C}$ range. Standard α -alumina was used as reference. The sample for soot oxidation was prepared by mixing and grinding carbon, powdered Fe_3O_4 and alumina (average particle size ~ 450 nm, Condea Chemie, Germany) in the weight ratio 1:4:5 in an agate mortar. The inert alumina powder was added to prevent any thermal runaways.

Please refer chapter two for the chemicals used and the details of characterisation techniques adopted here.

4.4 Results and discussion

4.4.1 Magnetic powder characterisation

4.4.1.1 TEM characterisation

Magnetic nanocrystals were synthesised by ammonia precipitation technique in different alcohol-water mixed solvents at 40° and 80°C . All the as-synthesised IO powders were typically black in colour indicating the formation of magnetite crystals as the dominant phase. Selected bright-field TEM images, size distribution histograms depicting the mean size and its distribution, and SAED patterns of few representative magnetite specimens prepared in water as well as different alcohol-water solvents are shown in Fig. 4.1. Magnetite formation follows a crystallisation pathway involving the nanometer-sized intermediate primary particles that fuse to form the crystalline IO phase which grow

further to spheroidal particles of size ~ 10 nm on extending the reaction (Baumgartner *et al.*, 2013).

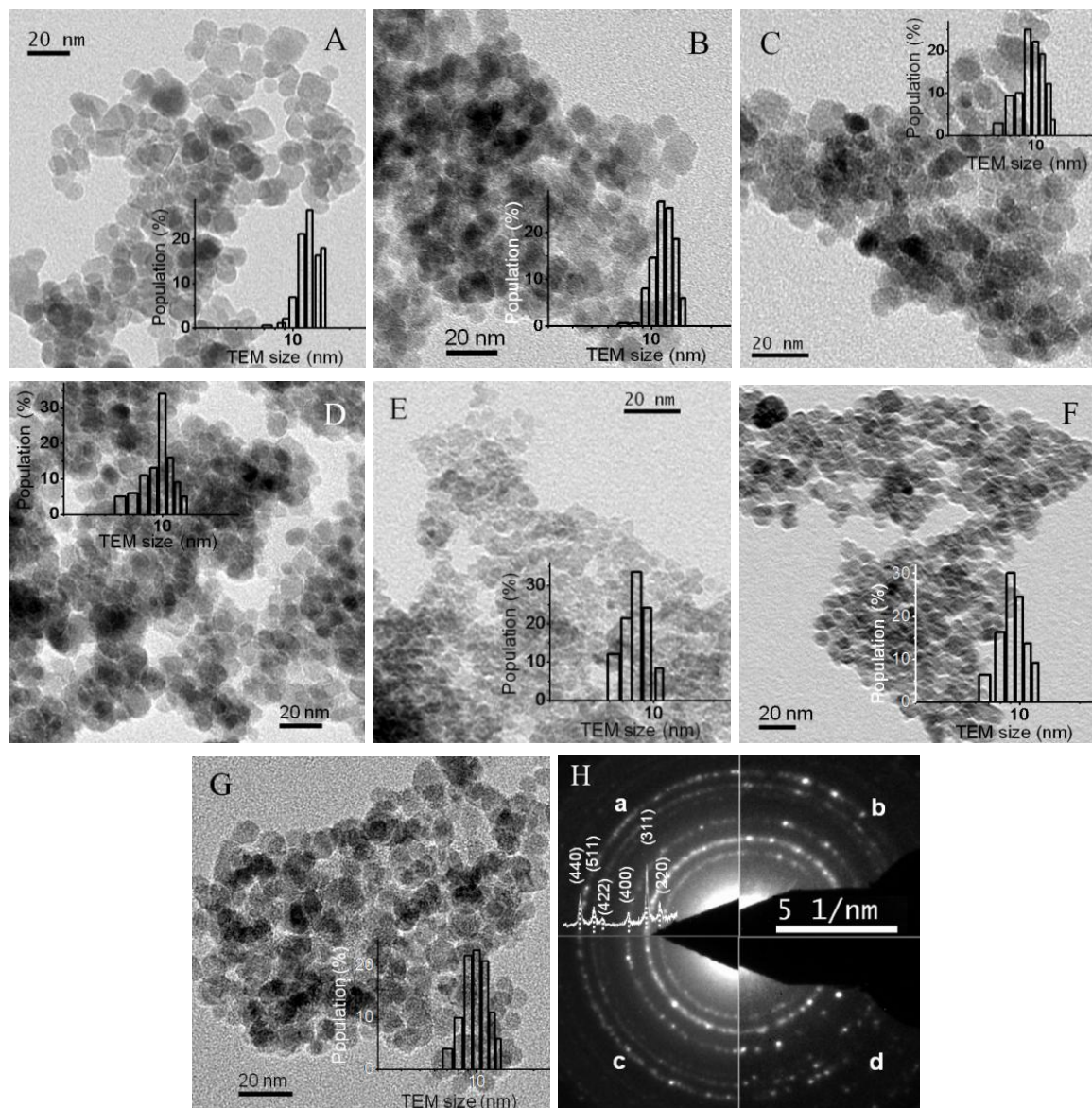


Fig. 4.1 TEM images of magnetite nanocrystals synthesised at 40°C in (A) water and different mixed solvents with (B) EA, (C) *n*PA, (D) IPA, (E) EG, (F) DEG and (G) PEG. The size distribution histograms of the corresponding nanocrystals for all the specimens are presented as inset to TEM images. (H) SAED patterns of (a) DEG and its matching the X-ray diffractogram with their (*hkl*) planes marked, (b) EG, (c) *n*PA and (d) PEG.

Average sizes were arrived from the inspection of multiple TEM images on 100–120 particles and is presented in Table 4.2. Relatively large spheroidal particles ca. $\sim 12.6 \pm 1.9$ nm was produced in water (panel A). When the reaction medium was changed to mixed solvents with mono- or poly-ol type of alcohols with appreciably lower dielectric constants, more or less polyhedral shaped smaller particles of average sizes in 8.28–10.4

nm range with solvents in the order EG < DEG < nPA ≈ IPA < PEG < EA < WA, were obtained. In alcohol–water solvents, the electrostatic attraction between initially precipitated primary particles is relatively low due to the lower dielectric constant of the solution. The possibility of primary particles to agglomerate and grow is thus drastically reduced. Therefore, monodisperse NPs with narrow size distribution can easily be obtained. In mixed solvents with poly-ols e.g., EG, DEG and PEG, no such trend was observed. Though 1:1 EG-water mix has the highest dielectric constant (58.95) among the solvents used in this work, next to water, it has produced smallest particles of average size 8.28 ± 1.22 nm. This is probably due to the presence of di-ol functional groups in this alcohol. High molecular weight poly-ols e.g., PEG, DEG etc. with high binding affinities to primary NPs act as surfactant and hinder the growth of particles by steric effect. From the TEM micrographs, it is difficult to comment on the degree of agglomeration among NPs synthesised from different alcohols. The standard deviation (σ) of size was minimum at ~ 1.3 nm for NPs from both EG (size 8.28 nm) and PEG (10.2 nm) followed by 1.53 nm in DEG (9.46 nm) whereas the same from water (12.6 nm) and EA (10.26 nm) were 1.9 nm and 1.67 nm respectively. So it is appropriate to conclude here that we are able to control the polydispersity by controlling the solvent characteristics. The size variation in magnetite crystals synthesised in different solvents suggests the strong dependence of crystal growth with dielectric constant of precipitating media. SAED patterns of DEG, EG, nPA, and PEG given in panel H show clear Debye–Scherrer rings for (220), (311), (400), (422), (511) and (440) planes with corresponding interplanar spacings 0.2967, 0.2532, 0.2099, 0.1715, 0.1616 and 0.1485 nm respectively matching the XRD pattern of DEG (JCPDS card no. 19-0629). In addition, the bright diffraction rings indicate that the NPs are well crystallised. The NPs synthesised at 80°C in the respective medium were grown into larger sizes (see Fig. 4.2). The mean size and its distribution of EG magnetite product have grown from 8.28 ± 1.22 nm to 9.18 ± 1.3 nm (EG80) as the precipitation temperature increased by two times. Similarly the average size for PEG and PEG80 were found to be 10.2 ± 1.34 and 12.8 ± 1.5 nm respectively. The elemental composition of Fe₃O₄ specimens was done by EDAX. The peaks characteristic to ‘O’ and Fe-atoms were observed in the EDAX spectrum along with signals from C and Cu, the latter two belong to carbon coated copper TEM grid (inset of Fig. 4.2C). The atomic ratio of Fe to O from the EDS spectrum is 3:6.2 which is slightly oxygen rich due to the presence of hydroxyls

compared to that in stoichiometric magnetite (3:4). It may be due to the surface OH group associated with under co-ordinated Fe atoms at the NPs surfaces and edges.

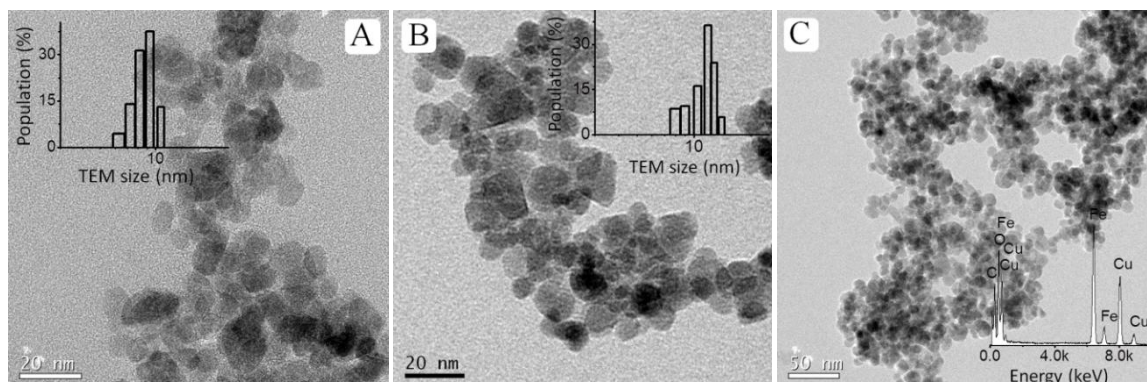


Fig. 4.2 TEM image of (A) EG and (B and C) PEG magnetite precipitated at 80°C. Inset is the size distribution of respective sample and EDS pattern of PEG originates from the carbon-coated copper grid.

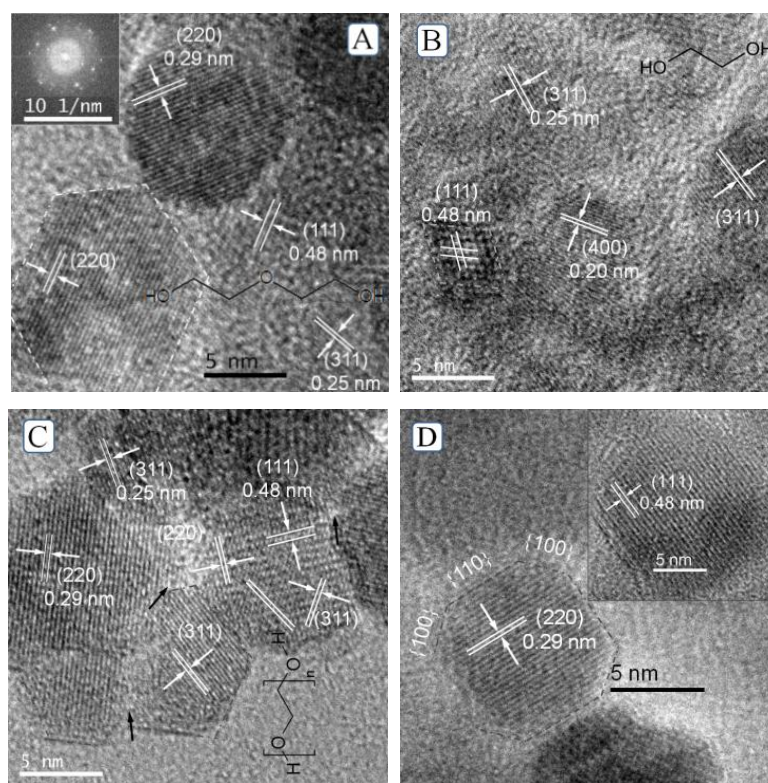


Fig. 4.3 HR-TEM images of magnetite nanocrystals fabricated in (A) DEG with its fast Fourier transform, (B) EG, (C) PEG and (D) *n*PA (inset is another magnified crystal). The corresponding polyol structures are also shown as insets in respective figures. Point defects in the nanocrystals are marked with black arrow heads in (C).

Clustering observed in TEM micrographs is attributed partly to the drying artefact on the TEM grid. The most important contributor to the formation of clusters is the interfacial and magnetic interactions among NPs and tendency to reduce the high surface free energy by clustering. The effect of induction of surface hydration and electric double layer over

MNP surface due to the mono/poly-ol mediated process on the state of clustering/growth of NPs is investigated by PCS in a later section.

Representative HR-TEM images of selected magnetite specimens with different projections are provided in Fig. 4.3. Fourier filtering was used to extract the lattice fringe information. The crystals resemble elongated hexagonal (panel A), beveled cubes (2D) and two-dimensional projected contours (Liang *et al.*, 2015). Various projected shapes can result when the NP is viewed along different crystallographic directions (Liang *et al.*, 2015). Although the particles shown in Fig. 4.3 are different in shape, all of them are enclosed with three low-energy {100}, {110} and {111} surfaces. Careful examination of the HR images indicates that all the NPs are indeed single crystals and fringes belonging to predominant (111), (220), (311) and (400) planes with corresponding d -spacings 0.4852, 0.2967, 0.2532 and 0.2099 nm could be identified. Point defects due to missing atoms or local deformation are observed on the nanocrystal surfaces in some instances, these are marked by arrow heads in Fig. 4.3C. The NPs have no apparent porosity with well-defined crystalline structures.

4.4.1.2 XRD analysis

The X-ray profiles of the magnetic products synthesised from mixed solvents of different ‘ ε ’ and temperatures are shown in Fig. 4.4. The diffraction patterns for all the powder samples show peaks for magnetite.

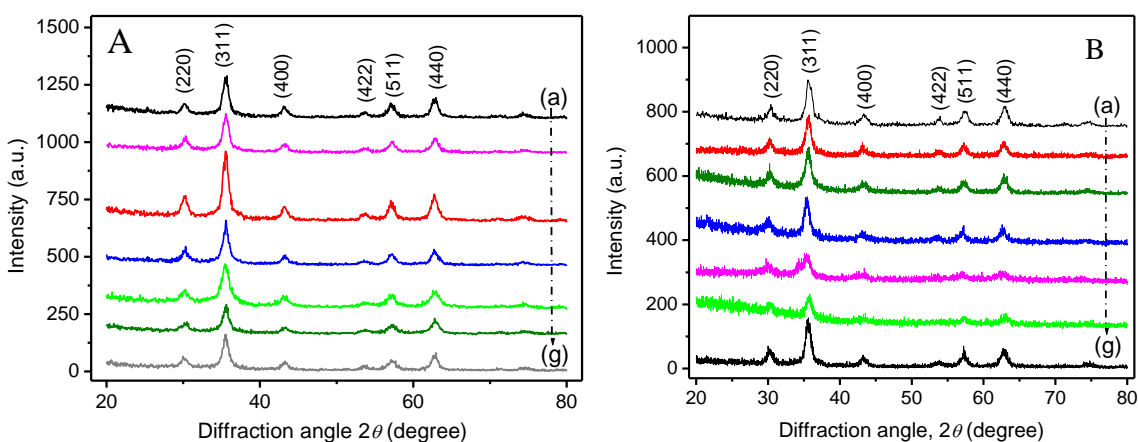


Fig. 4.4 (A) XRD patterns of magnetite crystals fabricated at (A) 40°C and (B) 80°C in a mixed solvents (a) WA, (b) EA, (c) *n*PA, (d) IPA, (e) EG, (f) DEG and (g) PEG.

The position and relative intensity of all diffraction peaks matched well with the characteristic finger-print reflections of standard Fe_3O_4 with cubic fluorite structure (JCPDS 19-0629) having space group $Fd\bar{3}m$ (227). The X-ray peaks in the EG/water

system are much broader than those in the other solvents. This is obviously due to the smallest particles produced in the EG/water system. The crystallite size was estimated using the width of (311) reflection, employing Debye–Scherrer equation (eqn 2.14). The crystal sizes are in 7.5–10 nm range and the results are shown in Table 4.2.

Table 4.2 Physical size, crystallite size and surface areal size of magnetite synthesised from mixed solvents of different dielectric constant at different temperatures

Sample/ ϵ (Furniss <i>et al.</i> , 1978)	$D_{\text{TEM}}@40^{\circ}\text{C}$ (nm) \pm SD	$D_{\text{XRD}}@40^{\circ}\text{C}$ (nm)	$D_{\text{BET}}@40^{\circ}\text{C}$ (nm)	$D_{\text{XRD}}@80^{\circ}\text{C}$ (nm)
WA/80.2	12.6 \pm 1.9	9.87	11.92	12.45
EA/52.4	10.26 \pm 1.67	9.72	10.33	11.12
<i>n</i> PA/50.25	9.93 \pm 1.45	9.69	13.71	11.86
IPA/50.05	10.03 \pm 1.48	9.59	10.31	12.03
EG/58.95	8.28 \pm 1.22	7.45	6.34	9.81
DEG/55.95	9.46 \pm 1.53	8.31	8.96	10.69
PEG/46.3	10.2 \pm 1.34	9.37	10.11	11.64

CI for WA is 91%, and it decreased to ~79% in EG and the same increased to 95% while increasing the precipitation temperature to 80°C. The average crystallite size grows with improved crystallinity while increasing reaction temperature in spite of the decrease in ϵ of the reaction medium at higher temperatures.

Table 4.3 Crystallinity indices (%) of synthetic magnetite precipitated at different temperatures

Solvent	CI (%)	
	40°C	80°C
WA	91.30	95.45
EA	82.13	88.57
<i>n</i> PA	84.89	83.87
IPA	88.92	88.88
EG	78.88	77.64
DEG	82.64	89.88
PEG	81.63	87.57

In many cases $D_{\text{XRD}} < D_{\text{TEM}}$, as D_{XRD} calculated employing Scherrer equation ignores broadening of the diffraction peaks due to the microstrain in the lattice. X-ray does not

often involve the amorphous layer on the magnetite NP surface (Iyengar *et al.*, 2014). The crystallinity indices (CI), as obtained from the XRD patterns of the nanocrystals precipitated at 40°, 80°C are in ~78-95% range, indicating reasonably high crystallinity (Table 4.3).

Standard Harris analysis (Fig. 4.5) on the XRD patterns confirmed that the nanocrystals synthesised from alcohol medium has proportionately higher active crystal facets while compared to the same from pure aqueous media. The texture coefficient data indicates that aqueous medium produced magnetite crystals with minimum exposed active (220) facet. Preferentially grown active {110} and {100} planes to texture coefficient values in the range 1.1 to 1.3 were obtained in all the alcohol solvents with the highest being ~1.3 in EG, DEG and PEG by inhibiting the growth of (311) and (511) crystal facets.

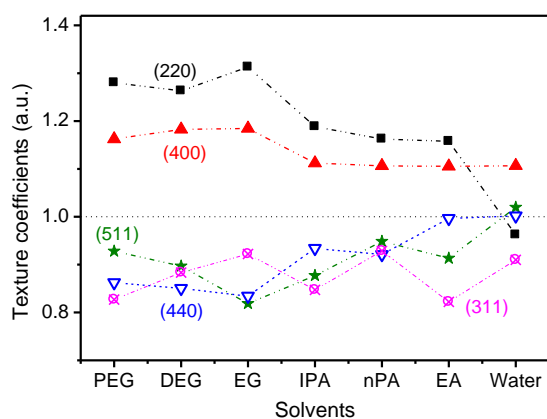


Fig 4.5 Calculated texture coefficients for the magnetite synthesised at 40°C.

We now note that aqueous precipitated magnetite in presence of PEG shows well developed and predominant {100} surfaces (T_C 1.163) as reported earlier (Liang *et al.*, 2015). Hence this study opens a ‘conceptual’ possibility of producing nanocrystals in alcohol-water medium with predominant active facets which may improve the physicochemical properties of the material and allows a superior performance.

4.4.1.3 Magnetic property

Fe_3O_4 nanocrystals are ‘soft’ magnetic materials, in the sense that they quickly switch magnetisation direction once the external magnetic field is reversed. This fact is experimentally shown with the help of VSM in Fig. 4.6. It is evident that all the specimens behaved ferromagnetic at room temperature (~300 K) with the hysteresis loops showing M_S , M_R and H_C and a comparison of these with the bulk (Dar and Shivashankar, 2014) is given in Table 4.4. The saturation magnetisation achieved are ~66, 68, 69 $emu.g^{-1}$ in EA,

IPA, nPA respectively and the M_S for the rest was clustered at $\sim 60 \text{ emu.g}^{-1}$ of sample. The obtained M_S values were lower than the reported value for bulk which is sufficient enough for biomedical applications. Such reductions may be the result of spin canting due to spin frustration and lattice strain in small particles manifested at the particle's surface preventing the co-linear spin arrangement on the A and B sub-lattices of the spinel magnetite (AB_2O_4) structure (Coey, 1971; Bødker *et al.*, 1994; Cornell and Schwertmann, 1996). This effect would become dominant with decreasing particle size. All the Fe_3O_4 specimens have significant coercivity (H_C , reverse field required to reduce M_R to zero) in the range 187–197 Oe and the M_R to the tune of $\sim 12\text{--}14 \text{ emu.g}^{-1}$ (inset of Fig. 4.6) except the pure magnetite produced in water showing negligible coercive field (3.95 Oe), M_R value (0.74 emu.g^{-1}) and a smaller M_S value (57 emu.g^{-1}).

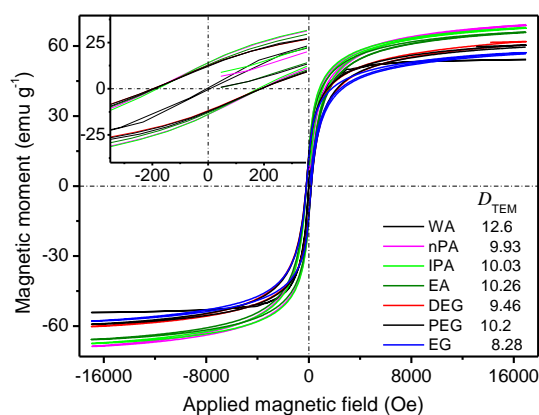


Fig. 4.6 Room temperature magnetisation studies on the magnetite powders synthesised at 40°C as a function magnetic field (up to 1.7 Tesla). Inset (left top) shows the respective zoomed hysteresis curves.

The reported coercive field for bulk magnetite is 115–150 Oe. In general, the enhancement in coercivity and reduction in M_S could be due to increased magnetite interparticle distance concomitant with a weaker dipolar interaction and other surface effects, which can be pronounced under certain conditions in the nano-regime (Guo *et al.*, 2008). An alternative explanation for the increase of the coercivity of the NPs, produced in alcohols with different polarity, comes from the stronger obstacles when the domains of magnetite try to turn under an applied field (Wu *et al.*, 2004). When the magnetite NPs are limited and entrenched in the left-over alcohol/glycol, can be considered as pinned. Since the hysteresis loops of the samples are sensitive to crystal size, they are useful for magnetic grain sizing of natural samples (Ghosh, 2006). High H_C in IO is largely governed by magnetocrystalline, shape, and magnetostrictive (stress-induced) anisotropy along with polycrystallinity (multi-domain nature) factor which further depends on the

local magnetic anisotropy and ferromagnetic exchange energy. The ferromagnetic exchange interaction is reported to determine the magnetic behaviour of the smaller crystals (Dar and Shivashankar, 2014).

Table 4.4 Detailed VSM analysis of magnetite powder at 300 K

Sample/ ε	M_S (emu.g ⁻¹)	M_R (emu.g ⁻¹)	H_C (Oe)
Bulk	84		115-150
WA/80.2	57.1	0.74	3.95
EA/52.4	65.82	13.0	188.2
nPA/50.25	68.79	14.1	187.2
IPA/50.05	67.62	14.2	180.3
DEG/55.95	61.89	12.4	195.5
PEG/46.3	60.33	12.5	197.2
EG/58.95	57.12	12.2	191.5

High H_C due to polycrystallinity is ruled out in our study as the D_{XRD} calculated from the X-ray peak broadening (Scherrer equation) $\leq D_{TEM}$ (Table 4.2). Furthermore, we have already established from the HR-TEM images (Fig. 4.3) that the NPs synthesised from all the solvents are single crystals. Compared to mono-ol solvent systems, the particles from poly-ol are relatively smaller and as the particle size decreases, the remanance decreases indicating “single domain” behaviour in the MNPs.

4.4.1.4 BET surface area analysis

The BET adsorption-desorption isotherms for all the specimens showed hysteresis loops of type IV of Brunauer’s classification, with an apparent hysteresis loop in the range 0–0.89 P/P₀, indicating the presence of mesopores (Fig. 4.7). The pores in the materials are in the mesoporous range (3.6–9.5 nm) and are interparticulate in nature. The magnetite products show relatively high surface areas (84–183 m².g⁻¹), as expected from their small particle sizes. The magnetite synthesised from alcohol mediated precipitation shows higher surface area (114-183 m².g⁻¹) when compared to aqueous product (84 m².g⁻¹). The size (D_{BET}) estimated from the nitrogen adsorption-desorption isotherms is somewhat larger than the size estimated from TEM (Table 4.2) for all except the crystals derived from EG, DEG and PEG solvents.

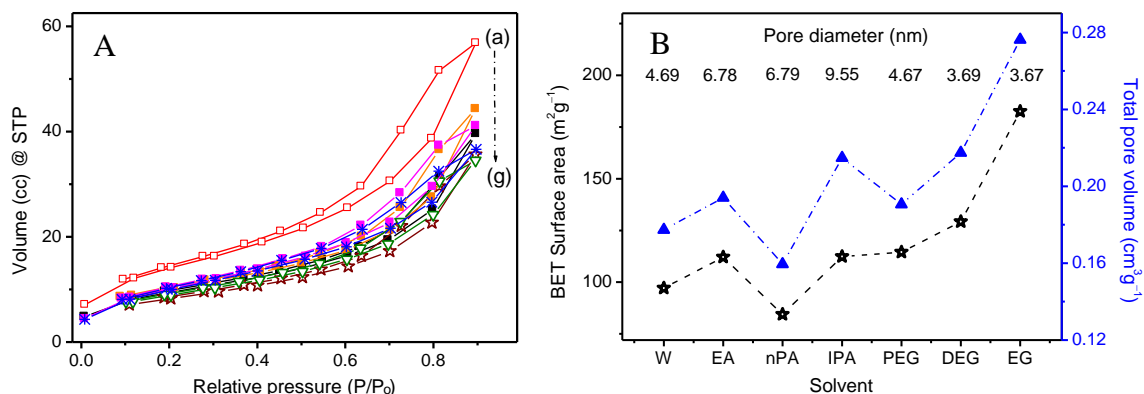


Fig 4.7 (A) BET adsorption-desorption isotherms for magnetite powders (a) EA, (b) IPA, (c) DEG, (d) W, (e) EG, (f) nPA, (g) PEG and (B) Surface area and total pore volume of the sample plotted against the corresponding solvents. Pore diameter mentioned as text.

Therefore, the particle size and surface area of MNPs can be tuned by changing the dielectric constant of reaction medium by selecting different alcohols.

4.4.1.5 Surface chemistry

FTIR spectra on dried magnetite specimens were taken at room temperature to ensure the structural aspects, attachment and interaction of the alcohol/glycol molecules with magnetite.

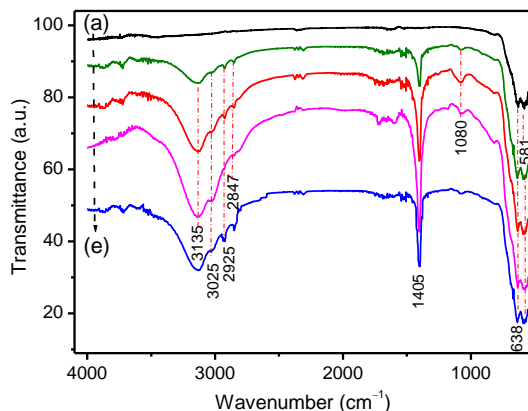


Fig. 4.8 FTIR spectra of magnetite powder (a) WA, (b) DEG, (c) PEG, (d) EA and (e) EG precipitated at 40°C.

Figure 4.8 shows the interaction of dried magnetite NPs obtained with poly-ol (EG, DEG & PEG)/ molo-ol as confirmed by FTIR spectra. The intense characteristic absorption bands of MNPs at 638 and 581 cm⁻¹ in all samples are attributed to Fe³⁺/ Fe²⁺-O₂ of tetrahedral and octahedral sites respectively in the spinel structure of Fe₃O₄ (Andrade *et al.*, 2009). Sharp absorption bands are also observed at 3135, 1405, 638 and 581 cm⁻¹ when compared to pure magnetite. Furthermore, the strong and broad OH stretching mode centred at 3135 cm⁻¹ in the case of EG, DEG, PEG and EA NPs confirms the presence of

corresponding alcohol/glycol on the surface, which provided a hydrophilic component to NPs, increasing their water solubility (Ebrahiminezhad *et al.*, 2012). Therefore, the FT-IR spectra showed the existence of vdW interactions between the chain of glycol/ethanol and MNPs and this is the reason for high aqueous dispersibility (Gupta *et al.*, 2010). The exposed hydroxyl groups also present the possibility for further functionalisation or binding with bioligands for biomedical applications.

4.4.2 Colloidal properties of aqueous ferrofluids

4.4.2.1 Hydrodynamic size and surface charge measurements

The crystalline non-agglomerated water dispersible magnetite NPs by alcohol mediated syntheses are attractive because they are readily dispersible in water using low energy ultrasonication and are able to form transparent colloidal suspension at ambient conditions. The hydrodynamic size, zeta potential, suspension stability, and optical photographs of the aqueous suspensions of magnetite nanocrystals (concentration 4.3 mM, slightly acidic pH) are illustrated in Fig. 4.9.

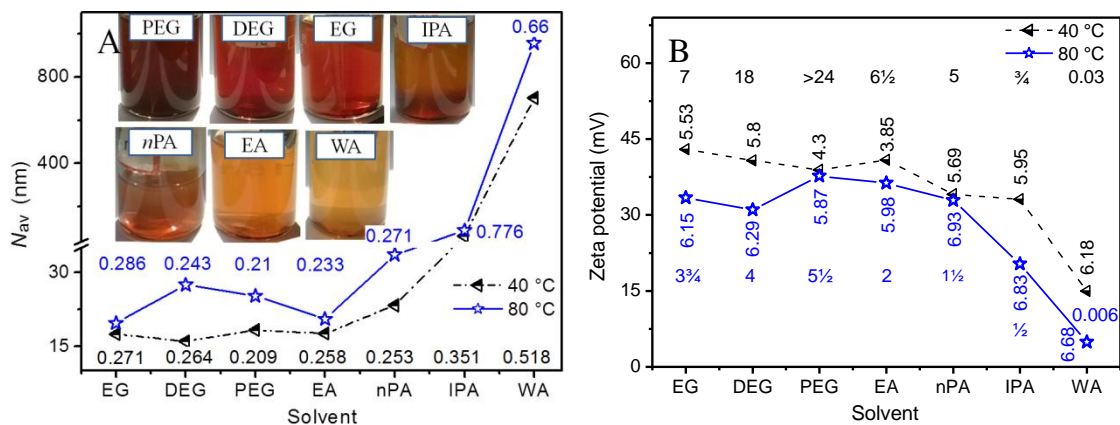


Fig. 4.9 (A) Hydrodynamic sizes and the corresponding PDI and (B) zeta potential as well as their stability (horizontal numeric) of the magnetite suspensions at their natural pH (vertical numeric), synthesised at 40° and 80°C in different alcohol-water mixed solvents. The optical images of the freshly prepared dispersions in water are shown as inset of panel A.

The number average size (N_{av}) of 16-33 nm in 40° and 80°C precipitated powders, except in water and IPA/water system, is ~2-3 times larger than its primary particles observed in the TEM (see Fig. 4.9 and Table 4.4). This is due to possibly tetrahedral or hexagonal close-packed assemblies of ~10 nm particles in suspension. The N_{av} is reliable as the PDI values are below 0.3, in most cases, indicative of narrow and monodisperse size distribution (Iyengar *et al.*, 2014). These aqueous magnetite fluids may find use in various growing *in vivo* biomedical applications. The colloidal stability of the NPs is closely

related to their surface chemistry. The average ζ -values are in the 20-43 mV range among which IPA has the least zeta potential, EG has the highest (43 mV) for poly-ol mixed solvents followed by EA (40.9 mV), highest among the mono-ol solvents (Fig. 4.9B and Table 4.5). The alcohol moieties behave slightly acidic when Fe_3O_4 crystals (IEP at pH ~ 6.7) are suspended in it and the suspension exhibits positive zeta potential due to positive surface charge over nanocrystal surfaces. The strong repulsive forces (electrostatic) among the particles counteract the attractive forces due to magnetic interaction and vdW attractive forces and prevent consequent clustering though the measurements were carried out at their natural pH (6–7) where no electrostatic repulsion is expected. The strong electrostatic repulsive forces can be elucidated by analysing the energy barrier for aggregation between two approaching particles based on DLVO theory which can be described as:

$$Vb = -\frac{A\kappa\alpha}{12} + 2\pi\epsilon\alpha\psi^2 \quad (4.2)$$

where α the particle diameter, ϵ the dielectric constant of the solution, and ψ the surface potential. The effective Hamaker A and Debye-Hückel parameter κ remain constants in our experimental conditions. So it is evident that the energy barrier Vb , largely depends on the dielectric constant of the medium.

It is interesting to note that the products of 40°C are easily dispersible and its colloidal stability is much higher than those produced at 80°C (Fig. 4.9). It is due to strong positive surface charge as indicated by the high zeta potential at their natural pH ~ 3.8 – 5.9 away from PZC (see Fig. 4.12). The narrow size distribution and the corresponding normalised single exponential decay of self-correlation coefficient for all MNP clusters produced at 40°C support the monodisperse nature especially for the poly-ol based MNPs (Fig. 4.10). EG, DEG, PEG, EA, *n*PA dispersions were found to have narrow size distribution which implies good stability whereas relatively less stable dispersions produced broader distribution due to aggregation (in the case of WA and IPA). PEG dispersion (D_{TEM} 10.2 nm) is very stable without any precipitation even after 6 months of storage. IPA slurry, with slightly smaller D_{TEM} size (10.03 nm) and higher CI, PDI as well as least ζ -potential next to water, precipitates completely in 5 days. This suggests that an additional mechanism i.e., steric effect in addition electrostatic stabilisation process (indicated by ζ -value of ~ 38 mV) is introduced by PEG chains (Masoudi *et al.*, 2012). Similar phenomenon was observed with the EG and DEG, but the suspension was stable

for 7 and 18 weeks respectively due to poorer stabilising efficiency of mono, di-ethylene glycol compared to the same of PEG and their Z_{av} sizes are slightly larger (Table 4.5).

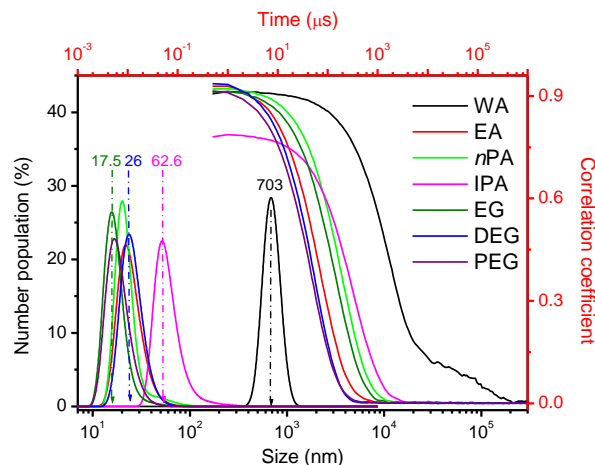


Fig. 4.10 The number size distribution profiles and its normalised self-correlation coefficient (correlograms) of the magnetite NPs synthesised at 40°C from the PCS measurement.

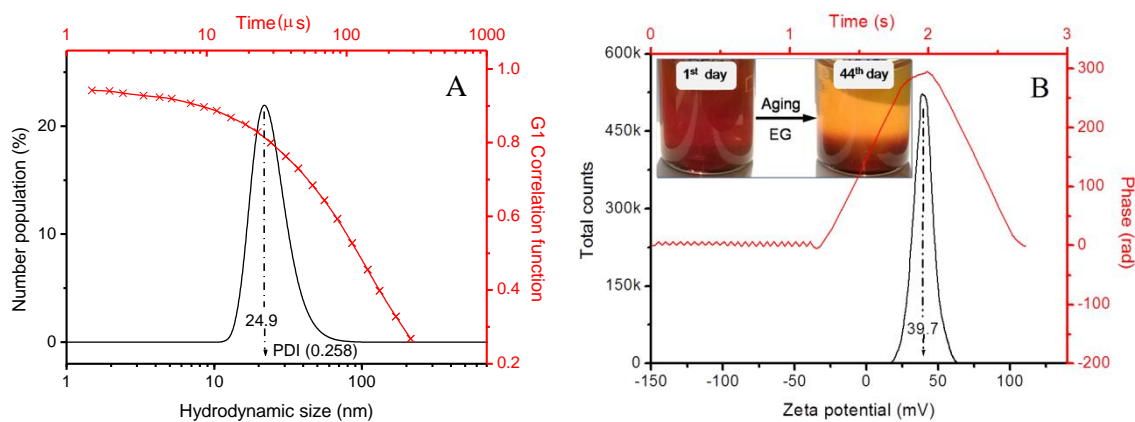


Fig. 4.11. (A) Hydrodynamic size plot along with the correlation data and (B) zeta potential graph with its phase plot for the EA dispersion in water. Inset is the colour gradient formed after incubation of EG for 44 days.

EA colloids did not sediment over 6½ weeks probably because of the electrostatic (higher ζ -potential ~40 mV) as well as steric effects and the interaction was supported by FTIR (Fig. 4.8). The PCS size along with the correlation fits and zeta potential data of one of the representative specimens (EA) are given in Fig. 4.11. Z_{av} size of ~25 nm with relatively low PDI value 0.252 is extracted from the good Cumulants fit to the auto-correlation function of the intensity fluctuations of scattered photons. The phase plot of this sample is excellent (Panel B in Fig. 4.11). Magnetite particles with interfacial and even magnetic interactions (due to their small remanence) are also reported to support the clustering process (Gittings and Saville, 1998) which contributes to the formation of fractal

aggregates (Ghosh, 2006) with large sediment volumes. With time, when the loose aggregates reach some critical size, the thermal motion is not able to hold them in suspension causing initiation of the sedimentation process. With time, large aggregates drag smaller particles with them, and create a significant depletion of nanometer-sized magnetite in the supernatant (Viota *et al.*, 2007) forming a colour gradient with which a clear colourless fluid zone at the top and gradual increase in colour intensity to the bottom. This phenomena was observed in all the mono- and poly-ol mediated nanocrystal slurries (optical photographs for EG are shown as inset of Fig. 4.11). As expected the aqueous suspension of bare MNPs (WA80 and WA) produced in water medium, have the least surface charge of 4.9 and 15 mV respectively with highly polydisperse nature ($PDI > 0.5$) and do not show any colloidal stability (precipitated within couple of hours of suspending). There is $-\text{OH}_2^+$ ions on the surface of bare NPs at $\text{pH} \sim 7$ in the vicinity of the isoelectric point of synthetic magnetite and the suspension is normally not stable (Mahmoudi *et al.*, 2011). Higher stability of bare MNP suspension may also be achieved at $\text{pH} > 10$, when ζ reaches almost a plateau in the ζ versus pH profile (Fig. 4.12).

4.4.2.2 pH dependent surface charge measurement

It once again consolidates the fact that the higher ζ -potential in a nanofluid confers greater colloidal stability. The zero charges on the surface of WA, nPA, PEG and EA magnetite were found to be at pH 6.9, 6.46, 6.47 and 6.4 respectively. Though the natural pH of glycol/alcohol mediated MNPs varies slightly from the water mediated NPs, the behaviour of zeta curves for all are almost same in the acidic to basic pH range (Fig. 4.12).

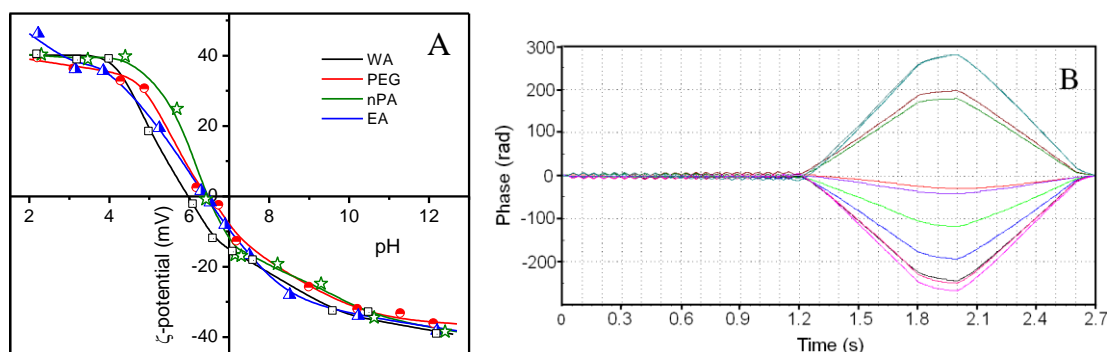


Fig. 4.12 (A) Variations in the zeta potentials of synthetic magnetite dispersion in Millipore water are shown as a function of the pH of the surrounding medium and (B) the associated phase changes.

This leads to the confirmation that magnetite MNP surface properties are unaltered irrespective of the synthetic media. The increase in particle size with increase in the

dielectric constant of the precipitating solvent is due to enhanced hydrogen bonding. The role of increased precipitation temperature and dielectric constant of solvents are: (1) the crystallinity and particle size of MNPs increase and colloidal stability in aqueous phase decreases; (2) increased precipitation temperature decreases the density of surface adsorbed alcoholic moieties thus causing poorer suspension stability. Glycol medium produced MNPs with narrow size distribution, as observed from D_{TEM} , which might have helped in producing stable suspension comparable to that in mono-ol medium and pure water at 40°C. EG dispersion is almost transparent and remains homogeneous without any visible precipitation or creaming.

4.4.2.3 Temperature dependent hydrodynamic properties

4.4.2.3.1 PEG based colloids

Figure 4.13 shows the temperature dependent hydrodynamic properties of PEG based colloid. The hydrodynamic size of 33.3 nm grew to 38.2 nm from 20° to 35°C, remains almost constant upto 45°C and then decreased back to 33.1 nm when the temperature was further increased to 65°C but interestingly N_{av} (number average) ~18 nm remains the same. As expected the concomitant change in mean count with Z_{av} may be due to the change in aggregate sizes. The increase in size and mean photon counts till 45°C may be due to slight transformation of cluster structure from initial hexagonal ($3 \times D_{\text{TEM}}$) to one-shell octahedral close-packed ($4 \times D_{\text{TEM}}$) and back to the hexagonal at ~65°C.

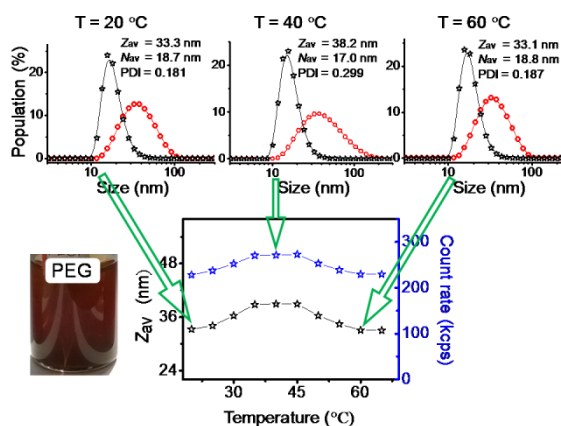


Fig. 4.13 The temperature dependent PEG agglomerate size in suspension by photon correlation spectroscopic study. Optical image of the PEG suspension is shown as inset.

The poly-ol (PEG, DEG and EG) mediated MNC based colloids are stable, do not grow and precipitate (all data not presented here) over 6-24 weeks as a function of temperature (up to 65°C). However, these colloids exhibited gradual size growth by 15-25% on

dilution (up to $\times 10$) due to partial desorption of the chemisorbed poly-ols, and hence are activated with respect to interaction with other NPs or NPCs (Stolarczyk *et al.*, 2009).

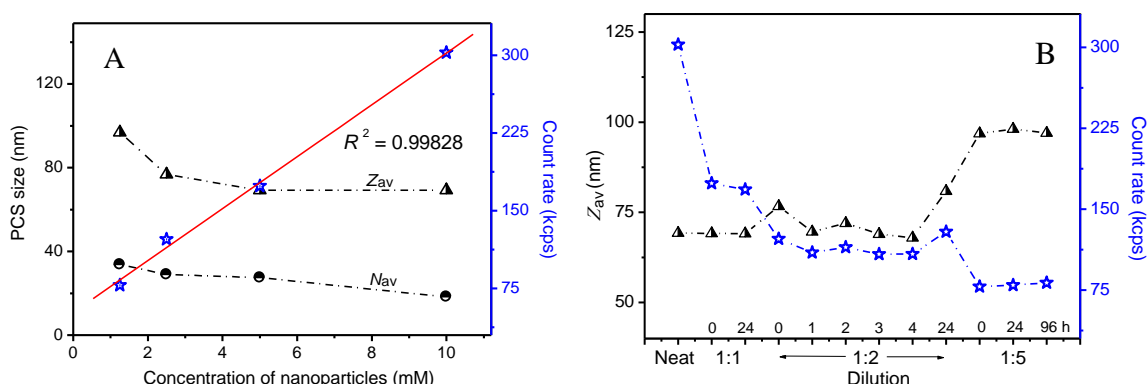


Fig. 4.14 The hydrodynamic size examined at various concentrations with mean count rate (A) immediately after dilutions and (B) the colloidal stability as a function of time for MNPs PEG suspension.

As anticipated, DLS data indicated a slight increase in hydrodynamic size of particles with steady decreasing count rate for PEG immediately after dilutions. A good linear relationship ($R^2 = 0.9983$) was observed between the count rate and NPs concentration in the range of 10–1.25 mM (Fig. 4.14).

4.4.2.3.2 DEG based colloids

Ageing studies

The colloidal property of ferrofluid was monitored while ageing by performing hydrodynamic size and turbidity (transmittance of visible light) measurement over a time period of 18 weeks and is presented in Fig. 4.15. The measured D_{PCS} value ~ 25 nm remained almost constant upto 100 days followed by slight increase to ~ 30 nm after 128 days with reasonable increase in photon count rate.

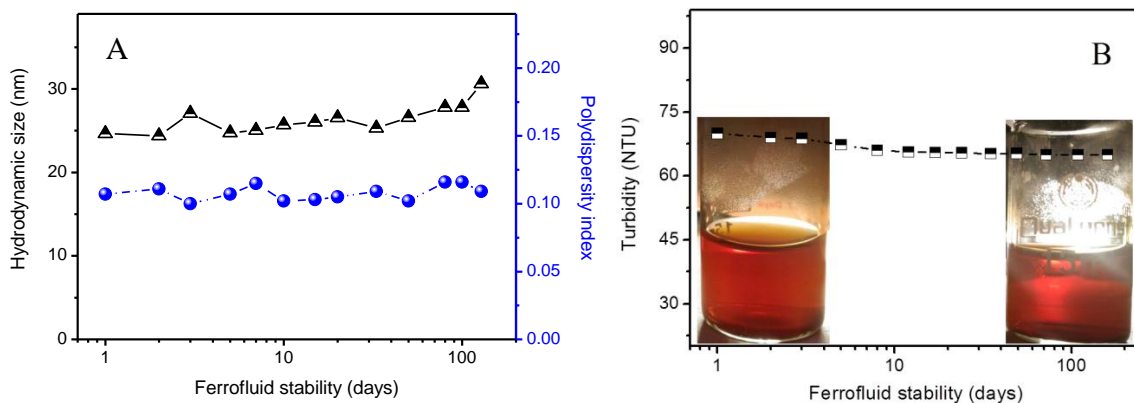


Fig. 4.15 Colloidal stability in terms of (A) hydrodynamic size and PDI from light scattering technique, and (B) turbidity on surface treated magnetite (MDG) ferrofluids against time at 25°C.

The PDI value of 0.1-0.116 strongly suggests the monodispersed nature of Fe_3O_4 NPs in suspension. The visible light transmittance increased slightly from initial 65 to ~ 70 NTU during 128 days of ageing. So the MDG nanofluids surpassed the stability of \sim a month reported for aqueous dodecanoic acid double layer stabilised magnetitic fluids (Ramimoghadam *et al.*, 2015), and glutathione stabilised Fe_3O_4 -Ag heterodimer (Jiang *et al.*, 2008), and couple of weeks for citrate/tartarate stabilised magnetic nanofluid (Goloverda *et al.*, 2009).

The particle size distribution and zeta potential as a function of pH of MDG ferrofluid on storage as measured by PCS are shown in Fig. 4.16. The hydrodynamic size of MDG was estimated as 24.7 nm with unimodal narrow size distribution of clusters for all the measurements at different point of time. This is due to probably self-assemblies (loose clusters) of four Fe_3O_4 particles of ~ 10.3 nm size as observed from TEM observation in a tetrahedral fashion (inset of Fig 4.16A). The average sizes of the same suspension after 7, 20 and 128 days are 25.1, 26.6 and 30.6 nm respectively. To further understand the stability of the suspension, the study of electrophoretic behavior through measurement of ζ -potential has been adopted. It is well known that stable suspensions have ζ -potential value beyond ± 30 mV (Yoon *et al.*, 2016).

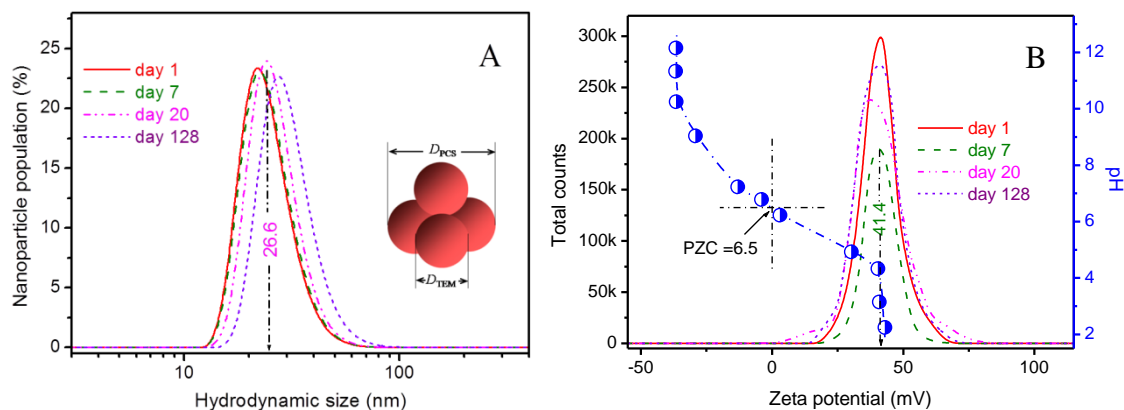


Fig. 4.16 Effect of ageing time on (A) size distribution and its (B) zeta potential of magnetite ferrofluid measured by PCS technique. Inset in ‘A’ is loose clusters of NPs indicating the PCS size.

There is a small rise in the average size (25 to 30 nm) with the ζ -potential remaining almost constant (41.4 to 40.3 mV) with ageing time indicating that a small degree of agglomeration. So the magnetite based nanofluid exhibits excellent stability at room temperature even after 128 days without changing their appearance. This dispersion

exhibited ζ -values from +43.3 to -36.3 mV in the wide pH range of 2.2 to 12.2 and the point of zero surface charge for this ferrofluid is pH 6.5 (Fig. 4.16B).

To demonstrate the effect same concentration as it influences the particle size in dispersion, three different concentrations 2.15, 0.7 and 0.36 mM of ferrofluids were prepared. It can be surmised that employing diethylene glycol as a surfactant cum solvent during nanoparticle nucleation and growth confers a high degree of stability to its suspension so that 520 G bar magnet (Fig. 4.17) is not able to cause precipitation (Douglas *et al.*, 2012).

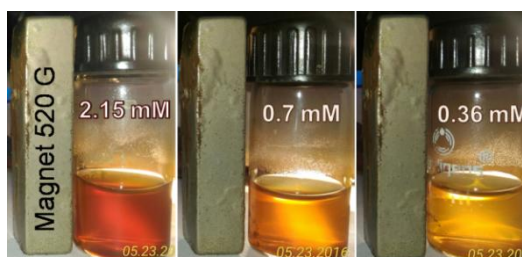


Fig. 4.17 The optical micrograph of as-prepared aqueous MDG ferrofluid upon application of an external magnetic field for ~10 min.

Glycol has strong affinity to the metal cations (Torres-Diaz and Rinaldi, 2014). The stability of all of these ferrofluid over temperature was evaluated by determining changes in hydrodynamic diameter and demonstrated in the following sections.

MDG: 2.15 mM colloids

To demonstrate the effect of heating, hydrodynamic diameter was evaluated on the ferrofluids at different temperatures in the range 20–65°C. Interestingly, small nano-clusters were observed in the dispersion and its uniformity was obvious from the PDI.

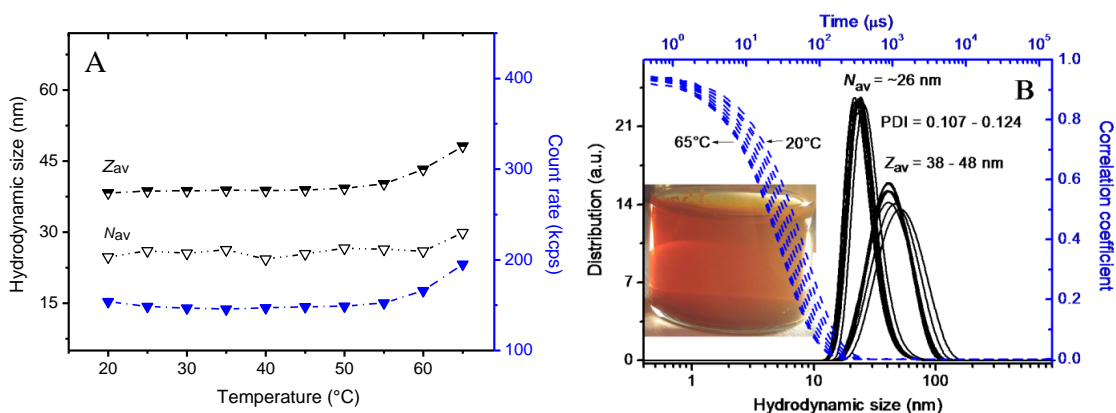


Fig. 4.18 PCS data on 2.15 mM MDG suspension with (A) hydrodynamic size and (B) its intensity and number-based size distribution along with raw correlograms (blue line) exposed to 20–65°C

Figure 4.18 shows the average hydrodynamic sizes, its distribution profiles along with their raw correlograms of the 2.15 mM Fe_3O_4 fluid exposed to different temperatures. The size (Z_{av} diameter) of the nanoparticle clusters was continuously monitored using Malvern NanoZS light spectrometer until the temperature reached 65°C. The majority (>99%) of the particles in the sample was 25 nm due to the presence of tetrahedral assemblies ($\sim 2.5 \times D_{\text{TEM}}$) and very few (0.01%) of them were large at 38 nm with overall PDI of 0.107 at 20°C. PDI_{TEM} is slightly larger (0.146) than the PDI from the light scattering technique, as TEM images include all sizes from small individual particles to large clusters. The low and very close PDI values (0.107–0.124) clearly indicate the presence of a single population of hydrated particles. The D_{PCS} and its distribution remain almost the same up to the temperature 40°C and gradually increased to ~ 30 nm at 65°C. During the small size increase while increasing the ferrofluid temperature from 20° to 65°C, the signal correlation dropped to zero after ~ 400 to 200 μs and is due to the decrease in viscosity of water from 1.003 cP at 20°C to 0.4379 cP at 65°C. The perfect parallel correlograms indicate the uniformity of distribution of clusters in suspension. So the conclusion from the temperature trend is that the MDG slurry is stable without any further clustering even at relatively higher temperatures.

MDG: 0.7 mM colloids

The ferrofluid of 3 times dilution on 2.15 mM concentration, the average hydrodynamic size decreased from ~ 30 to 13 nm while increasing the temperature to 65°C with the PDI of 0.158 (Fig. 4.19). It is notified that the dilution caused slight increment in size by ~ 5 nm as well as PDI value ~ 0.159 at 20°C compared to 2.15 mM nanofluid.

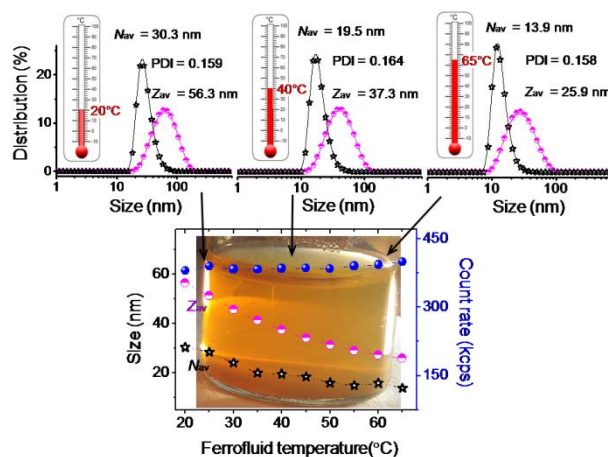


Fig. 4.19 The hydrodynamic size of 0.7 mM aqueous ferrofluids when exposure to different temperatures plotted against count rate and the corresponding size distribution at 20°, 40°, 65°C (top portion) by light scattering method.

While increasing the temperature, the $D_{\text{PCS}} \sim 30.3$ nm hexagonal close packed NP clusters (at 20°C) became $D_{\text{PCS}} \sim 19.52$ nm tetrahedral (at 40°C) followed by single primary NPs $D_{\text{PCS}} \sim 13.9$ nm (at 65°C) in aqueous medium (Fig. 4.20). The hydrodynamic size ($D_{\text{PCS}}=13.9$ nm) was achieved in this concentration at 65°C without any apparent NP clusters.

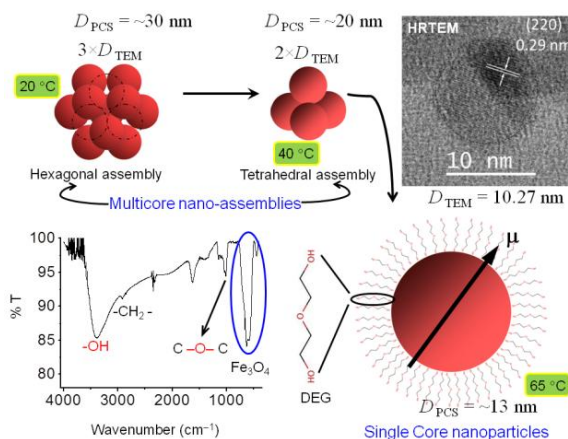


Fig. 4.20 The scheme for the magnetite nano-assemblies in the dispersion of 1:2 dilutions of figure 4.19 at 20°, 40°, 65°C and FTIR spectra on powder sample

D_{PCS} is larger than D_{mag} (11.7 nm) determined magnetically, suggesting an effective thickness of ~ 2.16 nm for the total solid and liquid non-magnetic hydrodynamic attachment. The reproducibility of the synthetic procedure in terms of size of the as-synthesised product was within acceptable limits ($\sim 3\%$). The hydroxyl groups of DEG coordinate to +ve magnetite NP surface to form a robust coating, while uncoordinated –OH groups extend out into the water solvent, conferring high degree of dispersibility in water and steric hindrance. The large number of uncoordinated –OH groups on the nanocrystal surface can be used for further linkage of biomolecules through the well-developed bioconjugation chemistry (Lalatonne *et al.*, 2004).

MDG: 0.36 mM Colloids

Figure 4.21 shows the diluted 0.36 mM ferrofluid containing majority of NPs retains its D_{PCS} size ~ 33 nm assembled in a hexagonal close-packed array. Though the obtained D_{PCS} is close to three times diluted ferrofluid $D_{\text{PCS}} = 30$ nm, the PDI value increased to ~ 0.169 due to very few (0.01%) of them are of ~ 62 nm clusters. Interestingly, the temperature didn't affect much on the cluster size upto 55°C and then the size increased slightly from 60–65°C. Concurrently, the correlation signal dropped in the range of 400 to 200 μs while increasing the ferrofluid temperature to 65°C.

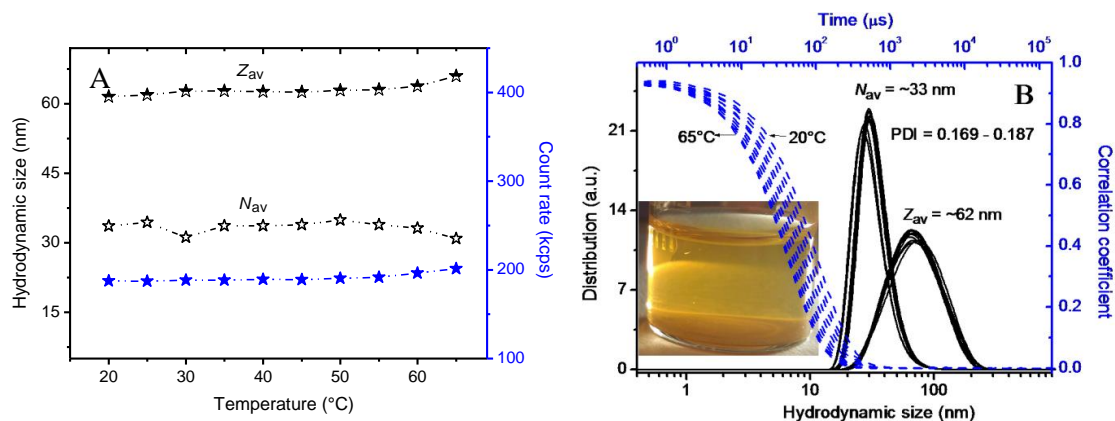


Fig. 4.21 The effect of the dispersion properties of MNPs in the suspensions (0.36 mM) (A) average size and its (B) intensity- and number-based size distribution along raw correlogram (blue solid line) of the sample exposed to 20 to 65°C on the PCS profile.

Each tiny particle is thoroughly coated with DEG to inhibit clumping and thus the surface treated superparamagnetic NPs offered good colloidal stability in water even after the magnetic field or temperature exposure with no evidence of flocculation or settling.

Table 4.5 Colloidal properties such as intensity weighted mean hydrodynamic diameters (Z_{av}), the number weighted mean size (N_{av}), polydispersity index, stability and the surface charge for all the samples

Solvent	Zeta (mV)	pH	D_{PCS} (nm)		PDI	Stability (week)
			Z_{av}	N_{av}		
WA	15	6.18	1215	703	0.518	0.03
EA	40.9	3.85	51.4	24.9	0.258	6½
nPA	34.1	5.69	135.7	23.4	0.253	5
IPA	33.1	5.95	227.2	62.6	0.351	¾
EG	43	5.53	100.5	17.5	0.271	7
DEG	40.8	5.8	38.7	16.1	0.264	18
PEG	38.9	4.3	34.1	18.8	0.209	>24
WA80	4.9	6.68	4820	956.9	0.664	0.006
EA80	36.3	5.98	90.3	20.6	0.233	2
nPA80	32.9	6.93	140.3	33.6	0.271	1½
IPA80	20.3	6.83	354	89.3	0.776	½
EG80	33.4	6.15	160.7	19.7	0.286	¾
DEG80	31	6.29	146.3	27.5	0.243	4
PEG80	37.7	5.87	124.6	25.3	0.21	5½

The ferrofluid prepared from NPs produced in different alcohol-water mixed solvents were kept at room temperature in a tightly closed transparent glass vials. As mentioned in Table 4.5, the results demonstrate that there was no precipitation appearing in the dispersion after standing for reasonable time period and the hydrodynamic size almost did not change. With increase of precipitation temperature from 40° to 80°C, the transparency of dispersion drops gradually due to poorer dispersibility. The ferrofluid concentration (2.15, 0.7 and 0.36 mM) used here are quite high and it is sufficient enough for both MRI and magnetic hyperthermia treatment. It is obvious from the reported studies, the iron amount internalization detected per cell could vary from a few picograms to more than a hundred picograms, and it is strongly affected by the NP coating layer (dextran, citrate, polymer etc.) and to potential aggregation of NPs on cells (Kakwere *et al.*, 2015). The magnetic field used here 520 G is very low because non-invasive MRI systems using magnetite as the contrast agents are now being practiced routinely in clinical practices that subject patients to static background magnetic fields in excess of 1.5 T, exposed for a limited time (<1 h) (Perrin and Souques, 2012).

4.4.3 Comparison of particles size from various techniques

The particle sizes of magnetite nanocrystals determined by XRD, BET, TEM and DLS techniques are summarised graphically in Fig. 4.22. Particle sizes estimated from different techniques provide different meaningful information. The size obtained from the X-ray profile fitting (D_{XRD}) indicates the average crystallite size of particles. Particle size from BET surface area (D_{BET}) is calculated from the nitrogen adsorption–desorption isotherms with the assumption that the particles are spherical. However, the D_{TEM} is the physical size obtained by direct viewing of particles under TEM.

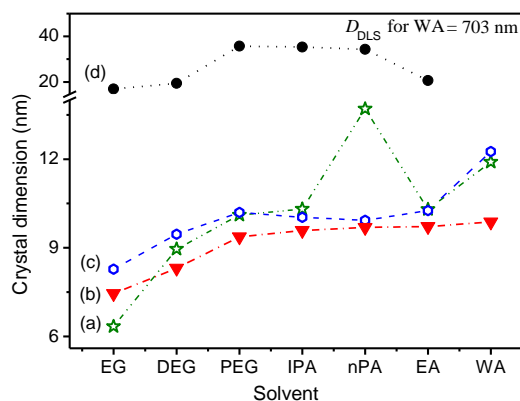


Fig. 4.22 Particle sizes obtained from (a) BET, (b) XRD, (c) TEM and (d) DLS techniques on magnetite synthesised at 40°C.

In many cases $D_{\text{XRD}} < D_{\text{TEM}}$, as D_{XRD} calculated employing Scherrer equation ignores broadening of the diffraction peaks due to the microstrain in the lattice and X-ray does not often involve the amorphous layer on the magnetite NP surface (Iyengar *et al.*, 2014).

Thermal analysis

Presence of organic layers on the surface of the NPs was further confirmed by TG-DTA. The thermogravimetry patterns of magnetite specimens synthesised from mixed solvents are presented in Fig. 4.23. All the TG profiles show very similar patterns with three-step decomposition in the temperature range 50–1000°C. The aqueous precipitated magnetite presents a simple two stage thermal decomposition at ~225 and 330°C consisting of a total loss of ~6% whereas the total losses are ~11.8, 13.9, 16.7% for PEG, DEG and EG respectively at temperatures >800°C.

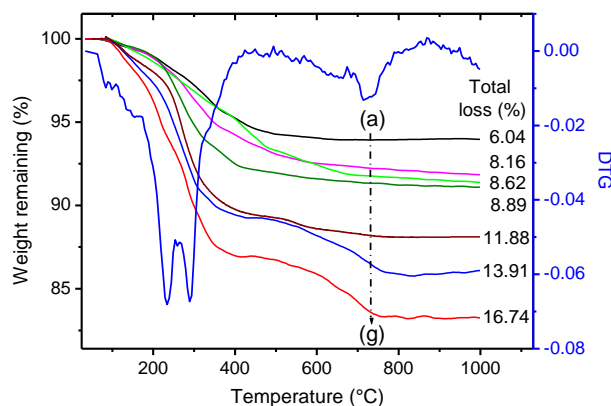


Fig. 4.23 Thermal analyses patterns of magnetite powders synthesised at 40°C from 1:1 combination of water with different solvents (a) WA, (b) *n*PA, (c) EA, (d) IPA, (e) PEG, (f) DEG and (g) EG and DTG of representative specimen DEG.

The peak centred at ~120°C is responsible for the removal of structural water from the lattice followed by an exothermic peak at ~250°C for the removal of unwashed salt from the material along with alcohols attached to the nanocrystals surfaces. The last peak for a small loss at ~670°C is due to burning of carbon/graphitic products from the decomposition of poly-ols. The weight loss is greater in EG compared to the same with other poly-ols, as the smaller NPs have higher surface areas available to adsorb poly-ol moieties. The TG patterns of *n*PA, EA and IPA are clustered with the loss ~8.5%.

4.4.4 Catalytic property of MNPs powder

The catalytic activity of the Fe_3O_4 powders was evaluated by measuring the peak combustion temperature (T_p) and the total heat evolved (ΔH) during the Fe_3O_4 catalysed combustion of carbonaceous diesel soot in excess of O_2 and is shown in Fig. 4.24. The

poly-ol mediated products (PEG, DEG and EG) showed better activity due to relatively smaller sizes with abundant active (220) and (400) crystal facets. The figure shows that catalytic activity, in terms of the total heat evolved from the carbon soot combustion, varies from a minimum of 7.6 kJ.g^{-1} for WA, to a maximum of 12.0 kJ.g^{-1} , for DEG. The T_P are, as expected, inversely related with the total heat evolved; the extremes are 485.2° and 438.6°C for WA and PEG, respectively. The energy evolved during soot burning were relatively lower at $\sim 9 \text{ kJ.g}^{-1}$ in mono-ol based products e.g., IPA, *n*PA and EA, may be due to the lower T_C values for active (220) and (400) planes (~ 1.2 and 1.1 respectively).

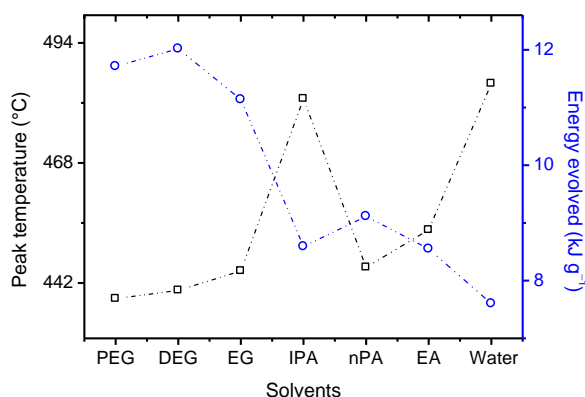


Fig. 4.24 Differential thermal analyses patterns of magnetite powders synthesised at 40°C from PEG, DEG, EG, IPA, *n*PA, EA and WA.

In comparison to T_P of WA, the same decreased by 39.8 and 31.7°C in *n*PA and EA respectively where as it remains almost unchanged at 481°C in IPA. So we conclude that the activity of a magnetite material is attributable mainly to the energetics of the reaction on the exposed (220) and (400) crystal facets in addition to the available surfaces.

4.5 Conclusions

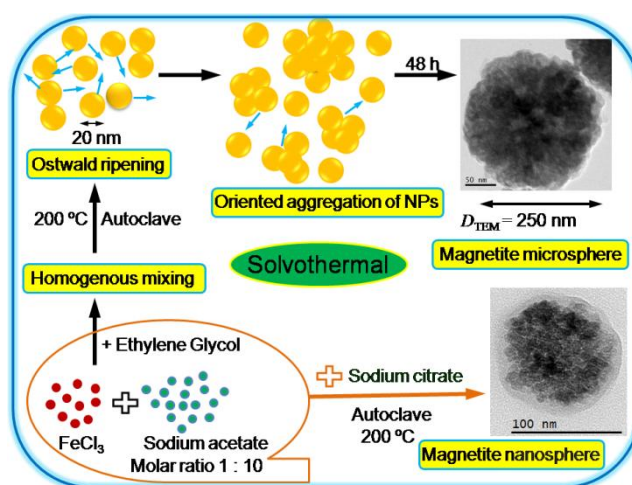
Magnetite nanocrystals have been synthesised via homogeneous precipitation in solvents with decreasing the ‘ ε ’ of medium using 1:1 EA, *n*PA, IPA, EG, DEG and PEG with water at 40° and 80°C . The presence of alcohol/glycol content (by TG-DTA and FTIR) and the precipitation temperature are vital for the control of agglomeration, suspension stability, size and crystallinity of magnetite. IPA magnetite is relatively crystalline (CI $\sim 89\%$) next to water, with highest magnetisation of $\sim 68 \text{ emu.g}^{-1}$. The crystals observed from the HR-TEM have a mixture of multi-faceted polyhedral shapes, all of which contains abundant under coordinated atoms located on the edges and corners, serving as extra active sites for the chemical reaction. The PEG, DEG and EG powders showed better catalytic activity due to smaller particles with abundant active (220) and (400)

crystal facets. Nanofluids with greater aqueous stability were obtained from relatively lower precipitation temperature at 40°C. Furthermore, monodispersed transparent colloidal suspension of PEG showed stability over a period of 6 months. The hydrodynamic diameter was <20 nm in the temperature trend upto 65°C. PCS measurements indicated that the MDG magnetite at different concentrations and temperatures of measurement which confirmed the presence of ‘single particle dispersion’, ($D_{PCS} \approx 13$ nm). These MNPs and stable colloids open up opportunities for improving existing biomedical/industrial applications and designing novel technologies in the future.

Shape selective fabrication

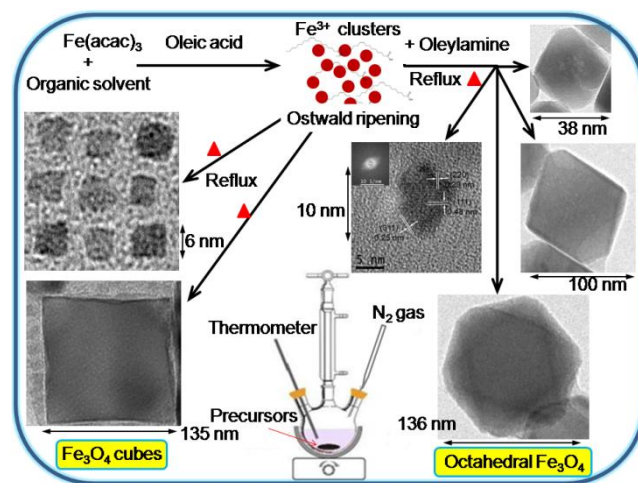
5.1 Graphical abstract

The fabrication of monodispersed magnetite nano-, micro-sphere, cube, truncated octahedra has been successfully achieved by controlled high temperature process. Spheres have been synthesised by thermal treatment of ferric salt in ethylene glycol at 473 K under autogenous pressures of the solvents and were subsequently coated/decorated with silica or silver NPs. The monodisperse spheres with tunable diameter in the range of 70–250 nm has been achieved by varying the reaction time, with precursor concentration and temperature held constant. Introduction of Na-citrate into above mixture produces ~70 nm spheres.



Each spherical cluster is a self-assembly of ~10–20 nm sized primary MNPs. The M_s value gradually increases with increasing the autoclaving time, at 48 h, the magnetite spheres exhibited $M_s = \sim 80 \text{ emu.g}^{-1}$. This result clearly proved that the crystallinity could be improved by Ostwald ripening of nanocrystals through a dissolution–recrystallisation process. The silicate extracted from the cheap precursor rice hull ash, a waste by-product of Agro industries. The magnetite spheres of core-shell framework were finally covered with outer shell of silica possess $207 \text{ m}^2.\text{g}^{-1}$ BET surface area. Biocompatibility of silver NPs loaded nanospheres were studied on MDA-MB-426 cell lines and nuclear morphology examined by DAPI staining after 24 h exposure to nanospheres. High quality single crystalline nano-dimensional Fe_3O_4 cube as well as truncated octahedral were

achieved by thermal decomposition of $\text{Fe}(\text{acac})_3$ in high-boiling organic solvents. These methods offer an efficient chemical pathway to synthesise highly monodisperse magnetite nanocrystals (MNCs) with high atom economy and a precise control over the phase compositions. The strong coordinating property of oleyl surfactant toward selective crystallographic facets facilitates the fabrication of three dimensional (3D) morphology MNCs. Cubes are grown in the range of $\sim 6\text{--}135\text{ nm}$ in a mono surfactant system whereas octahedra ($10\text{--}135\text{ nm}$) are formed with the aid of the mixed surfactant. The crystal structure, particle size, shapes and phase purity of the samples were investigated in detail by TEM, SAED, EDX, XPS and XRD. BF-TEM view on as-prepared MNCs exhibited a well defined assembly of uniform Fe_3O_4 with narrow size distribution and 3D morphology. The XRD results showed that all the MNCs are phase pure highly crystalline Fe_3O_4 with finger-print diffraction peaks. The products exhibited the attractive magnetic properties with high M_S were examined by PPMS. The NCs have also been further characterised by Mössbauer spectra.



Such kind of architectures possess high saturation magnetisation, well-defined structure, and the porous channels and cavity in silica shell have added benefit of providing a robust platform for incorporating diverse functionalities into a single nanosphere for the drug storage, delivery, and release. To evaluate the toxicity of the as synthesised nanocrystals, in particular any toxicity resulting from the synthetic methodology, selected magnetite specimens of different shapes were investigated *in vitro* using HCT 116 and MDA-MB-468 cells as model systems for evaluating human colon and breast cancer epithelial cell viability, respectively.

5.2 Introduction

The fabrication of MNCs has been immensely hunted not only for their fundamental scientific interest but also for many technological applications on account of their unique properties imparted by their nano-dimension (Iyengar *et al.*, 2016). The development of efficient methods for the synthesis of nanostructures with well-defined sizes and shapes is one of the key trends to apply MNCs in various fields i.e., immobilising proteins, enzymes, and other bioactive agents in analytical biochemistry, medicine, and biotechnology. Most materials having high magnetic moment, such as cobalt and nickel, are toxic, susceptible to oxidation and hence limited in their biomedical applications, but Fe_3O_4 is suitable for *in vivo* applications due to its safe assimilation of iron through homeostasis by cells (Garcia-Jimeno and Estelrich, 2013). The synthesis of monodisperse nanocrystals is of key importance for the next-generation molecular nanosystems, where each molecule in the nano-system has a specific structure and plays a different role.

It is necessary to develop new synthetic routes, to control the range of achievable particle sizes and shape without significant deterioration of their magnetic properties. Magnetic properties of NCs depend on various parameters, such as size, its distribution, interparticle distance, shape, condition of synthesis and stabilising surfactants. In order to improve or rationally tune the shape-dependent functional properties, such as magnetism, remains a tough challenge to correlate the synthetic parameters and shape of products. If kinetically controlled process dominates, the shape is determined by the rate at which the different crystal faces grow. If the particles are formed in thermal equilibrium, their shape or crystal habits result from minimising the surface energy. In the later case, the surfaces are determined by performing a Wulff construction (Kumar and Nann, 2006). According to selective adsorption model, a mixture of surfactants is required for anisotropic crystal growth. Selective adsorption of this mixture is responsible for modification of the surface free energy of individual crystallographic faces thereby differences in growth along different crystal facets. In the nucleation process, octahedral Fe_3O_4 NCs always crystallises as nucleus and predominantly (111) facets get exposed, due to its energetics (Yang *et al.*, 2011). The rate of growth of different facets are determined by the surface energy, and the general sequence for the surface energies of magnetite structure is $\gamma\{111\} < \gamma\{100\} < \gamma\{110\}$ (Wang *et al.*, 2012). The thermodynamics dictates according to the surface free energy minimisation principle, the theoretical growth habit (equilibrium morphology) of the Fe_3O_4 crystal is octahedral (Zhang *et al.*, 2007), because the growth

rate along the (100) direction is faster than along the (111) plane, so the (100) plane will be gradually decreased. One can tune the crystal size and shape via controlling the growth rate of different facets in a delicate balance either by utilising the inherent crystal structure property or by external factors such as application of surfactants, different solvent, temperature, pH, time etc. Faster growth along the $\langle 100 \rangle$ facets could lead to octahedral crystals (Wang *et al.*, 2010). Faster growth along the $\{111\}$ planes will produce shapes bounded by six homogeneous $\{100\}$ crystal facets, and thus form cubes. The *fcc* structure with six $\{100\}$ facets, which have relatively high surface energies, is a less stable morphology. Nanocubes have a specific exposed crystal facet, which provide an ideal model for the study of surface related properties (Murphy, 2002) and can maximise crystal packing and produce a highly compact structure with mainly exposure of six homogeneous $\{100\}$ crystal facets. Since the energy required to create catalytically important oxygen vacancy defects (oxygen storage capacity) is low for the low indexed surfaces (100) and (110) of semiconductor oxides compared to other stable low indexed lattice planes like (111), the amount of oxygen vacancies on (100) planes is very high, which indirectly causes a change in the local electronic and valence arrangement that stabilises the trivalent oxidation state. These large numbers of oxygen vacancy defects on (100) planes are favourable for oxygen anion mobility and therefore theoretically give a high oxygen storage capacity and catalytic activity especially for multi-oxidation processes (Deori *et al.*, 2014).

Park *et al.*, controlled the crystal size by modifying the amount of solvent, heating profile and/or reaction time (Park *et al.*, 2004). But a systematic study of the influence of each of those parameters has not been reported yet. Xiong and co-workers produced 50 nm sized magnetite nanocubes from a solvothermal reaction of ferrocene with H_2O_2 in a mixture containing polyvinyl pyrrolidone, water and alcohol (Xiong *et al.*, 2007). The Kim *et al.* synthesised monodisperse Fe_3O_4 nanocubes with sizes ranging from 20 to 160 nm via thermal decomposition of $\text{Fe}(\text{acac})_3$ in a mixed solution of OA and benzyl ether at 290°C (Kim *et al.*, 2009). In their work, it was found that the longer reaction time and the higher monomer concentration were responsible for the anisotropic growth of nanocrystals.

In this chapter, a general approach for the fabrication of monodisperse, hydrophilic, biocompatible and single-crystalline magnetite as well as ferrite microspheres by a solvothermal reduction method. Magnetite spheres synthesised were monodisperse with diameters tunable in the range of 100–300 nm. Fe_3O_4 cubes and truncated octahedrons

have been fabricated through the technique purportedly involved the decomposition of $\text{Fe}(\text{acac})_3$ as single iron precursor in benzyl ether by a one-step reflux procedure to swot the influence of oleyl chemistry. We have studied in detail the effect of modifying the molar ratio of iron salts-to-surfactant on the resulting crystal shape and size. The use of OA enable the preparation of cubic-shaped large ~ 135 nm single crystals magnetite, and exhibited excellent magnetic properties very close to that of bulk magnetite. Furthermore, the range of sizes may further be lessened up to ~ 6 nm just by vigorous stirring while refluxing. The use of mixed surfactant (OA and OAm) keeping the solvent same has been found to facilitate the formation of truncated octahedra with range of sizes from 10 nm up to ~ 135 nm by modifying the ratio of surfactant and stirring during the growth process. The synthetic strategy demonstrated here may provide an effective route to large scale synthesis of different spinel ferrites and other metal oxide nanocrystals with tunable size and shape, and thus high magnetic response. Cytotoxicity was measured by two forms of viability assays: the MTT assay, the WST assay.

5.3 Experimental

5.3.1 Fabrication of magnetite sphere

About 6.5 mmol of ferric chloride was dissolved in 78 ml EG; a polyhydric alcohol with boiling point of $196\text{--}198^\circ\text{C}$ to form a clear solution, followed by the addition of 65 mmol sodium acetate. The mixture was stirred vigorously for 30 min to obtain homogenous suspension and then sealed in a Teflon lined stainless-steel autoclave. To investigate the morphology and structure evolution during the synthesis process, the reaction was quenched at different times and sampled the intermediate product for further analysis.

Table 5.1 List of magnetite spheres synthesised by solvothermal treatment

Sample	Iron precursors	Additive	Autoclaving time (h)	Temperature ($^\circ\text{C}$)
MS2	$\text{Fe}(\text{Cl})_3$	sodium acetate	2	200
MS4	same	same	4	200
MS8	same	same	8	200
MS16	same	same	16	200
MS24	same	same	24	200
MS48	same	same	48	200
NH16	same	Ammonium acetate	16	200
NS	same	Sodium acetate + Na_3Cit	16	200
FeAc48	$\text{Fe}(\text{acac})_3$	Sodium acetate	48	200

The autoclave was heated to and maintained at 200°C for 2–48 h. The reactor was subsequently cooled to room temperature. The initial yellowish suspensions turned into black, indicating magnetite formation on hydrothermal treatment. The reduction product magnetite (~0.5 g) was magnetically retrieved, thoroughly washed, and dried in a reduced pressure at 60°C for 6 h.

The microspheres were also synthesised with ammonium acetate instead of sodium acetate for 16 h and are labelled as NH16. FeAc48 is obtained by replacing ferric chloride with ferric acetylacetonate by 48 h reaction, keeping the rest of the conditions same. Nanospheres ‘NS’ have been fabricated by adding 2.17 mmol of trisodium citrate (Na₃Cit) into the ferric chloride, EG and sodium acetate mixture stated in the preceding paragraph and autoclaved at 200°C for 16 h. Details of magnetite spheres prepared with varying precursors, processing time, temperature and sample designations were listed in Table 5.1

5.3.1.1 Acid treatment on magnetic microspheres

The magnetic microspheres prepared above (0.5 g) were dispersed ultrasonically in 100 ml of 0.1 M HCl for ~15 min. Then the treated microspheres were redispersed in 25 ml of 0.2 M HCl for few seconds and the supernatant was decanted completely by magnetic means. These surface treated magnetite dispersion was subjected to mechanical stirring by high-speed homogeniser (IKA T25 ULTRA-TURRAX®, IKA®-Werke GmbH & Co.KG, Germany) with a speed in the range of 8200 rpm for 1.5 h at ambient temperature. The resulting acid treated microspheres were magnetically retrieved, thoroughly washed, and vacuum dried.

5.3.2 Silica precursor extraction from rice husk ash (RHA)

An acid washing step was used to remove the small quantities of minerals prior to silica extraction from RHA in the following manner. About 10 g portion of RHA samples were dispersed in 60 ml distilled water, and the pH was adjusted to 1 using 1 N HCl. These dispersions were stirred for 2 h, filtered and the RHA residue was washed with 100 ml of water. The residues were used for silica extraction adapting a method of (Kalapathy *et al.*, 2000). 100 ml portions of 2N NaOH were added to the washed RHA powder and boiled for 1 h with constant stirring to dissolve silica to produce a sodium silicate solution. The solutions were filtered through filter paper, and the carbon residues were washed with boiling water. The filtrates and washings were allowed to cool to room temperature and were titrated with 2N HCl with constant stirring to pH 7. Silica gels started to precipitate

when the pH decreased to <10. The silica gels formed were aged for 18 h. Millipore water was added to break the gels into slurry, then centrifuged for 15 min at 2500 g rcf (Heal Force, Neofuge 15R), the clear supernatants were discarded and the washing step was repeated. The solution was further diluted and used for synthesis of the magnetite–silica composite. The gel was dried at 80°C for 2 days to produce powder form.

5.3.3 Core-shell nanostructures

5.3.3.1 Magnetite microspheres @silica

To prevent the oxidation and leaching of the magnetite, a sol-gel approach was employed to provide a silica shell over the magnetic core. As-prepared 0.1 g Fe₃O₄ spheres were dispersed ultrasonically in water, were added dropwise to 2.25 ml of sodium silicate extract in which pH was adjusted to ~7 using 1M HCl. The reaction was allowed to proceed for 7 h under stirring. The resulting Fe₃O₄@SiO₂ microspheres were washed with methanol by magnetic decantation for four times and dried at 60°C in vacuum oven. The sample is designated as ‘MS48@Si’.

5.3.3.2 Silver decorated magnetite nanospheres

The citric acid-coated Fe₃O₄ nanospheres (750 mg) were sonicated in 75 ml Millipore water for 30 min. 225 ml aqueous solution of silver nitrate containing 388 mg Ag(NO₃)₂ was added, and the mixture was continuously stirred for 30 min. Finally 45 ml 0.2 M freshly prepared NaBH₄ solution was added to it and the resulting mixture was stirred for another 20 min upon cooling in an ice bath. The product ‘NSAg’ was collected using a magnet, washed with deionised water, and dried in a vacuum oven at 60°C for 24 h.

5.3.4 Fabrication of magnetite cube

To synthesise magnetite nanocrystals of ultra-small cube of about 6.5 nm edge length, 2 mmol of Fe(acac)₃ was mixed with 4 mmol of OA in 105 mmol of benzyl ether. The Fe(acac)₃-to-OA molar ratio was 1:2. First, the solution was heated up to 120°C with a constant heating rate of 6-7°C/min under an N₂ blanket flow and vigorous stirring. After 1 h of constant heating at this temperature, the solution was heated to 290°C (benzyl ether b.pt.) under vigorous magnetic stirring. The reaction mixture was kept under reflux for ~30 min, and the initial transparent solution became turbid and black. The resulting solution containing nanocrystals was then cooled to room temperature, ~30 ml acetone and ethanol mixture (1:1) was added to the solution and the flask was kept over a bar

magnet to fasten the sedimentation process. Black solid precipitate was collected by magnetic decantation and was washed repeatedly with acetone until free from impurities. The synthesised nanocrystals were obtained in powder form after drying at 60°C under vacuum and stored in desiccators, labelled as CU6 (See Table 5.2).

Table 5.2 List of magnetite cube and octahedra synthesised by thermal decomposition of iron acetylacetonate in high boiling solvent

Sample	Fe(acac) ₃ /OAm molar ratio	OA/OAm molar ratio	Reflux duration (h)	Physical disturbance
CU6	1:4	-	½	Magnetic stirring
CU135	1:4	-	1	-
OC10	1:4	1:1	½	Magnetic stirring
OC40	1:2	2:1	½	Magnetic stirring
OC100	1:2	4:1	½	-

The same reaction mixture used for CU6 were subjected to rapid heating, after 1 h holding time of 120°C, to 290°C in ~10 min and reflux for 30 min with no physical disturbance (stirring). The sample is labelled as CU135.

5.3.5 Fabrication of magnetite truncated octahedra

Fe(acac)₃ (1 mmol) was added to a mixed surfactants OA (4 mmol) and OAm (4 mmol) in benzyl ether (132 mmol). The Fe(acac)₃-to-OA molar ratio was 1:4. The reaction mixture was degassed at 120°C for 1 h and then the flask was heated further to 290°C under vigorous magnetic stirring. The reaction mixture was maintained at this reflux condition under N₂ for 30 min. After cooling to room temperature, acetone was added to the solution and the flask was kept over a bar magnet to hasten the sedimentation process. The settled black solid was collected by magnetic decantation and washed thoroughly with acetone, dried and stored in a dessicator, designated as ‘OC10’.

About 2 mmol of Fe(acac)₃ was mixed with 4 mmol of OA and 2 mmol OAm in 105 mmol of benzyl ether produced ‘OC40’. By changing the mixed surfactant OA/OAm ratio from 2:1 to 4:1, ‘OC100’ nanocrystals were fabricated. Furthermore, keeping the same surfactant ratio of ‘OC100’ and doubling the overall precursor concentration produced ‘OC135’ magnetite crystals.

5.3.6 Non-specific adsorption of proteins

Bovine serum albumin (BSA) solution (mg.ml⁻¹) was prepared in phosphate buffered saline (PBS) buffer (pH 7.4). About 5 mg Fe₃O₄ was dispersed in 5 ml BSA solution and

the suspension was aged at room temperature for overnight while stirring to reach the adsorption equilibrium. Free BSA concentration in supernatant was estimated by performing Bradford assay (Bradford, 1976) using a UV–vis spectrophotometer by recording the absorbance at ~590 nm. The amount of non-specifically adsorbed BSA could be calculated, from the standard calibration curve, by the difference in the initial and the final protein concentration in supernatant.

5.3.7 *In vitro* biocompatibility assessment

5.3.7.1 Cell culture and exposure to nanomaterials: dose response studies

(a) *Breast cancer cell line*

Breast cancer cells (MDA-MB-468) were obtained from the National Centre for Cell Sciences, Pune. Cells were seeded in 24-well plates (10^4 cells/well) and cultured in DMEM supplemented with 10% fetal bovine serum, benzylpenicillin (100 U/ml), and streptomycin (10 μ g/ml). Cells were seeded and maintained at 37°C in a humidified incubator with 5% CO₂. After 18 h culture, cells were exposed to DMEM with varying concentrations of NS, NSAg NPs (10, 30, 50, 80 and 100 μ g/ml). A negative control was provided using the culture medium without the nanoparticles.

Cytotoxicity MTT assay

Cytotoxicity was evaluated using a non-radioactive, colorimetric MTT assay (Mahmoudi *et al.*, 2010). After 24, and 48 h of incubation with extract medium, 500 μ l of MTT reagent (0.5 mg/ml in PBS) was added to each well and the cells were incubated at 37°C for 3 h in the 5% CO₂ incubator. Mitochondrial dehydrogenases of viable cells reduced the yellowish water-soluble MTT to water-insoluble formazan crystals, which were dissolved by adding solvent (DMF/H₂O) and incubated for 1 h. The cell culture medium was aspirated cautiously, after addition of DMF to each well and mixed thoroughly. The absorbance was monitored at 570 nm, with 630 nm as a reference wavelength using a microtiter plate reader (Bio-Rad, CA, USA). The results are expressed as percentage of viability compared with the untreated control and analysed in triplicate. To assess the effects of the NPs on the cell morphology, the plates were also examined by fluorescence microscopy (Leica, USA).

(b) Colon carcinoma cell line

Human colon carcinoma HCT-116 epithelial cell line (CCL 247) was originally purchased from American Type Culture Collection (ATCC, Manassas, VA). Cell line was seeded in 96-well plates (10^4 cells/well) and was cultured as sub confluent monolayer in 250 μ l DMEM supplemented with 10% FBS, 1% PEN-STREP and 0.1% Fungisone at 37°C in 5% CO₂ containing humidified atmosphere: a more-reliable way of identifying cytotoxicity by *in vitro* assessments is to use particles surfaces saturated (via interaction) with DMEM prior to use. After one day in culture, cells were exposed to DMEM (150 μ l) with varying concentrations of NPs (25, 50, 75 and 100 μ g/ml). After 24 h incubation with NPs, the cells were then washed once, replenished with fresh media (150 μ l), and incubated for an additional 48 h. A negative control was provided using the culture medium without the NPs.

Cytotoxicity WST assay

About 10^4 - 10^5 HCT-116 cells were added in 96-well plate to a final volume of 100 μ l culture medium/well for complete adherence. In WST assay, the reduced tetrasolium salt is water-soluble. Therefore, no DMSO extraction is necessary. After cell exposure, a total of 10 μ l of WST-1 reagent was added to each well and then incubated at 37°C for 0.5 to 4 h in the 5% CO₂ incubator. The absorbance of formed formazan dye was quantified at 450 nm (reference: 650 nm) using a microtiter plate reader (Bio-Rad, CA, USA). The viability of cells was determined as the percent cell survivability of the untreated control and all the experiment were performed in triplicate.

A linear relationship between cell viability and absorbance can be established. The percent cell survivability of the wells treated with different concentrations of NPs relative to control wells which received DMEM alone was calculated by:

$$\text{Cell viability (\%)} = \left(\frac{A_{\text{Sample}}}{A_{\text{Control}}} \right) \times 100 \quad (5.1)$$

where A_{Sample} and A_{Control} are the absorbance of surviving cells treated with or without NPs, respectively.

5.3.7.2 Cell staining

Fixation of cells involved 24 h incubation with the NPs, followed by washing 3 times with sterile PBS, followed by 15 min incubation with 2% formaldehyde in PBS at room temperature. After washing cells 3 times with PBS again, they were mounted on clean glass slides using mounting medium without/with DAPI (50 μ M, for 20 min) for nuclear

staining. The sample cover slips were then mounted on slides using glycerol and the slides were viewed directly using a fluorescence microscopy (Leica, USA) equipped with a 405 nm diode and 488 nm laser for collection of DAPI and FITC (fluorescein isothiocyanate; green) emission signals, respectively at 60× original magnification. The fluorescence images were digitised and processed using Adobe Photoshop software.

Please refer chapter two for the chemicals used and the details of characterisation techniques adopted here.

5.4 Results and discussion

5.4.1 Solvothermal method

5.4.1.1 Physico-chemical characterisation of nano/microspheres

The magnetite micro and nano-spheres were synthesised by a solvothermal reduction of FeCl_3 at 200°C in ethylene glycol using sodium acetate as an alkali source. The final autoclaved product was black indicating the formation of magnetite. We confirmed the presence of Fe_3O_4 phase by XRD and HR-TEM. In order to understand the formation process, time-dependent experiments were carried out and the resulting products collected at different reacting times were analysed by electron microscopy. The size and shape of the products as well as the material phase were examined by FESEM and TEM. The size of the Fe_3O_4 microspheres was influenced by reaction time and the concentration of starting materials. The average particle size and its distribution were calculated by inspecting multiple FESEM images on 200–250 particles. Fig. 5.1 reveals that hydrothermal treatment of Fe-chloride and sodium acetate produced large magnetite particles in the range 100–300 nm. Further, extension of reaction time helps formation of larger spherical shapes with narrow distribution. Solvothermal reaction for ~2 h produced irregular or near spherical NPs with 222 ± 83 nm (Fig. 5.1A).

The NPs spontaneously tend to aggregate to form clusters as shown in Fig. 5.1A and B due to their high surface energy. After 2 h of solvothermal reaction, the NPs aggregated into micron size (Fig. 5.1B) which has grown to 250 ± 55 nm after 8 h hold (MS8, Fig. 1C). As the reaction proceeded (16–72 h), the size of the 3D spherical nanostructures grew gradually and the morphology became well-defined. While 16, 24 h reaction time further increases the size to 260 ± 60 and 275 ± 70 nm respectively (Fig. 5.1D, E) as more nano-scale particles obviously clustered on the spherical-like structures. No further growth was observed (254 ± 47 nm) when the hydrothermal treatment was extended further to 48 h. At

the same time, few tiny spherical particles were consumed and large clusters of ~500 nm will probably undergo dissolution recrystallisation for the formation of uniform sized microspheres.

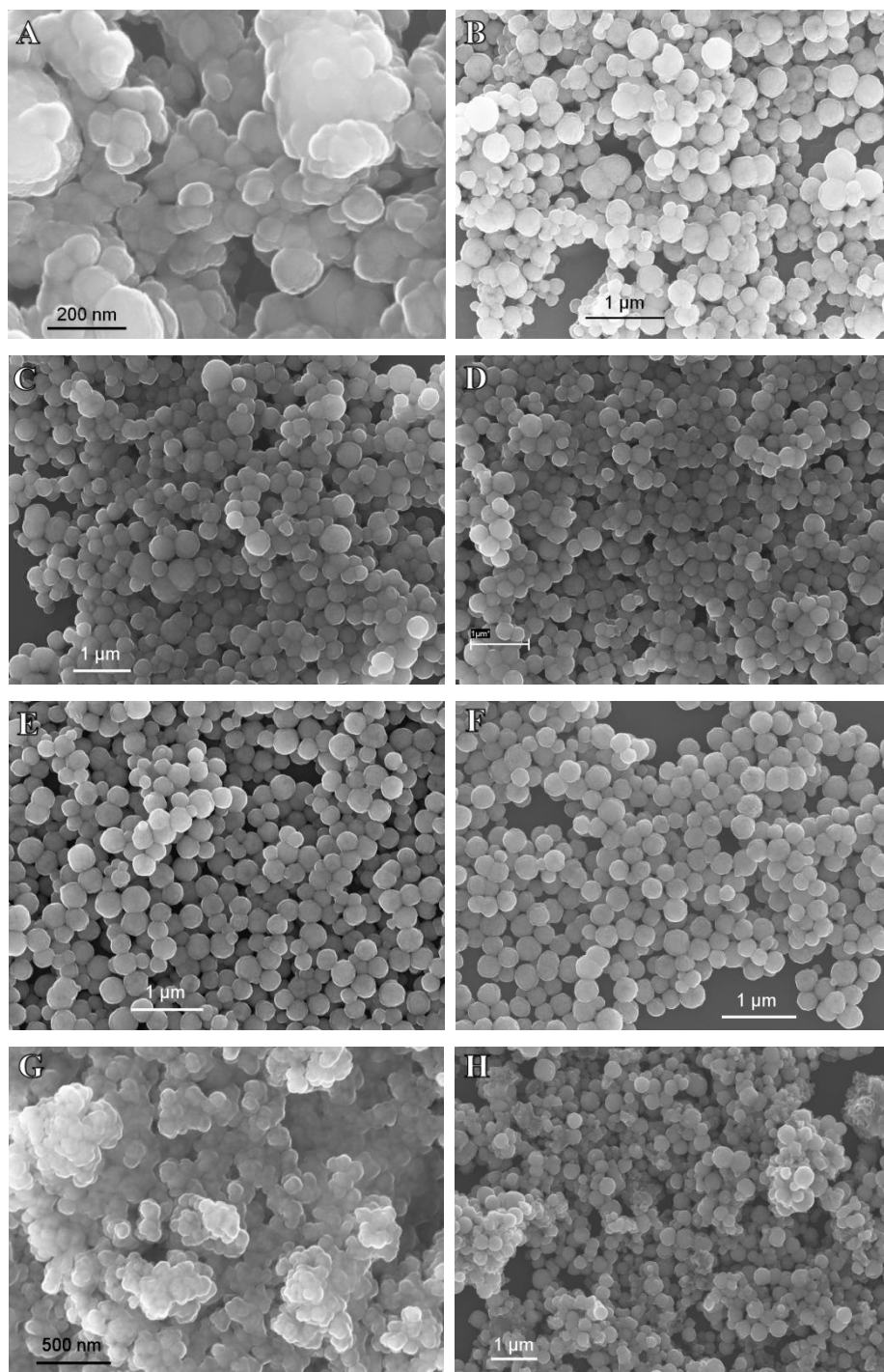


Fig. 5.1 FESEM images of the products synthesised in different reaction time: (A) MS2, (B) MS4, (C) MS8, (D) MS16, (E) MS24, (F) MS48, (G) FeAc48 and (H) NH16.

Just 2 h was not enough for the crystal oriented to spherical assembly (Fig. 5.1). Therefore, the reaction time is a key influential factor on the morphology. These images

suggest that the size of the resultant Fe_3O_4 nano- and sub-micro clusters is strongly dependent on the autoclaving time. By replacing the reducing agent sodium acetate with ammonium acetate, the magnetite spheres (NH16) did not grow well with slightly smaller size of 245 ± 65 nm when compared with ST16 (Fig. 5.1H).

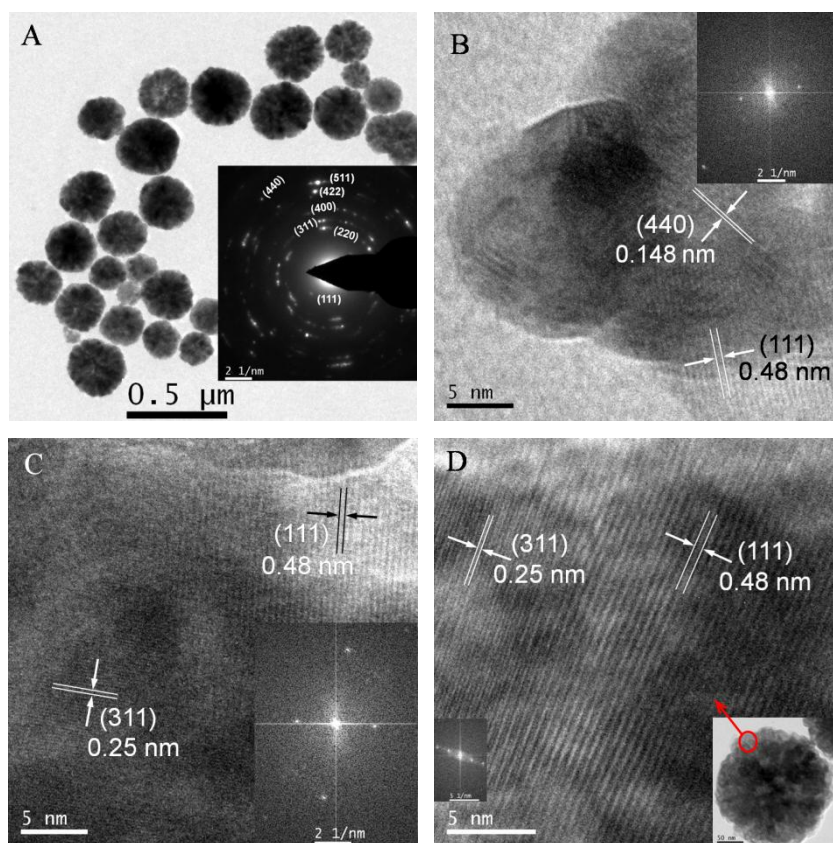


Fig. 5.2 The representative high-magnification TEM images of spherical aggregate ‘MS48’ synthesised at 200°C for 48h (A) bright field image with its SAED as inset, (B, C and D) HRTEM showing different crystal faces and its corresponding FFT as inset.

In the case of FeAc48 (Fig. 5.1G), ferric acetylacetonate was used as iron source with precursor concentration and temperature held constant, the spheres were grown in nano meter range. Figure 5.2A shows selected representative images of the magnetite, which are spherical and have very narrow size distributions. Selected area electron diffraction patterns taken on individual Fe_3O_4 microspheres reveal distinct Debye–Scherrer rings corresponding to (220), (311), (400), (422), (511) and (440) planes with corresponding interplanar spacings 0.2967, 0.2532, 0.2099, 0.1715, 0.1616 and 0.1485 nm which is characteristic of magnetite with polycrystalline nature of these samples.

HRTEM analysis provided more detailed structural information on the microspheres. A representative TEM image of the typical Fe_3O_4 microspheres labelled as ‘MS48’ is shown in Fig. 5.2, in which randomly chosen HRTEM images (panels B, C and

D) further support the highly crystalline nature of the particles. Clear lattice fringes (111), (311) and (440) with corresponding interplanar spacings 0.48, 0.25 and 0.148 nm, confirms the formation of pure magnetite phase (JCPDS Card No. 19-0629) in the microspheres. The crystalline structures of magnetite were characterised by powder XRD (Fig. 5.3 A) also. The patterns can easily be indexed to *fcc* Fe_3O_4 .

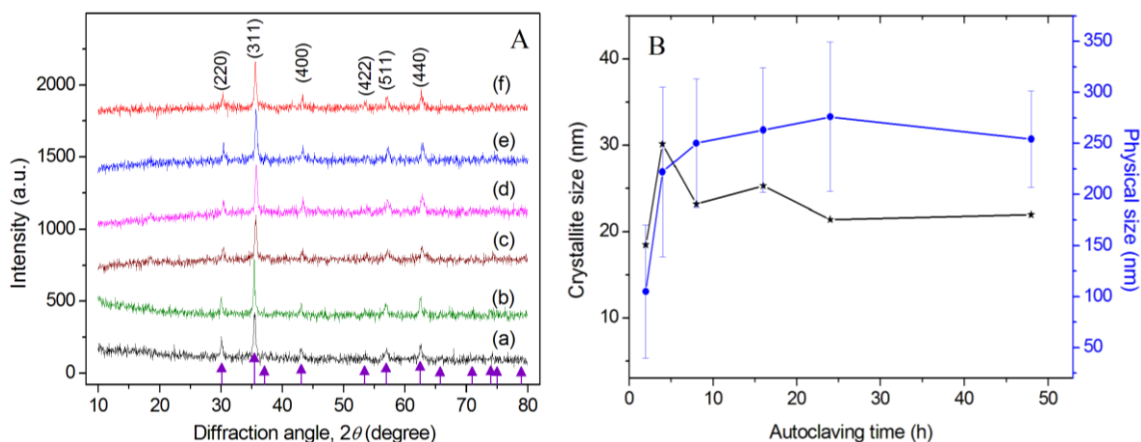


Fig. 5.3 (A) Powder XRD patterns of magnetite microspheres formed (a) 2 (b) 4 (c) 8 (d) 16 (e) 24 and (f) 48 h duration, the vertical drop lines (black) are the theoretical Bragg positions for inverse spinel magnetite phase following JCPDS Card No. 19-0629, (B) comparison of physical size and crystallite size of spheres over autoclaving reaction time.

Following Scherrer equation, the average crystallite sizes calculated from the X-ray line broadening on microspheres were ~18.5, 30.1, 23.2, 25.3, 21.4 and 22 nm for the reaction duration of 2, 4, 8, 16, 24 and 48 h respectively indicating almost no change in the crystal dimension on prolonging the hydrothermal treatment.

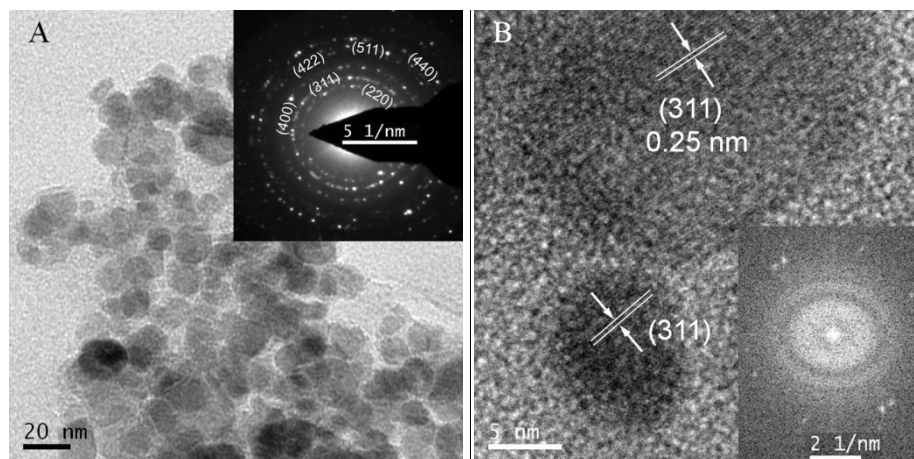


Fig. 5.4 (A) BF image of broken MS48 spheres with its SAED pattern and (B) HRTEM image with its FFT

The TEM images of acid treated MS48 with its SAED pattern (Fig. 5.4) confirmed the microspheres are made of $\sim 18 \pm 3.4$ nm primary particles which is a close to the crystallite size $D_{\text{XRD}} \sim 22$ nm of MS48. The formation of microspheres is through self-assembly of single-crystals of magnetite of size ~ 20 nm in an ordered fashion. Acid treatment in the previous section showed primary magnetite particle size in the same range corroborating our present finding. The main driving force for oriented aggregation of NPs can be generally attributed to the tendency for reducing the high surface energy through both the attachment among the primary NPs and their movement caused by various interactions such as Brownian motion (Cao *et al.*, 2008).

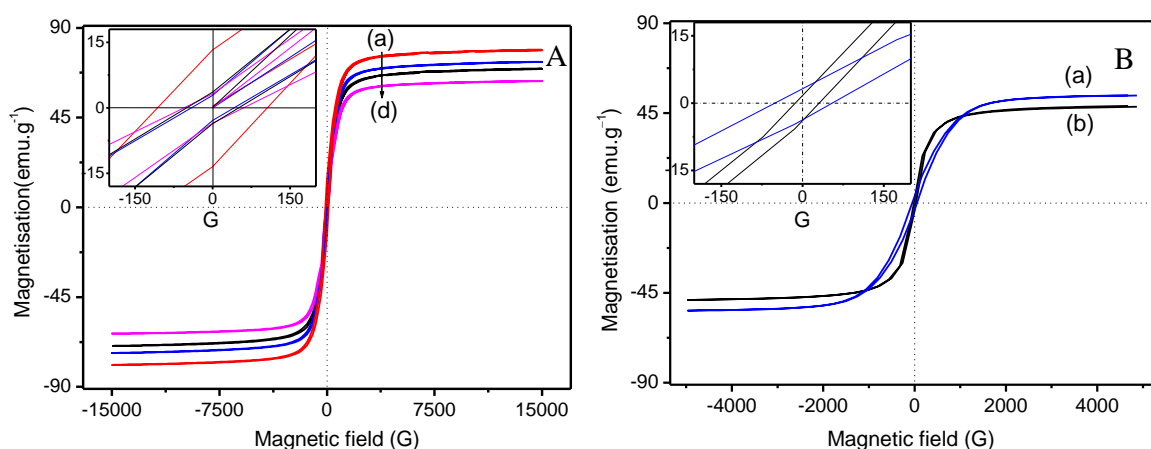


Fig. 5.5 (A) Hysteresis loop of the as-prepared Fe₃O₄ sub-microspheres at (a) 48, (b) 24, (c) 16 and (d) 8 h solvothermal reaction. Inset is the zoomed area of the hysteresis loop in the range ± 200 Oe. (B) VSM profiles of (a) NH16 and (b) FeAc48.

Magnetic properties of the as-prepared Fe₃O₄ spheres were investigated with VSM. The magnetisation curves at 300 K in an applied magnetic field sweeping from -15 to $+15$ kG are shown in Fig. 5.5. From the plot of M versus H , the M_s values of Fe₃O₄ spherical clusters of size 249, 263, 276 and 254 nm were calculated as 63.28, 68.38, 72.94 and 78.69 emu.g^{-1} , corresponding to spheres synthesised with 8, 16, 24 and 48 h reaction time respectively. The M_s values are slightly lower than the theoretical value of bulk Fe₃O₄ (92 emu.g^{-1}) (Cao *et al.*, 2008). It is well known that the size of magnetic particles has a significant influence on their magnetic properties. As the particle gets smaller, the magnetic effective volume accounts for a smaller proportion and the specific M_s decreases. The sizes of hierarchical sub-microspheres are 200–300 nm, so their smaller size leads to lower saturation magnetisation as compared with that of bulk Fe₃O₄. This result proved that the crystallinity and monodispersity could be improved by prolonged reaction time, which agrees well with the TEM studies (Fig. 5.2). Comparing with MS16,

NH16 had 14% reduction of M_s value. FeAc48 sample had reduction of $\sim 39\%$ (M_s) in comparison with MS48 due to the smaller spheres. The inset of Fig. 5.5 shows an expanded low-field hysteresis curve which reveals ferromagnetic behaviour to some extent, with a small coercivity and remanent magnetisation though the NPs as the building blocks of hierarchical spherical assembly (Fig. 5.5 and Table 5.3), respectively.

Table 5.3 Comparison of M_s , M_R and H_C values of as-synthesised hierarchical Fe_3O_4 spheres observed from the corresponding VSM profiles

Sample	M_s (emu. g^{-1})	M_R (emu. g^{-1})	H_C (Oe)
MS8	69.4	3.6	47.9
MS16	63.3	3.2	54.5
MS24	72.9	2.8	41.1
MS48	78.7	13.3	106.8
NH16	54.4	3.4	50.4
FeAc48	48.1	1.8	12.3
Bulk	92	-	-

In order to verify the chemical composition of the synthesised product, XPS spectra was taken in the region of 0–1100 eV binding energy. From the XPS survey spectrum in Fig. 5.6, the peaks attributed to the core levels of Fe 2p, O 2p, Fe 3p and C 1s, where Fe 2p electron core level is characterised by $2p_{1/2}$ and $2p_{3/2}$ peaks respectively.

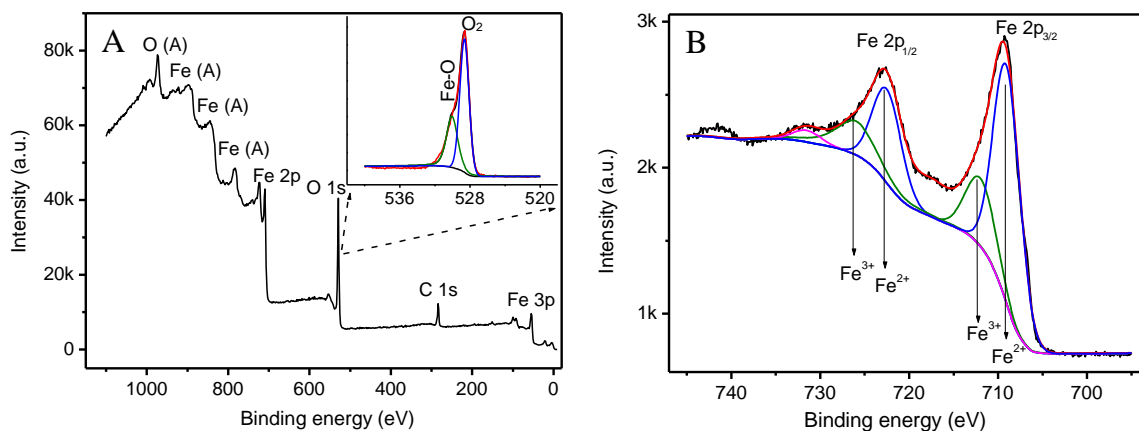


Fig. 5.6 XPS (A) wide spectrum and (B) high resolution spectra of Fe 2p and O1s (Inset of A) of MS48 sphere.

From the high-resolution XPS scan shown in Fig. 5.6B, Fe_3O_4 was confirmed according to the typical characteristic double peaks of $\text{Fe } 2p_{3/2}$ and $\text{Fe } 2p_{1/2}$ at 709 and 723 eV binding

energies, respectively. The double peaks are broadened due to the appearance of Fe^{2+} and Fe^{3+} which is confirmed after deconvolution of the spectra, in agreement with the literature. The relative areas of Fe^{2+} and Fe^{3+} were calculated with the value of 0.33:0.68, corresponding to that of the stoichiometric Fe_3O_4 . The absence of shake-up satellite signal at ~ 719 eV further confirms the Fe_3O_4 (Dar and Shivashankar, 2014). Deconvolution of O 1s peaks around the binding energy ~ 530 eV showed the presence of lattice oxygen (inset of Fig. 5.6A).

5.4.1.2 Cores-shell nanostructures

Magnetite microsphere@silica

Figure 5.7 shows the TEM images and EDS of MS48 as well as silica coated MS48@Si nanostructures. As expected there is no change in the size and crystal morphology of the microspheres on silica coating. EDS (Fig. 5.7D) provides the atomic ratio of Fe:O to be 3:5.72 and 5.29% Si content in MS48@Si. Fe:O ratio in MS48 is 3:5.2.

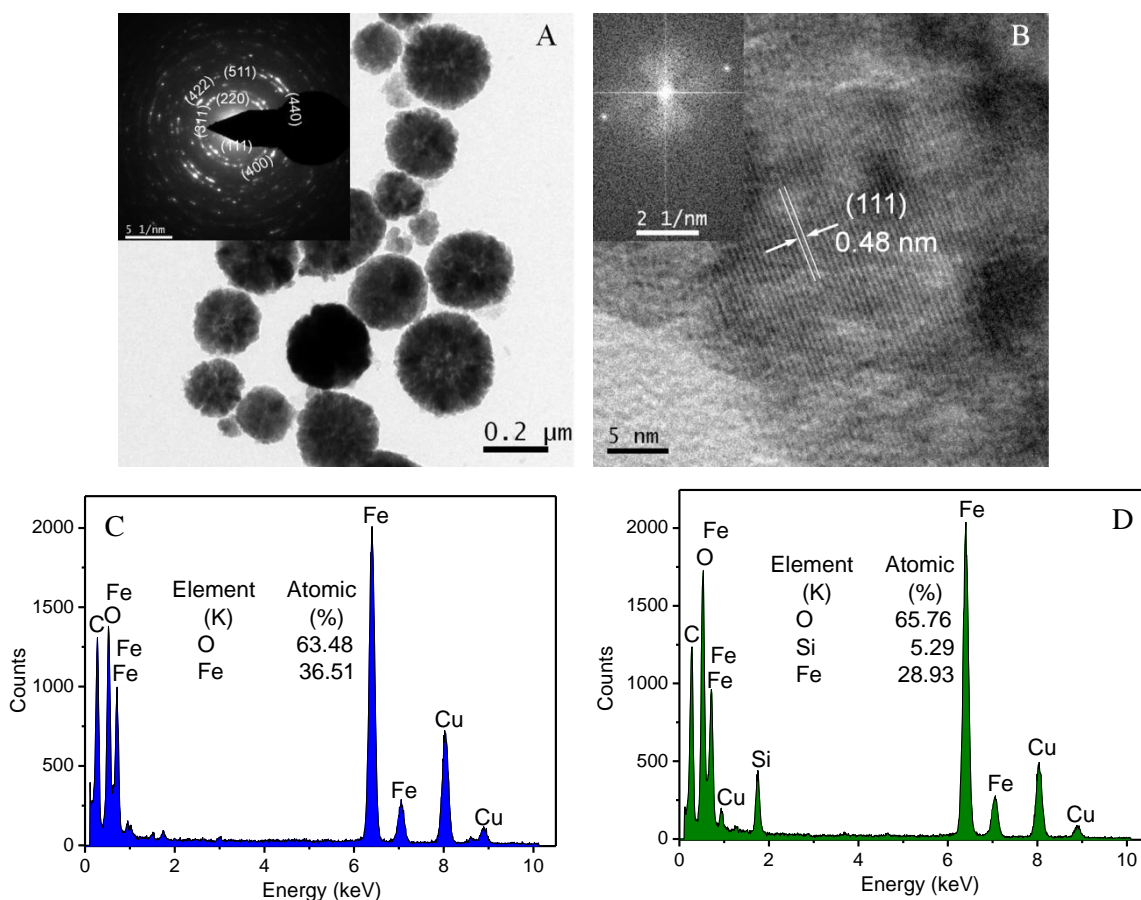


Fig. 5.7 The TEM images of spherical aggregate MS48@Si core-shell nanostructure (A) bright field image with its SAED as inset, (B) HRTEM marked with (111) crystal face and its corresponding FFT as inset. The EDS elemental composition of (C) MS48 and (D) MS48@Si.

The excess oxygen in MS48@Si with respect to MS48 is due to the presence of additional oxygen sources from structural water in hydrated silica shell. The XPS method is very suitable for surface investigation due to a high surface sensitivity. In the XPS spectra (Fig. 5.8A) the Fe, Si, O and C elements were identified and their concentrations were calculated. From the shape and shift of the XPS spectra, the chemical bonding of surface elements was inferred. The results obtained from the high resolution XPS analysis indicate the signal at 101.3 eV corresponds to the SiO₂ in the oxide layer, appended on magnetite microsphere surfaces after being coated with silica. The interaction through hydroxyl groups of left over ethylene glycol or magnetite surface (Fe-OH), a network structure siloxane (Si-O-Si) might have formed between them.

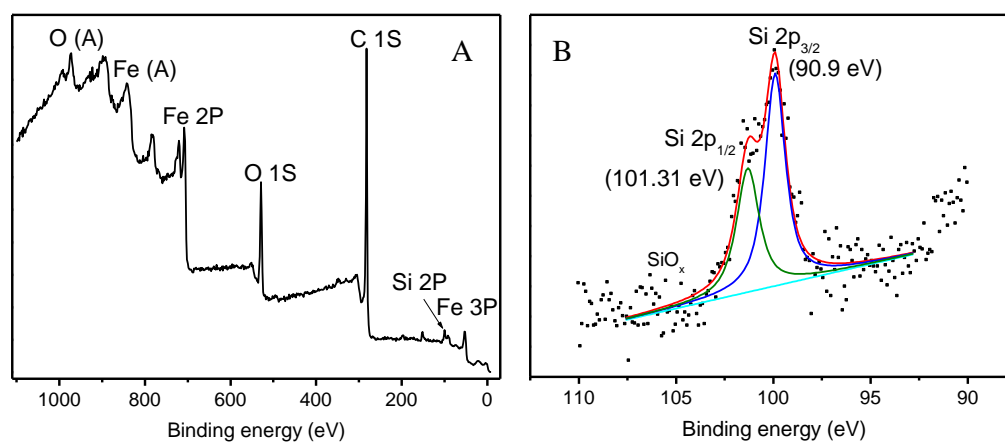


Fig. 5.8 (A) XPS wide spectrum and high resolution (B) Si 2p spectrum of MS48@Si nanostructures

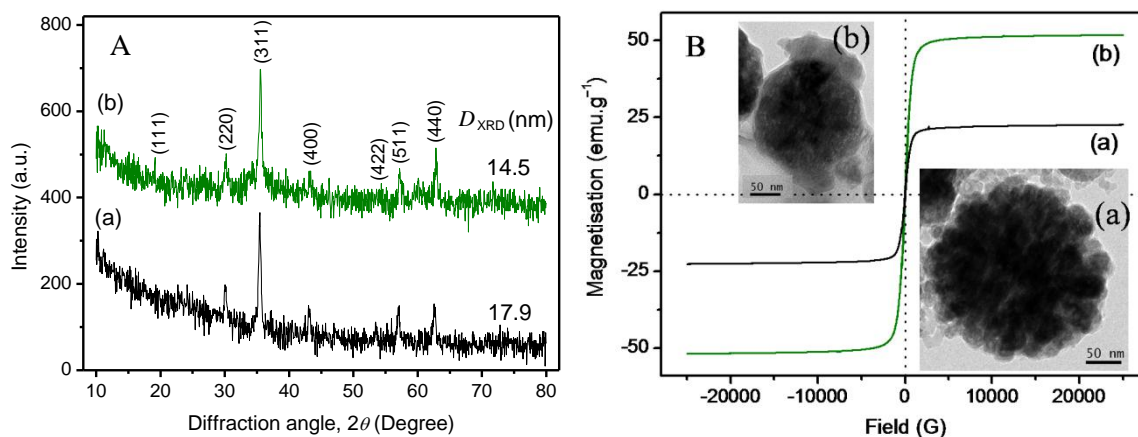


Fig. 5.9 (A) XRD patterns and (B) VSM profiles of (a) Fe₃O₄@SiO₂ and (b) Fe₃O₄@Ni-silicate.

As-prepared microspheres via a solvothermal reaction were coated with silica layer by sol gel method to get Fe₃O₄@SiO₂ core-shell microspheres. Then, the obtained Fe₃O₄@SiO₂ core-shell microspheres were hydrothermally treated in aqueous NiCl₂.6H₂O and

ammonia solution at 120°C, leading to the formation of Fe₃O₄@Ni-silicate yolk–shell microspheres. The XRD, PPMS profiles and TEM images of core-shell as well as yolk-shell microspheres are shown in Fig. 5.9.

The crystallographic structure and phase purity of the as-synthesised products are identified by XRD. The crystallite size of Fe₃O₄@SiO₂ and Fe₃O₄@Ni-silicate were found to be 17.9 and 14.5 nm respectively as calculated from Scherrer's formula. After coating with the silica layer, no characteristic peaks of other magnetite materials can be detected, indicating the silica layer is amorphous alongwith reasonable drop in M_S value to 22.9 emu.g⁻¹. PPMS data further confirms that the synthesised microspheres possess a typical yolk–shell structure as the magnetic layer (nickel) on the surface Fe₃O₄@Ni-silicate is responsible for significant improvement of saturation magnetisation 51.9 emu.g⁻¹ value.

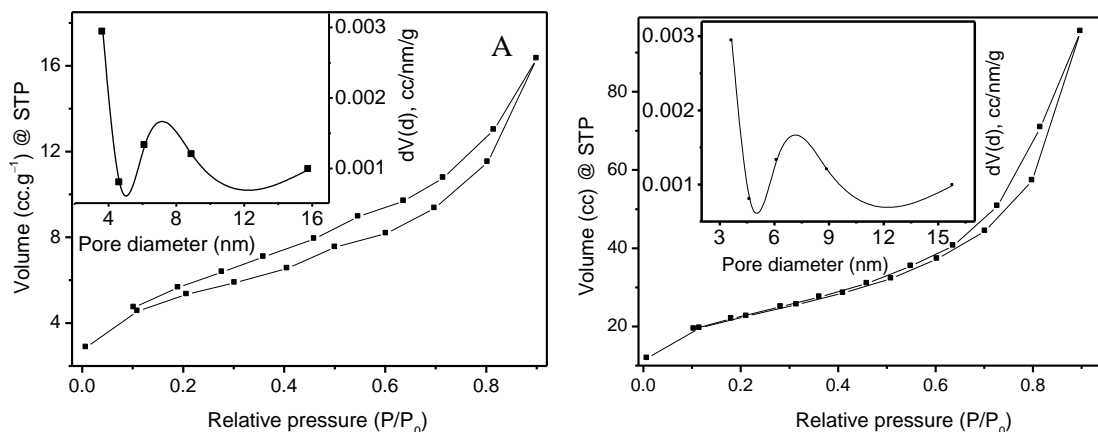


Fig. 5.10 (A) Volume N₂ adsorbed versus relative pressure for the powder samples (A) MS48 Fe₃O₄ spheres and (B) extracted silica precursor at 77 K. Inset shows the plot of pore size distribution derived from the BJH analysis.

Figure 5.10 shows the nitrogen adsorption–desorption isotherms and the corresponding pore size distribution profiles of two representative magnetite and silica specimens. The complete analyses of the isotherms are provided in Table 5.4.

Table 5.4 The details of BJH pore distribution desorption and BET surface area of extracted silica precursor and microspheres MS48

Sample	BJH pore distribution desorption				BET	Size, S_{SA} (nm)
	Surface area (m ² .g ⁻¹)	Pore volume (cm ³ .g ⁻¹)	Pore diameter (nm)	Total pore volume (cm ³ .g ⁻¹)	Surface area (m ² .g ⁻¹)	
Silica	145	0.357	15.433	0.3982	207	5.6
MS48	9	0.02	3.659	0.02527	18	64.4

Both the graphs show hysteresis loops of type IV of Brunauer's classification, indicating the presence of mesopores in the powders. The plot of dv/dr versus pore size determined by BJH method shows that the pores (inset of Fig. 5.10) are in the mesoporous range (5-10 nm) and is attributed to the interspaces of the constituent particles. It is obvious that the surface area of magnetite powders decreased when it is large spherical clusters (Table 5.4). The particle size (D_{SA}) measured by nitrogen adsorption is somewhat smaller than the size estimated from TEM analysis (Fig. 5.2).

Silver decorated magnetite nanospheres

Though the excess EG acts as both the solvent and reductant, Na_3Cit was chosen because the three carboxylate groups have strong coordination affinity to Fe III ions favours the attachment of citrate groups on the magnetite surface and prevents them from aggregating into large single crystals as occurred previously. Moreover, Na_3Cit is widely used in food and drug industry and citric acid is one of products from tricarboxylic acid cycle (TCA), a normal metabolic process in human body. Fig. 5.11D shows the powder XRD pattern of citric acid coated magnetite nanospheres (NS) as well as silver loaded (NSAg). The NSAg diffraction peak can be attributed to either cubic-phase Fe_3O_4 (JCPDS Card, No 19-0629) or Ag (JCPDS card, No 04-0783). No diffraction peaks belonging to impurities are observed in this pattern. These results indicate that the product consists of crystalline Fe_3O_4 and Ag.

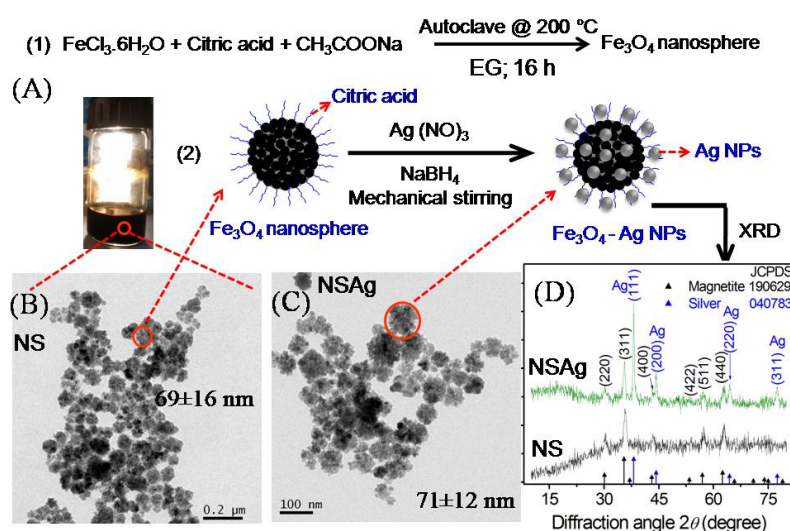


Fig. 5.11 (A) Schematic representation of core shell nanostructures fabrication and (B, C) TEM images and (D) powder XRD patterns of the NS and NSAg, the vertical drop lines (black) are the theoretical Bragg positions for inverse spinel magnetite phase and Ag (blue) following JCPDS Card No. 19-0629 and 04-0738 respectively are presented in different colours.

The lattice constants of Fe_3O_4 and Ag calculated by the peak positions are 0.8368 nm and 0.4079 nm, both of which are in good agreement with the reported ones of Fe_3O_4 (0.8396 nm) and Ag (0.4086 nm). The particle sizes of Ag and Fe_3O_4 estimated by the peak widths are 9.86 and 24.09 nm, according to Scherrer's formula. The crystallite size of magnetite before and after silver loading weren't change at all. It is noticed that the peak intensities of silver are high in comparison with those of Fe_3O_4 , probably caused by the abundance of silver NPs on the surface of magnetic material along with large lattice stress from the interface of Ag/ Fe_3O_4 and the high crystallinity. Figure 5.12 shows the XPS survey of NSAg sample. After loading of Ag, the peaks due to C 1s, O 1s, and Ag 3d can be seen. The core level Ag 3d XPS signal is shown in Fig. 5.14C. The binding energies of Ag $3d_{3/2}$ and Ag $3d_{5/2}$ are 367.6 and 373.6 eV respectively.

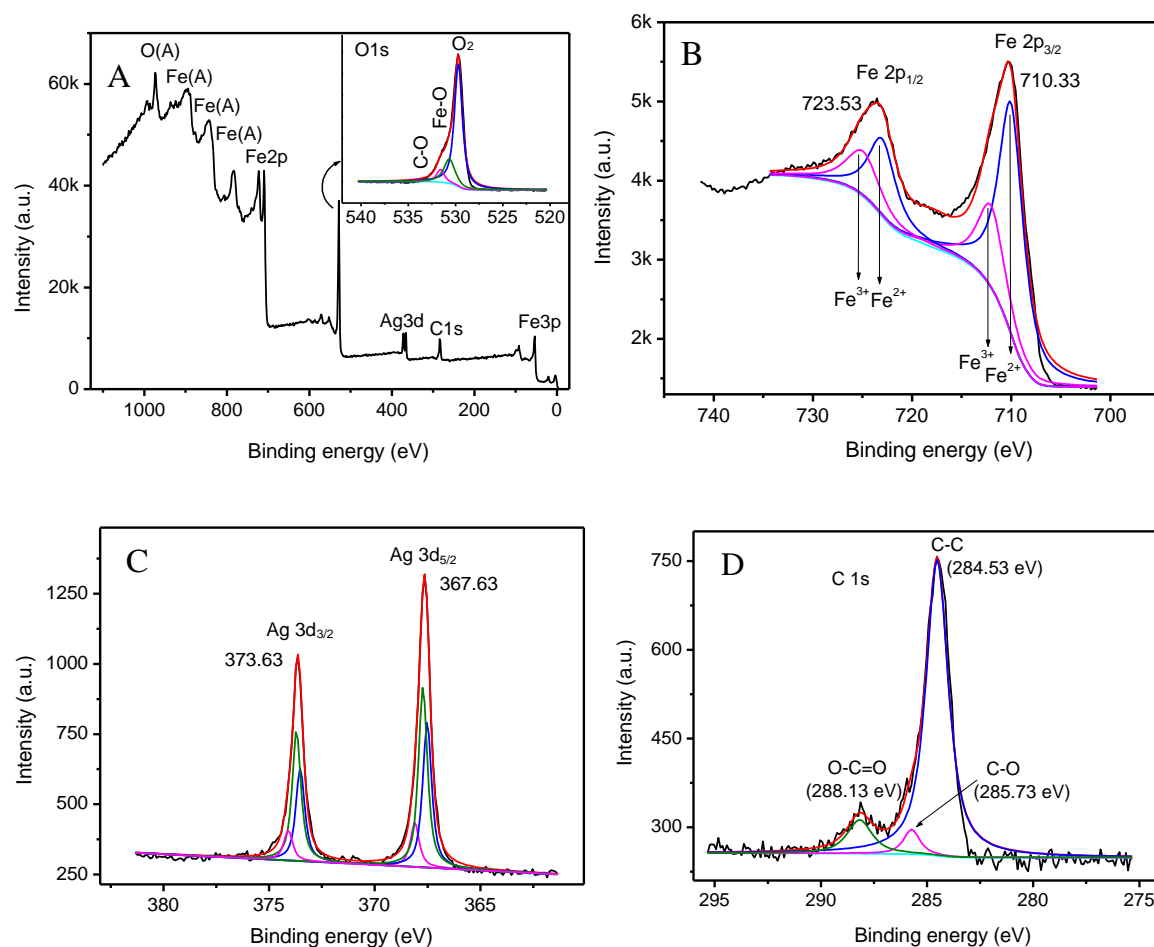


Fig. 5.12 (A) XPS survey spectra of nanosphere, (B) the details of the Fe $2p_{1/2}$ and Fe $2p_{3/2}$ peaks (C) Ag $d_{3/2}$ and Ag $3d_{5/2}$ and (D) C 1s spectra of silver decorated nanospheres.

The splitting of the 3d doublet of Ag was ~ 6 eV, suggesting the formation of metallic silver. As Ag can be easily oxidised by oxygen, it is possible that part of Ag on the surface was AgO. The core-level O 1s at 532.3 eV was attributed to lattice oxygen (inset of Fig.

5.12A). The relative surface area of Fe^{2+} : Fe^{3+} were calculated after deconvolution of Fe 2p spectra, which is maintained at 1:2 i.e., stoichiometry of magnetite.

5.4.1.3 Protein adsorption capacity

In biological applications, low level unspecific adsorption and strong specific reactions are anticipated. In this section, the unspecific binding between BSA and different magnetite spheres or modified Fe_3O_4 were examined.

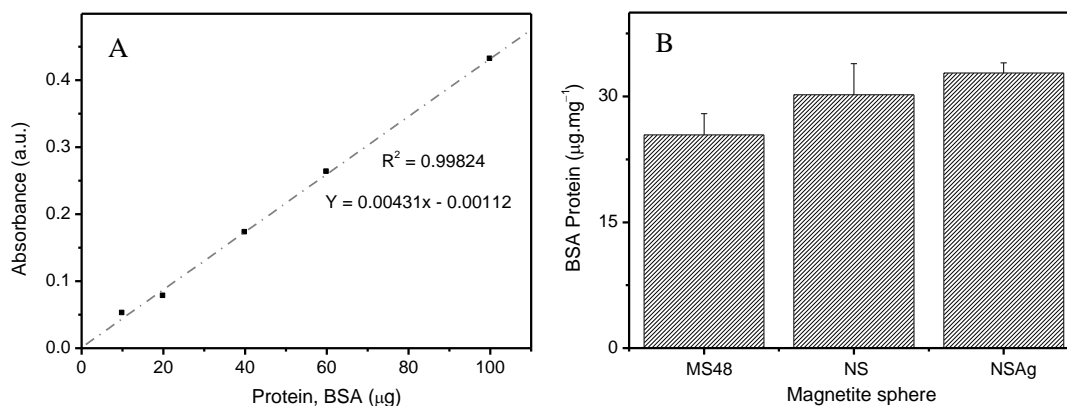


Fig. 5.13 Bovine serum albumin adsorption capacity of spheres was quantified by Bradford's assay (A) calibration curve of known protein concentration and (B) amount of BSA adsorbed per gram of sample.

The comparison on the binding capacity of BSA to MS48, NS and NSAg Fe_3O_4 spheres are shown in Fig. 5.13. It was found that the BSA binding capacity to spheres at physiological pH (7.4) are 25.43, 30.2 and 32.8 $\mu\text{g}/\text{mg}$ of Fe_3O_4 , respectively.

5.4.1.4 Cell culture: Dose dependent cytotoxicity assessment

To examine the feasibility of the obtained magnetite particles in bio-related fields, the cytotoxicity was investigated. The effect of the magnetite spheres (~ 70 nm) on cell proliferation have been assessed with human breast carcinoma cells (MDA-MB-468) by means of a MTT assay (Fig. 5.14). The MDA-MB-468 cell line was treated with five different concentrations of NS and NSAg and the cell survivability was measured by MTT assay (Fig. 5.14). In this condition, the cell viability for NSAg showed dose-dependent toxicity and was maintained greater than 80% cell proliferation upto the concentration of $80 \mu\text{g}\cdot\text{ml}^{-1}$ whereas the biocompatible magnetite core-citrate shell of NS alone showed nearly $\sim 100\%$ proliferation and do not induce acute cytotoxicity even at the level of a few tenths of a microgram ($100 \mu\text{g}\cdot\text{ml}^{-1}$) within 24 h.

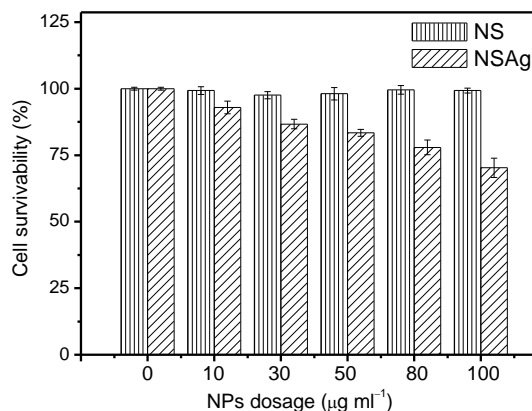


Fig. 5.14 Cell survivability of MDA cells exposed to different concentrations of magnetite nanospheres (NS) and silver loaded magnetite nanospheres (NSAg) determined by the MTT assay after 24 h. Results are the mean \pm SD (vertical bars) of three independent experiments each carried out in triplicate.

5.4.1.5 Fluorescent microscopic examination of cells

After 24 h, cell morphology was analysed by fixing the cells on chamber slides followed by stained with blue 4'-6-diamidino-2-phenylindole (DAPI: 1.5 $\mu\text{g/mL}$ in PBS solution) for 10 min. DAPI staining is useful in identifying pyknotic or fragmented nuclei resulting from apoptosis or cell death and any irregularities in cell shape. The nuclei of MDA-MB-468 cells treated with magnetic nanocrystals (NS and NSAg) were intact as observed under a fluorescent microscope (Fig. 5.15A–F), indicating that the cells were viable and morphologically similar to the control cells.

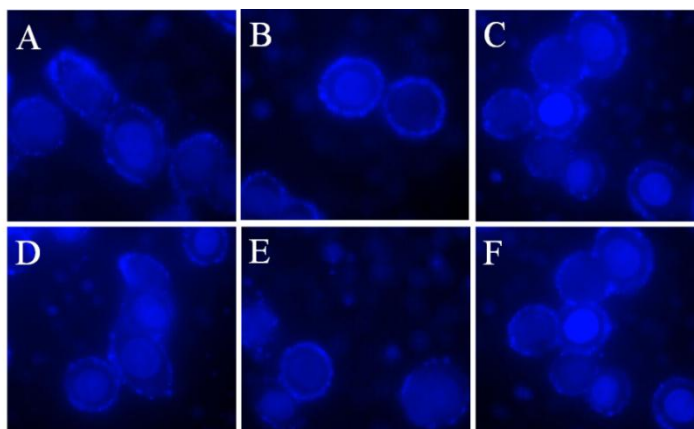


Fig. 5.15 Fluorescence images of (A, D) control HCT 116 cell and MNPs (B, E) NSAg and (C, F) NS treated cells with their nuclei stained by DAPI are blue. The scale bar corresponds to 20 μm .

Hence, these nanospheres are excellent candidates for *in vivo* delivery of chemotherapeutic drugs for cancer therapy and many other therapeutic applications. Based on MTT assay, the as-synthesised NSAg and NS showed no significant toxicity to MDA-MB-468 cells and did not affect cell morphology. We believe that this synthesis is a

significant step forward towards the manufacturing of magnetite nanocrystals not only with regard to the reaction conditions that avoid toxic capping agents limiting the biomedical applicability but also in terms of the potential for industrial scale-up.

5.4.2 Thermal decomposition method

The current synthetic methodology produces magnetite nanocrystals of different morphology and size. Surfactants form a basic requirement for crystal stabilisation against oxidation and their steric demand controls the nanocrystals with different morphology by tuning growth rate of the specific crystal facets. Moreover, truncated octahedra and cube shape are engineered by OA/OAm and OA-only systems along with heating temperature/rate and physical stimuli. The majority of crystal growth occurs quickly (within few minutes) after the nucleation. Size of the nanocrystals couldn't be controlled by shortening or prolonging the growth duration rather Ostwald ripening broadens the size distribution at prolonged time (Kovalenko *et al.*, 2007). The heating hold-step is a common protocol in reflux-based syntheses and is used to separate the nucleation and growth phases following LaMer mechanism (Douglas *et al.*, 2012). In all experiment, the hold temperature of 120°C was chosen to encourage the formation of coordination complexes between the iron precursor, solvent and the growth duration (reflux) to 30 min.

5.4.2.1 Morphology/structural characterisation of cube/truncated octahedra

In the first set of experiments, only deprotonated OA molecules were used. TEM micrographs and the corresponding SAED patterns of as-synthesised magnetite NCs are presented in Fig. 5.16. The representative BF-TEM images demonstrate the formation of cube shaped Fe₃O₄ nanocrystals and the degree of monodispersity. Even though the particles resemble square shape under the 2D TEM view, observation of clear side planes under higher magnification (inset of Fig. 5.16B) implied the formation of 3D cube morphology. The nanocrystals are observed to have a uniform edge length, sharp edges and corners, and flat facets with only atomic steps. The degree of monodispersity or narrow particle size distribution of the as-synthesised crystals from the histogram is confirmed (inset of Fig. 5.16B) and the mean particle size, calculated from the micrographs of small and large cubes are ~6.4 and ~134 nm with a standard deviation of 0.82 and 34 respectively. The high-resolution TEM (HRTEM) image showed the highly crystalline nature of the nanocubes (Fig. 5.16C), and the measured *d*-spacing 4.18 Å is twice the value of the magnetite (400) plane with corners of (111).

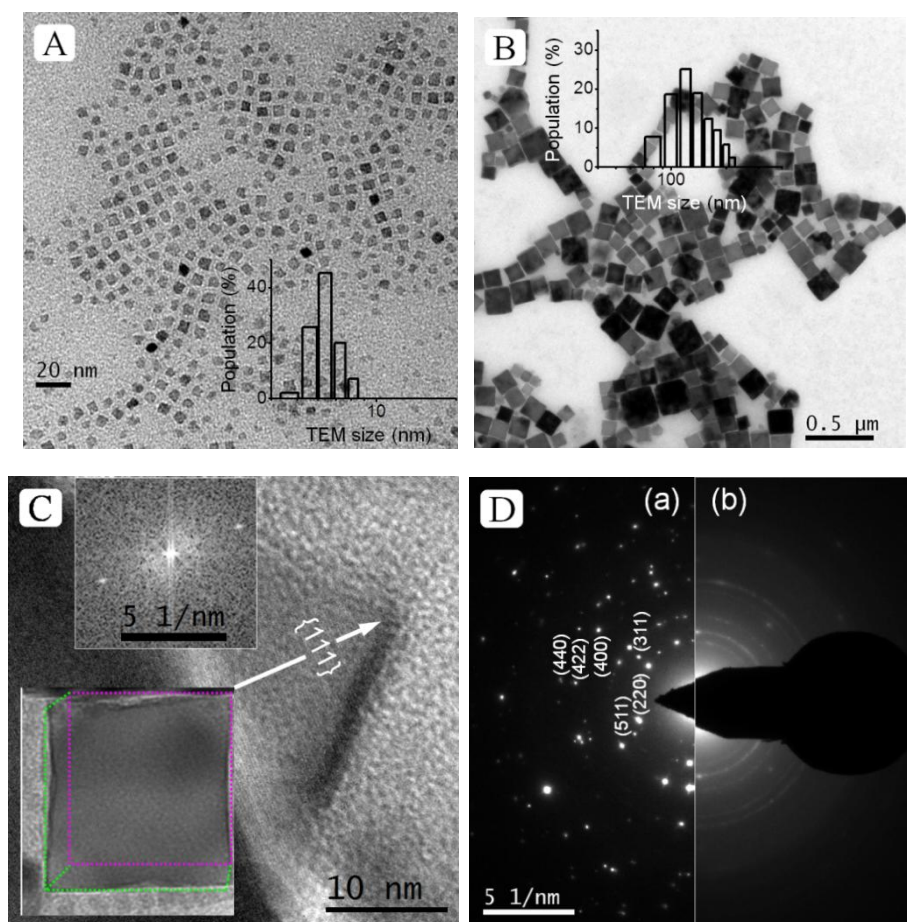


Fig. 5.16 TEM image of (A) lower (B) higher magnification (C) HRTEM and (D) SAED patterns of magnetite nanocube. Insets are histograms (A, B) and FFT (C).

The ultra-small cubes are well separated due to less magnetic attraction imposed by smaller size as well as presence of surfactant layer. Meanwhile, Fig. 5.16B crystals appear to form chain like structures due to the strong magnetostatic interaction between dipoles that exists in the synthesised ~ 135 nm cubes. Such a phenomenon may be due to a pronounced Ostwald ripening in the synthesised nanocubes of large sizes in an undisturbed condition (no external barrier such as magnetic stirring during reflux). SAED in Fig. 5.16D shows diffraction patterns corresponding to (220), (311), (400), (422), (511) and (440) crystal planes of Fe_3O_4 with inverse spinel structure (JCPDS No. 19-0629) and the same recorded on an isolated crystal of ~ 135 nm size reveals single-crystal-like diffraction (Fig. 5.16D). The diffraction spots are widened into narrow arcs that indicate polycrystalline nature of ultrafine cubical primary nanocrystals (panel 'b' Fig. 5.18D).

In a second set of experiment, truncated octahedra crystals were obtained with tuneable size in the range of 10 to 135 nm by careful adjustment of OA:OAm surfactant ratio from 1:1 to 4:1 and growth kinetic modulation (Fig. 5.17). The mixed stabiliser

directs the nuclei to grow isotropically along the three crystallographic axes to truncated octahedra. As the amount of the OAm increases significantly, not only does the {111} surface show saturated surface coverage, the surface {100} is also coordinated by the same restricting overall growth and leading to the formation of small ~10 nm truncated octahedral NCs (Fig 5.17A), also the nanocrystal surface prevents them from aggregation by means of the surfactant layer. This result can be explained by the fact that OAm possesses comparatively weak, isotropic binding to iron centres on the surface of crystals whereas OA strongly binds selectively to crystal facets due to its high oxophilicity and encourages anisotropic growth in the (100) rather than (111) direction (Douglas *et al.*, 2012). The interaction between a surfactant and a crystal surface can occur in many ways and is mainly based on dipole–dipole, hydrogen bond, electrostatic or vdW interactions.

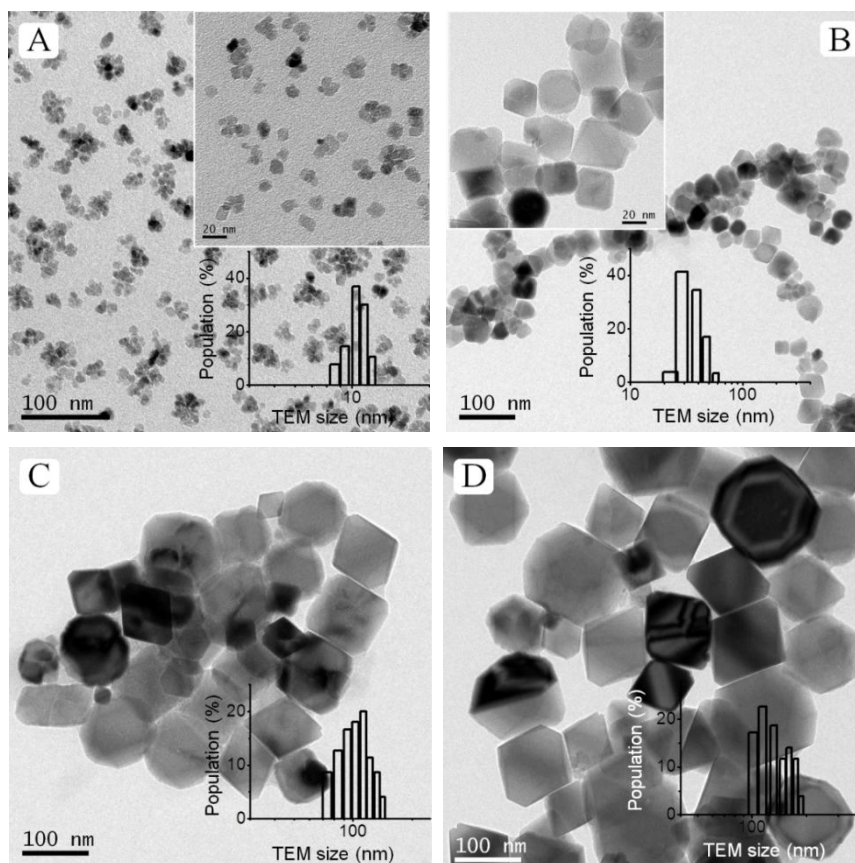


Fig. 5.17 TEM images of size tuned (A) 10 nm, (B) 36 nm, (C) 100 nm and (D) 135 nm magnetite truncated octahedra and their histograms inserted to each image.

OAm has an amine head group which can only bind as a single motif to the surface, whereas different binding motifs are possible for carboxyl group of OA such as monodentrate, bridged, or chelating. By only considering the three binding modes of OA compared to one binding mode for OAm and ignoring the effect of electron affinity, a

comparison between carboxyl and amine groups makes it clear that (statistically) OA has a greater probability of binding to surface Fe atoms than OAm if they are competing for the same Fe^{2+} or Fe^{3+} atom on the NC surface (Harris *et al.*, 2015). Figure 5.17B and C shows about 36 and 100 nm octahedra formed under low OAm concentration. When the amount of OAm decreased significantly, up to 1 mmol, the product (Fig. 5.17D) exhibited large truncated octahedral shapes, owing to all crystal faces being coordinated by OA:OAm capping ligands and showing saturated surface coverage, thus directing the nuclei to grow large 3D single crystals under no physical stimuli. These results suggest that finer shape control over the nanocrystals can be achieved through selective stabilisation of crystal facets by surfactants and growth kinetic modulation.

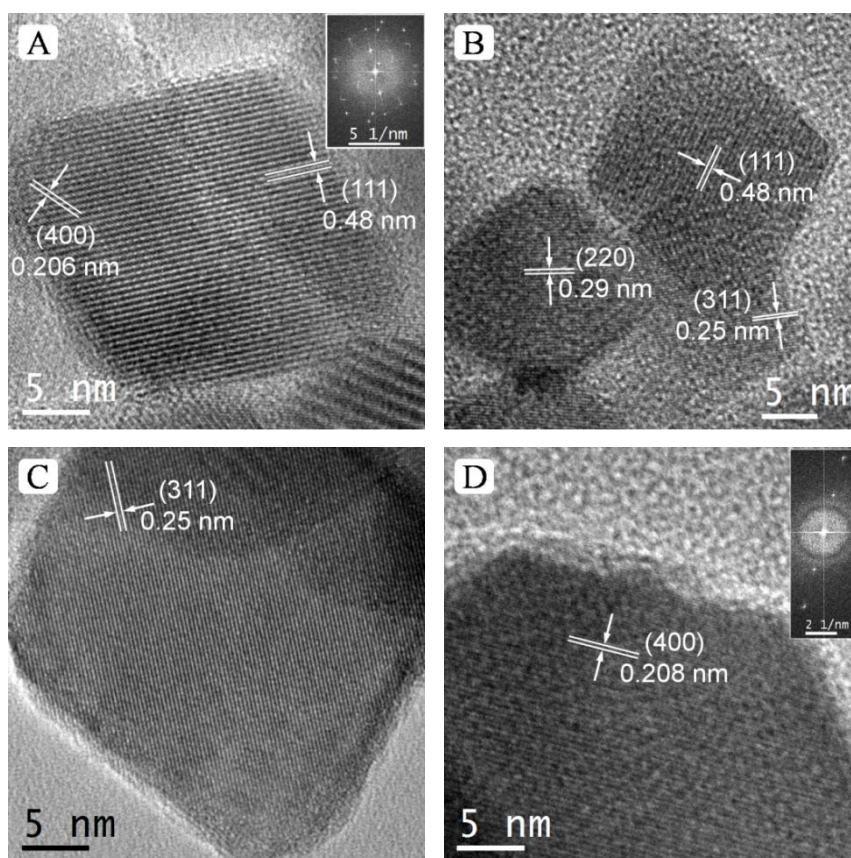


Fig. 5.18 High resolution-TEM images of full view and corners and edges of truncated octahedral crystals.

The high resolution image depicting the lattice fringes of typical truncated octahedral crystals of magnetite are shown in Fig. 5.18. The octahedra look to be rhombohedral shape when viewed in 2D array (Fig. 5.18A and B). High resolution micrographs shown in Fig 5.18B and D are the corners and side planes of magnetite, lattice fringes and atomic positions can be clearly observed in the all the crystals. The

interplanar spacings were determined from the HRTEM image as 0.48, 0.29, 0.25, 0.206 nm as marked, which corresponds to the (111), (220), (311) and (400) reflections of *fcc* Fe₃O₄. The formation of regular, linear assemblies is noted for both the cube and truncated octahedral samples owing to the strong dipolar magnetic interaction. The purity of the dispersed nanocrystals has been confirmed by performing EDS attached to the TEM which shows the presence of Fe and O peaks in all NCs (data not shown here). In addition, C peak is mainly from surface adsorbed OA or OAm and the Cu and C peaks are obtained from the carbon coated copper grid on which the nano-fluid dispersion is deposited.

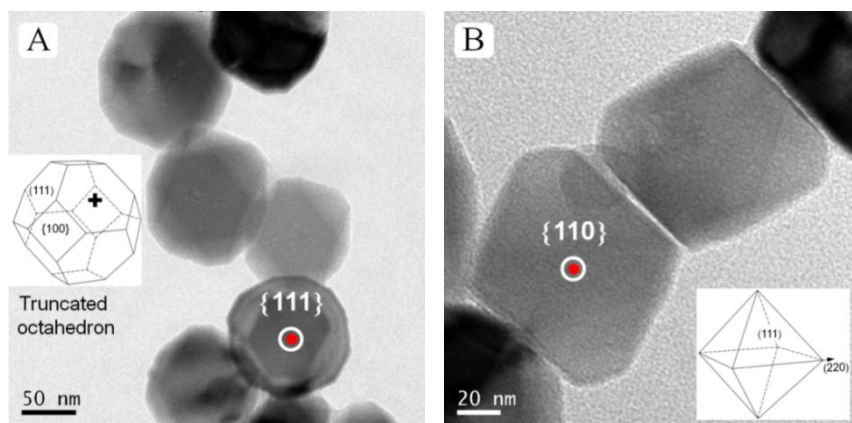


Fig. 5.19 Projection of truncated octahedral Fe₃O₄ NCs along different direction and the definition of particle size.

On the basis of the TEM results shown in Fig. 5.16-19, it is proposed that both thermodynamic and kinetic factors dictate the shape evolution of the Fe₃O₄ nanocrystals at different stages of the reaction and the organic surfactants also play important roles in the synthesis. Based on the HRTEM study, it is concluded that surfactant modulate the growth rate along certain directions, which results in a variety of nanocrystal shapes.

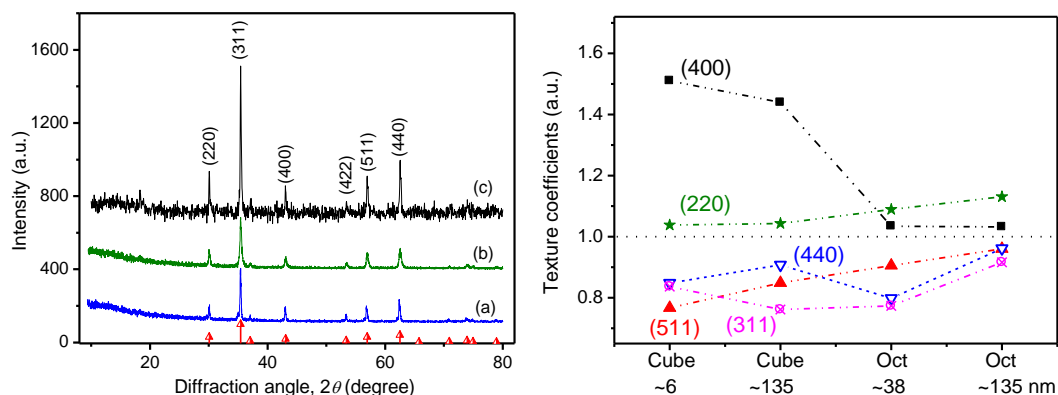


Fig. 5.20 (A) XRD patterns and (B) its texture coefficient of (a) CU135 (b) OC10 and (c) OC40 magnetite sample.

XRD patterns collected on dried powders of all MNCs product are shown in Fig. 5.20. Diffraction peaks can be clearly seen and indexed Debye-Scherrer rings corresponding to (220), (311), (400), (422), (511) and (440) planes of *fcc* magnetite ($\text{Fe}^{2+}\text{Fe}^{3+}_2\text{O}_4$) inverse spinel crystal structure (JCPDS 19-0629). The strong and sharp peaks revealed that Fe_3O_4 particles are well crystallised. Texture coefficient results are displayed in Fig. 5.20B and as expected, the predominance of (400) active crystal facets are more pronounced in CU6 and CU135 due to cubic shape compared to truncated octahedra where equal predominance of all facets as per the JCPDS data.

5.4.2.2 Lorentzian site analysis on Mössbauer spectra

To determine the exact iron oxide phase of the nanocrystal systems, Mössbauer spectra recorded on CU135 and OC135 specimens, are similar to those usually observed for magnetite (Fig. 5.21). The experimental spectra were fitted with a Lorentzian profile using the Recoil program and corresponding fitting parameters extracted from the resultant fits for both samples are summarised in Table 5.5. One can unambiguously identify two resolved sextets, the outer sextet is attributed to Fe^{3+} in the A site of inverse spinel magnetite while the other inner sextet is ascribed to Fe^{3+} ions located in the B site. It is clear from the isomer shift (δ) values that both the Fe^{2+} and Fe^{3+} ions are present in the samples.

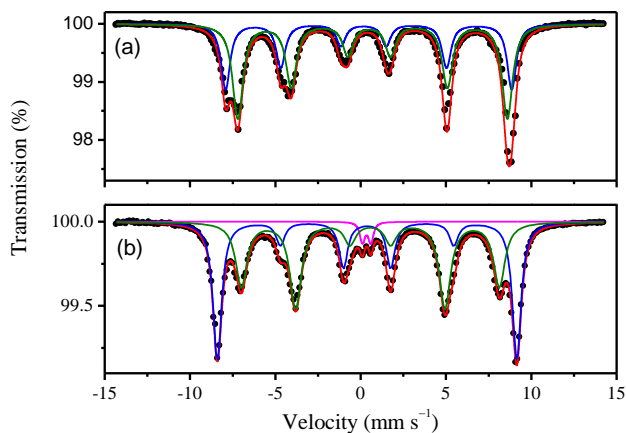


Fig. 5.21 ^{57}Fe transmission Mössbauer spectra of (a) CU135 and (b) OC135 recorded at room temperature. Scatter symbols represent the experimental data and the solid continuous lines correspond to the fits obtained by Lorentzian site analysis of the Recoil program.

The sextet with a lower δ value and higher hyperfine field (B_{hf}) is assigned to Fe^{3+} ions at the tetrahedral (A) site and the other sextet with a higher δ value and lower B_{hf} is attributed to iron ions at the octahedral [B] site. The δ values corresponding to tetrahedral (δ_{A}) and octahedral (δ_{B}) sites of the OC135 sample are found to be 0.37 and 0.56 $\text{mm}\cdot\text{s}^{-1}$ respectively with respect to $\alpha\text{-Fe}$ ($\delta=0.0 \text{ mm}\cdot\text{s}^{-1}$) foil. For CU135, δ_{A} and δ_{B} are found to

be 0.32 and 0.61 mm.s⁻¹ respectively. The different values of δ for OC135 and CU135 samples illustrates that the s-electron density at the Mössbauer active nuclear site is significantly affected by the morphology. The range of values of isomer shift indicates that iron exists in Fe³⁺ valence state with high spin configuration in the prepared samples. The sextet area leading to a Fe_{tetra}³⁺/Fe_{octa}^{3+,2+} ratio of CU135 and OC135 are found to be 0.6 and 0.9 respectively, which exceeds the theoretical ratio 0.5, thus this phenomena is called super non-stoichiometry in oxygen or cationic vacancies.

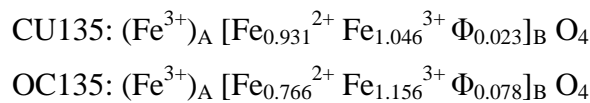
Table 5.5 The Hyperfine magnetic field, isomer shift, quadrupole splitting (ϵ), linewidth and relative area in tetrahedral and octahedral sites of Fe³⁺ in NCs derived from Mössbauer spectra recorded at room temperature

Sample	Site	δ (± 0.03) (mm.s ⁻¹)	ϵ (± 0.03) (mm.s ⁻¹)	B_{hf} (± 0.4) (T)	Width (± 0.03) (mm.s ⁻¹)	Area (%)
CU135	A	0.32	0.15	52	0.30	37.5
	B	0.61	0.10	49	0.35	62.5
OC135	A	0.37	0	54.4	0.32	46.3
	B	0.56	0	46.7	0.40	51.1
	Doublet	0.34	0.5	-	0.18	2.6

In contrast to relative intensity ratio 1:2 corresponding to Fe between A and B sites in bulk inverse spinel magnetite, (Fe³⁺)_A [Fe²⁺Fe³⁺]_B O₄. The dynamic electronic disorder creates vacancy during the formation process resulting in slight deviation from stoichiometric magnetite with the formula (Fe³⁺)_A [Fe_(1-3x)²⁺Fe_(1+2x)³⁺Φ_x]_B O₄, where Φ represents the cation vacancy at [B] site and x represents the correction factor for actual stoichiometric proportion in the sample. The value of x can be extracted from the Mössbauer spectra using the following equation:

$$\frac{R_B}{R_A} = \frac{(2-6x)}{(1+5x)} \quad (5.1)$$

where R_B/R_A are the relative area ratio of [B] to (A) site. We observed the global composition of CU135 and OC135 as



The complexity of iron chemistry, whereby numerous phase and structural types are produced from the same iron solution by just varying one of several experimental

conditions rendering the reaction mechanism difficult to investigate. It is very essential to identify magnetism within iron oxide.

5.4.2.3 ZFC-FC magnetic measurements

Figure 5.22 shows the magnetisation of CU135 and OC135 as a function of temperature measured at 100 Oe after zero-field cooling (ZFC) and also with 100 Oe field cooling (FC). A comparison between the typical M-H loops of CU135 and OC135 samples measured at 300 K are shown as inset of Fig. 5.22. At 300 K, both the nanocrystals exhibit a superparamagnetic behaviour with small value of coercivity and remanence. The M_S value is greatly affected by crystallinity of the sample. The M_S value of similar sized (~ 135 nm) magnetite crystals CU135 and OC135 are found to be 89.23 and 82.31 emu.g^{-1} at 4 T respectively, which is higher than ~ 79 emu.g^{-1} for 250 nm magnetite spheres prepared by solvothermal treatment of $\text{Fe}(\text{Cl})_3$ in ethylene glycol and is very close to 92 emu.g^{-1} for bulk magnetite (Frison *et al.*, 2013).

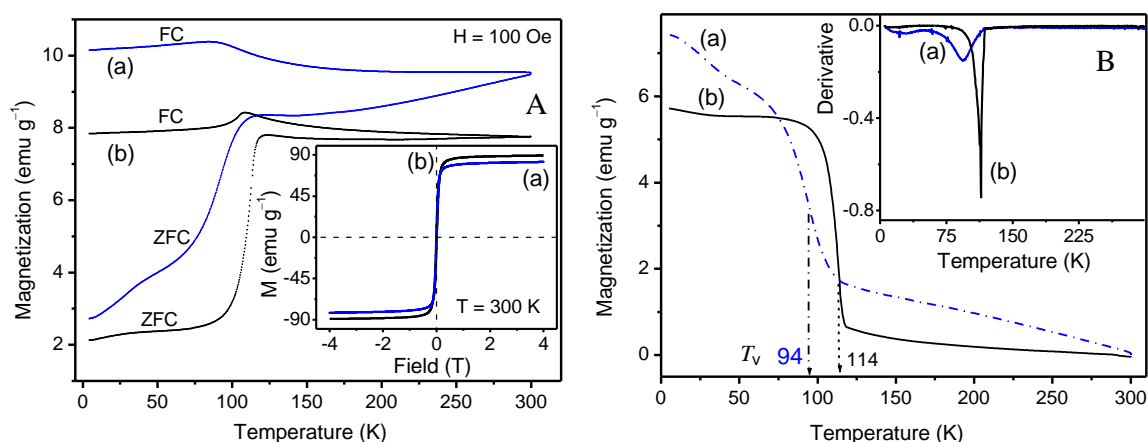


Fig. 5.22 (A) ZFC and FC magnetisation curves and (B) its difference curves of the (a) OC135 (b) CU135 crystals under an applied field of 100 Oe; the inset is the hysteresis loop of the same Fe_3O_4 crystals at 300 K.

This result indicates the formation of well-defined crystalline structure for the as-synthesised magnetite as illustrated in TEM images. The nanocubes exhibit higher M_S than that of truncated octahedra, which indicates that the magnetic properties show the shape dependence.

Though the magnetic moment of Fe^{3+} ($5 \mu_B$) is higher as compared to that of Fe^{2+} ($4 \mu_B$), the trivalent irons in [A] and (B) are antiferromagnetically oriented and cancel each other's net magnetic moment of $4 \mu_B$ per formula unit in case of inverse spinel structure. Theoretically, a higher value of M_S is expected as the concentration of Fe^{2+} ions at octahedral sites in the CU135 sample is higher than the OC135 sample. This leads to an

increase in net magnetisation per unit formula for the CU135 sample. The room temperature Mössbauer study is consistent with this result, revealing higher average B_{hf} for the CU135 sample as compared to the OC135 sample.

When an external magnetic field is applied, more and more particles orient their magnetic moments parallel to the applied field with temperature increase. The temperature at which the thermal energy ($k_B T$) overcomes the magnetic anisotropy energy of nanoparticles is referred to as the blocking temperature, T_B (Yang *et al.*, 2011). Above T_B the sample is paramagnetic and below T_B , it is ferromagnetic (Liu and Zhang, 2001). In the case of FC procedure, magnetisation monotonically increases with temperature. The divergence of FC and ZFC curves below T_B is attributed to the existence of magnetic anisotropy barriers. We observed both enhanced magnetisation and a severe increase of the blocking temperature (T_B , maximum of the ZFC curve) at ~ 124 and ~ 300 K for CU135 and OC135 samples respectively. However, if a distribution of sizes is present, the peak temperature deviates from the true T_B which contributes to the Mössbauer line-width. Since the size of the nanocrystals is almost same for both the samples, different T_B are explained considering different morphology. An increase of T_B is related to an increase of the magnetic dipole–dipole interactions (Lima *et al.*, 2013; Mandel *et al.*, 2013). An increasing number of particles in the cluster intensifies the interaction and induces an upward shift of T_B (Mandel *et al.*, 2013). It should be noted that, for both the samples, the temperature of irreversibility (where FC and ZFC curves meet) was far away from the T_B , suggesting dipole-dipole interparticle interactions and size-polydispersity within the sample (Lartigue *et al.*, 2012).

Table 5.6 The saturation magnetisation (M_S), reduced remanent magnetisation (M_R/M_S) and coercivities (H_C) as determined at 300 K upto 4 Tesla for cube and truncated octahedral particles.

Magnetite	M_S (emu.g ⁻¹)	M_R/M_S	H_C (Oe)	T_B (K)	T_V (K)	D_{TEM} (nm)
CU135	89.23	0.072	62.37	124	114	134.54 ± 34.04
OC135	82.31	0.078	93.13	300	94	135.78 ± 26.46

The blocking temperatures (T_B ; witnessing the ferromagnetic–superparamagnetic transition) and the broadness of the maxima of the ZFC curves strongly depend on the average particle size and the degree of polydispersity. T_B values reported in Table 5.6 with other relevant magnetic features, suggests that the anisotropy in barrier heights increase, likely because of large dipole–dipole interactions between particles of larger size.

Broadening of the ZFC curves also increases with the D_{TEM} and σ_{TEM} , implying a broader distribution of energy barriers to magnetic moments reorientation (Frison *et al.*, 2013). A detailed analysis of both FC and ZFC curves and their difference plot (Fig. 5.22B) shows the characteristic Verwey transition (T_V) temperature $\sim 114^\circ$, $\sim 94^\circ\text{C}$ for CU135 and OC135 respectively. For stoichiometric bulk magnetite, there is an apparent magnetic transition at ~ 119 K, which corresponds to Verwey transition originating from fast electron hopping between the Fe^{2+} and Fe^{3+} ions on the octahedral B sites occurs (Jia *et al.*, 2007) which is responsible for the high electrical conductivity of magnetite above T_V (Shebanova and Lazor, 2003). It is also believed that due to the change of crystal symmetry from cubic to monoclinic structure and charge-orbital ordering (Huang *et al.*, 2006). The Verwey transition is a special character of magnetite, and this observation further confirms the structure of the product, while for maghemite products, no magnetic transition is observed in its ZFC-FC curves (Jia *et al.*, 2007).

5.4.2.4 XPS spectra analysis

The high resolution XPS spectrum of as-prepared CU135 and OC135 nanocrystals shown in Fig. 8 were used to study particularly the valence states of iron. Fe 2p electron core levels are split into $2p_{3/2}$ and $2p_{1/2}$ components, which is due to the spin-orbit coupling characterised by series of peaks (Fig. 5.23AB). The double well defined peaks were seen at binding energies of 710.17 eV and 723.97 eV in the CU135 sample in agreement with the reported values of Fe $2p_{3/2}$ and Fe $2p_{1/2}$ core level XPS peaks (Zhang *et al.*, 2007), which in OC135 appeared at 710.59 eV and 723.93 eV. Each double peak in high resolution Fe 2p scan is broadened due to the appearance of Fe^{2+} and Fe^{3+} in magnetite which is in agreement with the reported literature. In both the case, it is pertinent that the absence of shake-up satellite signal at ~ 719 eV further confirms the presence of both Fe^{3+} and Fe^{2+} species in the lattice of Fe_3O_4 (Li *et al.*, 2010; Dar and Shivashankar, 2014). The relative areas of Fe^{2+} and Fe^{3+} were calculated with the value of 0.33:0.67, corresponding to that of the stoichiometry of Fe_3O_4 , which could also be shown as $\text{FeO}\cdot\text{Fe}_2\text{O}_3$. The observed O1s peak at 529.76 eV for CU135 and 531.7 eV (OC135) is asymmetric with a shoulder on the higher binding energy side, indicating more phases of O element. Deconvolution of O1s peaks around the binding energy 530 eV showed multiplet formation which distinguished between lattice oxygen in Fe_3O_4 , those bound to hydrocarbons (surfactant), O-H bond adsorbed by FeO from air under ambient condition (Li *et al.*, 2010).

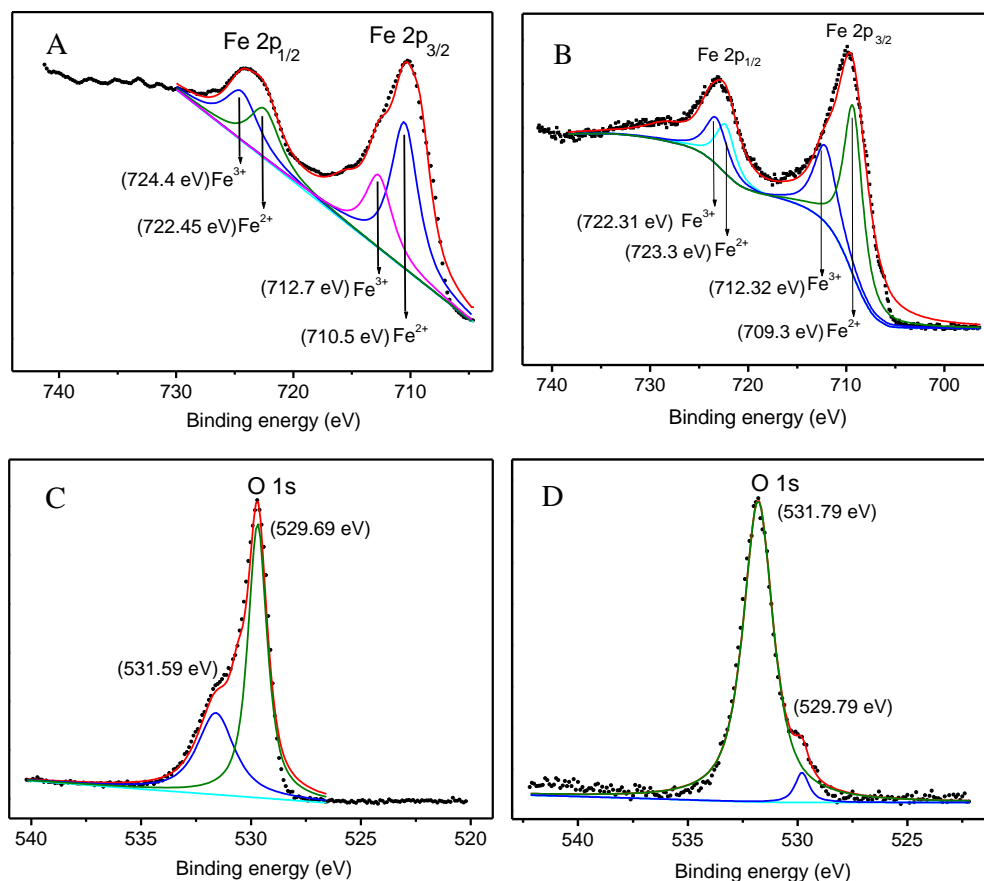


Fig. 5.23 High resolution XPS (A, B) Fe 2p (C, D) and O 1s spectra of CU135 (A, C) and OC135 (B, D) samples. The solid red line over a dotted raw data is a typical fit by XPS software.

The XPS results substantiate to the Mössbauer data, magnetite phase and also confirm the formation of chemical bonds between the magnetite substrate and the surfactant.

5.4.3 Cell culture: Dose dependent cytotoxicity of MNPs

The aim of this study was to investigate and compare the cytotoxicity of NCs with various morphology/ surface chemistry on human colorectal carcinoma HCT116 (ATCC[®] CCL-247[™]) cell line. The magnetite nanomaterials used in cell cytotoxicity study were ~10 nm SAPT, ~250 nm MS48, NSAg, CB135, and OC135. Cytotoxicity of NCs was investigated by WST cell proliferation assay, which is based on the production of formazan from WST-1 by mitochondrial dehydrogenases in viable cells, on HCT 116 cell line after 24 and 48 h incubation is shown in Fig. 5.24. After 24 h exposure at varying doses of SAPT, MS48, NSAg, CB135 and OC135 magnetite crystals, HCT116 cell viabilities detected by the WST assay resulted in explicit dose-dependent reduction (Fig. 5.24A). The results confirmed the significant differences between cellular responses to the same condition. When the cells were treated at lower doses 25 and 50 $\mu\text{g}\cdot\text{ml}^{-1}$, the

cytotoxicity of SAPT nanocrystals was statistically greater than that with MS48 but close to that of CB135 and NSAg.

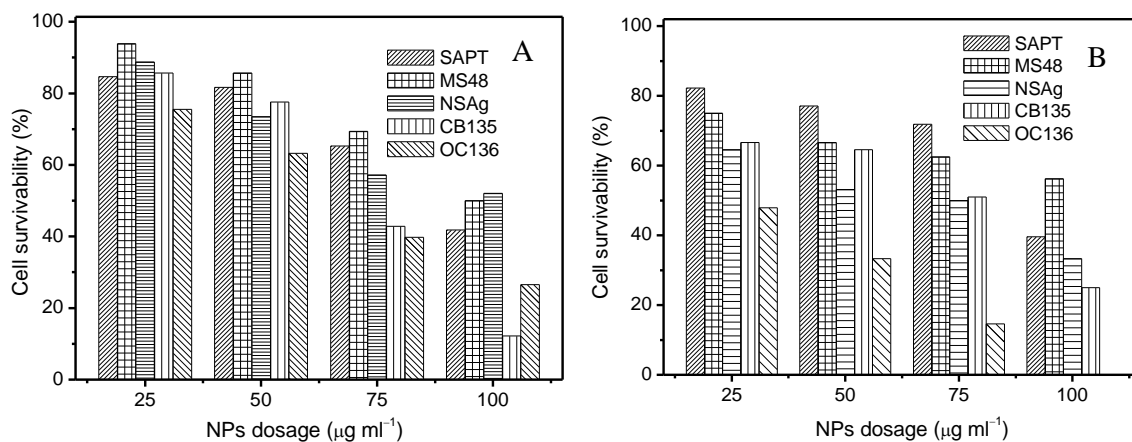


Fig. 5.24 Cell survivability of HCT 116 cells exposed to morphologically different magnetite nanocrystals with different concentrations determined by the WST assay after (A) 24 and (B) 48 h.

After exposure dose increased from 75 to 100 $\mu\text{g}\cdot\text{ml}^{-1}$, OC135 and CB135 induced a much greater reduction of cellular activity than SAPT, MS48, NSAg. However, at higher dosage levels at 100 $\mu\text{g}\cdot\text{ml}^{-1}$, the cell survivabilities of SAPT, MS48, NSAg, CB135 and OC135 were respectively inhibited by 41.8, 50, 52, 12.2 and 26.5%, compared with the control group, which revealed that the dose-dependent cytotoxicity. The greatest cell survivability loss (87.8%) was found at significantly elevated dose 100 $\mu\text{g}\cdot\text{ml}^{-1}$ in CB135. Actually we have chosen much higher level of concentration range than many of the reported work (Gao *et al.*, 2009). As expected more cytotoxicity for 48 h duration and at high concentrations, since magnetic NCs accumulated with the cells for a longer time.

5.4.3.1 Fluorescent microscopic examination of cells

To visualise the morphology of the cell damage due to the presence of the nanocrystals, the cells were stained with DAPI and FITC (Fig. 5.25). Since neither significant apoptosis nor necrosis occurred in cells exposed to the MS48, MAg and NSAg (see above), but the formation of gas vesicles may be responsible for the CU135 and OC135 nanocrystal toxicity through local changes in the ionic equilibrium.

The toxicological effects of morphologically different nanocrystals with different size may be attributed to their surface properties that originate from the specific ‘nano’ size effect and are ultimately determined from chemical compositions. Nanocrystals of cube and truncated octahedra may have different active exposed crystal planes and thus surface effects along with nanosize that increase the number of structural defects as well

as disrupting the well-structured electronic configuration of the material, so as to give rise to altered electronic properties on the particle surface (Donaldson *et al.*, 2002).

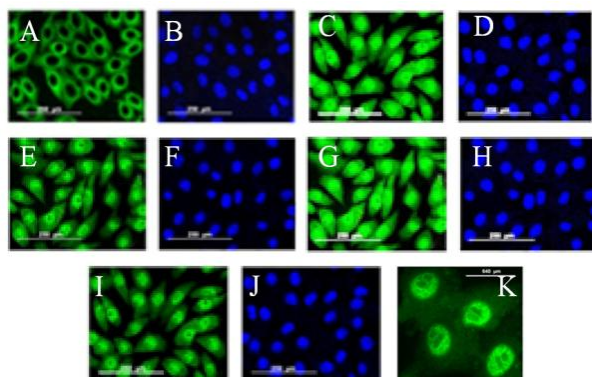


Fig. 5.25 Fixing and staining the HCT 116 cells for morphology and nuclear examination after 24 h exposure to (A, B) CU135, (E, F) OC135, (I, J) MS48, (C, D) NSAg and (G, H) SAPT nanocrystals with respect to (K) control. Scale bar is 640 μm Blue colour fluorescence due to DAPI nuclear staining and green fluorescence due to FITC staining.

This could establish specific ‘surface groups’ that could function as reactive sites. ‘Surface groups’ can make nanocrystals hydrophilic or hydrophobic, lipophilic or lipophobic, or catalytically active or passive. The extent of these changes and their importance strongly depends on the chemical composition of the material (Nel *et al.*, 2006).

During the cytotoxicity assay, the MNPs are added to DMEM which contains many sources of proteins, vitamins, amino acids, etc. in fetal bovine serum. Mahmoudi *et al.*, hypothesised that chloride ions may be able to get attached to Fe in competition with the hydroxyl groups (Mahmoudi *et al.*, 2010). As a result, not only the amount of Cl^- ions is decreased in the diffuse double layer of MNPs in the DMEM medium, but also the composition of the DMEM medium can be changed due to the attraction of proteins, amino acids, and vitamins in the diffuse double layer. Cedervall *et al.* showed that the particle characteristics (i.e., size, charge and hydrophobicity) can significantly effect the proteins affinity to the surface of NPs (Cedervall *et al.*, 2007). As a result there could be significance difference in cell response to the exposed nanocrystals due to surface characteristics (Mahmoudi *et al.*, 2010). It is worth adding that the maximum and minimum amount of Cl^- that the cells may tolerate is reported to be 130 and 70 mM (normal range: 103–112 mM), respectively (Guyton, 2006) and these amounts existed in the composition of DMEM medium under consideration.

5.5 Conclusions

The solvothermal reduction method has been used to successfully produce size-tailored microspheres. This approach provides a one step, simple, and inexpensive method for the preparation of monodisperse magnetic microspheres with a tunable diameter range of 100–350 nm. The ferric chloride iron source with sodium acetate produced well formed relatively large spheres when compared to ferric acetylacetonate or ammonium acetate. One-pot synthesis of monodisperse nanocube and truncated octahedra with controlled size is facile without a laborious multistep seed-mediated growth. A facile thermal decomposition route controllably fabricated single-crystalline Fe₃O₄ polyhedra possessing active basal facets with high yield. Structural characterisation by XRD and magnetisation study indicates that the composition of the target material is maintained in the nanocrystals of Fe₃O₄. The magnetisation Fe₃O₄ spheres have reached 63, 68, 73 and 79 emu.g⁻¹ with reaction times of 8, 16, 24 and 48 h respectively. The magnetite spheres are highly magnetic ($M_s = \sim 80$ emu.g⁻¹ in MS48) and can be manipulated by an external magnetic field. The large ~ 135 nm nanocubes and OC135 octahedra were found to be superparamagnetic at 300 K and the M_s value is $\sim 89, 82$ emu.g⁻¹ respectively. The magnetic properties of the products were sensitive to the crystal size. Furthermore, the 2D assembly of monodisperse Fe₃O₄ nanocrystals probably leads to future prospects toward using nanocrystals as one bit magnetic media to achieve high density data storage, thus promising in the future large-scale application, owing to its low-toxicity materials, and high yields. The magnetite spheres of core-shell framework were finally covered with outer shell of silica by this amenable to bulk production for industrial requirements. The WST and MTT assay results indicate that magnetite supported continuous growth of both MDA-MB-426 and HCT 116 cells on their surfaces. A significant differences ($P > 0.05$) were found in cellular proliferation among five concentrations during the whole culture process. Thus, the morphology, size and dosage of NPs have obvious effect on this cell proliferation within the measured concentrations. Future investigations may provide more understanding of the relationship between surface properties and cellular uptake, translocation, metabolism, oxidative effects and other biological effects of different nanoparticles *in vivo* and *in vitro*. We believe that these hydrophilic and biocompatible microspheres will have important applications not only in advanced magnetic materials and ferrofluid technology, but also in biomedical fields such as biomolecular separations,

targeted drug delivery, cancer diagnosis and treatment, as well as magnetic resonance imaging.

Overall conclusions and future scope

Size and shape tuned magnetic iron oxide nanocrystals were successfully fabricated by three different wet chemical techniques such as coprecipitation, solvothermal, thermal route. The synthesised magnetite nanocrystals are monodisperse, highly magnetic. Shape-selective fabrication has been achieved by applying modifications on published methods by proper selection of the type and concentration of Fe precursors, dielectric constant of reaction media, precipitation temperature, reaction time, *in situ* or post synthetic surface functionalisation treatment. The process was amenable to bulk production for industrial requirements.

Superparamagnetic magnetite/maghemite core-shell nanostructures with size in the range ~8–13 nm were successfully achieved by aqueous ammonia coprecipitation technique in the temperature range of 33–90°C. The activation energy for the growth of nanocrystallites was ~6.15 kJ.mol⁻¹ as estimated by Arrhenius eqn. The kinetically controlled, as grown NPs were found to possess a preferential (311) orientation of the *fcc* phase, with highest magnetic susceptibility of ~57 emu.g⁻¹. The mean crystallite size (D_{TEM} –2.5 nm) and microstrain ($5.5\text{--}8.9 \times 10^{-3}$) involved in the as-synthesised nanocrystals were evaluated from the X-ray peak broadening by Williamson–Hall technique. In addition to FTIR and Raman spectra, Rietveld structural refinement of XRD confirms the magnetite phase with 5–20% maghemite in the sample. VSM and Mössbauer spectral data allowed us to fit the magnetite/maghemite content to a core-shell model where the shell is 0.2–0.3 nm thick maghemite over 7.8 nm magnetite core. The D_{mag} derived from the Langevin computations were slightly smaller than D_{TEM} which may be due to the supposedly presence of a magnetically “dead” layer of atoms over maghemite shell at the surface. With a view to establish the temperature and Raman laser power relationship, evolution of different iron oxide phases due to the oxidation under heat treatment as well as Raman from the laser spot with increasing power (5, 25, 50 mW). The overall iron oxide phase content were quantified in annealed magnetic sample at various temperatures and correlated with Raman spectra.

The nanocrystalline magnetite, used in highly stable TMA aqueous ferrofluid, has been synthesised by ammonia coprecipitation in physiological saline and had a BET

surface area of $106 \text{ m}^2 \cdot \text{g}^{-1}$. The highest magnetic susceptibility of 64.68 and $58 \text{ emu} \cdot \text{g}^{-1}$ were achieved before and after peptisation with TMAH. The reduced M_S value of $58 \text{ emu} \cdot \text{g}^{-1}$ in TMA specimen is due to its reduced crystal dimension along with small contribution of the presence of non-magnetic TMAH. TG-DTA, EDAX, as well as XPS and FTIR spectra confirmed the presence of surface coordinated tetramethyl group in TMA. The TMA suspensions are stable over a year without any loss due to precipitation. The novelty of this work is that this is a successful attempt to correlate the stability of ultra-stable ferrofluid against time and temperature by PCS in conjunction with colloid surface properties. The hydrodynamic size of the magnetite one-shell nanocluster was controlled within $28.3\text{--}32.3 \text{ nm}$ range in a wide temperature range ($20\text{--}65^\circ\text{C}$). The monodispersity of these MNPs containing aqueous ferrofluid have no effect on heating which has great potential in hyperthermia and may find suitable in various biomedical and industrial applications.

It was also demonstrated that evaluation of non-aqueous ferrofluids for the real world applications requires a proper understanding of all the characteristics, rheological and magnetic properties of NP suspensions. The magneto rheological properties of oil based ferrofluid has been tested and the findings are as follows: (i) with increasing shear rate (10 to 10^3), ferrofluids manifest non-Newtonian behaviour of decrease in viscosity, (ii) application of magnetic field ($0\text{--}0.7 \text{ T}$) enhances the non-Newtonian behaviour, (iii) the viscosity of the ferrofluids increases by increasing the NP loading 10 and 20% . Herschel-Bulkley model accurately fits to the shear stress data giving the yield stress thereof, increases with the increase in both magnetic field and concentration of NP loading. Increased NP loading decreases the magnitude of viscosity hysteresis during magnetic sweep experiments. During the pulsed application of magnetic field, the trend in the variation of viscosity changes completely as the shear rate is decreased from a 10^3 to 10^{-3} . The excellent rheological switching property is suitable for many technological applications.

Magnetite nanocrystals have been synthesised via homogeneous precipitation in solvents with decreasing the ' ε ' of medium using $1:1$ EA, *n*PA, IPA, EG, DEG and PEG with water at 40 and 80°C . The presence of alcohol/glycol content (by TG-DTA and FTIR) and the precipitation temperature are vital for the control of agglomeration, suspension stability, size and crystallinity of magnetite. IPA magnetite is relatively crystalline (CI $\sim 89\%$) next to water, with highest magnetisation of $\sim 68 \text{ emu} \cdot \text{g}^{-1}$. The

crystals observed from the HR-TEM have a mixture of multi-faceted polyhedral shapes, all of which contains abundant under coordinated atoms located on the edges and corners, serving as extra active sites for the chemical reaction. The PEG, DEG and EG powders showed better catalytic activity due to smaller particles with abundant active (220) and (400) crystal facets. Ferrofluids with greater aqueous stability were obtained from relatively lower precipitation temperature at 40°C. The colloidal suspension of PEG showed stability over a period of 6 months. The hydrodynamic diameter was <20 nm in the temperature trend upto 65°C. Light scattering measurements have been carried out on aqueous suspension of the MDG magnetite at different concentrations and temperatures of measurement which confirmed the presence of 'single particle dispersion', ($D_{PCS} \approx 13$ nm).

Size-tailored microspheres (100–270 nm) were successfully produced by solvothermal reduction method. This is a simple one step approach for the preparation of monodisperse magnetic spheres with tunable dimension. Monodispersity, crystallinity and saturation magnetisation of magnetite was found to increase with increase in autoclaving time. The magnetisation value of Fe_3O_4 spheres gradually increased to 63, 68, 73 and 79 $emu.g^{-1}$ with increasing the reaction time 8, 16, 24 and 48 h respectively. Ferric chloride iron precursor with sodium acetate produced well formed relatively large sphere when compared to ferric acetylacetonate or ammonium acetate. Core-shell nanostructures (Fe_3O_4 microspheres/silica and nanospheres/silver) as well as yolk-shell frame work nanostructures (Fe_3O_4 microspheres/silica/Ni-silicate) were thoroughly examined by TEM, SEM, XRD and XPS. After 24 h incubation of NS and NSAg with MDA-MB-468 cell line, cell cytotoxicity MTT assay was performed. Both the magnetite samples are biocompatible when compared to spherical or cubic crystals; cells were also stained with DAPI which showed no remarkable structural changes when compared to control.

Highly monodisperse nanocube and truncated octahedra with controllable size is fabricated in high yield through facile on step thermal decomposition route without a laborious multistep seed-mediated growth. Structural characterisation by XRD and magnetisation study indicated that the composition of the target material is Fe_3O_4 . The large ~135 nm cubes and truncated octahedra were found to be superparamagnetic at 300 K and the M_S value is ~89, 82 $emu.g^{-1}$ samples respectively. The magnetic properties of the products were sensitive to the crystal size. Furthermore, the 2D assembly of monodisperse Fe_3O_4 nanocrystals probably leads to future prospects toward using

nanocrystals as one bit magnetic media to achieve high density data storage, thus promising in the future large-scale application.

The WST and MTT assay results indicate that magnetite NPs (SAPT, MS48, NSAg, OC135 and CU135) supported continuous growth of both MDA-MB-426 and HCT 116 cells at low concentration range. Significant differences ($P > 0.05$) were found in cellular proliferation among five concentrations ($25\text{-}100\ \mu\text{g}\cdot\text{ml}^{-1}$) of each sample during the whole cell culture process. Thus, the morphology, size and dosage of NPs have obvious effect on this cell proliferation within the measured concentrations. The biocompatibility and non-interacting nature has to be introduced to OC135 and CU135 nanocrystals by surface modification with silica. A silica layer on a magnetic particle; single particle modification is possible with the addition of right amount of silicate. We believe that these hydrophilic and biocompatible SAPT, MS48, NSAg microspheres will have important applications not only as advanced magnetic materials and ferrofluid technology, but also in biomedical fields such as biomolecular separations, targeted drug delivery, cancer diagnosis and treatment, as well as magnetic resonance imaging. Future investigations may provide more understanding of the relationship between surface properties and cellular uptake, translocation, metabolism, oxidative effects and other biological effects of different nanoparticles *in vivo* and *in vitro*.

The limited time and vastness of the area left the scope of much more to do in future. The most important work which could be done as a direct extension of this thesis, is a thorough study of these size tuned morphologically different NPs used for drug delivery applications. The work could be extended to testing some of the more stable aqueous suspensions in animals under MRI conditions. Once these issues are resolved, wide scale MNPs-mediated targeted disease treatment will no doubt become a reality. The production of high quality MNPs naturally facilitates the exploration of their applications, and magnetic nanomaterials indeed show many useful applications in several fields. Moreover, the design and fabrication of sophisticated, multifunctional nanostructures based on MNPs have recently been attracting increased research effort, especially for biological applications. One such example, in clinical field, is that covalently attach oxygen-sensitive fluorescence dyes to the magnetite nanocrystals surface aiming to develop magnetic/luminescent nanocrystals-based glucose sensors. It is possible to re-use the enzymes immobilised on MNPs for successive glucose measurements in multiple samples. This approach particularly needed in third world countries where high tech diagnostics aids are inaccessible to the bulk of rural population.

References

- Allard-Vannier, E., Cohen-Jonathan, S., Gautier, J., Herve-Aubert, K., Munnier, E., Souce, M., Legras, P., Passirani, C. and Chourpa, I. "Pegylated magnetic nanocarriers for doxorubicin delivery: A quantitative determination of stealthiness *in vitro* and *in vivo*" *European Journal of Pharmaceutics and Biopharmaceutics* 2012, **81** (3) 498-505.
- Amutha, R., Muruganandham, M., Lee, G. J., Batalova, V. N., Mokrousov, G. and Wu, J. J. "Solvent free synthesis and catalytic activity of alpha-Fe₂O₃ nanomaterial" *Advanced Science Letters* 2011, **4** (2) 496-500.
- An, K., Park, M., Yu, J. H., Na, H. B., Lee, N., Park, J., Choi, S. H., Song, I. C., Moon, W. K. and Hyeon, T. "Synthesis of uniformly sized manganese oxide nanocrystals with various sizes and shapes and characterization of their T1 magnetic resonance Relaxivity" *European Journal of Inorganic Chemistry* 2012, **2012** (12) 2148-2155.
- Andrade, A. L., Souza, D. M., Pereira, M. C., Fabris, J. D. and Domingues, R. Z. "Synthesis and characterization of magnetic nanoparticles coated with silica through a sol-gel approach" *Cerâmica* 2009, **55** (336) 420-424.
- Armstrong, T. I., Davies, M. C. and Illum, L. "Human serum albumin as a probe for protein adsorption to nanoparticles: Relevance to biodistribution" *Journal of Drug Targeting* 1997, **4** (6) 389-398.
- Aviles, M. O., Mangual, J. O., Ebner, A. D. and Ritter, J. A. "Isolated swine heart ventricle perfusion model for implant assisted-magnetic drug targeting" *International Journal of Pharmaceutics* 2008, **361** (1-2) 202-208.
- Bae, K. H., Park, M., Do, M. J., Lee, N., Ryu, J. H., Kim, G. W., Kim, C., Park, T. G. and Hyeon, T. "Chitosan oligosaccharide-stabilized ferrimagnetic iron oxide nanocubes for magnetically modulated cancer hyperthermia" *ACS Nano* 2012, **6** (6) 5266-5273.
- Baumgartner, J., Dey, A., Bomans, P. H. H., Le Coadou, C., Fratzl, P., Sommerdijk, N. A. J. M. and Faivre, D. "Nucleation and growth of magnetite from solution" *Nature Materials* 2013, **12** (4) 310-314.
- Bean, C. P. and Livingston, J. D. "Superparamagnetism" *Journal of Applied Physics* 1959, **30** (4) S120-S129.

- Bersani, D., Lottici, P. P. and Montenero, A. "Micro-Raman investigation of iron oxide films and powders produced by sol-gel syntheses" *Journal of Raman Spectroscopy* 1999, **30** (5) 355-360.
- Bertrand, F., German, S.-A., Anwar, A., Irune, V., Gemma, B., Yolanda, R. D. M. and Lennart, B. "Dispersion and surface functionalization of oxide nanoparticles for transparent photocatalytic and sunscreens" *Science and Technology of Advanced Materials* 1994, **14** (2) 023001.
- Bharde, A. A., Parikh, R. Y., Baidakova, M., Jouen, S., Hannoyer, B., Enoki, T., Prasad, B. L. V., Shouche, Y. S., Ogale, S. and Sastry, M. "Bacteria-mediated precursor-dependent biosynthesis of superparamagnetic iron oxide and iron sulfide nanoparticles" *Langmuir* 2008, **24** (11) 5787-5794.
- Bødker, F., Mørup, S. and Linderoth, S. "Surface effects in metallic iron nanoparticles" *Physical Review Letters* 1994, **72** (2) 282-285.
- Bonnemain, B. "Superparamagnetic agents in magnetic resonance imaging: Physicochemical characteristics and clinical applications - A review" *Journal of Drug Targeting* 1998, **6** (3) 167-174.
- Boxall, C., Kelsall, G. and Zhang, Z. "Photoelectrophoresis of colloidal iron oxides. Part 2.- Magnetite (Fe₃O₄)" *Journal of the Chemical Society-Faraday Transactions* 1996, **92** (5) 791-802.
- Bradford, M. M. "A rapid and sensitive method for the quantitation of microgram quantities of protein utilizing the principle of protein-dye binding" *Analytical Biochemistry* 1976, **72** (1) 248-254.
- Buyevich, Y. A., Ed. (1999). Fluid Dynamics in Fine Suspension Flow. In Advances in the Flow and Rheology of Non-Newtonian Fluids, The Netherlands: Elsevier.
- Cao, S. W., Zhu, Y. J. and Chang, J. "Fe₃O₄ polyhedral nanoparticles with a high magnetization synthesized in mixed solvent ethylene glycol-water system" *New Journal of Chemistry* 2008, **32** (9) 1526-1530.
- Cavaliere-Jaricot, S., Darbandi, M., Kuçur, E. and Nann, T. "Silica coated quantum dots: a new tool for electrochemical and optical glucose detection" *Microchimica Acta Biomaterialia* 2008, **160** (3) 375-383.
- Cedervall, T., Lynch, I., Lindman, S., Berggard, T., Thulin, E., Nilsson, H., Dawson, K. A. and Linse, S. "Understanding the nanoparticle-protein corona using methods to

- quantify exchange rates and affinities of proteins for nanoparticles" *Proceedings of the National Academy of Sciences of the United States of America* 2007, **104** (7) 2050-2055.
- Chen, C. P., Gunawan, P. and Xu, R. "Self-assembled Fe₃O₄-layered double hydroxide colloidal nanohybrids with excellent performance for treatment of organic dyes in water" *Journal of Materials Chemistry* 2011, **21** (4) 1218-1225.
- Chen, H. I. and Chang, H. Y. "Homogeneous precipitation of cerium dioxide nanoparticles in alcohol/water mixed solvents" *Colloids and Surfaces a-Physicochemical and Engineering Aspects* 2004, **242** (1-3) 61-69.
- Chen, L. (2014). Surface functionalization and bioconjugation of nanoparticles for biomedical applications, The University of Western Ontario: 1903.
- Chen, M., Pica, T., Jiang, Y.-B., Li, P., Yano, K., Liu, J. P., Datye, A. K. and Fan, H. "Synthesis and self-assembly of *fcc* phase FePt nanorods" *Journal of the American Chemical Society* 2007, **129** (20) 6348-6349.
- Chowdhury, M. R., Fester, V., Kale, G. and Cespedes, O. "Hydrothermal precipitation of beta-FeOOH nanostructure(s) in mixed solvent: study of their morphological and structural evolution" *Journal of Nanoparticle Research* 2014, **16** (5) 2412.
- Coey, J. M. D. "Noncollinear spin arrangement in ultrafine ferrimagnetic crystallites" *Physical Review Letters* 1971, **27** (17) 1140-1142.
- Colombo, U., Gazzarrini, F. and Lanzavecchia, G. "Mechanisms of iron oxides reduction at temperatures below 400°C" *Materials Science and Engineering* 1967, **2** (3) 125-135.
- Comberg, U. and Wriedt, T. "Comparison of scattering calculations for aggregated particles based on different models" *Journal of Quantitative Spectroscopy and Radiative Transfer* 1999, **63** (2) 149-162.
- Cornell, R. M. and Schwertmann, U. (1996). The iron oxides: structure, properties, reactions, occurrences and uses. The iron oxides. New York, VCH: 117.
- Cornell, R. M. and Schwertmann, U. (2003). Electronic, Electrical and Magnetic Properties and Colour. The Iron Oxides, Wiley-VCH Verlag GmbH & Co. KGaA: 111-137.
- Corot, C., Robert, P., Idee, J. M. and Port, M. "Recent advances in iron oxide nanocrystal technology for medical imaging" *Advanced Drug Delivery Reviews* 2006, **58** (14) 1471-1504.

- Cushing, B. L., Kolesnichenko, V. L. and O'Connor, C. J. "Recent advances in the liquid-phase syntheses of inorganic nanoparticles" *Chemical Reviews* 2004, **104** (9) 3893-3946.
- Cvek, M., Mrlik, M. and Pavlinek, V. "A rheological evaluation of steady shear magnetorheological flow behavior using three-parameter viscoplastic models" *Journal of Rheology* 2016, **60** 687-694.
- Daou, T. J., Pourroy, G., Begin-Colin, S., Greneche, J. M., Ulhaq-Bouillet, C., Legare, P., Bernhardt, P., Leuvrey, C. and Rogez, G. "Hydrothermal synthesis of monodisperse magnetite nanoparticles" *Chemistry of Materials* 2006, **18** (18) 4399-4404.
- Dar, M. I. and Shivashankar, S. A. "Single crystalline magnetite, maghemite, and hematite nanoparticles with rich coercivity" *RSC Advances* 2014, **4** (8) 4105-4113.
- Denardin, J. C., Brandl, A. L., Knobel, M., Panissod, P., Pakhomov, A. B., Liu, H. and Zhang, X. X. "Thermoremanence and zero-field-cooled/field-cooled magnetization study of $\text{Co}_x(\text{SiO}_2)_{1-x}$ granular films" *Physical Review B* 2002, **65** (6) 064422.
- Deng, H., Li, X. L., Peng, Q., Wang, X., Chen, J. P. and Li, Y. D. "Monodisperse magnetic single-crystal ferrite microspheres" *Angewandte Chemie-International Edition* 2005, **44** (18) 2782-2785.
- Deori, K., Gupta, D., Saha, B. and Deka, S. "Design of 3-dimensionally self-assembled CeO_2 nanocube as a breakthrough catalyst for efficient alkylarene oxidation in water" *ACS Catalysis* 2014, **4** (9) 3169-3179.
- Dieckmann, R., Mason, T. O., Hodge, J. D. and Schmalzried, H. "Defects and cation diffusion in magnetite (111) tracer diffusion of foreign tracer cations as a function of temperature and oxygen potential" *Berichte der Bunsengesellschaft für physikalische Chemie* 1978, **82** (8) 778-783.
- Donaldson, K., Brown, D., Clouter, A., Duffin, R., MacNee, W., Renwick, L., Tran, L. and Stone, V. "The pulmonary toxicology of ultrafine particles" *Journal of Aerosol Medicine-Deposition Clearance and Effects in the Lung* 2002, **15** (2) 213-220.
- Dong, Y. C., Hu, M. J., Ma, R. G., Cheng, H., Yang, S. L., Li, Y. Y. and Zapien, J. A. "Evaporation-induced synthesis of carbon-supported Fe_3O_4 nanocomposites as anode material for lithium-ion batteries" *Crystengcomm* 2013, **15** (7) 1324-1331.
- Dorofeev, G. A., Streletskii, A. N., Povstugar, I. V., Protasov, A. V. and Elsukov, E. P. "Determination of nanoparticle sizes by X-ray diffraction" *Colloid Journal* 2012, **74** (6) 675-685.

- Douglas, F. J. (2012). Synthesis and nanocharacterisation of magnetic nanoparticles: from cubes and spheres to octapods and wires. School of Chemistry, College of Science and Engineering, University of Glasgow.
- Douglas, F. J., MacLaren, D. A. and Murrie, M. "A study of the role of the solvent during magnetite nanoparticle synthesis: tuning size, shape and self-assembly" *RSC Advances* 2012, **2** (21) 8027-8035.
- E. Lima, J., Biasi, E. D., Mansilla, M. V., Saleta, M. E., Granada, M., Troiani, H. E., Effenberger, F. B., Rossi, L. M., Rechenberg, H. R. and Zysler, R. D. "Heat generation in agglomerated ferrite nanoparticles in an alternating magnetic field" *Journal of Physics D: Applied Physics* 2013, **46** (4) 045002.
- Ebrahiminezhad, A., Ghasemi, Y., Rasoul-Amini, S., Barar, J. and Davaran, S. "Impact of aminoacid coating on the synthesis and characteristics of iron oxide nanoparticles" *Bulletin of the Korean Chemical Society* 2012, **33** (12) 3957-3962.
- Erdemoglu, M. and Sarikaya, M. "Effects of heavy metals and oxalate on the zeta potential of magnetite" *Journal of Colloid and Interface Science* 2006, **300** (2) 795-804.
- Fertman, V. E., Ed. (1990). in Magnetic Fluids Guidebook: Properties and Applications, Hemisphere Publishing Corporation: New York.
- Feynman, R. P. (1959). "There's plenty of room at the bottom." from a talk reported at <http://www.zyvex.com/nanotech/feynman.html>.
- Friak, M., Schindlmayr, A. and Scheffler, M. "Ab initio study of the half-metal to metal transition in strained magnetite" *New Journal of Physics* 2007, **9** doi:10.1088/1367-2630/9/1/005.
- Frison, R., Cernuto, G., Cervellino, A., Zaharko, O., Colonna, G. M., Guagliardi, A. and Masciocchi, N. "Magnetite-maghemite nanoparticles in the 5-15 nm range: correlating the core-shell composition and the surface structure to the magnetic properties. A total scattering study" *Chemistry of Materials* 2013, **25** (23) 4820-4827.
- Furniss, B. S., Hannaford, A. J., Rogers, V., Smith, P. W. G. and Tatchell, A. R., Eds. (1978). Vogel's textbook of practical organic chemistry. England, English publisher book society/ Longman.
- Gao, J., Gu, H. and Xu, B. "Multifunctional magnetic nanoparticles: Design, synthesis, and biomedical applications" *Accounts of Chemical Research* 2009, **42** (8) 1097-1107.

References

- Gao, L., Li, W., Wang, J. and Guo, J. K. "Influence of some parameters on the synthesis of ZrO₂ nanoparticles by heating of alcohol-aqueous salt solutions" *Journal of Nanoparticle Research* 1999, **1** (3) 349-352.
- Garcia-Jimeno, S. and Estelrich, J. "Ferrofluid based on polyethylene glycol-coated iron oxide nanoparticles: Characterization and properties" *Colloids and Surfaces A-Physicochemical and Engineering Aspects* 2013, **420** 74-81.
- Ghosh, S. (2006). The preparation of magnetic nanoparticle assemblies for biomedical applications. School of Chemical Sciences. Ireland, Dublin City University, Ireland: 215.
- Ghosh, S., Carty, D., Clarke, S. P., Corr, S. A., Tekoriute, R., Gun'ko, Y. K. and Brougham, D. F. "NMR studies into colloidal stability and magnetic order in fatty acid stabilised aqueous magnetic fluids" *Physical Chemistry Chemical Physics* 2010, **12** (42) 14009-14016.
- Ghosh, S., Divya, D., Remani, K. C. and Sreeremya, T. S. "Growth of monodisperse nanocrystals of cerium oxide during synthesis and annealing" *Journal of Nanoparticle Research* 2010, **12** (5) 1905-1911.
- Gibson Jr, E. K., McKay, D. S., Thomas-Keprta, K. L., Wentworth, S. J., Westall, F., Steele, A., Romanek, C. S., Bell, M. S. and Toporski, J. "Life on Mars: evaluation of the evidence within Martian meteorites ALH84001, Nakhla, and Shergotty" *Precambrian Research* 2001, **106** 15-34.
- Gittings, M. R. and Saville, D. A. "The determination of hydrodynamic size and zeta potential from electrophoretic mobility and light scattering measurements" *Colloids and Surfaces a-Physicochemical and Engineering Aspects* 1998, **141** (1) 111-117.
- Goetze, T., Gansau, C., Buske, N., Roeder, M., Gornert, P. and Bahr, M. "Biocompatible magnetic core/shell nanoparticles" *Journal of Magnetism and Magnetic Materials* 2002, **252** (1-3) 399-402.
- Golas, P. L., Louie, S., Lowry, G. V., Matyjaszewski, K. and Tilton, R. D. "Comparative study of polymeric stabilizers for magnetite nanoparticles using ATRP" *Langmuir* 2010, **26** (22) 16890-16900.
- Goloverda, G., Jackson, B., Kidd, C. and Kolesnichenko, V. "Synthesis of ultrasmall magnetic iron oxide nanoparticles and study of their colloid and surface chemistry" *Journal of Magnetism and Magnetic Materials* 2009, **321** (10) 1372-1376.

- Gref, R., Domb, A., Quellec, P., Blunk, T., Müller, R. H., Verbavatz, J. M. and Langer, R. "The controlled intravenous delivery of drugs using PEG-coated sterically stabilized nanospheres" *Advanced Drug Delivery Reviews* 1995, **16** (2-3) 215-233.
- Grössinger, R. "Characterisation of hard magnetic materials" *Journal of Electrical Engineering* 2008, **59** (7/s) 15-20.
- Guardia, P., Perez, N., Labarta, A. and Batlle, X. "Controlled synthesis of iron oxide nanoparticles over a wide size range" *Langmuir* 2010, **26** (8) 5843-5847.
- Guo, X. and Xiao, P. "Effects of solvents on properties of nanocrystalline hydroxyapatite produced from hydrothermal process" *Journal of the European Ceramic Society* 2006, **26** (15) 3383-3391.
- Guo, Z., Hahn, H. T., Lin, H., Karki, A. B. and Young, D. P. "Magnetic and magnetoresistance behaviors of particulate iron/vinyl ester resin nanocomposites" *Journal of Applied Physics* 2008, **104** (1) 014314.
- Guo, Z., Park, S., Hahn, H. T., Wei, S., Moldovan, M., Karki, A. B. and Young, D. P. "Giant magnetoresistance behavior of an iron/carbonized polyurethane nanocomposite" *Applied Physics Letters* 2007, **90** (5) 053111.
- Gupta, K., Jana, P. C. and Meikap, A. K. "Optical and electrical transport properties of polyaniline-silver nanocomposite" *Synthetic Metals* 2010, **160** (13-14) 1566-1573.
- Gurzau, E. S., Neagu, C. and Gurzau, A. E. "Essential metals - case study on iron" *Ecotoxicology and Environmental Safety* 2003, **56** (1) 190-200.
- Guyton, A. C., Ed. (2006). Text book of medical physiology W.B. Saunders Co., Philadelphia, Pennsylvania.
- Hamada, S. and Matijević, E. "Ferric hydrous oxide sols. IV. Preparation of uniform cubic hematite particles by hydrolysis of ferric chloride in alcohol-water solutions" *Journal of Colloid and Interface Science* 1981, **84** (1) 274-277.
- Harisinghani, M. G., Barentsz, J., Hahn, P. F., Deserno, W. M., Tabatabaei, S., van de Kaa, C. H., de la Rosette, J. and Weissleder, R. "Noninvasive detection of clinically occult lymph-node metastases in prostate cancer" *New England Journal of Medicine* 2003, **348** (25) 2491-9.
- Harris, R. A., Shumbula, P. M. and van der Walt, H. "Analysis of the interaction of surfactants oleic acid and oleylamine with iron oxide nanoparticles through molecular mechanics modeling" *Langmuir* 2015, **31** (13) 3934-3943.

- He, Y. T., Wan, J. M. and Tokunaga, T. "Kinetic stability of hematite nanoparticles: the effect of particle sizes" *Journal of Nanoparticle Research* 2008, **10** (2) 321-332.
- Hosono, T., Takahashi, H., Fujita, A., Joseyphus, R. J., Tohji, K. and Jeyadevan, B. "Synthesis of magnetite nanoparticles for AC magnetic heating" *Journal of Magnetism and Magnetic Materials* 2009, **321** (19) 3019-3023.
- Hou, Y. L., Xu, Z. C. and Sun, S. H. "Controlled synthesis and chemical conversions of FeO nanoparticles" *Angewandte Chemie-International Edition* 2007, **46** (33) 6329-6332.
- Hrianca, I., Caizer, C. and Schlett, Z. "Dynamic magnetic behavior of Fe₃O₄ colloidal nanoparticles" *Journal of Applied Physics* 2002, **92** (4) 2125-2132.
- Huang, D. J., Lin, H. J., Okamoto, J., Chao, K. S., Jeng, H. T., Guo, G. Y., Hsu, C. H., Huang, C. M., Ling, D. C., Wu, W. B., Yang, C. S. and Chen, C. T. "Charge-orbital ordering and verwey transition in magnetite measured by resonant soft X-ray scattering" *Physical Review Letters* 2006, **96** (9) 096401.
- Huang, J. P. and Yu, K. W. "Magneto-controlled nonlinear optical materials" *Applied Physics Letters* 2005, **86** (4) 041905.
- Iyengar, S. J., Joy, M., Ghosh, C. K., Dey, S., Kotnala, R. K. and Ghosh, S. "Magnetic, X-ray and mössbauer studies on magnetite/maghemite core-shell nanostructures fabricated through an aqueous route" *RSC Advances* 2014, **4** (110) 64919-64929.
- Iyengar, S. J., Joy, M., Maity, T., Chakraborty, J., Kotnala, R. K. and Ghosh, S. "Colloidal properties of water dispersible magnetite nanoparticles by photon correlation spectroscopy" *RSC Advances* 2016, **6** (17) 14393-14402.
- Iyengar, S. J., Joy, M., Mohamed, A. P., Samanta, S., Ghosh, C. K. and Ghosh, S. "Fabrication of magnetite nanocrystals in alcohol/water mixed solvents: catalytic and colloid property evaluation" *RSC Advances* 2016, **6** (65) 60845-60855.
- Jeong, U., Teng, X., Wang, Y., Yang, H. and Xia, Y. "Superparamagnetic colloids: Controlled synthesis and niche applications" *Advanced Materials* 2007, **19** (1) 33-60.
- Jha, D. K., Shameem, M., Patel, A. B., Kostka, A., Schneider, P., Erbe, A. and Deb, P. "Simple synthesis of superparamagnetic magnetite nanoparticles as highly efficient contrast agent" *Materials Letters* 2013, **95** 186-189.
- Jia, C. J., Sun, L. D., Yan, Z. G., Pang, Y. C., You, L. P. and Yan, C. H. "Iron oxide tube-in-tube nanostructures" *Journal of Physical Chemistry C* 2007, **111** (35) 13022-13027.

- Jiang, J., Gu, H., Shao, H., Devlin, E., Papaefthymiou, G. C. and Ying, J. Y. "Bifunctional Fe₃O₄-Ag heterodimer nanoparticles for two-photon fluorescence imaging and magnetic manipulation" *Advanced Materials* 2008, **20** (23) 4403-4407.
- Jolivet, J. P., Ed. (2000). in metal oxide chemistry and synthesis: From solution to solid state, Wiley: Chichester.
- Jolivet, J. P., Chaneac, C. and Tronc, E. "Iron oxide chemistry. From molecular clusters to extended solid networks" *Chemical Communications* 2004, **5** 481-487.
- Jubb, A. M. and Allen, H. C. "Vibrational spectroscopic characterization of hematite, maghemite and magnetite thin films produced by vapor deposition" *ACS Applied Materials & Interfaces* 2010, **2** (10) 2804-2812.
- Kakwere, H., Pernia Leal, M., Materia, M. E., Curcio, A., Guardia, P., Niculaes, D., Marotta, R., Falqui, A. and Pellegrino, T. *ACS Applied Materials & Interfaces* 2015, **7** (3), 10132-10145.
- Kalapathy, U., Proctor, A. and Shultz, J. "A simple method for production of pure silica from rice hull ash" *Bioresource Technology* 2000, **73** (3) 257-262.
- Kim, D., Lee, N., Park, M., Kim, B. H., An, K. and Hyeon, T. "Synthesis of uniform ferrimagnetic magnetite nanocubes" *Journal of the American Chemical Society* 2009, **131** (2) 454-455.
- Kim, D. K., Mikhaylova, M., Wang, F. H., Kehr, J., Bjelke, B., Zhang, Y., Tsakalakos, T. and Muhammed, M. "Starch-coated superparamagnetic nanoparticles as MR contrast agents" *Chemistry of Materials* 2003, **15** (23) 4343-4351.
- Kodama, R. H., Berkowitz, A. E., McNiff, E. J. and Foner, S. "Magnetic nanoparticles" *Journal of Magnetism and Magnetic Materials* 1999, **200** (1-3) 359-372.
- Kovalenko, M. V., Bodnarchuk, M. I., Lechner, R. T., Hesser, G., Schaffler, F. and Heiss, W. "Fatty acid salts as stabilizers in size- and shape-controlled nanocrystal synthesis: The case of inverse spinel iron oxide" *Journal of the American Chemical Society* 2007, **129** (20) 6352-6353.
- Krishnan, A., Sreeremya, T. S., Murray, E. and Ghosh, S. "One-pot synthesis of ultra-small cerium oxide nanodots exhibiting multi-colored fluorescence" *Journal of Colloid and Interface Science* 2013, **389** (1) 16-22.

- Krishnan, R. V. and Banerjee, A. "Harmonic detection of multipole moments and absolute calibration in a simple, low-cost vibrating sample magnetometer" *Review of Scientific Instruments* 1999, **70** (1) 85-91.
- Kumar, S. and Nann, T. "Shape control of II–VI semiconductor nanomaterials" *Small* 2006, **2** (3) 316-329.
- Lai, K. L., Jiang, W., Tang, J. Z., Wu, Y., He, B., Wang, G. and Gu, Z. W. "Superparamagnetic nano-composite scaffolds for promoting bone cell proliferation and defect reparation without a magnetic field" *RSC Advances* 2012, **2** (33) 13007-13017.
- Lai, Y., Yin, W., Liu, J., Xi, R. and Zhan, J. "One-pot green synthesis and bioapplication of l-Arginine-capped superparamagnetic Fe₃O₄ nanoparticles" *Nanoscale Research Letters* 2010, **5** (2) 302-307.
- Lalatonne, Y., Richardi, J. and Pileni, M. P. "Van der Waals versus dipolar forces controlling mesoscopic organizations of magnetic nanocrystals" *Nature Materials* 2004, **3** (2) 121-125.
- Lartigue, L., Hugounenq, P., Alloyeau, D., Clarke, S. P., Levy, M., Bacri, J.-C., Bazzi, R., Brougham, D. F., Wilhelm, C. and Gazeau, F. "Cooperative organization in iron oxide multi-core nanoparticles potentiates their efficiency as heating mediators and MRI contrast agents" *ACS Nano* 2012, **6** (12) 10935-10949.
- Lauterbur, P. C. "Image formation by induced local interactions - examples employing nuclear magnetic-resonance," *Nature* 1973, **242** (5394) 190-191.
- Lee, S. H., Lu, Z. Y., Babu, S. V. and Matijevic, E. "Chemical mechanical polishing of thermal oxide films using silica particles coated with ceria" *Journal of Materials Research* 2002, **17** (10) 2744-2749.
- Lefebure, S., Menager, C., Cabuil, V., Assenheimer, M., Gallet, F. and Flament, C. "Langmuir monolayers of monodispersed magnetic nanoparticles coated with a surfactant" *Journal of Physical Chemistry B* 1998, **102** (15) 2733-2738.
- Levy, M., Quarta, A., Espinosa, A., Figuerola, A., Wilhelm, C., Garcia-Hernandez, M., Genovese, A., Falqui, A., Alloyeau, D., Buonsanti, R., Cozzoli, P. D., Garcia, M. A., Gazeau, F. and Pellegrino, T. "Correlating magneto-structural properties to hyperthermia performance of highly monodisperse iron oxide nanoparticles prepared by a seeded-growth route" *Chemistry of Materials* 2011, **23** (18) 4170-4180.
- Lewinski, N., Colvin, V. and Drezek, R. "Cytotoxicity of nanoparticles" *Small* 2008, **4** (1) 26-49.

- Li, B., Cao, H., Shao, J., Qu, M. and Warner, J. H. "Superparamagnetic Fe₃O₄ nanocrystals@graphene composites for energy storage devices" *Journal of Materials Chemistry* 2011, **21** (13) 5069-5075.
- Li, X., Si, H., Niu, J. Z., Shen, H., Zhou, C., Yuan, H., Wang, H., Ma, L. and Li, L. S. "Size-controlled syntheses and hydrophilic surface modification of Fe₃O₄, Ag, and Fe₃O₄/Ag heterodimer nanocrystals" *Dalton Transactions* 2010, **39** (45) 10984-10989.
- Li, Y., Zhu, H., Gu, H., Dai, H., Fang, Z., Weadock, N. J., Guo, Z. and Hu, L. "Strong transparent magnetic nanopaper prepared by immobilization of Fe₃O₄ nanoparticles in a nanofibrillated cellulose network" *Journal of Materials Chemistry A* 2013, **1** (48) 15278-15283.
- Li, Y. S., Church, J. S. and Woodhead, A. L. "Infrared and Raman spectroscopic studies on iron oxide magnetic nanoparticles and their surface modifications" *Journal of Magnetism and Magnetic Materials* 2012, **324** (8) 1543-1550.
- Li, Z., Chen, H., Bao, H. B. and Gao, M. Y. "One-pot reaction to synthesize water-soluble magnetite nanocrystals" *Chemistry of Materials* 2004, **16** (8) 1391-1393.
- Liang, C., Huang, S., Zhao, W., Liu, W., Chen, J., Liu, H. and Tong, Y. "Polyhedral Fe₃O₄ nanoparticles for lithium ion storage" *New Journal of Chemistry* 2015, **39** (4) 2651-2656.
- Liebau, F. "Ordered microporous and mesoporous materials with inorganic hosts: definitions of terms, formula notation, and systematic classification" *Microporous and Mesoporous Materials* 2003, **58** (1) 15-72.
- Liu, C. and Zhang, Z. J. "Size-dependent superparamagnetic properties of Mn spinel ferrite nanoparticles synthesized from reverse micelles" *Chemistry of Materials* 2001, **13** (6) 2092-2096.
- Liu, D. and Snee, P. "Water-soluble semiconductor nanocrystals cap exchanged with metalated ligands" *ACS Nano* 2010, **5** (1) 546-550.
- Lo, B. and Waite, T. D. "Structure of hydrous ferric oxide aggregates" *Journal of Colloid and Interface Science* 2000, **222** (1) 83-89.
- Luhar, A. K. and Hurley, P. J. "Evaluation of TAPM, a prognostic meteorological and air pollution model, using urban and rural point-source data" *Atmospheric Environment* 2003, **37** (20) 2795-2810.

- Lukashova, N. V., Savchenko, A. G., Yagodkin, Y. D., Muradova, A. G. and Yurtov, E. V. "Structure and magnetic properties of iron oxide nanopowders" *Metal Science and Heat Treatment* 2013, **54** (9-10) 550-554.
- Luo, B., Xu, S., Ma, W.-F., Wang, W.-R., Wang, S.-L., Guo, J., Yang, W.-L., Hu, J.-H. and Wang, C.-C. "Fabrication of magnetite hollow porous nanocrystal shells as a drug carrier for paclitaxel" *Journal of Materials Chemistry* 2010, **20** (34) 7107-7113.
- Maaßen, S., Fattal, E., Muller, R. H. and Couvreur, P. "Cell cultures for the assessment of toxicity and uptake of polymeric particulate drug carriers" *S.T.P. Pharma Sciences* 1993, **3** (1) 11-22.
- Mahendran, V. and Philip, J. "Nanofluid based optical sensor for rapid visual inspection of defects in ferromagnetic materials" *Applied Physics Letters* 2012, **100** (7) 073104.
- Mahmoudi, M., Laurent, S., Shokrgozar, M. A. and Hosseinkhani, M. "Toxicity evaluations of superparamagnetic iron oxide nanoparticles: cell "vision" versus physicochemical properties of nanoparticles" *ACS Nano* 2011, **5** (9) 7263-7276.
- Mahmoudi, M., Simchi, A., Imani, M., Shokrgozard, M. A., Milani, A. S., Haefeli, U. O. and Stroeve, P. "A new approach for the *in vitro* identification of the cytotoxicity of superparamagnetic iron oxide nanoparticles" *Colloids and Surfaces B-Biointerfaces* 2010, **75** (1) 300-309.
- Majewski, P. and Thierry, B. "Functionalized magnetite nanoparticles - synthesis, properties and bio-applications" *Critical Reviews in Solid State and Materials Sciences* 2007, **32** (3-4) 203-215.
- Mandel, K., Hutter, F., Gellermann, C. and Sextl, G. "Stabilisation effects of superparamagnetic nanoparticles on clustering in nanocomposite microparticles and on magnetic behaviour" *Journal of Magnetism and Magnetic Materials* 2013, **331** 269-275.
- Marinescu, G., Patron, L., Culita, D. C., Neagoe, C., Lepadatu, C. I., Balint, I., Bessais, L. and Cizmas, C. B. "Synthesis of magnetite nanoparticles in the presence of aminoacids" *Journal of Nanoparticle Research* 2006, **8** (6) 1045-1051.
- Masala, O. and Seshadri, R. "Synthesis routes for large volumes of nanoparticles" *Annual Review of Materials Research* 2004, **34** 41-81.
- Masoudi, A., Hosseini, H. R. M., Shokrgozar, M. A., Ahmadi, R. and Oghabian, M. A. "The effect of poly(ethylene glycol) coating on colloidal stability of superparamagnetic iron oxide nanoparticles as potential MRI contrast agent" *International Journal of Pharmaceutics* 2012, **433** (1-2) 129-141.

- Meledandri, C. J., Stolarczyk, J. K., Ghosh, S. and Brougham, D. F. "Nonaqueous magnetic nanoparticle suspensions with controlled particle size and nuclear magnetic resonance properties" *Langmuir* 2008, **24** (24) 14159-14165.
- Müller, R. H., Lück, M., Harnisch, S. and Thode, K., Eds. (1997). in scientific and clinical applications of magnetic carriers, Plenum Press, New York.
- Murad, E. and Schwertmann, U. "Temporal stability of a fine grained magnetite" *Clays and Clay Minerals* 1993, **41** (1) 111-113.
- Murphy, C. J. "Nanocubes and nanoboxes" *Science* 2002, **298** (5601) 2139.
- Narayanan, T., Sakthi Kumar, D., Yoshida, Y. and Anantharaman, M. "Strain induced anomalous red shift in mesoscopic iron oxide prepared by a novel technique" *Bulletin of Materials Science* 2008, **31** (5) 759-766.
- Nel, A., Xia, T., Madler, L. and Li, N. "Toxic potential of materials at the nanolevel" *Science* 2006, **311** (5761) 622-627.
- Ninjabdar, T. and Brougham, D. F. "Epoxy ring opening phase transfer as a general route to water dispersible superparamagnetic Fe₃O₄ nanoparticles and their application as positive MRI contrast agents" *Advanced Functional Materials* 2011, **21** (24) 4769-4775.
- Nowak, J., Wolf, D. and Odenbach, S. "A rheological and microscopical characterization of biocompatible ferrofluids" *Journal of Magnetism and Magnetic Materials* 2014, **354** 98-104.
- Ozkaya, T., Toprak, M. S., Baykal, A., Kavas, H., Köseoğlu, Y. and Aktaş, B. "Synthesis of Fe₃O₄ nanoparticles at 100°C and its magnetic characterization" *Journal of Alloys and Compounds* 2009, **472** (2) 18-23.
- Park, J., An, K. J., Hwang, Y. S., Park, J. G., Noh, H. J., Kim, J. Y., Park, J. H., Hwang, N. M. and Hyeon, T. "Ultra-large-scale syntheses of monodisperse nanocrystals" *Nature Materials* 2004, **3** (12) 891-895.
- Pascal, C., Pascal, J. L., Favier, F., Moubtassim, M. L. E. and Payen, C. "Electrochemical synthesis for the control of gamma-Fe₂O₃ nanoparticle size. Morphology, microstructure, and magnetic behavior" *Chemistry of Materials* 1999, **11** (1) 141-147.
- Pecora, R., Ed. (1985). Dynamic light scattering: Applications of photon correlation spectroscopy New York, Plenum Press.
- Perrin, A. and Souques, M. (2012) Electromagnetic fields, environment and health, pp. 11-24, Springer Paris

- Philip, J., Jaykumar, T., Kalyanasundaram, P. and Rai, B. "A tunable optical filter" *Measurement Science & Technology* 2003, **14** (8) 1289-1294.
- Piao, Y., Kim, J., Bin Na, H., Kim, D., Baek, J. S., Ko, M. K., Lee, J. H., Shokouhimehr, M. and Hyeon, T. "Wrap-bake-peel process for nanostructural transformation from beta-FeOOH nanorods to biocompatible iron oxide nanocapsules" *Nature Materials* 2008, **7** (3) 242-247.
- Pinheiro, P. C., Daniel-da-Silva, A. L., Tavares, D. S., Pilar Calatayud, M., Goya, G. F. and Trindade, T. "Fluorescent magnetic bioprobes by surface modification of magnetite nanoparticles" *Materials* 2013, **6** (8) 3213-3225.
- Pinna, N., Grancharov, S., Beato, P., Bonville, P., Antonietti, M. and Niederberger, M. "Magnetite nanocrystals: Nonaqueous synthesis, characterization, and solubility" *Chemistry of Materials* 2005, **17** (11) 3044-3049.
- Pu, S. L., Chen, X. F., Chen, L. J., Liao, W. J., Chen, Y. P. and Xia, Y. X. "Tunable magnetic fluid grating by applying a magnetic field" *Applied Physics Letters* 2005, **87** (2) 021901.
- Qiu, L., Zhao, Y. B., Cao, N., Cao, L. Q., Sun, L. and Zou, X. Y. "Silver nanoparticle-gated fluorescence porous silica nanospheres for glutathione-responsive drug delivery" *Sensors and Actuators B-Chemical* 2016, **234** 21-26.
- Qu, X. F., Zhou, G. T., Yao, Q. Z. and Fu, S. Q. "Aspartic-acid-assisted hydrothermal growth and properties of magnetite octahedrons" *Journal of Physical Chemistry C* 2010, **114** (1) 284-289.
- Ramimoghadam, D., Bagheri, S. and Hamid, S. B. A. "In-situ precipitation of ultra-stable nano-magnetite slurry" *Journal of Magnetism and Magnetic Materials* 2015, **379** 74-79.
- Rashin, M. N., Kutty, R. G. and Hemalatha, J. "Novel coconut oil based magnetite nanofluid as an ecofriendly oil spill remover" *Industrial & Engineering Chemistry Research* 2014, **53** (40) 15725-15730.
- Remani, K. C. and Ghosh, S. "Nanocrystalline ceria through homogeneous precipitation in alcohol-water mixed solvent" *Transactions of the Indian Ceramic Society* 2009, **68** (4) 185-188.
- Respaud, M. "Magnetization process of noninteracting ferromagnetic cobalt nanoparticles in the superparamagnetic regime: Deviation from Langevin law" *Journal of Applied Physics* 1999, **86** (1) 556-561.

- Rietveld, H. M. "The crystal structure of some alkaline earth metal uranates of the type M_3UO_6 " *Acta Crystallographica* 1966, **20** (4) 508-513.
- Roco, M. (2006). "Conceptual risk governance framework for nanotechnology" retrieved on Sep 22, 2016 from http://crnano.typepad.com/crnblog/2006/03/new_risks_new_f.html.
- Rosensweig, R. E. "Heating magnetic fluid with alternating magnetic field" *Journal of Magnetism and Magnetic Materials* 2002, **252** (1-3) 370-374.
- Rossi, L. M., Quach, A. D. and Rosenzweig, Z. "Glucose oxidase-magnetite nanoparticle bioconjugate for glucose sensing" *Analytical and Bioanalytical Chemistry* 2004, **380** (4) 606-613.
- Roy, A., Srinivas, V., Ram, S., A., D. T. J. and Goff, J. P. "A comprehensive structural and magnetic study of Ni nanoparticles prepared by the borohydride reduction of $NiCl_2$ solution of different concentrations" *Journal of Applied Physics* 2006, **100** (9) 094307.
- Rudy, T. P., Goodson, F. R. and Dudley, M. E. (1989). Iron oxide catalyst propellant, and method for making same. US, Google Patents.
- Sakellari, D., Mathioudaki, S., Kalpaxidou, Z., Simeonidis, K. and Angelakeris, M. "Exploring multifunctional potential of commercial ferrofluids by magnetic particle hyperthermia" *Journal of Magnetism and Magnetic Materials* 2015, **380** 360-364.
- Shebanova, O. N. and Lazor, P. "Raman spectroscopic study of magnetite ($FeFe_2O_4$): a new assignment for the vibrational spectrum" *Journal of Solid State Chemistry* 2003, **174** (2) 424-430.
- Shebanova, O. N. and Lazor, P. "Raman study of magnetite (Fe_3O_4): laser-induced thermal effects and oxidation" *Journal of Raman Spectroscopy* 2003, **34** (11) 845-852.
- Shen, L. F., Laibinis, P. E. and Hatton, T. A. "Bilayer surfactant stabilized magnetic fluids: Synthesis and interactions at interfaces" *Langmuir* 1999, **15** (2) 447-453.
- Shi, H., Tan, L., Du, Q., Chen, X., Li, L., Liu, T., Fu, C., Liu, H. and Meng, X. "Green synthesis of Fe_3O_4 nanoparticles with controlled morphology using urease and their application in dye adsorption" *Dalton Transactions* 2014.
- Shima, P. D. and Philip, J. "Tuning of thermal conductivity and rheology of nanofluids using an external stimulus" *The Journal of Physical Chemistry C* 2011, **115** (41) 20097-20104.
- Shimizu, K., Ito, A., Lee, J. K., Yoshida, T., Miwa, K., Ishiguro, H., Numaguchi, Y., Murohara, T., Kodama, I. and Honda, H. "Construction of multi-layered cardiomyocyte

- sheets using magnetite nanoparticles and magnetic force" *Biotechnology and Bioengineering* 2007, **96** (4) 803-809.
- Shimoiizaka, J., Nakatsuka, K., Jujita, T. and Kounosu, A. "Sink-float separators using permanent magnets and water based magnetic fluid" *IEEE Transactions on Magnetics* 1980, **16** (2) 368-372.
- Shinkai, M. "Functional magnetic particles for medical application" *Journal of Bioscience and Bioengineering* 2002, **94** (6) 606-613.
- Shinoda, K., Jeyadevan, B., Kasai, M., Nakatani, I., Oka, H. and Tohji, K. "Characterization of inherent clusters in water-based magnetite magnetic fluid" *Journal of Magnetism and Magnetic Materials* 2002, **252** (1-3) 141-143.
- Sidhu, P. S., Gilkes, R. J. and Posner, A. M. "Mechanism of the low temperature oxidation of synthetic magnetites" *Journal of Inorganic and Nuclear Chemistry* 1977, **39** (11) 1953-1958.
- Smit, J. and Wijn, H. P. J., Eds. (1959). in Ferrites, John Wiley & Sons: New York.
- Smith, B., Ed. (1999). Infrared spectral interpretation-A systematic approach, CRC Press, Boca Raton, London, New York, Washington DC.
- Sreeremya, T. S., Thulasi, K. M., Krishnan, A. and Ghosh, S. "A novel aqueous route to fabricate ultrasmall monodisperse lipophilic cerium oxide nanoparticles" *Industrial & Engineering Chemistry Research* 2012, **51** (1) 318-326.
- Stolarczyk, J. K., Ghosh, S. and Brougham, D. F. "Controlled growth of nanoparticle clusters through competitive stabilizer desorption" *Angewandte Chemie-International Edition* 2009, **48** (1) 175-178.
- Strbak, O., Kopcansky, P. and Frollo, I. "Biogenic magnetite in humans and new magnetic resonance hazard questions" *Measurement Science Review* 2011, **11** (3) 85-91.
- Strom, V., Olsson, R. T. and Rao, K. V. "Real-time monitoring of the evolution of magnetism during precipitation of superparamagnetic nanoparticles for bioscience applications" *Journal of Materials Chemistry* 2010, **20** (20) 4168-4175.
- Sun, C., Lee, J. S. H. and Zhang, M. "Magnetic nanoparticles in MR imaging and drug delivery" *Advanced Drug Delivery Reviews* 2008, **60** 1252-1265.
- Sun, C. Q. "Dominance of broken bonds and nonbonding electrons at the nanoscale" *Nanoscale* 2010, **2** (10) 1930-1961.

- Sun, S. H., Murray, C. B., Weller, D., Folks, L. and Moser, A. "Monodisperse FePt nanoparticles and ferromagnetic FePt nanocrystal superlattices" *Science* 2000, **287** (5460) 1989-1992.
- Sundaram, P. A., Augustine, R. and Kannan, M. "Extracellular biosynthesis of iron oxide nanoparticles by *Bacillus subtilis* strains isolated from rhizosphere soil" *Biotechnology and Bioprocess Engineering* 2012, **17** (4) 835-840.
- Tadmor, R., Rosensweig, R. E., Frey, J. and Klein, J. "Resolving the puzzle of ferrofluid dispersants" *Langmuir* 2000, **16** (24) 9117-9120.
- Tang, J., Myers, M., Bosnick, K. A. and Brus, L. E. "Magnetite Fe₃O₄ nanocrystals: Spectroscopic observation of aqueous oxidation kinetics" *Journal of Physical Chemistry B* 2003, **107** (30) 7501-7506.
- Tian, Y., Yu, B. B., Li, X. and Li, K. "Facile solvothermal synthesis of monodisperse Fe₃O₄ nanocrystals with precise size control of one nanometre as potential MRI contrast agents" *Journal of Materials Chemistry* 2011, **21** (8) 2476-2481.
- Tjong, S. C. and Chen, H. "Nanocrystalline materials and coatings" *Materials Science & Engineering R-Reports* 2004, **45** (1-2) 1-88.
- Torres-Diaz, I. and Rinaldi, C. "Recent progress in ferrofluids research: novel applications of magnetically controllable and tunable fluids" *Soft Matter* 2014, **10** (43) 8584-8602.
- Tu, Z., Zhang, B., Yang, G., Wang, M., Zhao, F., Sheng, D. and Wang, J. "Synthesis of poly(ethylene glycol) and poly(vinyl pyrrolidone) co-coated superparamagnetic iron oxide nanoparticle as a pH-sensitive release drug carrier" *Colloids and Surfaces a-Physicochemical and Engineering Aspects* 2013, **436** 854-861.
- Uchida, M., Flenniken, M. L., Allen, M., Willits, D. A., Crowley, B. E., Brumfield, S., Willis, A. F., Jackiw, L., Jutila, M., Young, M. J. and Douglas, T. "Targeting of cancer cells with ferrimagnetic ferritin cage nanoparticles" *Journal of the American Chemical Society* 2006, **128** (51) 16626-16633.
- Usami, T., Kagawa, K. and Kawazoe, M. (2007). Deodorizing catalyst used for air cleaner, contains complex oxide support of cerium oxide and magnetite, supporting manganese as catalyst component. JP, Daikin Kogyo Kk.
- Van Der Hoeven, P. C. and Lyklema, J. "Electrostatic stabilization in non-aqueous media" *Advances in Colloid and Interface Science* 1992, **42** 205-277.

References

- Vaz, C. A. F., Hoffman, J., Posadas, A. B. and Ahn, C. H. "Magnetic anisotropy modulation of magnetite in $\text{Fe}_3\text{O}_4/\text{BaTiO}_3$ (100) epitaxial structures" *Applied Physics Letters* 2009, **94** (2) 022504.
- Viota, J. L., Gonzalez-Caballero, F., Duran, J. D. G. and Delgado, A. V. "Study of the colloidal stability of concentrated bimodal magnetic fluids" *Journal of Colloid and Interface Science* 2007, **309** (1) 135-139.
- Wang, J., Xia, T., Wu, C., Feng, J., Meng, F., Shi, Z. and Meng, J. "Self-assembled magnetite peony structures with petal-like nanoslices: one-step synthesis, excellent magnetic and water treatment properties" *RSC Advances* 2012, **2** (10) 4220-4227.
- Wang, X., Liu, X., Lai, L., Li, S., Weng, J., Zhou, Z., Cui, Q., Chen, X., Cao, M. and Zhang, Q. "Syntheses, properties and electrochemical activity of carbon microtubes modified with amino groups" *Advanced Functional Materials* 2008, **18** (12) 1809-1823.
- Wang, X., Zhao, Z., Qu, J., Wang, Z. and Qiu, J. "Shape-control and characterization of magnetite prepared via a one-step solvothermal route" *Crystal Growth & Design* 2010, **10** (7) 2863-2869.
- Watt, M., Ed. (1997). The Principles and Practice of Electron Microscopy, Cambridge University Press, Cambridge.
- Web. "Web of science core collection on nano" retrieved on September 22, 2016.
- Wei, H. and Wang, E. "Nanomaterials with enzyme-like characteristics (nanozymes): next-generation artificial enzymes" *Chemical Society Reviews* 2013, **42** (14) 6060-6093.
- Williams, D. B. and Carter, C. B., Eds. (2009). Transmission electron microscopy: A textbook for materials science, Springer.
- Winau, F., Westphal, O. and Winau, R. "Paul Ehrlich--in search of the magic bullet" *Microbes and Infection* 2004, **6** (8) 786-789.
- Wriedt, T. "A review of elastic light scattering theories" *Particle & Particle Systems Characterization* 1998, **15** (2) 67-74.
- Wu, M., Xiong, Y., Peng, Z., Jiang, N., Qi, H. and Chen, Q. "The enhanced coercivity for the magnetite/silica nanocomposite at room temperature" *Materials Research Bulletin* 2004, **39** (12) 1875-1880.
- Wu, W., Wu, Z. H., Yu, T., Jiang, C. Z. and Kim, W. S. "Recent progress on magnetic iron oxide nanoparticles: synthesis, surface functional strategies and biomedical applications" *Science and Technology of Advanced Materials* 2015, **16** (2) 023501.

- Wu, W., Xiao, X. H., Ren, F., Zhang, S. F. and Jiang, C. Z. "A comparative study of the magnetic behavior of single and tubular clustered magnetite nanoparticles" *Journal of Low Temperature Physics* 2012, **168** (5-6) 306-313.
- Wu, W., Xiao, X. H., Zhang, S. F., Zhou, J. A., Fan, L. X., Ren, F. and Jiang, C. Z. "Large-scale and controlled synthesis of iron oxide magnetic short nanotubes: shape evolution, growth mechanism, and magnetic properties" *Journal of Physical Chemistry C* 2010, **114** (39) 16092-16103.
- Xiao, K., Li, Y. P., Luo, J. T., Lee, J. S., Xiao, W. W., Gonik, A. M., Agarwal, R. G. and Lam, K. S. "The effect of surface charge on in vivo biodistribution of PEG-oligocholic acid based micellar nanoparticles" *Biomaterials* 2011, **32** (13) 3435-3446.
- Xiao, L., Li, J., Brougham, D. F., Fox, E. K., Feliu, N., Bushmelev, A., Schmidt, A., Mertens, N., Kiessling, F., Valldor, M., Fadeel, B. and Mathur, S. "Water-soluble superparamagnetic magnetite nanoparticles with biocompatible coating for enhanced magnetic resonance imaging" *ACS Nano* 2011, **5** (8) 6315-6324.
- Xiong, Y., Ye, J., Gu, X. and Chen, Q.-w. "Synthesis and assembly of magnetite nanocubes into flux-closure rings" *The Journal of Physical Chemistry C* 2007, **111** (19) 6998-7003.
- Xu, Z. C., Shen, C. M., Tian, Y. A., Shi, X. Z. and Gao, H. J. "Organic phase synthesis of monodisperse iron oxide nanocrystals using iron chloride as precursor" *Nanoscale* 2010, **2** (6) 1027-1032.
- Yan, J.-F. and Liu, J. "Nanocryosurgery and its mechanisms for enhancing freezing efficiency of tumor tissues" *Nanomedicine-Nanotechnology Biology and Medicine* 2008, **4** (1) 79-87.
- Yan, Q., Zhang, Z., Zhang, Y., Umar, A., Guo, Z., O'Hare, D. and Wang, Q. "Hierarchical Fe₃O₄ core-shell layered double hydroxide composites as magnetic adsorbents for anionic dye removal from wastewater" *European Journal of Inorganic Chemistry* 2015, **2015** (25) 4182-4191.
- Yang, C., Wu, J. J. and Hou, Y. L. "Fe₃O₄ nanostructures: synthesis, growth mechanism, properties and applications" *Chemical Communications* 2011, **47** (18) 5130-5141.
- Yang, H., Liu, C., Yang, D., Zhang, H. and Xi, Z. "Comparative study of cytotoxicity, oxidative stress and genotoxicity induced by four typical nanomaterials: the role of particle size, shape and composition" *Journal of Applied Toxicology* 2009, **29** (1) 69-78.

- Yang, H., Ogawa, T., Hasegawa, D. and Takahashi, M. "Synthesis and magnetic properties of monodisperse magnetite nanocubes" *Journal of Applied Physics* 2008, **103** (7) 07d526.
- Yang, H. M., Park, C. W., Woo, M. A., Kim, M. I., Jo, Y. M., Park, H. G. and Kim, J. D. "HER2/neu antibody conjugated poly(amino acid)-coated iron oxide nanoparticles for breast cancer MR Imaging" *Biomacromolecules* 2010, **11** (11) 2866-2872.
- Yathindranath, V., Rebbouh, L., Moore, D. F., Miller, D. W., van Lierop, J. and Hegmann, T. "A versatile method for the reductive, one-pot synthesis of bare, hydrophilic and hydrophobic magnetite nanoparticles" *Advanced Functional Materials* 2011, **21** (8) 1457-1464.
- Yoon, K. Y., Xue, Z., Fei, Y., Lee, J. H., Cheng, V., Bagaria, H. G., Huh, C., Bryant, S. L., Kong, S. D., Ngo, V. W., Rahmani, A.-R., Ahmadian, M., Ellison, C. J. and Johnston, K. P. "Control of magnetite primary particle size in aqueous dispersions of nanoclusters for high magnetic susceptibilities" *Journal of Colloid and Interface Science* 2016, **462** 359-367.
- Yu, B. Y. and Kwak, S.-Y. "Self-assembled mesoporous Co and Ni-ferrite spherical clusters consisting of spinel nanocrystals prepared using a template-free approach" *Dalton Transactions* 2011, **40** (39) 9989-9998.
- Zhang, D. E., Zhang, X. J., Ni, X. M., Song, J. M. and Zheng, H. G. "Fabrication and characterization of Fe₃O₄ octahedrons via an EDTA-assisted route" *Crystal Growth & Design* 2007, **7** (10) 2117-2119.
- Zhang, H., Lim, H., Wei, J. and Wong, C. "Size and shape evolution of magnetite nanocrystals in water-soluble system" *Nanoscience and Nanotechnology Letters* 2011, **3** 155-160.
- Zhang, L., He, R. and Gu, H.-C. "Oleic acid coating on the monodisperse magnetite nanoparticles" *Applied Surface Science* 2006, **253** (5) 2611-2617.
- Zhang, Y., Zhu, G., Lu, J., Guo, Z. and Cao, J. "Graphyne as a promising substrate for high density magnetic storage bits" *Rsc Advances* 2015, **5** (107) 87841-87846.
- Zhang, Z., Boxall, C. and Kelsall, G. H. "Photoelectrophoresis of colloidal iron oxides 1. Hematite (α -Fe₂O₃)" *Colloids and Surfaces A: Physicochemical and Engineering Aspects* 1993, **73** 145-163.



CrossMark
 click for updates

Cite this: *RSC Adv.*, 2014, 4, 64919

Magnetic, X-ray and Mössbauer studies on magnetite/maghemite core–shell nanostructures fabricated through an aqueous route†

Srividhya J. Iyengar,^a Mathew Joy,^a Chandan Kumar Ghosh,^b Subhrajyoti Dey,^c Ravinder K. Kotnala^d and Swapankumar Ghosh^{*a}

Uniform 6–13 nm sized 0D superparamagnetic Fe₃O₄ nanocrystals were synthesized by an aqueous ‘co-precipitation method’ under a N₂ atmosphere as a function of temperature to understand the growth kinetics. The crystal phases, surface charge, size, morphology and magnetic characteristics of as-synthesized nanocrystals were characterized by XRD, Raman spectroscopy, FTIR, TG-DTA, BET surface area, dynamic light scattering along with zeta potential, HR-TEM, EDAX, vibrating sample magnetometry and Mössbauer spectroscopy. TEM investigation revealed highly crystalline spherical magnetite particles in the 8.2–12.5 nm size range. The kinetically controlled as-grown nanoparticles were found to possess a preferential (311) orientation of the cubic phase, with a highest magnetic susceptibility of ~57 emu g⁻¹. The Williamson–Hall technique was employed to evaluate the mean crystallite size and microstrain involved in the as-synthesized nanocrystals from the X-ray peak broadening. In addition to FTIR and Raman spectra, Rietveld structural refinement of XRD confirms the magnetite phase with 5–20% maghemite in the sample. VSM and Mössbauer spectral data allowed us to fit the magnetite/maghemite content to a core–shell model where the shell is 0.2–0.3 nm thick maghemite over a magnetite core. The activation energy of <10 kJ mol⁻¹ calculated from an Arrhenius plot for the complex process of nucleation and growth by diffusion during synthesis shows the significance of the precipitation temperature in the size controlled fabrication processes of nanocrystals. Brunauer–Emmett–Teller (BET) results reveal a mesoporous structure and a large surface area of 124 m² g⁻¹. Magnetic measurement shows that the particles are ferromagnetic at room temperature with zero remanence and zero coercivity. This method produced highly crystalline and dispersed 0D magnetite nanocrystals suitable for biological applications in imaging and drug delivery.

Received 26th September 2014
 Accepted 18th November 2014

DOI: 10.1039/c4ra11283k

www.rsc.org/advances

Introduction

Magnetite (Fe₃O₄, containing Fe²⁺ and Fe³⁺ in the 1 : 2 ratio), crystallizes in the inverse cubic spinel structure *Fd3m* above the so-called Verwey transition temperature ~120 K.¹ The oxygen atoms form the close-packed face-centered-cubic (fcc) lattices with the iron atoms occupying the interstitial positions.² Fe₃O₄ nanoparticles exhibit unique and tunable fundamental size- and shape-dependent novel magnetic, optical, and other unique properties due to quantum confinement effects *i.e.*, the

nanometer size effect and have attracted great attention in recent years. The crystal chemistry of Fe₃O₄ is of considerable interest to mineralogists and materials scientists because of its extensive applications in magnetic resonance imaging (MRI) for imaging the brain and the central nervous system,^{3–5} for assessing cardiac function,⁶ as a drug delivery/gene-delivery platform,⁷ ferro-fluids, MICR ink,⁸ cell targeting,⁹ magnetic force based tissue engineering,^{10,11} magnetically controllable catheters, glucose sensing,¹² sensing tumor by magneto-impedance,¹³ and magnetic separation of biological materials. Outstanding magneto-electrical properties have also been reported in strain induced magnetite.^{14,15} Recent technological advances in smart multifunctional nanobiomagnetic platforms offer exciting opportunities in personalized medicine for more accurate early prognosis, monitoring and treatment of various diseases without jeopardizing healthy tissues by identifying unique biochemical markers of disease before the appearance of symptoms obviates the need.¹⁶ Nanocrystalline Fe₃O₄ often exhibits superparamagnetic behavior. Néel relaxation of superparamagnetic Fe₃O₄ is an effective way to heat up the

^aAdvanced Clay & Traditional Ceramics Division, CSIR-Central Glass & Ceramics Research Institute, Kolkata-700032, India. E-mail: swapankumar.ghosh2@mail.dcu.ie; srividhyaji@gmail.com; Fax: +91 33 24730957; Tel: +91 33 23223546

^bSchool of Material Science & Nanotechnology, Jadavpur University, Kolkata-700032, India

^cDepartment of Physics, Jadavpur University, Kolkata-700032, India

^dMaterials Physics and Engineering, CSIR-National Physical Laboratory, New Delhi-110 012, India

† Electronic supplementary information (ESI) available. See DOI: 10.1039/c4ra11283k

nanocrystals and the surrounding tissue by transferring energy from the external magnetic field in therapeutic hyperthermia and, more recently, in the development of theranostic technologies.^{1,17}

Large surface area to volume ratio for nanoparticles provides enormous driving force for diffusion, especially at elevated temperatures.¹⁸ Colombo *et al.* calculated the activation energy for the reduction of iron oxides (hematite, maghemite and magnetite) at 150° to 400 °C under reductive atmosphere.¹⁹ Brus *et al.* reported the diffusion controlled aqueous oxidation kinetics of magnetite nanoparticles.²⁰ Although magnetite nanocrystals prepared by the precipitation technique have been extensively studied, to the best of our knowledge, seldom efforts have been devoted on its growth kinetics during crystallisation. Magnetite NPs are susceptible to undergo surface oxidation in air to maghemite ($\gamma\text{-Fe}_2\text{O}_3$), and hence the control of magnetic properties at these very small sizes still remains a challenge. Average size estimation by transmission electron microscopy (TEM) is by analyzing rather a limited number of nanoparticles (typically 100–300) compared to $>10^{12}$ NPs investigated by X-ray diffraction (XRD) and vibrating sample magnetometry (VSM).²¹ Debye–Scherrer formula, though widely been used to estimate crystal sizes, underestimates the grain size as it ignores the line broadening due to microstrain in the lattice as a result packing defects/dislocation structures *etc.*²² Application of Williamson–Hall (W–H) method on X-ray profiles not only estimate the crystallite sizes but also isolates the peak broadening due to internal lattice strain.²³

Over the past couple of decades numerous techniques have been proposed to synthesize nano-sized Fe_3O_4 particles, such as sol–gel,²⁴ hydrothermal/solvothermal^{1,25} thermal decomposition,²⁶ reverse micelles,²⁷ polyol,²⁸ sonolysis,²⁹ gamma ray irradiation,³⁰ microwave plasma synthesis.³¹ Majority of these synthetic methods involves thermal decomposition of organo-metallic precursors or metal complexes in the presence of surfactants that enables precise control of both size and its distribution. Despite such advantages, lipophilic nature of the nanoparticle (NP) surfaces and cost of reactants presently make these synthetic methods not viable for biomedical applications.²¹ Nevertheless, the aqueous coprecipitation of Fe^{2+} and Fe^{3+} salts using an alkali remains the most intensively studied, modified and improved method to find economic and environmental friendly pathways for fabrication of controlled metal oxide nanostructures. Most of the industrial applications of magnetite demand highly magnetic nanoparticles with precise knowledge of size, lattice strain/defects and minimal surface passivation. Crystal dimension of nanomaterials affect key colloid properties such as rheology, film gloss, catalytic activity, chemical sensing *etc.*³² Very often increasing mismatch of magnetic NP size and its saturation magnetization values (and as a result increasing magnetic anisotropy) is reported with decreasing size in magnetite NPs. This is due to the presence of a magnetically dead layer of oxidized 15–30% amorphous component (with a thickness varying between 0.3 and 1.0 nm) over the maghemite shell of magnetite–maghemite core–shell structure.²¹ We show that there are size-dependent changes in the local structure and oxidation state of the oxide shell, the

relative fraction of maghemite increasing at the expense of magnetite as the core dimensions decrease. This size/structure correlation has been explained in terms of morphological and structural disorder arguments.³³

In this communication, we report the estimation of the crystal dimensions of magnetite synthesized through surfactant free aqueous coprecipitation route from the TEM, XRD, and magnetization profiles by Langevin fit. The XRD data were analyzed by Rietveld refinement. The magnetite phase was confirmed from the X-ray, TEM, Raman and Fourier transform infrared (FTIR) spectroscopy. The maghemite content in magnetite was determined from the Mössbauer spectral fitting. The magnetic powder was thoroughly characterized by thermal analyses (TG-DTA), surface area analysis, hydrodynamic size and zeta potential measurements. The activation energy for growth of size tailored magnetite crystals was calculated by employing Arrhenius equation. The crystal dimensions were carefully correlated in terms of maghemite layer content over magnetite core in a core–shell model.

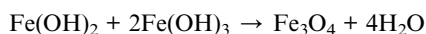
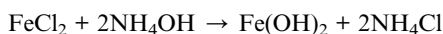
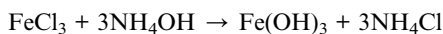
Experimental section

Materials

Fe(II) chloride (98%) and Fe(III) chloride (97%) were procured from Sigma Aldrich Chemicals. Ammonia solution (25 wt%) and common solvents *ca.* acetone, ethanol (analytical grade) *etc.* were purchased from Merck, India. All the syntheses, washings and dilutions were done with Millipore water (Millipore, specific resistivity 18.2 $\text{M}\Omega\text{ cm}$ @ 25 °C). Millipore water for synthetic purposes was purged with XL grade (99.999%) nitrogen gas for deaeration.

Experimental

The procedure adopted here is a modification of the method of Shen *et al.*³⁴ To elucidate the formation process of Fe_3O_4 nanocrystal in a size tailored manner, 4.2 mmol $\text{FeCl}_2 \cdot 4\text{H}_2\text{O}$ and 8.4 mmol $\text{FeCl}_3 \cdot 6\text{H}_2\text{O}$ (such that $\text{Fe}^{3+}/\text{Fe}^{2+} = 2$) were dissolved in 35 ml deionized water previously deaerated by purging nitrogen gas in a 100 ml three-neck round bottom flask whose central neck was connected to a water-cooled condenser. A thermometer and a glass pipette for N_2 gas purge were connected through thermometer pockets to the other two necks. The reaction mixture was heated slowly to 90 °C over a hot plate magnetic stirrer while continuous stirring. The clear off-yellow color of the suspension turned to muddy orange at ~ 80 °C indicating the complete hydrolysis of ferrous and ferric chlorides. After heating the reaction mixture for ~ 30 min at 90 °C, ~ 7 ml NH_3 solution was added while vigorous stirring. The orange colored suspension immediately turned black indicating the formation of magnetite crystals. At this point the net Fe^{2+} concentration was 100 mM. The temperature was maintained at 90 °C for further 30 min to allow crystal growth. The sequence of magnetite formation from the ferrous and ferric chlorides *via* hydrated ferrous and ferric oxides during alkali precipitation may be given as³⁵



The suspension was cooled naturally to ambient temperature. The resultant pH of the reaction mixture was ~ 11 . The entire experiment was carried out carefully under a closed nitrogen atmosphere. The precipitated black solid was collected by magnetic decantation with a help of permanent neodymium iron boron magnet (520 G strength), and washed five times with 1 : 1 acetone and methanol mixture. This magnetite is designated as T90. Similarly, magnetites (~ 1 g) were produced using the same precursor concentrations at temperatures 33, 45, 60, and 75 °C under identical conditions and were named as T33, T45, T60, and T75. After the final washing, the precipitates were collected and dried at room temperature in a vacuum oven.

The powder XRD patterns were recorded with Bruker D8 Advanced diffractometer equipped with source $\text{CuK}\alpha_1$ radiation ($\lambda = 1.5406 \text{ \AA}$) with a step size of $0.05^\circ 2\theta$ and a scan speed of 4° min^{-1} . The mean crystallite size and microstrain involved in as-synthesized nano magneto-crystalline samples were estimated by the Cauchy–Cauchy (CC) approach also known as Williamson–Hall³⁶ plot from the linear dependence line-profiling of prominent X-ray diffraction peaks of $\beta_{2\theta} \cos \theta$ versus $\sin \theta$ as described in eqn (1):

$$\beta_{2\theta} \cos \theta = 2\varepsilon \sin \theta + 0.9 \lambda / D \quad (1)$$

where D is the crystal size, ε is the maximum microdeformation of a lattice, $\beta_{2\theta}$ is the integral width of the diffraction peaks at angle θ by the eqn (2):

$$\beta_{2\theta} = \frac{I \cdot I}{I_{\text{Max}}} \quad (2)$$

Strain is estimated from the slope (2ε) and the average crystal size (D) from the intercept ($0.9\lambda/D$) of the linear regression assuming the particles are spherical. W–H analysis is sometimes used as a complementary method to confirm TEM values and to make them more robust from the statistical point of view. We adopted Rietveld powder structure refinement analysis³⁷ of X-ray powder diffraction step scan data using the JAVA based program MAUD,³⁸ to obtain the structural and microstructural refinement parameters through a least-square method. The experimental profiles are fitted with the most suitable pseudo-Voigt (pV) analytical function³⁷ with asymmetry and the background of each pattern is fitted with a fourth order polynomial function.

Standard Harris analysis was performed on X-ray data of magnetite powders³⁹ to estimate preferred orientation of specific crystal planes and is expressed as texture coefficient $C(h_i k_i l_i)$, following eqn (3),

$$C(h_i k_i l_i) = \frac{I(h_i k_i l_i)}{I_o(h_i k_i l_i)} \left[\frac{1}{n} \sum \frac{I(h_i k_i l_i)}{I_o(h_i k_i l_i)} \right]^{-1} \quad (3)$$

where, $I(h_i k_i l_i)$ is the diffraction intensity of the $(h_i k_i l_i)$ plane of the particular sample under investigation, $I_o(h_i k_i l_i)$ is the intensity of the $(h_i k_i l_i)$ plane from the standard JCPDS powder diffraction pattern for the corresponding peak i , and n is the number of reflections taken in to account. FTIR spectra on magnetite samples were taken at room temperature on a Perkin-Elmer Spectrum 100 spectrophotometer in the $400\text{--}4000 \text{ cm}^{-1}$ range with average of 50 scans. The powder specimens were pressed into small discs using spectroscopically pure KBr (Sigma-Aldrich, $\geq 99\%$) matrix with sample to KBr ratio $\sim 1 : 100$ to evaluate the structural aspects of magnetite. The Raman spectrometer is equipped with an optical microscope (Olympus Confocal Raman Optics micrometer), a thermoelectrically cooled (-60°C) charge-coupled device (CCD) detector and a CCD camera (resolution 1340×1100) that can provide a good laser beam. The Raman spectra were collected by 514.5 nm radiation from an argon ion laser (Stellar Pro, 50 mW) on Princeton Instruments Acton SP2500. Samples were compacted into a 1 mm cavity held on an anodized aluminum plate. The laser beam was focused on the sample by a $\times 50$ lens to a spot size of *ca.* 5–6 μm . Coaxial backscatter geometry was employed for signal collection with spectral resolution of $\sim 1 \text{ cm}^{-1}$. The Raman shifts were calibrated using the 520 cm^{-1} line of a silicon wafer. The spectra were collected using 2.5 mW laser power over the range $1000\text{--}200 \text{ cm}^{-1}$ and accumulation over 10 scans, each with an exposure time of 10 s to reduce noise further. Crystal dimensions can also be estimated from the magnetization curves based on the theory of superparamagnetism as proposed by Bean and co-workers.^{40–42} To fit the magnetization curves, we assume that individual grains are single crystals without mutual interaction and each particle has an inner single-domain core with the spontaneous magnetization. The magnetization of N number of ideal non-interaction superparamagnetic nanoparticles, each with identical magnetic moment μ , at constant temperature T in magnetic field H is given by Langevin function eqn (4),

$$M(H) = N\mu \left\{ \left(\frac{e^{2\left(\frac{\mu H}{k_B T}\right)} + 1}{e^{2\left(\frac{\mu H}{k_B T}\right)} - 1} \right) - \frac{k_B T}{\mu H} \right\} \quad (4)$$

where k_B and $N\mu$ are the Boltzmann constant and saturation magnetization (M_s) of the synthesized sample.

The magnetization curves were fitted using a nonlinear-least squares routine to obtain two parameters: the log-mean single particle moment, μ , and M_s . The size, called “magnetic size”, is significantly smaller than the physical size obtained from TEM. Magnetic measurements of the powder sample were made using VSM (Lakeshore 7305, US) at 298 K and Physical Property Measurement System (PPMS, Cryogen, UK). ^{57}Fe Mössbauer spectra of the two selected specimens T33 and T90 were recorded at room temperature by means of a standard constant acceleration transmission mode with a $\sim 50 \text{ mCi } ^{57}\text{Co}$ diffused in rhodium matrix using a $\alpha\text{-Fe}$ foil for calibration. The experimental profiles were fitted to Lorentzian functions by least-square method with RECOIL software package. The average size and the morphologies of magnetite nanoparticles and its

crystal structure were ascertained by the high resolution transmission electron microscopy (HR-TEM) using a FEI Tecnai 30 G² S-Twin HR-TEM operated at 300 kV equipped with a Gatan CCD camera. The chemical composition was determined on several crystal grains by using an EDAX spectrometer equipped with high-angle annular dark-field detector with beam scanning capability (Fischione Instruments, Inc., USA) with TIA analysis software. The standard deviation of size was calculated using the formula eqn (5),

$$\sigma = \sqrt{\frac{1}{N} \sum_{i=1}^N (x_i - \bar{x})^2} \quad (5)$$

where N is sampling number, x_i is random variable, \bar{x} is mean size and the size distribution is calculated using probability density eqn (6), based on a log-normal function

$$p(D) = \frac{1}{D\sigma_1\sqrt{2\pi}} \exp\left\{-\frac{[\ln(D/D_0)]^2}{2\sigma_1^2}\right\} \quad (6)$$

where σ is standard deviation, D is size, and D_0 is the mean size.

The specific surface area and pore size distribution of the magnetite powders were determined from the N₂ adsorption data following BET technique at 77 K using a surface area analyser (Quantachrome Instruments version 10.01). Surface area analyses were conducted on powder samples after degassing them at 200 °C for 3 h. The thermogravimetric (TG) analysis was used to investigate the thermal reactions of the synthesized nanocrystals using a Simultaneous Thermal Analyzer (STA-6000, Perkin-Elmer, The Netherlands) under ultrapure nitrogen purge. The thermograms were collected with a ramp of 10 °C min⁻¹ in the temperature range 50–1000 °C.

Results and discussion

Magnetite nanoparticles were synthesized by the economic, non-toxic aqueous coprecipitation method at different reaction temperatures in the range 33° to 90 °C. The synthesized iron oxide powders (T33 to T90) were typically black in color indicating the presence of magnetite as the dominant phase, although ancillary γ -Fe₂O₃ may not be completely excluded. The bright field HR-TEM images for selected samples T90, T75, T60 and T33 are shown in Fig. 1 (additional images are provided in Fig. S1 in the ESI†). TEM images show spherical, crystalline and well resolved particles with narrow size distribution in 6–13 nm range. Apparently the particles do not interact with each other at room temperature which will be further investigated by the magnetization measurements in a later section (Fig. 3). The TEM results shown in Fig. 1 reveal that the precipitation temperature increases the average particle size of T33 from 7.76 ± 1.94 nm to 10.84 ± 1.97 nm in T60, while 75 °C reaction temperature further increases the size to 12.32 ± 1.63 nm.

On the other hand, the magnetite synthesized at 90 °C doesn't improve the equilibrium size much but most particles fall in relatively wider 12.42 ± 1.87 nm size range (Fig. 1A). The particle size and number based size distribution of

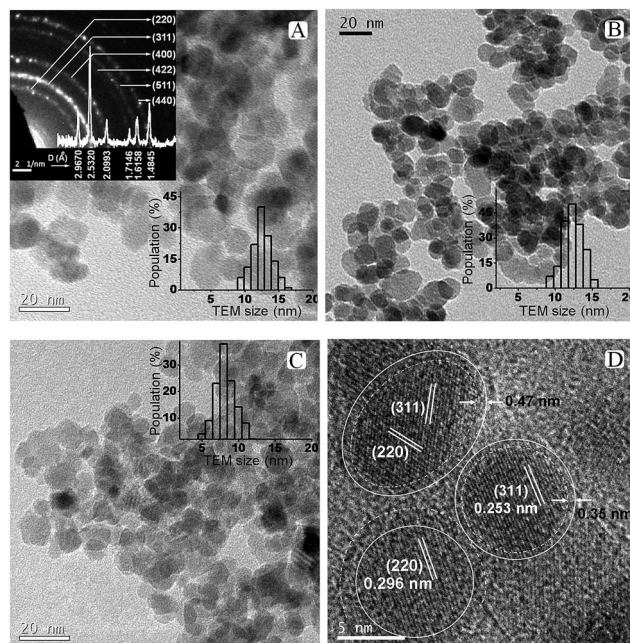


Fig. 1 Bright-field TEM images of as synthesized magnetite nanoparticles (A) T90 with its SAED pattern (inset), (B) T75, (C) T33, and (D) HR-TEM of T33 indicating clear crystalline core surrounded by amorphous shell (marked with white line). The size distribution histograms of the corresponding nanocrystals for all the images are presented as inset to each image.

nanoparticles are calculated by probability density function (eqn 6) from the inspection of multiple TEM images on 100–200 particles. These results suggest that the size of the resultant Fe₃O₄ nanocrystals is strongly dependent on the precipitation temperature. Careful examination of the high resolution images indicates that all the nanoparticles are single crystals and fringes corresponding to predominant (311) and (220) planes could be identified. Selected area diffraction (SAED) patterns of T90 (inset of Fig. 1A) shows clear Debye-Scherrer rings corresponding to (220), (311), (400), (422), (511) and (440) planes with corresponding interplanar spacings 0.2967, 0.2532, 0.2099, 0.1715, 0.1616 and 0.1485 nm respectively (JCPDS card no. 19-0629). The careful observation of HR-TEM images clearly reveals crystallographically different core-shell morphology in nanocrystals of T33 with amorphous shell of thickness ~0.3–0.5 nm. The atomic ratio of Fe:O of the nanoparticles measured by EDAX (Fig. S1 in ESI†) is 3 : 4. Within the limits of sensitivity (≤3%), these EDAX data also suggest that the nanoparticles have no detectable impurities: the signal from C and Cu was due to the carbon film over the copper TEM grid.

The X-ray diffraction patterns of Fe₃O₄ synthesized at different temperatures and Rietveld analysis on the XRD pattern of T33 are shown in Fig. 2. All Bragg's planes could be indexed to face centered cubic inverse spinel magnetite of *Fd3m*, #227 space group with lattice constant a in the range 0.8340–0.8366 nm whereas the same for bulk magnetite is 0.8396 nm (JCPDS card no. 19-0629).

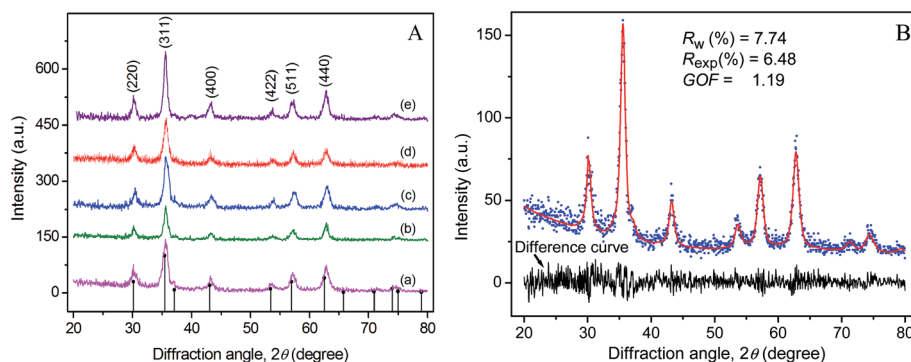


Fig. 2 (A) X-ray diffraction patterns of magnetites (a) T33, (b) T45, (c) T60, (d) T75, and (e) T90. The vertical drop lines in (A) are the theoretical Bragg positions for inverse spinel magnetite phase following JCPDS Card no. 19-0629. (B) is a typical Rietveld fit (solid line) for T33 over the corresponding raw XRD data (dots). The noisy layer in (B) is the difference curve between the XRD profile and the Rietveld simulation.

Broad diffraction peaks (Fig. 2A) indicate the nanocrystalline nature of the particles. When the reaction temperature was increased in steps from 33 to 90 °C, a slight progressive narrowing of the X-ray diffraction peaks occurred as a result of crystal growth and reduction of microstrain in the lattice originating from defects. The match of the X-ray pattern with its Rietveld fit and the resultant almost spike less difference pattern indicates the quality of fit in magnetite–maghemite mixed phases in the synthesized sample. The Rietveld analyses of X-ray patterns of T33 and T90 (Fig. S4 in ESI†) allowed us to estimate the relative concentrations of magnetite phase as 89.2 and 87.3% respectively which is compatible with a core–shell model where the shell is 0.2–0.3 nm thick in $D_{\text{TEM}} = 8.2$ and 12.5 nm particles in T33 and T90 respectively. The core–shell structure was also observed from HR-TEM images (Fig. 1). The fit parameters are consistent with reported data in the literature.⁴³ Fig. 3 shows the field dependent magnetic properties of the synthesized Fe_3O_4 samples (T33 and T90), measured by VSM at room temperature as well as PPMS at different temperatures with higher field resolution. The hysteresis loops apparently pass through the origin which indicates zero coercivity and zero remanence (Fig. 3A), signifying that the samples are in the superparamagnetic state with unstable magnetization at this

temperature⁴⁴ and the samples possess higher magnetization at 250 K due to reduced thermal energy (Fig. 3B).

In contrast to saturated magnetization (M_s) of ferromagnetic Fe_3O_4 nanoparticles, measured by Tian *et al.*,⁴⁵ we observed unsaturated magnetic behavior in our synthesized nanoparticles that confirms the superparamagnetic nature. On careful examination of the high resolution magnetization data (Fig. 3B) it is observed that both T33 and T90 display coercivities to the extent of mere 21 and 16 Oe respectively. Appearance of the coercivity may be attributed to the long range magnetic dipolar interactions. The magnetization profiles as a function of H/T (inset of Fig. 3B) are very much close to each other suggesting non-interactive nature of the particles. However, small deviation between the curves in the high field region and the presence of coercive field indicate that the mutual interaction is not absolutely zero *i.e.*, a weak interaction exists among them.⁴⁶ Due to the asymptotic increase of magnetization for high fields (see Fig. 3), the saturation magnetization value can be obtained from the fitting of the M vs. $1/H$ curves, extrapolating the magnetization value to $1/H = 0$.⁴⁷ According to inset of Fig. 3A, the observed magnetization for T90 and T33 are 48.44 and 56.11 emu g^{-1} respectively. The curves were fitted with Langevin function in order to get M_s of samples and the obtained fitting parameters are summarized in Table 1. It is noteworthy to

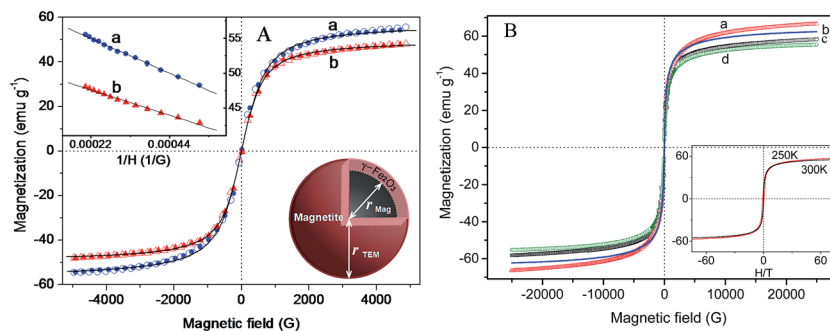


Fig. 3 Magnetization versus applied magnetic field data (A) with low field resolution for selected magnetite (a) T33 and (b) T90 specimens and (B) higher field resolution from PPMS at (a) T33 at 250 K, (b) T33 at 300 K, (c) T90 at 250 K and (d) T90 at 300 K and its inset represents the magnetization data as a function of H/T for T90. Typical Langevin fits are represented by solid black lines in (A).

mention that the M_s of our synthesized samples is greater than that of Fe_3O_4 nanosheets of thickness ~ 10 nm and nanorods of length > 100 nm and diameter of ~ 10 nm,⁴⁸ but is quite less than bulk Fe_3O_4 (92 emu g^{-1})⁴⁹ and the reduction of M_s may be attributed to the disordered surface spin or spin canting behavior at the surface of the nanoparticles and change in degree of inversion.

It is worthy to mention that M_s of T33 is higher than that of T90 *i.e.*, bigger particle has lower value of M_s . The magnetic sizes of T90 ($D_{\text{mag}} = 10.83$ nm) from our computations are smaller than the physical size measured by TEM ($D_{\text{TEM}} = 12.42$ nm). It is reasonable to assume that the difference may be attributed to the presence of magnetically inactive outer layer that is responsible for suppression of magnetization in our synthesized samples.^{47,50} As it is well known that Fe_3O_4 having inverse spinel structure in bulk possesses mixed spinel structure in nano-phase and the degree of inversion decreases with increase in particle size. Since T90 has larger size than T33, the reduction of magnetization in case of T90 may be ascribed to the reduction of the degree of inversion. Interestingly, it has been observed that D_{TEM} for T33 (8.2 nm) is smaller than D_{mag} (9.86 nm) *i.e.*, magnetic size is overestimated by approximately 10% in comparison to TEM size. Such overestimation was previously observed by few researchers and can be explained on the basis of either perturbation in the Langevin function caused by interparticle interactions that was ignored during fitting⁵¹ or the consideration of single size distribution of the particles. In order to get a better information, the magnetic sizes (D_{mag}) were also calculated by using eqn (7),^{52,53}

$$D_{\text{mag}} = \left(\frac{18kT}{\pi} \frac{\chi}{\rho M_s^2} \right)^{\frac{1}{3}} \quad (7)$$

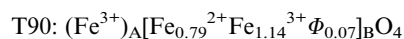
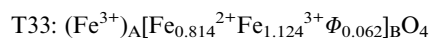
where χ and ρ represent susceptibility $\left(\frac{dM}{dH} \right)_{H \rightarrow 0}$ and density of the material respectively. Eqn (7) gives D_{mag} as 6.6 nm for T33 and remove the discrepancy that emerged from the Langevin curve analysis.

⁵⁷Fe Mössbauer spectra of T33 and T90 samples shown in Fig. 4 consist of two sextets and a single doublet pattern depending on the size and crystallinity of the particles. The outer sextet of smaller area corresponds to Fe^{3+} in tetrahedral (A) sites while the inner sextet with larger area corresponds to Fe^{3+} and Fe^{2+} in octahedral (B) sites. However, the weak doublet peak signifies the presence of some particles lying below the critical size for superparamagnetic relaxation at the measurement time-scale. The average hyperfine magnetic field (HMF) decreased in the magnetic powder specimens from T33 synthesized at 33 °C to T90 prepared at 90 °C (Table 2). This

drop may be attributed to the lower net magnetic moment per unit formula for T90 as determined by the Fe^{3+} ion concentration at octahedral site in comparatively larger particles. The relative area ratio of two Fe^{3+} sextets for both the samples reveals that the concentration of Fe^{3+} ions at the octahedral (B) site is lower than that at the tetrahedral (A) site.

The isomer shift (δ) values corresponding to tetrahedral (δ_A) and octahedral (δ_B) sites of the magnetite specimens (Table 2) illustrate that the s-electron density at the Mössbauer active nuclear site is significantly affected by the rise in precipitation temperature. Nevertheless, the value of the isomer shift of Fe^{3+} in the A site is higher than that generally reported for the micrometric bulk magnetite,¹ indicating a possible charge transfers in the A site also.

Negative quadrupole shift (QS) for both the samples may be attributed to the oblate charge distribution of Fe. The ferric character of the Fe ion is also manifested by the magnitude of the magnetic hyperfine fields and is proportional to the spin of the ferric ion.⁴⁵ The sextet area leading to a $\text{Fe}_{\text{tetra}}^{3+}/\text{Fe}_{\text{octa}}^{3+,2+}$ ratio of T33 and T90 is found to be 0.80 (42.5/52.8) and 0.85 respectively, in contrast to the theoretical ratio 0.50. Such intensity ratios, which exceeds 0.50, are called super stoichiometry in oxygen or cationic vacancies.¹ In contrast to relative intensity ratio 1 : 2 corresponding to Fe between A and B sites in bulk inverse spinel magnetite, $(\text{Fe}^{3+})_A[\text{Fe}^{2+}\text{Fe}^{3+}]_B\text{O}_4$, we observed the global composition of T33 and T90 as,



where Φ represents the cation vacancy at the B-site. The stoichiometry implies that the Fe_3O_4 content in T33 sample was 81.4% and the rest being Fe_2O_3 . T90 contains slightly lower amount of magnetite at 79%. The relatively larger fraction of oxidized Fe^{3+} (maghemite) in T90 may be attributed to the dominating effect of higher precipitation temperature though T33 has a larger fraction of surface atoms. The Φ -value clearly indicates the formation of non-stoichiometric magnetite with some Fe^{2+} deficient lattice sites. If we assume the overall shape of the magnetic nanocrystals are spherical and the oxidized γ - Fe_2O_3 phase exists as shell of uniform thickness over magnetite in a core-shell model, one can easily compute the 18.6% maghemite in a 8.2 nm crystal to ~ 0.27 nm thick shell as shown in Fig. 4. Similarly, 79% magnetite content in 12.4 nm T90 is compatible with 11.6 nm core/0.47 nm shell (Fig. 4B). The thicknesses of maghemite shells obtained from magnetization studies are close match to the same observed from TEM micrography. The formation process of maghemite shell over

Table 1 The detailed analysis from the Langevin fit of the magnetite samples

Sample	Exp M_s (emu g^{-1})	Cal M_s (emu g^{-1})	μ (emu NP^{-1})	R^2	Standard error	D_{mag} (nm)
T33	56.11	57.22	1.48869×10^{-16}	0.9995	± 1.04	9.86
T90	48.44	49.86	1.71487×10^{-16}	0.9998	± 0.54	10.83

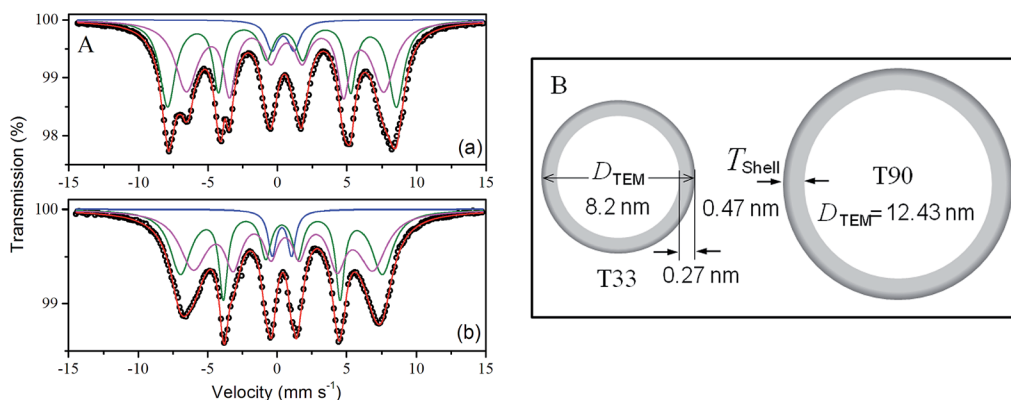


Fig. 4 (A) ^{57}Fe transmission Mössbauer spectra of (a) T33 and (b) T90 recorded at room temperature. Symbols represent the experimental data and the continuous lines correspond to the simulated data and (B) schematic representation of core-shell frameworks in T33 and T90.

magnetite core begins by dissociative oxygenation of Fe^{2+} cations at the surface. This phenomenon generates surface Fe^{3+} cations along with cation vacancies. The Fe^{2+} ions diffuse out from the inner oxide core to the surface to attain the Fe^{3+} state. During this process, the outer oxide layer thickens and a radial compositional gradient is established producing a core-shell structure, with maghemite being more abundant in proximity to the surface of the particles forming shell. In order to observe superparamagnetism, as shown in Fig. 3, the time-scale of the measurement t_m should exceed the superparamagnetic relaxation time (τ), which is usually in the order of 10^{-9} to 10^{-10} s.¹⁰ The critical size D_c of the particles to be superparamagnetic may be calculated empirically from the equation $D_c = (\ln t_m/\tau)^{1/3}$. In the measurement of magnetization, the observation time $t_m \sim 1$ s, and hence the superparamagnetic relaxation can be observed in particles with of size 10^1 to 10^2 nm. In a Mössbauer study the measurement time is much shorter ($t_m \sim 10^{-8}$ s), and therefore manifestation of superparamagnetism is expected in particles of much finer sizes.⁵⁴

The grain sizes obtained from the W-H plots showed almost linear increase with increasing precipitation temperature indicating crystal growth during precipitation (Fig. S2 in ESI†). A steady increase in the lattice strain was observed (in the range $4.0\text{--}7.2 \times 10^{-3}$) with decrease in the particle size (Fig. S2†).⁵⁵ It is interesting to note that the estimated (D_{XRD}) from the W-H

technique for all the nanocrystals are within $D_{\text{TEM}} - 2.5$ nm as the shell of amorphous layer has not contributed to the X-ray diffraction. The deviation is more in the crystals synthesized at higher temperatures. Atoms at the surface and edges are under-coordinated with the presence of broken bonds. As the crystal dimension decreases, the surface area-to-volume ratio increases resulting in a increased broken bond density at the surface causing the remaining bonds to contract spontaneously with an associated increase in bond strength, which in turn produces localized strain.⁵⁶ A decrease in the lattice parameter to 8.3596 Å was observed when the particle size increased from 7.3 to 8.4 nm as a result of possible higher surface oxidation of magnetite crystals to $\gamma\text{-Fe}_2\text{O}_3$. The cell constant decreased slightly further to ~ 8.3544 Å on increasing size to 9.7 nm and remained almost constant thereafter. W-H analysis of X-ray data confirmed that the lattice parameter and crystal lattice strains in magnetite nanoparticles are primarily dependant on the crystal sizes. The preferential orientation of the crystallites along different crystal planes (hkl), texture coefficients, $C(hkl)$ in the Fe_3O_4 nanocrystals (Fig. S3†) shows preferentially grown $\{110\}$ planes to texture coefficient value of 1.323 in T45 because of the growth confinement of (311), (440) and (511) crystal facets and reduced slightly further to 1.288 in T90 (synthesized at 90 °C). Fe_3O_4 with predominant active (220) planes (T45 to T90) is of great potential in catalytic applications. A $C(hkl)$ value of

Table 2 Values of room temperature ^{57}Fe Mössbauer parameters by Lorentzian site analysis using Recoil program

Sample	Site	Isomer shift, δ^a (mm s^{-1})	Quadrupole splitting, ΔE_Q^a (mm s^{-1})	Average hyper fine field, B_{hf}^b (Tesla)	Width ^a (mm s^{-1})	Area fraction ^c (%)
T33	Doublet	0.40	1.60	—	0.45	4.7
	Sextet (A)	0.42	−0.08	51.0	0.55	42.5
	Sextet [B]	0.60	−0.06	44.0	0.65	52.8
T90	Doublet	0.35	1.40	—	0.35	6.2
	Sextet (A)	0.32	−0.02	45.1	0.45	43.1
	Sextet [B]	0.52	−0.08	40.0	0.60	50.7

^a Standard deviation equal to ± 0.03 . ^b Standard deviation equal to ± 0.4 . ^c Standard deviation equal to ± 0.2 .

1 indicates a particle with randomly oriented crystallites, while a larger value indicates an abundance of crystallites oriented to that (hkl) plane.⁵⁷ The high-index planes usually have higher surface energy. The energy for different crystal planes is in the order $\gamma(111) < \gamma(100) < \gamma(110) < \gamma(220)$ for the face-centered-cubic magnetite phase.⁵⁸

The Arrhenius plot for the samples prepared at temperatures in the range 33–90 °C (Fig. S4†) gave the activation energy from the gradient of the linear regression as 6.15 kJ Mol⁻¹ under the condition of homogeneous growth of nanocrystallites. This energy is responsible for initiating the complex process of nucleation and growth by diffusion as well as secondary growth by Ostwald ripening. In the case of ammonia precipitated magnetite crystals, the activation energy is relatively small as the nanocrystals have large surface area and its poor crystallinity. The growth process involves a dissolution–crystallisation mechanism allowing a decrease of the free enthalpy of the system by reduction of the surface area.⁴²

FTIR spectra on selected magnetite specimens conducted in air are shown in Fig. 5. FTIR spectra also confirm the presence of fcc magnetite in the materials as was previously confirmed from the TEM and XRD data (Fig. 1 and 2). The IR absorption bands in the 630–550 cm⁻¹ range is attributed to the vibrations of Fe–O bonds in tetrahedral and octahedral sites⁵⁹ and must have been resulted from the split of the ν_1 band at ~570 cm⁻¹.⁶⁰ The band at ~440 cm⁻¹ in T90 is due to the octahedral Fe only and corresponds to the ν_2 band of Fe–O of bulk magnetite (~370 cm⁻¹) shifted to a higher wavenumber. The intensity reduction of the band at ~590 cm⁻¹ from T90 to T33 is probably due to part of the Fe₃O₄ being reduced to elementary iron.⁶¹ The presence of O–H stretching vibration at ~3411 cm⁻¹ and O–H deformed vibration (bending modes) at 1630 cm⁻¹ are attributed to the presence of coordinated OH groups or water molecules with the unsaturated surface Fe atoms.⁶² C–O stretching vibrations of CO₃²⁻ anion at 1400 cm⁻¹ (ν_3) in both the samples are due to atmospheric CO₂.⁶³ A small absorption band at 2911 cm⁻¹ is due to the ν_s (–CH) vibrations from the residual

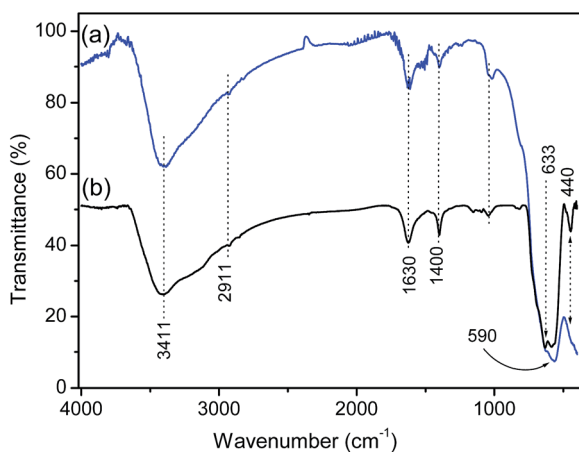


Fig. 5 FTIR spectra of the as-obtained (a) T33, and (b) T90 magnetite nanocrystals.

solvents left after washing and drying steps. Raman spectra presented in Fig. S6† (see ESI) have also indicated the presence of predominantly magnetite with a small amount of maghemite (γ -Fe₂O₃) as impurity in the black magnetic products (T75 and T90).

Fig. 6 shows the thermal analysis patterns (TG/DTA), nitrogen adsorption–desorption isotherms and the corresponding pore size distribution profiles of two representative magnetite specimens. The complete analyses of the isotherms are provided in Table 3. Both T33 and T90 showed hysteresis loops of type IV of Brunauer's classification, indicating the presence of mesopores in the powders.

The plot of dv/dr versus pore size determined by the Barrett–Joyner–Halenda (BJH) method shows that the pores (inset of Fig. 6A) are in the mesoporous range (5–10 nm) and is attributed to the interspaces of the constituent particles. It is obvious that the surface area of magnetite powders decreased with increase in size while increasing the precipitation temperature (Table 3). The particle size (D_{SA}) measured by nitrogen adsorption is somewhat larger than the size estimated from TEM analysis (Fig. 1). This discrepancy can possibly be explained by agglomeration of smaller particles to form larger ones, thereby effectively reducing the collective surface area. The problem of agglomeration in dried NPs was particularly aggravated by the possible magnetic interactions and strong hydrogen bonding among them. The thermogram of magnetite (T90) shows a total weight loss of ~3.8% in two stages on heating the powder sample to 1000 °C. The first drop in the TG pattern at ~100 °C is attributed to the physisorbed water remotion. The rate of loss increased till ~500 °C and it could be attributed to the removal of multi-layers of water of hydration from the surface of the nanoparticles as well as dehydration of iron oxyhydroxide (FeOOH) formed by ambient moisture. A small weight gain of ~0.4%, observed in the temperature range 685–860 °C is due to oxidation of magnetite to γ -Fe₂O₃, though the experiment was conducted with continuous nitrogen purge. It is obvious that the thermal behavior of synthetic magnetite depends on the formation temperature, which affects the particle size. The finer magnetite crystals (*e.g.*, 10–20 nm) rapidly undergo transition to maghemite at ~150 °C; whereas the larger magnetite particles are more thermally stable and do not start the transition to maghemite until about 315 °C.²

The mean hydrodynamic diameter (Z -average) is based on the intensity of scattered photons from the colloidal particles in suspension. The Z -average size measured by dynamic light scattering of T60, is 36.2 nm with a polydispersity index (PDI) of 0.417 (Fig. S5†) though the D_{TEM} for T60 is only 10.84 nm. The PCS size is approximately 3 times larger than the physical size measured by TEM could be due to presence of one-shell hexagonal close-pack clusters of a total of maximum 13 particles with average hydrodynamic diameter of $\sim 3 \times D_{TEM}$ which is 32.5 nm, close to 36.2 nm. The zeta potential is the electrical potential measured at the shear plane, and represents the portion of the charge that can exert electrostatic attraction and repulsion forces on other particles. The T60 sample exhibit ζ values in the range +44.1 to –43.9 mV for the NP dispersion in the pH range 2.8 to 12. The resulting aqueous dispersions were

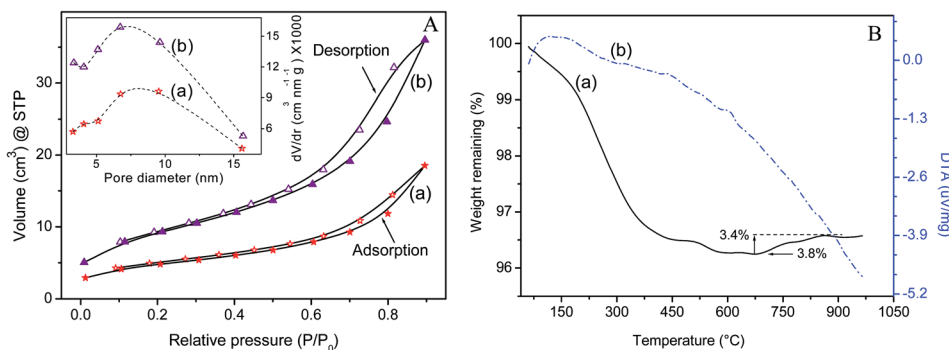
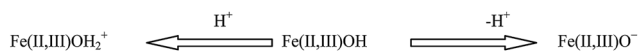


Fig. 6 (A) Volume N₂ adsorbed versus relative pressure of Fe₃O₄ nanocrystals at 77 K for the powder samples (a) T90 and (b) T33. Inset shows the plot of pore size distribution derived from the BJH analysis. (B) Thermal analysis curves (a) TG and (b) differential thermal analysis representing the effects of thermal treatment on T90 in pure nitrogen atmosphere.

Table 3 Surface area, total pore volume, pore diameter and size of as synthesized magnetite in different conditions

Sample	BJH pore distribution desorption					
	Surface area (m ² g ⁻¹)	Pore volume (cm ³ g ⁻¹)	Pore diameter (nm)	Total pore volume (cm ³ g ⁻¹)	BET surface area (m ² g ⁻¹)	Size, D _{SA} (nm)
T90	51.252	0.106	9.531	0.1197	67.974	17.04
T75	75.917	0.145	6.782	0.1586	90.52	12.79
T60	89.601	0.174	5.141	0.1889	105.245	11.005
T45	85.438	0.165	6.720	0.1836	108.474	10.68
T33	106.230	0.195	6.729	0.2113	123.616	9.37

stable in basic conditions, with the point of zero charge (pH_{PZC}) at pH ~6.45 which is close to already reported data.⁶⁴ The corresponding surface reactions may be expressed as



The resulting aqueous dispersions were stable in basic conditions. In acidic pH, the dominating surface species is tentatively Fe(II,III)OH₂⁺, implying positive zeta potentials. With increasing pH, the ζ decreases and Fe(II,III)OH becomes dominating species around pH_{PZC}. At alkaline pH, the surface species Fe(II,III)O⁻ is mainly responsible for the negative ζ.⁶⁵

Conclusions

Monodisperse magnetite nanoparticles with size in the range 6–13 nm were successfully synthesised by ammonia precipitation technique in the temperature range 33–90 °C. The X-ray diffraction and the Rietveld refinement confirm the inverse spinel structure of cubic phase of magnetite as dominating phase. The activation energy for the growth of nanocrystallites during relatively higher temperature of precipitation was estimated to be ~6.15 kJ mol⁻¹ which is responsible for initiating the complex process of nucleation and growth by diffusion. W-H technique indicated crystal dimensions within D_{TEM}-2.5 nm as the shell of amorphous layer has not contributed to the X-ray diffraction. The lattice strains calculated were relatively high and in the range 5.5–

8.9 × 10⁻³ with very small variations for samples T33 to T90. The magnetic sizes (D_{mag}) derived from the Langevin computations were smaller than the physical sizes from TEM analysis due to the supposedly presence of a magnetically “dead” layer of atoms over maghemite shell at the surface. Hence, precipitation method produced monodispersed magnetite nanocrystals with magnetite-maghemite core-shell structures suitable for biological applications.

Acknowledgements

The authors are grateful to the Director, Central Glass and Ceramic Research Institute, Kolkata for permission and extending facilities to carry out the above work. SJI and MJ acknowledge CSIR and UGC for their fellowships. Staff members of HR-TEM, XRD, and Central Instrumentation Facility are also acknowledged for their assistance in obtaining data. This work was supported by the 12 FYP CSIR Network project ESC-0103 and CSC-0135.

Notes and references

- 1 T. J. Daou, G. Pourroy, S. Begin-Colin, J. M. Greneche, C. Ulhaq-Bouillet, P. Legare, P. Bernhardt, C. Leuvrey and G. Rogez, *Chem. Mater.*, 2006, **18**, 4399.
- 2 H. T. Jeng and G. Y. Guo, *Phys. Rev. B: Condens. Matter Mater. Phys.*, 2002, **65**, 094429.

- 3 H. M. Yang, C. W. Park, M. A. Woo, M. I. Kim, Y. M. Jo, H. G. Park and J. D. Kim, *Biomacromolecules*, 2010, **11**, 2866.
- 4 Y. Piao, J. Kim, H. Bin Na, D. Kim, J. S. Baek, M. K. Ko, J. H. Lee, M. Shokouhimehr and T. Hyeon, *Nat. Mater.*, 2008, **7**, 242.
- 5 D. K. Kim, M. Mikhaylova, F. H. Wang, J. Kehr, B. Bjelke, Y. Zhang, T. Tsakalakos and M. Muhammed, *Chem. Mater.*, 2003, **15**, 4343.
- 6 M. O. Aviles, J. O. Mangual, A. D. Ebner and J. A. Ritter, *Int. J. Pharm.*, 2008, **361**, 202.
- 7 M. Chorny, I. Fishbein, B. B. Yellen, I. S. Alferiev, M. Bakay, S. Ganta, R. Adamo, M. Amiji, G. Friedman and R. J. Levy, *Proc. Natl. Acad. Sci. U. S. A.*, 2010, **107**, 8346.
- 8 S. H. Lee, Z. Y. Lu, S. V. Babu and E. Matijevic, *J. Mater. Res.*, 2002, **17**, 2744.
- 9 M. Uchida, M. L. Flenniken, M. Allen, D. A. Willits, B. E. Crowley, S. Brumfield, A. F. Willis, L. Jackiw, M. Jutila, M. J. Young and T. Douglas, *J. Am. Chem. Soc.*, 2006, **128**, 16626.
- 10 K. L. Lai, W. Jiang, J. Z. Tang, Y. Wu, B. He, G. Wang and Z. W. Gu, *RSC Adv.*, 2012, **2**, 13007.
- 11 K. Shimizu, A. Ito, J. K. Lee, T. Yoshida, K. Miwa, H. Ishiguro, Y. Numaguchi, T. Murohara, I. Kodama and H. Honda, *Biotechnol. Bioeng.*, 2007, **96**, 803.
- 12 L. M. Rossi, A. D. Quach and Z. Rosenzweig, *Anal. Bioanal. Chem.*, 2004, **380**, 606.
- 13 M. Shinkai, *J. Biosci. Bioeng.*, 2002, **94**, 606.
- 14 C. A. F. Vaz, J. Hoffman, A. B. Posadas and C. H. Ahn, *Appl. Phys. Lett.*, 2009, **94**, 022504.
- 15 H. F. Tian, T. L. Qu, L. B. Luo, J. J. Yang, S. M. Guo, H. Y. Zhang, Y. G. Zhao and J. Q. Li, *Appl. Phys. Lett.*, 2008, **92**, 063507.
- 16 D. Patel, A. Kell, B. Simard, J. X. Deng, B. Xiang, H. Y. Lin, M. Gruwel and G. H. Tian, *Biomaterials*, 2010, **31**, 2866.
- 17 S. Ghosh, D. Carty, S. P. Clarke, S. A. Corr, R. Tekoriute, Y. K. Gun'ko and D. F. Brougham, *Phys. Chem. Chem. Phys.*, 2010, **12**, 14009.
- 18 S. Ghosh, D. Divya, K. C. Remani and T. S. Sreeremya, *J. Nanopart. Res.*, 2010, **12**, 1905.
- 19 U. Colombo, F. Gazzarrini and G. Lanzavecchia, *Mater. Sci. Eng.*, 1967, **2**, 125.
- 20 J. Tang, M. Myers, K. A. Bosnick and L. E. Brus, *J. Phys. Chem. B*, 2003, **107**, 7501.
- 21 R. Frison, G. Cernuto, A. Cervellino, O. Zaharko, G. M. Colonna, A. Guagliardi and N. Masciocchi, *Chem. Mater.*, 2013, **25**, 4820.
- 22 S. C. Tjong and H. Chen, *Mater. Sci. Eng., R*, 2004, **45**, 1.
- 23 G. A. Dorofeev, A. N. Streletskii, I. V. Povstugar, A. V. Protasov and E. P. Elsukov, *Colloid J.*, 2012, **74**, 675.
- 24 N. J. Tang, W. Zhong, H. Y. Jiang, X. L. Wu, W. Liu and Y. W. Du, *J. Magn. Magn. Mater.*, 2004, **282**, 92.
- 25 H. Wei, N. Insin, J. Lee, H. S. Han, J. M. Cordero, W. H. Liu and M. G. Bawendi, *Nano Lett.*, 2012, **12**, 22.
- 26 Y. F. Wang, Z. W. Zhu, F. Xu and X. L. Wei, *J. Nanopart. Res.*, 2012, **14**, 755.
- 27 J. Lee, Y. Lee, J. K. Youn, H. Bin Na, T. Yu, H. Kim, S. M. Lee, Y. M. Koo, J. H. Kwak, H. G. Park, H. N. Chang, M. Hwang, J. G. Park, J. Kim and T. Hyeon, *Small*, 2008, **4**, 143.
- 28 J. Wan, W. Cai, X. Meng and E. Liu, *Chem. Commun.*, 2007, 5004.
- 29 J. Pinkas, V. Reichlova, R. Zboril, Z. Moravec, P. Bezducka and J. Matejkova, *Ultrason. Sonochem.*, 2008, **15**, 257.
- 30 S. Z. Wang, H. W. Xin and Y. T. Qian, *Mater. Lett.*, 1997, **33**, 113.
- 31 D. Vollath, D. V. Szabo, R. D. Taylor and J. O. Willis, *J. Mater. Res.*, 1997, **12**, 2175.
- 32 O. Masala and R. Seshadri, *Annu. Rev. Mater. Res.*, 2004, **34**, 41.
- 33 L. Signorini, L. Pasquini, L. Savini, R. Carboni, F. Boscherini, E. Bonetti, A. Giglia, M. Pedio, N. Mahne and S. Nannarone, *Phys. Rev. B: Condens. Matter Mater. Phys.*, 2003, **68**, 8.
- 34 L. F. Shen, P. E. Laibinis and T. A. Hatton, *Langmuir*, 1999, **15**, 447.
- 35 I. Nedkov, T. Merodiiska, L. Slavov, R. E. Vandenberghe, Y. Kusano and J. Takada, *J. Magn. Magn. Mater.*, 2006, **300**, 358.
- 36 B. L. Cushing, V. L. Kolesnichenko and C. J. O'Connor, *Chem. Rev.*, 2004, **104**, 3893.
- 37 H. M. Rietveld, *Acta Crystallogr.*, 1966, **20**, 508.
- 38 L. Lutterotti and P. Scardi, *J. Appl. Crystallogr.*, 1990, **23**, 246.
- 39 A. Krishnan, T. S. Sreeremya, E. Murray and S. Ghosh, *J. Colloid Interface Sci.*, 2013, **389**, 16.
- 40 C. P. Bean, *J. Appl. Phys.*, 1955, **26**, 1381.
- 41 C. P. Bean and I. S. Jacobs, *J. Appl. Phys.*, 1956, **27**, 1448.
- 42 C. P. Bean and J. D. Livingston, *J. Appl. Phys.*, 1959, **30**, S120.
- 43 V. Yathindranath, L. Rebbouh, D. F. Moore, D. W. Miller, J. van Lierop and T. Hegmann, *Adv. Funct. Mater.*, 2011, **21**, 1457.
- 44 Z. C. Xu, C. M. Shen, Y. A. Tian, X. Z. Shi and H. J. Gao, *Nanoscale*, 2010, **2**, 1027.
- 45 Y. Tian, B. B. Yu, X. Li and K. Li, *J. Mater. Chem.*, 2011, **21**, 2476.
- 46 M. Respaud, *J. Appl. Phys.*, 1999, **86**, 556.
- 47 C. Liu and Z. J. Zhang, *Chem. Mater.*, 2001, **13**, 2092.
- 48 H. Shi, L. Tan, Q. Du, X. Chen, L. Li, T. Liu, C. Fu, H. Liu and X. Meng, *Dalton Trans.*, 2014, **43**, 12474.
- 49 S. W. Cao, Y. J. Zhu and J. Chang, *New J. Chem.*, 2008, **32**, 1526.
- 50 R. H. Kodama, *J. Magn. Magn. Mater.*, 1999, **200**, 359.
- 51 C. Pascal, J. L. Pascal, F. Favier, M. L. E. Moubtassim and C. Payen, *Chem. Mater.*, 1999, **11**, 141.
- 52 B. Y. Yu and S.-Y. Kwak, *Dalton Trans.*, 2011, **40**, 9989.
- 53 T. Ozkaya, M. S. Toprak, A. Baykal, H. Kavas, Y. Koseoglu and B. Aktas, *J. Alloys Compd.*, 2009, **472**, 18.
- 54 N. V. Lukashova, A. G. Savchenko, Y. D. Yagodkin, A. G. Muradova and E. V. Yurtov, *Met. Sci. Heat Treat.*, 2013, **54**, 550.
- 55 T. Narayanan, D. Sakthi Kumar, Y. Yoshida and M. Anantharaman, *Bull. Mater. Sci.*, 2008, **31**, 759.
- 56 C. Q. Sun, *Nanoscale*, 2010, **2**, 1930.
- 57 T. S. Sreeremya, K. M. Thulasi, A. Krishnan and S. Ghosh, *Ind. Eng. Chem. Res.*, 2012, **51**, 318.

- 58 C. Yang, J. J. Wu and Y. L. Hou, *Chem. Commun.*, 2011, **47**, 5130.
- 59 A. L. Andrade, D. M. Souza, M. C. Pereira, J. D. Fabris and R. Z. Domingues, *Ceramica*, 2009, **55**, 420.
- 60 G. Marinescu, L. Patron, D. C. Culita, C. Neagoe, C. I. Lepadatu, I. Balint, L. Bessais and C. B. Cizmas, *J. Nanopart. Res.*, 2006, **8**, 1045.
- 61 Y. C. Dong, M. J. Hu, R. G. Ma, H. Cheng, S. L. Yang, Y. Y. Li and J. A. Zapien, *CrystEngComm*, 2013, **15**, 1324.
- 62 A. Ebrahimezhad, Y. Ghasemi, S. Rasoul-Amini, J. Barar and S. Davaran, *Bull. Korean Chem. Soc.*, 2012, **33**, 3957.
- 63 C. P. Chen, P. Gunawan and R. Xu, *J. Mater. Chem.*, 2011, **21**, 1218.
- 64 J. J. Carlson and S. K. Kawatra, *Miner. Process. Extr. Metall. Rev.*, 2013, **34**, 269.
- 65 Z. X. Sun, F. W. Su, W. Forsling and P. O. Samskog, *J. Colloid Interface Sci.*, 1998, **197**, 151.

CrossMark
click for updatesCite this: *RSC Adv.*, 2016, 6, 14393

Colloidal properties of water dispersible magnetite nanoparticles by photon correlation spectroscopy†

Srividhya J. Iyengar,^a Mathew Joy,^a Titir Maity,^b Jnananjan Chakraborty,^c
Ravinder K. Kotnala^d and Swapankumar Ghosh^{*a}

We report the development of ultra-stable aqueous colloidal dispersion of magnetite nanocrystals produced by aqueous 'coprecipitation method'. Magnetic nanofluids were prepared by dispersing the Fe₃O₄ NPs in water medium in the presence of tetramethylammonium hydroxide (TMAH). The synthesized nanocrystals were characterized by XRD, TG-DTA, XPS and TEM for evaluating the phase, crystal structure and morphology. FTIR spectroscopy was used to shed light onto the nature of the interactions between TMAH and Fe₃O₄ NPs. The TMAH peptized nanofluids was clear translucent colloidal dispersion found to contain spheroidal nanoparticles of average size 13 nm with very narrow size distribution similar to TEM size. High-resolution microscopy indicated that all the NPs are indeed single crystals with truncated octahedral shape. Lattice fringes belonging to predominant (111), (220) and (311) planes could be identified. The M_s values estimated are 64.68 and 57.92 emu g⁻¹ at room temperature for NPs before and after peptization respectively and they are superparamagnetic. The key colloidal properties such as charge, hydrodynamic size, photon counts, dispersion stability and surface chemistry have been analyzed and compared with a dispersion of aqueous precipitated magnetite. The TMA suspensions are stable over a year without any loss due to precipitation. Photon scattering experiments have indicated the presence of very small NP clusters of 28 nm in aqueous suspensions. The lower extent of agglomeration in TMA promotes the one-shell clusters of primary nanoparticles, a fact which can forecast the stability of the ferrofluid. The change in surface charge of the magnetic fluid from -44 to +49 mV while varying the pH indicated the PZC at pH 5.98. The dynamic processes were investigated during the photon scattering experiment against time, temperature and concentration. The stability of the ferrofluid against time, temperature and concentration indicates the great potentials in biotechnology, selective catalysis and other industrial applications.

Received 11th December 2015
Accepted 25th January 2016

DOI: 10.1039/c5ra26488j

www.rsc.org/advances

Introduction

Magnetite (Fe₃O₄) nanoparticles (MNPs) in the form of powder or slurry have been attracting increasing interest worldwide for their size and shape-dependent novel magnetic, optical, and other unique properties.¹ Another interesting property that arises from finite size and surface effects is the existence of superparamagnetism at room temperatures, magnetizing strongly under an applied field, but retaining no permanent

magnetism once the field is removed.² Fe₃O₄ is the only FDA approved magnetic materials for use in humans since iron oxide NPs are generally well-tolerated *in vivo*.³ Magnetite suspensions are increasingly used in medical applications, such as tissue engineering scaffolds,⁴ targeting delivery and imaging (MRI).⁵ In the future, patients are more likely to be exposed to pharmaceutical products containing such particles.⁶ The main constituent of magnetite particles is ferrous-ferric oxide (FeO and Fe₂O₃) responsible for high saturation magnetization value. Magnetite as well as other nanoparticles (NPs) is usually stabilized using fatty acids or polymeric dispersants.^{7,8} Ferrofluids are smart colloidal dispersions of small single-domain magnetic particles suspended in a continuous base fluid whose rheological behaviour can be controlled by means of a magnetic field.⁹ The dispersions should satisfy the conditions of narrow size distribution and high stability without aggregation. Stable dispersions of MNPs have been prepared using various dispersion media such as water, hydrocarbons, diesters, alcohols, ketones, and amines.¹⁰ Due to their interesting stimulus-responsive properties, ferrofluids have been employed in

^aTechnical Coordination Cell, CSIR-Central Glass & Ceramics Research Institute, Kolkata-700032, India. E-mail: swapankumar.ghosh2@mail.dcu.ie; srividhyaji@gmail.com; Fax: +91 33 24730957; Tel: +91 33 23223546

^bAdvanced Material & Characterization Unit, CSIR-Central Glass & Ceramics Research Institute, Kolkata-700032, India

^cBioceramics & Coating Division, CSIR-Central Glass & Ceramics Research Institute, Kolkata-700032, India

^dMaterials Physics and Engineering, CSIR-National Physical Laboratory, New Delhi-110 012, India

† Electronic supplementary information (ESI) available. See DOI: 10.1039/c5ra26488j

various applications, such as magneto-optical wavelength filters,¹¹ high-density information storage,¹² to control fluids in space,¹³ nonlinear optical materials,¹⁴ optical grating,¹⁵ and defect sensors.¹⁶ Recently, exploration of novel uses of magnetic particles in the separations area has increased significantly.¹⁷ Among various dispersions, aqueous ferrofluids have been used in biomedical as well as industrial applications. For such applications as either MNPs or their clusters (MNPCs), the constituent particles must be highly magnetic, biocompatible and fully dispersible in biological media without aggregation with minimal surface passivation.¹⁸ Brownian motion of the NPs which improves with reduced particle size fortifies the stability of a magnetic fluid forming the colloidal system avoiding agglomeration and precipitation. To control the colloidal stability of ferrofluids, the steric or electrostatic (due to the electric double layer) repulsive forces must be more than the van der Waals, and magnetic dipolar attractive interactions.⁹ The classical approach applied in Derjaguin–Landau–Verwey–Overbeek (DLVO) theory is a way to forecast the net interaction energy implicating van der Waals, steric, and electrostatic forces in dilute dispersions.¹⁹ However, the magnetic properties will be nonexistent in particles less than 2 nm.¹³ Nevertheless, in the case of larger particles, agglomeration is a problem, as magnetic interactions are predominant. MNPs of diameter ~10 nm will have enough thermal energy which prevents sedimentation in a gravitational field.³

However, it is more difficult to maintain the stability of MNPC dispersions because thermal energy does not prevent coagulation produced by the van der Waals forces that induce strong short-range isotropic interactions,³ and the inter-particle magnetic dipolar attraction from single domain magnetic NPs.²⁰ Besides aggregations, MNPs are vulnerable to air oxidation.² The presence of aggregates and their sizes may affect a number of properties, such as the MRI signal of iron oxide NPs.²¹ In order to prevent air oxidation and aggregation, the critical requirement is therefore to surface-engineer the NPs with biocompatible surfactants, polymers, and inorganic materials that provide repulsive forces large enough to counter the attractive ones in the collision processes.^{10,22} Nevertheless, the production, stocking, and delivery costs of MNP powders are high because of environment issues. Therefore, the development of magnetite powder dispersion having superior stability as well as good biocompatibility is desirable.

It is a common observation that monodispersed NPs as evidenced by electron microscopy techniques often show polydispersity in aqueous suspensions due to clustering. The least hydrodynamic sizes reported so far are 4–8 times the TEM sizes for magnetite NPs, surface functionalized with PEG,^{3,23} citrate,²³ dehydroascorbic acid (vitamin-C),²⁴ diethylene glycol and *N*-methyl-diethanolamine,²⁵ and PEG-1000 and PVP K-30.²⁶ Majority of these reports used photon scattering technique just to derive size data for comparison as a part of routine characterization. Brougham *et al.* have carried out detailed investigation on the growth of magnetite NP clusters by competitive desorption of surfactant in apolar solvents.^{27,28} Commercial ferrofluids *e.g.*, Nanomags®-D-spio, FluidMAG-DX are also reported to form aggregates of variable size averaging at ~100 nm

though the crystallite size is 8.4 nm and are classified under “cluster type” and “multi domain cores” as a result of equilibrating magnetic, gravitational and electrostatic forces.²⁹ The uniformity of MNP aggregates in aqueous suspensions helps tune the heating efficiency in hyperthermia applications. In MRI, the dispersions in the relaxivity profile are modulated by the presence of MNP clusters of different sizes, thus making the efficacy of MNP based contrast agents magnetic field dependent. However, to the best of our knowledge there is no detailed study on the colloidal stability of aqueous suspensions of magnetite NPs and the effect of its concentration temperature and ageing time on clustering which is extremely important for predicting its application.

In this article, we report the preparation of an ultrastable aqueous colloidal suspension of magnetite, peptized by TMAH. The magnetite powders have also characterized for its crystallinity, phase, surface area, chemical composition, thermal analysis and magnetic properties. The key colloidal properties such as charge, hydrodynamic size, photon counts, dispersion stability and surface chemistry have been analyzed and compared with a dispersion of aqueous precipitated magnetite. The stability and the coagulation kinetics of the ferrofluids have been studied against the slurry concentration, temperature as well as time by photon correlation spectroscopy (PCS). We demonstrated, for the first time, the simple way one can control the uniformity of magnetic one-shell clusters in aqueous solution. The zeta (ζ) potential of magnetite ferrofluids was examined as a function of pH. The enhanced stability of peptized magnetite suspension has been correlated to the zeta potential and other colloidal properties, this places understanding of the colloidal behavior on a strong physical basis and shows pathways for achieving such ultrastable stability even in aqueous suspensions.

Experimental

Materials

Fe(II) chloride (98%) and Fe(III) chloride (97%), and 25% tetramethylammonium hydroxide aqueous solution were supplied by Sigma Aldrich Chemicals. Methanol (GR), sodium chloride and 25% ammonia were procured from Merck, India. All chemicals in this study were used without further purification. All the syntheses, washings and dilutions were carried out with Millipore water with resistivity 18.2 M Ω cm@25 °C. Ultrapure nitrogen gas (99.999%) was used for purging of water to remove dissolved oxygen.

Preparation

To fabricate magnetite nanocrystals for a batch of ~1 g, 4.5 mmol portion of FeCl₂·4H₂O and 9 mmol FeCl₃·6H₂O (such that Fe³⁺/Fe²⁺ = 2) were dissolved in 300 ml physiological saline which was previously deaerated by purging nitrogen gas for 30 min in a 500 ml three-neck round bottom flask. The above reaction mixture was heated to 80 °C over a hot plate magnetic stirrer while continuous stirring. The clear off-yellow colored solution turned into turbid muddy orange after ~30 min

indicating the hydrolysis of ferrous and ferric chlorides to corresponding hydroxides. The reactor was cooled naturally to 45 °C and was kept constant. About 7 ml NH₃ solution was added to the reactor while vigorous stirring. The off-yellow colored suspension immediately turned black indicating the formation of magnetite crystals. The temperature of the reactor was kept constant at 45 °C with stirring for further ~30 min to allow crystal growth. At this point the net Fe²⁺ concentration was 100 mM. The resultant pH of the reaction mixture was ~11. The suspension was then cooled naturally to ambient temperature. The settled black solid was collected by magnetic decantation and washed repeatedly with water until free from impurities. The wet precipitate was dried at 60 °C in a vacuum oven and preserved in a desiccator for further characterization. The above ammonia precipitated magnetite sample was labeled as 'AM'. The above procedure was repeated to produce 1 g wet AM for the subsequent functionalization steps.

Peptizing with TMAH to get homogeneous suspensions

About 4 ml of commercial 25% TMAH solution was added to the wet AM and peptized homogeneously. The magnetite specimen functionalized with TMAH was labeled as TMA. The TMA powder was re-dispersed in deaerated water and the resultant product was a stable nanofluid without any precipitation over a year. A TMA fluid of ~20% solid content was placed in a vial, and was subsequently subjected to a static magnetic field of several hundred Gauss. The particles remained dispersed in the fluid even in the presence of the external field indicating the formation of a stable colloidal dispersion.

Instrumental

The average size, morphology and the crystal structure of magnetite NPs were ascertained by the high resolution transmission electron microscopy (HR-TEM) using a FEI Tecnai 30 G² S-Twin HR-TEM operated at 300 kV equipped with a Gatan CCD camera. The mean size and its distribution was calculated using probability density equation based on a log-normal function. The chemical composition was determined on several crystal grains by means of energy dispersive spectrometry (EDS) by using an EDAX spectrometer equipped with high-angle annular dark-field detector with beam scanning capability (Fischione Instruments, Inc., USA) with TIA analysis software. The powder XRD patterns were recorded with Bruker D8 Advanced diffractometer equipped with source Cu K α ₁ radiation ($\lambda = 1.5406 \text{ \AA}$) 2θ range of 10–80° with a step size of 0.05° 2θ and a scan speed of 4° min⁻¹. The X-ray diffractograms exhibit classical line broadening associated with a fine crystal system. Debye–Scherrer expression (eqn (1)) was used on the (311) X-ray peak to deduce the crystallite size.

$$D_{\text{XRD}} = \frac{0.9\lambda}{\beta_{2\theta}\cos\theta} \quad (1)$$

Magnetic measurements of powder specimens were made using vibrating sample magnetometer (VSM), Lakeshore 7305, US at 300 K to determine the specific saturation magnetization.

Crystal dimensions can also be estimated from the magnetization curves based on the theory of superparamagnetism as proposed by Bean and co-workers.^{30–32} To fit the magnetization curves, we assume that individual grains are single crystals without mutual interaction and each particle has an inner single-domain core with the spontaneous magnetization. The magnetization of N number of ideal non-interaction superparamagnetic nanoparticles, each with identical magnetic moment μ , at constant temperature T in magnetic field H is given by Langevin function eqn (2),

$$M(H) = N\mu \left\{ \left(\frac{e^{\frac{2\left(\frac{\mu H}{k_B T}\right)}{+1}}}{e^{\frac{2\left(\frac{\mu H}{k_B T}\right)}{-1}}} \right) - \frac{k_B T}{\mu H} \right\} \quad (2)$$

where k_B and $N\mu$ are the Boltzmann constant and saturation magnetization (M_s) of the magnetite specimen.

The magnetization curves was fitted using a nonlinear-least squares routine to obtain two parameters: the log-mean single particle moment, μ , and the saturation magnetization, M_s . The “magnetic size”, D_{Mag} obtained is significantly smaller than the physical size obtained from TEM measurements. X-ray photoelectron spectroscopy (XPS) measurement of TMA coated magnetite nanocrystals was carried out on an XPS system (PHI 5000 Versa Probe II, ULVAC-PHI, INC., USA) using a monochromatic Al K α X-ray source (1486.6 eV). The XPS data was deconvoluted with XPSPEAK 4.1 software which produced stable and almost superimposable baselines, confirming the stability of the fits and helping to validate the interpretation.

The colloidal stability and the mean hydrodynamic size of the dispersed MNPCs were measured at 25 °C by PCS. The surface charge was estimated by measuring the zeta potential of their dispersion in water using a laser-Doppler velocimetry technique. The instrument uses a 4 mW He–Ne laser wavelength of 632.6 nm and a scattering angle of 273° using a Zetasizer Nano-ZS (Malvern Instruments, Malvern, UK). The TMA ferrofluid of different concentrations were exposed to the temperatures in the range 25–65 °C and the hydrodynamic sizes of TMA suspension were recorded at the interval of 10 °C. The results were obtained with theoretical refractive index of magnetite 2.42.³³ The correlograms resulted hydrodynamic size as intensity distribution by cumulants analysis method. This analysis also yields the polydispersity index (PDI) values, below 0.3 of which are indicative of unimodal size distribution with smaller values demonstrating increasing monodispersity. The zeta potential of the MNPCs was calculated from the mobility measurements, using the Smoluchowski formula. The pH of the dispersion was adjusted either with aqueous 10⁻³ M NaOH or H₂SO₄. The pH of well dispersed magnetite fluids was checked just before the zeta potential measurements.

FTIR spectra on magnetite samples were taken at room temperature on a Perkin-Elmer Spectrum 100 spectrophotometer in the 400–4000 cm⁻¹ range with average of 50 scans. The powders specimens were pressed into small discs using spectroscopically pure KBr (Sigma-Aldrich, ≥99%) matrix with sample to KBr ratio ~1 : 100 to evaluate the structural aspects

of magnetite. The thermogravimetric (TG) data was used to investigate the thermal decomposition and associated structural changes in the synthesized nanocrystals using a Simultaneous Thermal Analyzer (STA-6000, Perkin-Elmer, US) under ultrapure nitrogen purge. The thermograms were collected using a heating ramp of $10\text{ }^{\circ}\text{C min}^{-1}$ in the $30\text{--}1000\text{ }^{\circ}\text{C}$ temperature range. The specific surface area and pore size distribution of the magnetite powders were calculated from the N_2 adsorption data following the Brunauer–Emmett–Teller (BET) technique at 77 K using a surface area analyzer (TriStar II 3020 Version 3.02). Surface area (SA) analyses were conducted on powder samples after degassing them at $200\text{ }^{\circ}\text{C}$ for 3 h . Particle size (D_{BET}) was also calculated from the BET surface area (S_{SA}) using eqn with an assumption that all the particles are spherical and unclustered using $\rho = 5.18\text{ g cm}^{-3}$ for magnetite.²

Results and discussion

The synthesized iron oxide powders were typically black in color and were strongly attracted by the NdFeB bar magnet indicating the possible formation of magnetite crystals as the dominant phase in the reaction product. The TMA suspension kept their colloidal characteristics over a year with no visible sedimentation. Contrarily, the AM based ferrofluid sedimented completely after $\sim 1\text{ h}$, evidencing the larger and/or aggregated nature of AM particles. Fig. 1 shows the video frames of a thick slurry of TMA in presence of a strong bar magnet. The black slurry on ~ 50 times dilution turned in to a translucent wine-red solution (panel B).

Selected bright-field TEM images of low and higher magnifications of few representative of the magnetite crystals precipitated in physiological saline before and after surface functionalization with TMAH are shown in Fig. 2 (for more TEM images please see Fig. S1 in the ESI†).

The size distribution is calculated from the careful inspection on micrographs containing few hundreds of NPs. D_{TEM} is consistent with the average crystallites size (D_{XRD}) calculated by the Debye–Scherrer equation. The large individual as aggregated grains with sizes in the range $8\text{--}15\text{ nm}$ with an average of $11.6 \pm 1.9\text{ nm}$ was observed in AM. The TMA ferrofluid has more uniformly distributed sized NPs in the $8.5\text{ to }11\text{ nm}$ range with average $10.3 \pm 0.8\text{ nm}$ of narrow size distribution. This was actually expected, as TMAH acts as a surface-active agent favoring the dispersion of NPs. The mean size of the particles/aggregates is larger in the case of AM sample. Apparently the

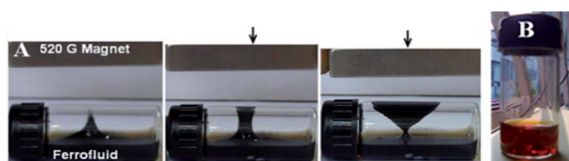


Fig. 1 (A) Frames from a video of a $\sim 20\text{ wt\%}$ TMA-based ferrofluid in a 15 ml glass vial being manipulated with a $\sim 500\text{ G}$ strength bar magnet, and (B) dilute suspension of TMA in water.

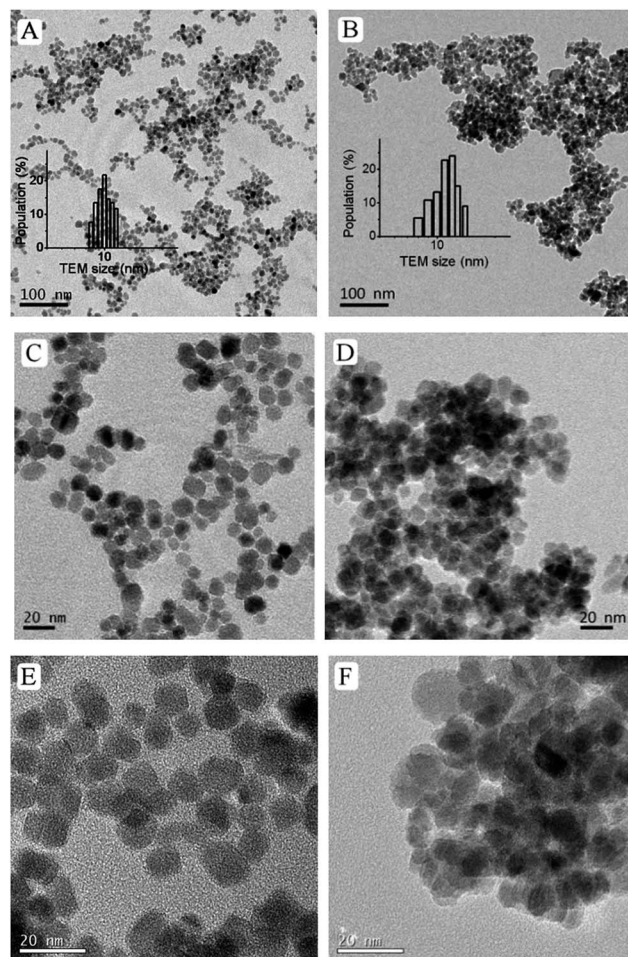


Fig. 2 TEM images of AM (B, D and F) and peptized TMA (A, C and E) suspensions at low and higher magnifications. Inset in A and B are the histogram representing size distribution.

particles have less interaction among them in TMA than that in AM at room temperature, which will be further investigated by the magnetization and light scattering measurements in later sections (Fig. 4 and 7).

Representative HR-TEM images of selected magnetite specimens with different projections and its electron diffractions are provided in Fig. 3. Careful examination of the HR images indicates that all the NPs are indeed single crystals and fringes belonging to predominant (111), (220) and (311) planes with corresponding d -spacings 0.48 , 0.29 and 0.25 nm could be identified. Fourier filtering was used to extract the lattice fringe information. Selected area electron diffraction (SAED) patterns of bare and coated magnetite given in Fig. 3D show clear Debye–Scherrer rings for (220), (311), (400), (422), (511) and (440) planes with corresponding interplanar spacings 0.2967 , 0.2532 , 0.2099 , 0.1715 , 0.1616 and 0.1485 nm respectively matching the XRD pattern of cubic inverse spinel magnetite (JCPDS card no. 19-0629). In addition, the bright diffraction spot in the rings indicate that the NPs are well crystallized. The EDS spectra of AM and TMA specimens taken during TEM analyses (Fig. S2 in ESI†) show the presence of Fe and O in the samples which also

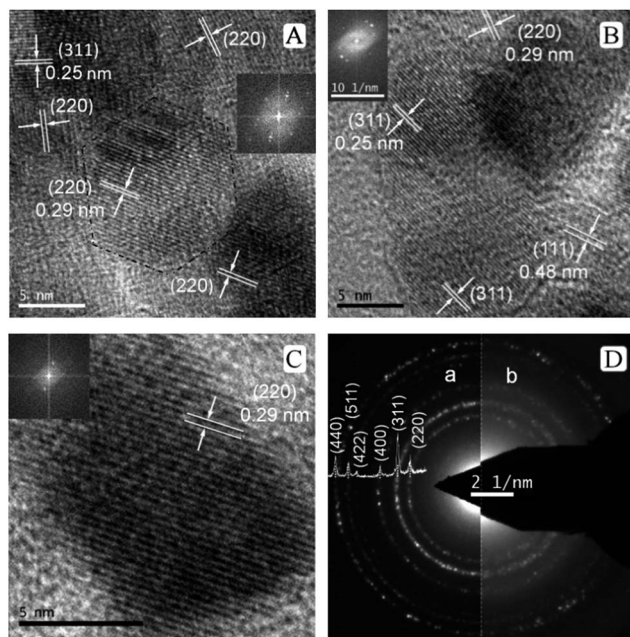


Fig. 3 (A–C) High resolution TEM images of TMA magnetite nano-crystals showing different crystal facets (311), (111) and (220) of cubic magnetite and their fast Fourier transforms are shown as inset. (D) Electron diffraction pattern of (a) bare AM and (b) TMA matched with X-ray diffraction pattern with their (hkl) planes marked.

confirms that the NPs have no detectable impurities: the signal corresponding to C and Cu was due to the carbon film over the copper TEM grid and as well as C from TMAH (panel B in Fig. S2†).

Fig. 4 shows the XRD and magnetization curves fitted with Langevin function at 300 K for the as synthesized AM as well as TMA. The diffraction patterns for all the powder samples are almost identical with the presence of characteristic finger-print reflections of magnetite. The peaks are identified as Fe_3O_4 with cubic fluorite structure (JCPDS 19-0629) having space group (227) shown as vertical drop lines. However, the peaks were significantly broader due to small crystallite size and associated lattice strain. The D_{XRD} are calculated to be 8.67 and 10.69 nm for AM and TMA respectively.

The magnetization curves indicate a superparamagnetic behavior for both the studied specimens, as evidenced by both zero coercivity and zero remanence on the magnetization loop. Due to the asymptotic increase of magnetization for high fields (see Fig. 4), the M_s value can be measured from the fitting of the M vs. $1/H$ curves, extrapolating the magnetization value to $1/H = 0$. The saturation magnetization for AM and TMA are 64.68 and 57.92 emu g^{-1} of sample respectively. The M_s value of TMA is $\sim 90\%$ of that of AM and is due to (i) lowering the proportion of magnetite by the presence of nonmagnetic organic molecules along with (ii) the smaller particle sizes (Fig. 2). The calculated values of M_s , individual magnetic moment, magnetic size of the NPs and fit results from Langevin function are presented in Table 1.

The mean diameter of the superparamagnetic TMA particles can therefore be estimated to be ~ 9.02 nm, which is smaller

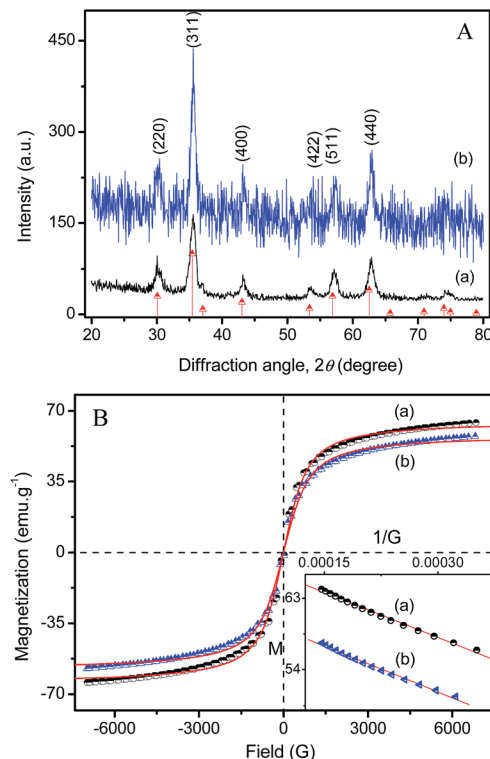


Fig. 4 (A) XRD patterns of synthetic magnetite crystals. The vertical drop lines are the theoretical Bragg positions for inverse spinel magnetite phase following JCPDS card no. 19-0629. (B) Magnetization versus applied magnetic field profiles with typical Langevin fits represented by solid red lines with the magnetization data as a function of $1/H$ for (a) AM and (b) TMA are shown in the inset.

than the average physical size of ~ 10.3 nm (magnetic core + non-magnetic outer shell) as determined from TEM measurements. XPS spectrum of TMA powder shown in Fig. 5 was used to study the valence states of Fe in the as-prepared NPs after functionalization. The XPS wide spectrum shows the peaks attributed to the core levels of O (A), Fe (A), Fe 2p and 3p, O 1s, C 1s where the Fe 2p electron core level is characterized by $2p_{1/2}$ and $2p_{3/2}$ series peaks. Fe $2p_{3/2}$ and Fe $2p_{1/2}$ double peaks correspond to the binding energies of 709 and 722 eV respectively (Fig. 5B). The double peaks in high resolution Fe 2p scan are broadened due to the appearance of Fe^{2+} ($2p_{3/2}$) and Fe^{2+} ($2p_{1/2}$) in magnetite which is in agreement with the reported literature.³⁴

The relative peak areas of Fe^{2+} and Fe^{3+} in the high resolution 2p scan were calculated as 0.33 : 0.61, close to that of the stoichiometric Fe_3O_4 , which could also be shown as $\text{FeO} \cdot \text{Fe}_2\text{O}_3$. The predominant peak at 528.3 eV is attributed to O 1s,³⁵ which can be deconvoluted to the binding energies of 528.3 and 529.6 eV belonging to the lattice oxygen in Fe_3O_4 . The lower intensity of the C 1s peaks compared to that of Fe and O proves that the organic layer around MNPs is substantially thinner. The asymmetric C 1s peak is deconvoluted into three peaks at 284.6, 285.5 and 290 eV (see inset Fig. 5A). The main peak at 284.6 eV is assigned to C–H bonds in methyl group,³⁶ and the second peak centred at 285.5 eV can be attributed to C–N bonds.³⁷ The first

Table 1 The detailed analysis from the Langevin fit of the magnetite samples

Sample	Exp M_s (emu g ⁻¹)	Cal M_s (emu g ⁻¹)	μ (emu per NP)	R^2	Standard error	D_{Mag} (nm)
AM	64.68	65.14	1.28×10^{-16}	0.9989	± 1.87	8.98
TMA	57.92	58.30	1.16×10^{-16}	0.9988	± 1.74	9.02

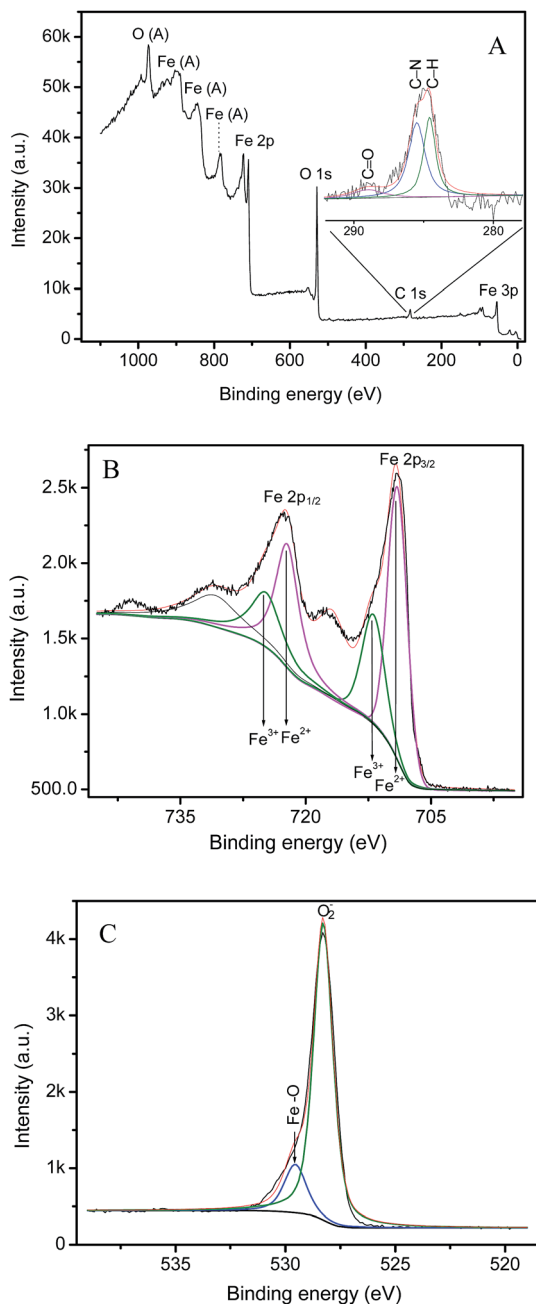


Fig. 5 (A) Survey spectrum and high resolution XPS, (B) Fe 2p, and (C) O 1s spectra of TMA sample. The solid red line over a raw data is a typical fit by XPS software.

two peaks of C 1s belonging to TMA attached electrostatically to the surface hydroxyls and the third very weak peak at 289 eV is ascribed to trace amount of CO₂ adsorbed onto the fine NPs

surface. The amount of residual TMAH in the dried TMA NPs was too little, so that the N 1s signal obtained by the XPS detector was very weak and almost absent.

The variations in the zeta potential of uncoated and TMA peptized magnetite as a function of the pH and their phase plots are shown in Fig. 6 and S3 in ESL.† The zeta potential is the electrical potential measured at the shear plane, and represents the portion of the charge that can exert electrostatic attraction and repulsion forces on neighboring particles in suspension. The magnitude of the ζ -potential is proportional to the amount of charge on the NPs surface. The ζ -potential values of AM and TMA suspensions at their natural pH and the suspension stability are shown in Table 2. Our experiments were performed at the natural pH of the AM suspension where no electrostatic repulsion is expected. Bare magnetite nanoparticle surfaces are slightly positively charged (pH 6.7) and the small electrostatic repulsive forces among the particles is not able to prevent particle–particle contact and consequent clustering as was indicated by the zeta potential of 4.9 mV (Table 2). TMA suspension peptized with strong organic base TMAH shows very high zeta potential of -44 mV in spite of dilution ($\sim 1 : 5$) and exhibited ultra stability over 1 year without any apparent precipitation. The $^+N(CH_3)_4$ cations of TMAH interact electrostatically with the OH groups attached to the bare magnetic NPs surface.

This surface structure creates electrostatic interparticle repulsion that can overcome the coagulation forces of magnetic

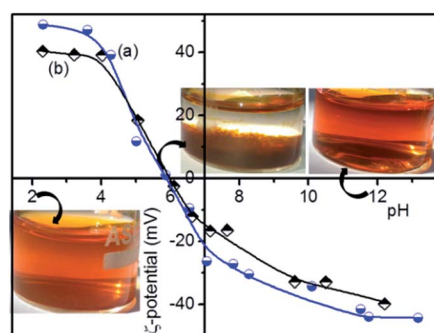


Fig. 6 Variations in the zeta potentials of (a) TMA and (b) AM magnetite suspended in Millipore water as a function of the fluid pH.

Table 2 Zeta potential of magnetite dispersion at their natural pH and its suspension stability

Sample	Zeta (mV)	pH	Stability
AM	+4.9	6.7	1 h
TMA	-44	11.75	>1 year

interaction and van der Waals attraction forces among NPs in water. Zeta potentials of the NPs are pH dependent and was observed to flip on both sides of the isoelectric point from positive surface charge (+ve zeta potential) in acidic pH to negatively charged surfaces as reflected in the negative zeta potential at basic pH. As pointed out in Fig. 6, the point of zero charge (PZC) slightly moved from 5.88 for unmodified NPs to higher pH values 5.98. Pristine magnetite NP dispersion exhibited ζ -values in the range of +40.3 to -39.8 mV in the 2 to 13.1 pH range. Adsorption of $[(\text{CH}_3)_4\text{N}]^+$ ions tend to increase the negative charge of the magnetite further to -44.2 mV at alkaline pH and increases positive charge to 48.7 mV in the acidic range. The TMA coated magnetite was extremely stable in both acidic and alkaline pH except for the pH close to their PZC between 5 and 7. The higher clustering tendency of NPs in AM can be explained by the bigger particle sizes and as a result higher crystallinity (Fig. 4A). In larger particles of well-crystallized magnetite, the bulk properties supersede surface properties, and they are expected to magnetically attract more strongly each other.³⁸

Moreover, the role of the ionic strength on the particle size also is largely dependent on the nature of the electrolyte. The smallest cations being the best screening ions, their influence on the surface charge is highest. Therefore, the TMA ferrofluid was stable above the pH > 7 and below pH < 5. The phase plot obtained with TMA sample is excellent in quality in all the pH ranges and flipped from negative to positive zeta while varying the pH from 13 to 2 shown in Fig. 6.

The hydrodynamic diameter (Z -average size, Z_{av}) and the corresponding correlation function against time are depicted in Fig. 7. Few snap shots of PCS plots from the machine for TMA slurry at various temperatures 25, 35, 45, 65 °C are shown in Fig. S4.† The overall yield of Fe_3O_4 into aqueous dispersed MNPs was >95% for TMA. The Z_{av} size was estimated by running the experiment in dynamic auto-mode using Zetasizer Nano ZS in which the machine optimizes all machine parameters to derive the best and reproducible size data. Aqueous dispersion of AM showed NPs in 33–825 nm size range with Z_{av} size of 129 nm with PDI 0.358 indicating polydisperse nature of the distribution. The calculated number distribution, N_{av} is 43 nm. This is further consolidated by the poor fit to the correlation function (panel A in Fig. 7). The signal correlation due to the random thermal motion of NPs reduced to ~ 0.74 after 100 μs in TMA where as the correlation of the signal takes a long time to decay and remained almost unchanged at ~ 1.0 at the same point of time (100 μs) in case of AM containing slow moving larger particles. The Z_{av} size for TMA is 28 nm with the presence of particles in the 8.7–91 nm size range which is ~ 2.5 times larger than D_{TEM} size of 10.3 nm (Fig. 2). The D_{PCS} of ~ 28 nm could be due to tetrahedrally arranged close-packed clusters of a total of maximum 4 particles with average hydrodynamic diameter of $\sim 2.5 \times D_{\text{TEM}} = 26$ nm which is very close to 28 nm. The algorithm in the Malvern size measurement software converts the intensity of photon signal to size by cumulants analysis. Photon scattering techniques rely on the fact that the intensity of scattered light increases by about a million times if the size of particles responsible for photon scattering increases

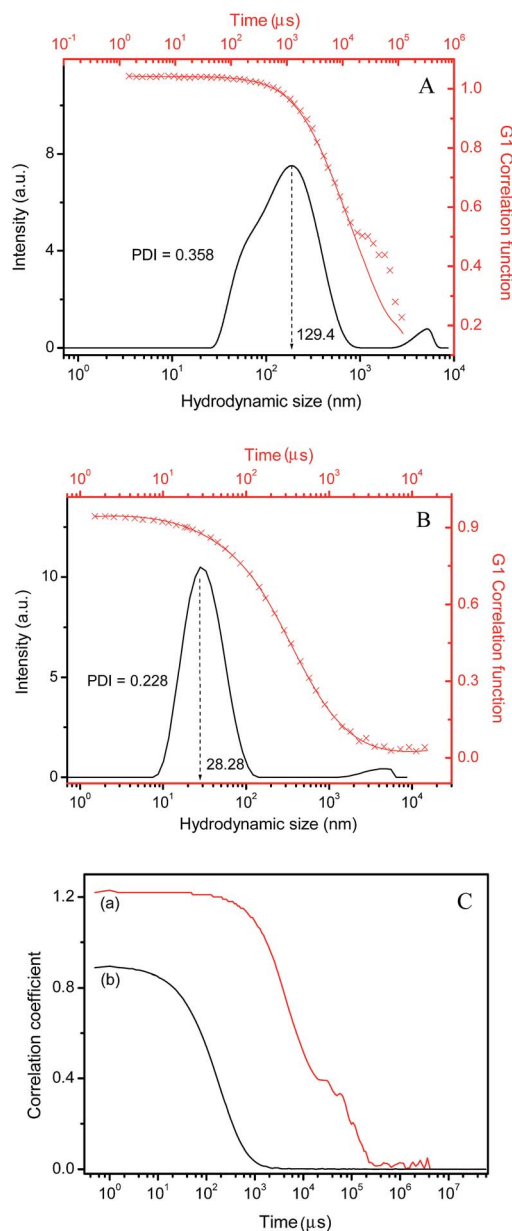


Fig. 7 Hydrodynamic size (Z_{av}) of (A) pure as well as (B) peptized synthetic magnetite. The correlation function of the same is plotted against time. (C) Raw correlation data of the (a) pure and (b) coated magnetite.

by one order of magnitude.³⁹ In other words, TMA suspension contains more than 99% 13 nm particles with <0.01% of 28 nm clusters. The PDI (0.228) indicates the complete absence of any larger aggregates as supported by good fit to the correlation data also.

To understand the clustering kinetics, hydrodynamic size, PDI, mean photon count in TMA slurry was recorded as a function of NP concentration, temperature and time and is provided in Fig. 8 and S5.† The measurement has been carried out under static mode when, ideally, the number of photons scattered is proportional to the Z_{av} of the scattering NPs. When the concentration of NPs was 25 mM (neat) as well as its 1 : 1

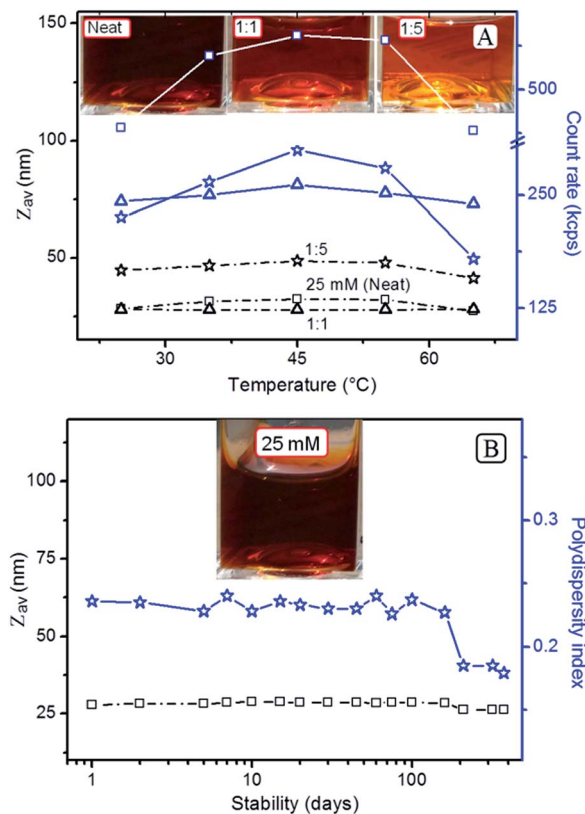


Fig. 8 (A) Z_{av} size and the colloidal stability as a function of temperature for MNPs suspension examined at various concentrations, the mean particle size (dotted line) plotted against mean count rate (solid line) with different concentrations neat (square box), 1 : 1 (triangle), 1 : 5 (star) dilutions. (B) Z_{av} and PDI of magnetite dispersion plotted as function of time. Insets are the corresponding TMA suspensions used in the experiments.

dilution, the dispersion exhibited the smallest reproducible Z_{av} size of *ca.* 28 nm which confirmed the excellent colloidal stability of TMA where as its N_{av} (13 nm), calculated from the intensity distribution, is close to the primary particle size as observed from TEM (10.3 nm). The Z_{av} size increased from 28 to 46 nm when NP concentration was decreased from an initial 25 mM to 4.2 mM with a concomitant decrease in the mean photon count rate from 450 to 260 keps. However, the TMA suspension was always stable irrespective of MNPCs concentrations in water.

When temperature for 25 mM slurry was increased from 25 to 45 °C, the hydrodynamic size 28.3 nm grew to 32.3 nm and decreased down to 27.3 nm when the temperature was further increased from 45° to 65 °C. The increase in size and mean photon counts till 45 °C may be due to the transformation of cluster structure from initial tetrahedral ($2.5 \times D_{TEM}$) to one-shell hexagonal close-packed ($3 \times D_{TEM}$) and back to the tetrahedral at ~65 °C. In the process, the count rate changed by ~22% from initial of 450 keps in 25 mM suspension. No obvious change in the Z_{av} size (~28 nm) was observed with ageing time extended even upto 12 months (panel B).

We observed that the ferrofluids are stable on ageing at room temperature over a year even after the temperature treatment,

with no evidence of flocculation or settling and there was no change in the hydrodynamic size. These results show that monodispersed nanoscale magnetite crystals have been synthesised in aqueous medium which retained its magnetic properties, with very good water dispersibility. This makes them suitable as a candidate for biomedical applications.

The FTIR and the thermal analysis patterns of magnetite specimens are presented in Fig. 9. The two most intense IR absorption bands in the 630–550 cm^{-1} range is attributed to the lattice vibrations of Fe–O bonds in tetrahedral and octahedral sites and must have been resulted from the split of the ν_1 band at ~570 cm^{-1} . The band at ~447 cm^{-1} is due to the octahedral Fe only and corresponds to the ν_2 band of Fe–O of bulk magnetite. FTIR spectra also confirm the presence of fcc magnetite in the materials as was previously confirmed from the TEM and XRD data (Fig. 2 and 4) also. The intensity reduction in TMA with respect to that of AM is probably due to the presence of tetramethylammonium ions on the Fe_3O_4 NP surface. The presence of O–H stretching vibration at ~3415 cm^{-1} and O–H deformed vibration (bending modes) at 1622 cm^{-1} are attributed to the presence of coordinated OH groups or water molecules with the unsaturated surface Fe atoms.⁴⁰

C–O stretching vibrations of CO_3^- anion at 1401 cm^{-1} (ν_3) in both the samples are due to atmospheric CO_2 .⁴¹ Small absorption bands at 2918 and 2847 cm^{-1} are due to the $\nu_{as}(\text{C–H})$ and $\nu_s(\text{–CH}_3)$ vibrations of tetramethyl group in TMA sample. The

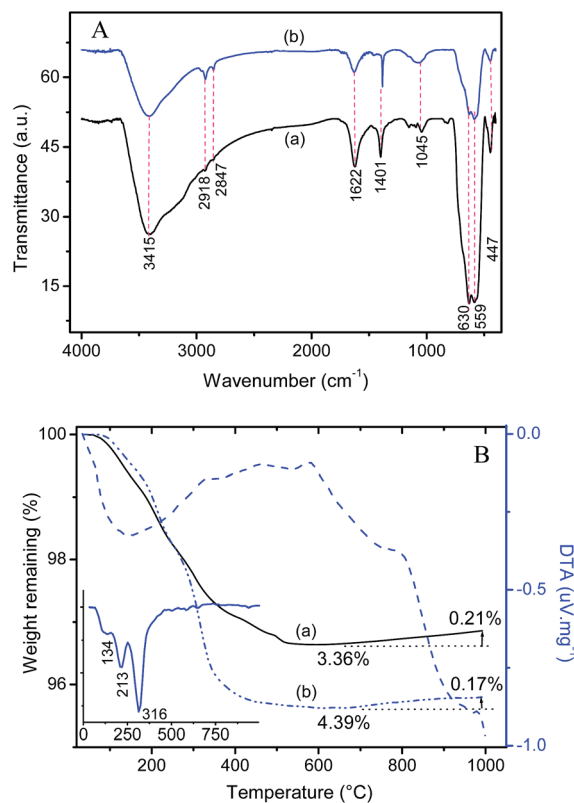


Fig. 9 (A) FTIR spectra, and (B) thermogravimetric and DTA profiles of (a) pure and (b) TMA magnetite. Inset in B is the first derivative of TG spectrum of TMA.

very small hump at $\sim 2918\text{ cm}^{-1}$ in AM might have come from some remaining oil impurities from the rust-protecting oil applied to the IR mould. The presence of which was confirmed by XPS also.

The TG profiles of AM and TMA show a total weight loss of 3.15 and 4.22% respectively with similar patterns of three-step decomposition in the temperature range 30–995 °C. The peak centred at $\sim 130\text{ °C}$ is responsible for the removal of molecular water confined in the pores and or chemisorbed on the crystal lattice. The next exothermic peak at $\sim 213\text{ °C}$ for the removal of crystalline water and unwashed chlorides from the material followed by the last peak for a huge loss nearly 4% at $\sim 310\text{ °C}$ is due to burning of carbon products from the decomposition of tetramethyl ammonium group attached to the nanocrystals surfaces in the case of TMA sample. The weight loss increased till $\sim 565\text{ °C}$ and it could be attributed to the removal of multi-layers of water of hydration from the surface of the NPs as well as dehydration of iron oxyhydroxide (FeOOH) formed in the ambient moisture. A small weight gain of $\sim 0.2\%$ was observed after 640 °C for AM and 0.21% after 668 °C onwards for TMA sample which is due to oxidation of magnetite to $\gamma\text{-Fe}_2\text{O}_3$, though the experiment was conducted under continuous nitrogen purge. The TMAH content in TMA magnetite can easily be calculated as 1.1%. When this is applied to the M_s value of AM, one can expect a value of 63.97 emu g^{-1} for TMA instead of actual 57.92 emu g^{-1} . We now conclude that nearly 9% reduction in the M_s value of TMA is due to its reduced crystal dimension of 10.3 nm compared to that (11.6 nm) in AM in addition to $\sim 1\%$ reduction due to the nonmagnetic chemical surrounding in TMA.

The pore structure and the BET surface area of the pure and peptized samples were investigated by nitrogen isothermal adsorption and is shown in Fig. 10. The isothermal gas adsorption–desorption exhibits a type IV profile according to the IUPAC nomenclature of mesoporous materials where the lower curve represents the adsorption of N_2 gas on the surfaces of the NPs, while the upper curve represents the progressive withdrawal; desorption of the adsorbed N_2 .^{42,43} Surface area was estimated from the desorption branch of the isothermal gas-

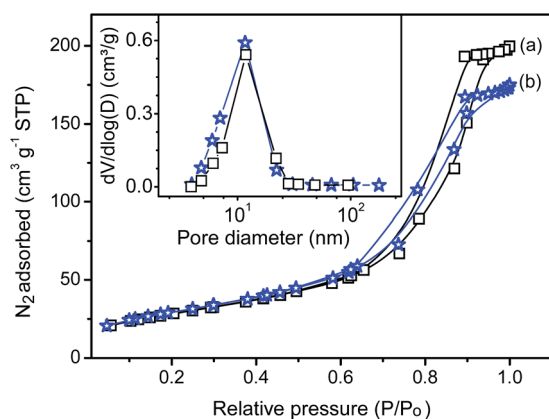


Fig. 10 Nitrogen isotherms and their pore size distribution profiles for magnetite nanocrystals (a) before and (b) after peptization with TMA.

Table 3 Crystal sizes obtained from different techniques TEM, XRD, magnetization curve, PCS and BET on magnetites

Sample	D_{TEM} (nm)	D_{XRD} (nm)	D_{Mag} (nm)	D_{PCS} (nm)	D_{BET} (nm)
AM	11.6	8.7	8.98	43	11.4
TMA	10.3	10.7	9.02	13	10.9

adsorption isotherm which indicated that there is no apparent changes in the pore structure on peptization.

The BET surface area of $106\text{ m}^2\text{ g}^{-1}$ in TMA with a pore volume of $0.3051\text{ cm}^3\text{ g}^{-1}$, is comparable to that of AM ($102\text{ m}^2\text{ g}^{-1}$, pore volume $0.3426\text{ cm}^3\text{ g}^{-1}$). From the isothermal gas desorption, based on the BJH method, a monodal pore size distribution of around $\sim 12\text{ nm}$ was estimated in both the magnetites. The BET SA in TMA ($106\text{ m}^2\text{ g}^{-1}$) can be equated to D_{BET} of 10.9 nm which is slightly larger than the D_{TEM} (10.3 nm) probably because of presence of surface coatings.² $102\text{ m}^2\text{ g}^{-1}$ in AM gives rise to a D_{BET} size of 11.4 nm which very close to the D_{TEM} of 11.6 nm. Probably the creation of SA due to the presence of interparticulate pores just counterbalanced the loss in SA due to clustering.

The magnetite nanocrystal dimensions, determined by TEM, XRD, Langevin fitting magnetization curve, PCS and BET techniques are summarized in Table 3. A very close observation is that the dry nanoparticles characterized by BET, TEM, XRD, magnetization curve, proven the mesoporous single crystalline uniform size distributed, superparamagnetic behavior of magnetite characteristic belongs to FCC inverse spinel crystal system. Size measurement based on the light scattering method is one of the most important techniques by which one can have in the *in situ* information on the state, clustering and extent of hydration of NPS in suspensions where there are many counter acting forces interating. The situation becomes more complicated when NPs are dispersed in water. The temperature, concentration and time dependent kinetics of growth of hydrodynamic size confirmed their stability of TMA suspension in this study.

Conclusions

The nanocrystalline magnetite, used in highly stable TMA nanofluid, have been synthesised by ammonia coprecipitation in physiological saline. HRTEM, SAED and XRD confirmed the magnetite phase belonging to FCC inverse spinel and had a BET SA of $106\text{ m}^2\text{ g}^{-1}$. The reduced M_s value of 58 emu g^{-1} in TMA specimen is due to its reduced crystal dimension along with small contribution of the presence of non-magnetic TMAH. TG-DTA, EDAX, as well as XPS and FTIR spectra confirmed the presence of surface coordinated tetramethyl group in TMA. TG-DTA as well as EDAX also confirmed the successful coating of tetramethyl ammonium hydroxide on nanoparticles in TMA. The reduced M_s value in TMA specimen is more due to its reduced crystal dimension along with small contribution of the presence of non-magnetic TMAH. The size of the magnetite one-shell nanoclusters was controlled within 28.3–32.3 nm range in a wide temperature range. The novelty of this work is that this is

an successful attempt to correlate the stability of ultra-stable colloidal suspension of the superparamagnetic NPs against time and temperature by simple photon correlation spectroscopy in conjunction with colloid surface properties. The monodispersity of these MNPs containing aqueous ferrofluid have no effect on heating which has great potential in hyperthermia and may find suitable in various biomedical and industrial applications.

Acknowledgements

The authors are grateful to the Director, Central Glass & Ceramic Research Institute, Kolkata for permission and extending facilities to carry out the above work. SJI and MJ acknowledge CSIR and UGC for their fellowships. SJI thanks Mrs Asha Krishnan for deconvoluting the XPS data. Staff members of XPS, XRD and MCID are also sincerely acknowledged. We thank 12 FYP CSIR Network project ESC-0103 for funding the PCS facility.

Notes and references

- 1 X. Li, H. Si, J. Z. Niu, H. Shen, C. Zhou, H. Yuan, H. Wang, L. Ma and L. S. Li, *Dalton Trans.*, 2010, **39**, 10984.
- 2 S. J. Iyengar, M. Joy, C. K. Ghosh, S. Dey, R. K. Kotnala and S. Ghosh, *RSC Adv.*, 2014, **4**, 64919.
- 3 S. Garcia-Jimeno and J. Estelrich, *Colloids Surf., A*, 2013, **420**, 74.
- 4 K. L. Lai, W. Jiang, J. Z. Tang, Y. Wu, B. He, G. Wang and Z. W. Gu, *RSC Adv.*, 2012, **2**, 13007.
- 5 Y. Piao, J. Kim, H. Bin Na, D. Kim, J. S. Baek, M. K. Ko, J. H. Lee, M. Shokouhimehr and T. Hyeon, *Nat. Mater.*, 2008, **7**, 242.
- 6 M. Mahmoudi, A. Simchi, M. Imani, M. A. Shokrgozard, A. S. Milani, U. O. Haefeli and P. Stroeve, *Colloids Surf., B*, 2010, **75**, 300.
- 7 Z. X. Sun, F. W. Su, W. Forsling and P. O. Samskog, *J. Colloid Interface Sci.*, 1998, **197**, 151.
- 8 R.-C. Wang, X.-B. Fu, X. Liu, H.-J. Liu, Y. Chen and J. Cui, *RSC Adv.*, 2013, **3**, 17016.
- 9 C. Galindo-Gonzalez, M. T. Lopez-Lopez and J. D. G. Duran, *J. Appl. Phys.*, 2012, **112**, 043917.
- 10 Y.-G. Han, M. Aoyagi, M. Kogiso, M. Asakawa and T. Shimizu, *Colloids Surf., A*, 2012, **395**, 63.
- 11 J. Philip, T. Jaykumar, P. Kalyanasundaram and B. Rai, *Meas. Sci. Technol.*, 2003, **14**, 1289.
- 12 Y. Zhang, G. Zhu, J. Lu, Z. Guo and J. Cao, *RSC Adv.*, 2015, **5**, 87841.
- 13 U. Jeong, X. Teng, Y. Wang, H. Yang and Y. Xia, *Adv. Mater.*, 2007, **19**, 33.
- 14 J. P. Huang and K. W. Yu, *Appl. Phys. Lett.*, 2005, **86**, 041905.
- 15 S. L. Pu, X. F. Chen, L. J. Chen, W. J. Liao, Y. P. Chen and Y. X. Xia, *Appl. Phys. Lett.*, 2005, **87**, 021901.
- 16 V. Mahendran and J. Philip, *Appl. Phys. Lett.*, 2012, **100**, 073104.
- 17 L. F. Shen, P. E. Laibinis and T. A. Hatton, *Langmuir*, 1999, **15**, 447.
- 18 T. Ninjbadgar and D. F. Brougham, *Adv. Funct. Mater.*, 2011, **21**, 4769.
- 19 F. Vereda, J. de Vicente and R. Hidalgo-Alvarez, *Colloids Surf., A*, 2008, **319**, 122.
- 20 D. Ramimoghadam, S. Bagheri and S. B. A. Hamid, *J. Magn. Magn. Mater.*, 2015, **379**, 74.
- 21 S. Ghosh, Ph. D. Thesis, Dublin City University, Ireland, 2006.
- 22 P. Majewski and B. Thierry, *Crit. Rev. Solid State Mater. Sci.*, 2007, **32**, 203.
- 23 E. Allard-Vannier, S. Cohen-Jonathan, J. Gautier, K. Herve-Aubert, E. Munnier, M. Souce, P. Legras, C. Passirani and I. Chourpa, *Eur. J. Pharm. Biopharm.*, 2012, **81**, 498.
- 24 L. Xiao, J. Li, D. F. Brougham, E. K. Fox, N. Feliu, A. Bushmelev, A. Schmidt, N. Mertens, F. Kiessling, M. Valldor, B. Fadeel and S. Mathur, *ACS Nano*, 2011, **5**, 6315.
- 25 L. Lartigue, P. Hugounenq, D. Alloeyau, S. P. Clarke, M. Levy, J.-C. Bacri, R. Bazzi, D. F. Brougham, C. Wilhelm and F. Gazeau, *ACS Nano*, 2012, **6**, 10935.
- 26 Z. Tu, B. Zhang, G. Yang, M. Wang, F. Zhao, D. Sheng and J. Wang, *Colloids Surf., A*, 2013, **436**, 854.
- 27 J. K. Stolarczyk, S. Ghosh and D. F. Brougham, *Angew. Chem., Int. Ed.*, 2009, **48**, 175.
- 28 D. Brougham and S. Ghosh, *US Pat.*, US 8435496 B2, 2013.
- 29 D. Sakellari, S. Mathioudaki, Z. Kalpaxidou, K. Simeonidis and M. Angelakeris, *J. Magn. Magn. Mater.*, 2015, **380**, 360.
- 30 C. P. Bean, *J. Appl. Phys.*, 1955, **26**, 1381.
- 31 C. P. Bean and I. S. Jacobs, *J. Appl. Phys.*, 1956, **27**, 1448.
- 32 C. P. Bean and J. D. Livingston, *J. Appl. Phys.*, 1959, **30**, S120.
- 33 R. M. Cornell and U. Schwertmann, The iron oxides: structure, properties, reactions, occurrences and uses, in *The iron oxides*, VCH, New York, 1996, p. 117.
- 34 Y. Lai, W. Yin, J. Liu, R. Xi and J. Zhan, *Nanoscale Res. Lett.*, 2010, **5**, 302.
- 35 B. Li, H. Cao, J. Shao, M. Qu and J. H. Warner, *J. Mater. Chem.*, 2011, **21**, 5069.
- 36 D. K. Jha, M. Shameem, A. B. Patel, A. Kostka, P. Schneider, A. Erbe and P. Deb, *Mater. Lett.*, 2013, **95**, 186.
- 37 X. Wang, X. Liu, L. Lai, S. Li, J. Weng, Z. Zhou, Q. Cui, X. Chen, M. Cao and Q. Zhang, *Adv. Funct. Mater.*, 2008, **18**, 1809.
- 38 T. Hosono, H. Takahashi, A. Fujita, R. J. Joseyphus, K. Tohji and B. Jeyadevan, *J. Magn. Magn. Mater.*, 2009, **321**, 3019.
- 39 C. J. Meledandri, J. K. Stolarczyk, S. Ghosh and D. F. Brougham, *Langmuir*, 2008, **24**, 14159.
- 40 A. Ebrahiminezhad, Y. Ghasemi, S. Rasoul-Amini, J. Barar and S. Davaran, *Bull. Korean Chem. Soc.*, 2012, **33**, 3957.
- 41 C. P. Chen, P. Gunawan and R. Xu, *J. Mater. Chem.*, 2011, **21**, 1218.
- 42 F. Liebau, *Microporous Mesoporous Mater.*, 2003, **58**, 15.
- 43 L. B. McCusker, F. Liebau and G. Engelhardt, *Pure Appl. Chem.*, 2001, **73**, 381.

PAPER

CrossMark
click for updatesCite this: *RSC Adv.*, 2016, 6, 60845

Fabrication of magnetite nanocrystals in alcohol/water mixed solvents: catalytic and colloid property evaluation†

Srividhya J. Iyengar,^a Mathew Joy,^a A. Peer Mohamed,^b Swati Samanta,^c Chandan Kumar Ghosh^d and Swapankumar Ghosh^{*a}

In this work, Fe₃O₄ nanocrystals have been synthesized by homogeneous precipitation in different alcohol/water (1 : 1) solvent mixtures at two different temperatures to elucidate the role of the dielectric constant (ϵ) of the reaction medium. The effects of different solvents on the catalytic activity of precipitated NPs in carbon combustion were examined. HRTEM images, SAED and XRD confirmed that the nanocrystals are of pure fcc inverse spinel Fe₃O₄ phase with narrow size distribution, and the crystals are completely dispersible in water. The morphological features of the nanocrystals, such as their surface termination and shape of the Fe₃O₄ NPs, were analyzed by HR-TEM. As ϵ decreases, the crystal size decreases for mono-ol systems compared to ~13 nm size in water, whereas ethylene glycol/water yields finer ~8.2 nm crystals although it has the highest ϵ among the mono-/poly-ols. A soot combustion study demonstrates that the catalytic activity is mainly due to the available surface area along with the exposure of active crystallographic facets. A study of the colloids by light scattering shows that the alcohol mediated process produces 16 to 33 nm MNP clusters composed of 2 to 3 particles in highly stable aqueous magnetic fluids. The relatively high temperature process favors higher crystallinity and particle size with reduced colloidal stability in the aqueous phase. The nanocrystalline powders and the dispersed colloids have excellent potential applications in biotechnology and selective catalysis and also as ferrofluids.

Received 30th April 2016

Accepted 8th June 2016

DOI: 10.1039/c6ra11225k

www.rsc.org/advances

Introduction

Magnetite (Fe₃O₄; ferrosferric oxide) is a well known magnetic material with high saturation magnetization. Ferromagnetic spinels are converted to superparamagnetic particles by reducing the crystal size to the nanoscale.¹ Nanofabricated Fe₃O₄ exhibits unique and tunable fundamental size- and shape-dependent magnetic, optical, and other properties.^{2,3} Magnetic materials are used in magneto-optical switches, sensors, modulators, optical circulators, and optical isolators⁴ and as magnetic adsorbents for anionic dye removal from waste water.⁵ Magnetic nanofluids or ferrofluids are colloidal

dispersions of single domain magnetic nanoparticles (MNPs) in a base fluid; they form a class of smart materials whose flow properties are adjustable *via* an external magnetic field.⁶ The interparticle interactions which contribute to the aqueous colloidal stability can be expressed as a form of extended Derjaguin–Landau–Verwey–Overbeek (DLVO) theory.⁷ In order to realize NPs with high levels of colloidal stability, there are two approaches: (1) high electrostatic repulsions among NPs, and (2) steric stabilization introduced by proper surface ligands. Bare MNPs synthesized in water are prone to aggregation because of (1) van der Waals and magnetic dipole–dipole attractive interactions,⁸ (2) less electrostatic repulsion between the nanoparticles, and (3) a tendency to reduce the high free energy associated with the huge surface area to volume ratio in small nanocrystals. These interactions result in precipitation when gravitational forces overcome the thermal motion of the NPs. Moreover, water-based magnetic fluids are unique for their complex stabilization mechanisms and structural coordination under different conditions, as opposed to magnetic fluids, which utilize organic polar carriers.⁹ It is essential to control both the primary particle size and agglomerate size of magnetic particles to obtain an optimum product.¹⁰ Stable aqueous ferrofluids have been successfully used in biomedical applications such as contrast agents for electromagnetic tomography (MRI)

^aProject Management Division, CSIR-Central Glass & Ceramics Research Institute, Kolkata-700032, India. E-mail: swapankumar.ghosh2@mail.dcu.ie; srividhyaji@gmail.com; Fax: +91 33 24730957; Tel: +91 33 23223546

^bFunctional Materials Section (MSTD), CSIR-National Institute for Interdisciplinary Science & Technology (NIIST), Trivandrum-695019, India

^cMaterial Characterization & Instrumentation Division, CSIR-Central Glass & Ceramic Research Institute, Kolkata-700032, India

^dSchool of Material Science & Nanotechnology, Jadavpur University, Kolkata-700032, India

† Electronic supplementary information (ESI) available: Additional TEM, EDS, XRD, crystallinity index, FTIR, PCS data, concentration/temperature trend, zeta potential vs. pH on nanofluids. See DOI: 10.1039/c6ra11225k

and hydraulic fracture diagnostics for imaging the brain and central nervous system, drug/gene-delivery platforms, tissue engineering, magnetically controllable catheters, and biosensors.² Major attention has also been directed toward the development of MNPs as sustainable nanocatalysts for specific chemical transformations having both economic and environmental significance, such as deodorizing catalysts,¹¹ oxide catalysts in solid propellants,¹² catalysts for exhaust gases of internal combustion engines¹³ and degradation of organic pollutants in waste water;¹⁴ the MNPs can easily be separated from the reaction mixture by an external magnetic field.

Magnetite nanocrystals can easily be synthesized by aqueous precipitation methods,² although they have the disadvantage of agglomeration of fine particles, which imposes a major challenge to the realization of the full potential of nanocrystalline powders. In the precipitation process, low dielectric constant solvents, *e.g.* alcohols, can alter the nucleation kinetics, which results in a reduction of the size and distribution of the resulting particles.^{15–17} Mono- or polyol alcohols in water-alcohol mixed solvent also act as surfactants and suppress the growth of nanocrystals during alkali precipitation of metal oxide nanocrystals.^{18,19} Guo and Xiao reported that the crystallite size and the crystallinity of the particles decreased with increasing IPA addition in hydrothermal reactions.²⁰ Ghosh *et al.* demonstrated that the radius (r) of nanocrystals produced in a precipitation reaction decreases with decreasing ϵ of the alcohol–water mixed solvent^{18,21} following eqn (1):

$$\frac{1}{r} = \frac{kT\rho}{2m\gamma} \ln C + \frac{\rho z_+ z_- e^2}{8\pi m \gamma \epsilon \epsilon_0 (r_+ + r_-)} \quad (1)$$

where ϵ_0 is the permittivity in a vacuum, r_+ and r_- are the radii of the charged z_+ and z_- ions, respectively, and e represents the charge of an electron (1.602×10^{-19} C). The solubility can be modulated by varying the composition of the solvent mixture. The formation (precipitation) of particles is strongly dependent upon the supersaturation of the solute, following classical nucleation theory. Supersaturation can be achieved by lowering the temperature, solvent evaporation, pH change, chemical reactions, alteration in solvent composition, *etc.* and is defined as the ratio of solute concentration (C) and saturation concentration; m is the molecular weight of the solute and γ is the interfacial energy between the solute and solution phases.

The effect of solvent can change the particle morphology; this effect is especially pronounced at higher concentrations of Fe-precursors (>0.5 M).²² Chowdhury *et al.* evaluated the effect of alcohol–water mixed solvents with alcohols such as butanol, propanol, ethanol and methanol on β -FeOOH nanorods under hydrothermal conditions.²² Cheng *et al.* reported a morphology evolution from compact microsphere-like single crystals to mesoporous hollow nanospheres by a polyol process.²³ Zhang *et al.* synthesized 15 to 300 nm magnetite crystals with controllably variable morphologies, including nanospheres to nano-octahedra/nano-hexaprisms in ethylene glycol–water mixed solvent.²⁴ Wang *et al.* fabricated well-defined micrometer sized magnetite crystals with star-shaped hexapods, octahedrons, concave octahedrons, and octahedral frameworks in IPA–water by a solvothermal approach.¹⁶ Magnetite NPs with

controlled morphologies such as core–shell structures and 1-D nanochains have also been reported by thermal decomposition in nonaqueous solvents.^{25–27} Estelrich *et al.* reported high molecular weight (2 to 10 kDa) PEG coated magnetite ferrofluids with dipole–cation binding between the ether group of PEG and the positively charged NP core with suspension stability over two years.¹⁹ Metal oxides become charged by the adsorption of hydrogen (H^+) or hydroxyl ions (OH^-) in aqueous suspensions, while remaining neutral at a specific pH called the point of zero charge (PZC).²⁸ Particles tend to aggregate as the electric potential approaches zero, known as the isoelectric point (IEP), under neutral conditions when there is no repulsion between the particles. It is well-known that under different colloidal conditions with potentials of either >20 mV or <-20 mV, particles repel each other (disruption of particle aggregation). The stability of the nanofluids and the clustering can easily be predicted from the zeta potential measurements. To avoid undesirable errors from using mathematical equations or the Henry formula to relate electrophoretic mobility to the ζ (zeta) potential of NPs, the surface charges of suspended particles are reported in terms of the ζ -potential.²⁹ Although the precipitation of metal oxides, *e.g.*, TiO_2 , ZrO_2 , CeO_2 , and SiO_2 , in alcohol/water mixed solvents has already been reported,^{7,15,21} there is no systematic study on the effect of solvents with variable dielectric constants and precipitation temperatures on magnetic nanocrystals; to the best of our knowledge, there is no study on the effect of solvents/precipitation temperatures on the catalytic and colloidal properties/stability of aqueous suspensions of magnetite NPs.

Herein, we report the effect of various alcohols with different polarities on the size, colloidal stability, reactivity, and other related properties of magnetite nanocrystals by ammonia precipitation. Six alcohols have been employed with decreasing ϵ value in the order of ethylene glycol (EG) $>$ diethylene glycol (DEG) $>$ ethanol (EA) $>$ *n*-propanol (*n*PA) $>$ isopropanol (IPA) $>$ polyethylene glycol (PEG). Mixed solvents of 1 : 1 water–alcohol produced small Fe_3O_4 NPs in the size range of 8 to 13 nm. The powders as well as the nanofluids have been characterized thoroughly by various techniques. The crystal structure and magnetic properties of the resulting colloidal particles have been investigated by X-ray diffraction (XRD), transmission electron microscopy (TEM), thermal analysis (TG-DTA), and vibrating sample magnetometry (VSM). The hydrodynamic size as well as the zeta potential was evaluated by photon correlation spectroscopy (PCS). To evaluate the colloidal stability, extensive zeta potential measurements have been carried out. The catalytic activity of the crystals investigated by diesel soot combustion have been explained in terms of the texture coefficients of different crystal planes, sizes and BET surface areas. This study lays a strong foundation to relate this activity on a physical basis for future nanomaterial development.

Experimental

Materials

For the synthesis of pure and surface functionalized magnetite nanocrystals, the chemicals used, Fe(II) chloride (98%) and

Fe(III) chloride (97%), were supplied by Sigma Aldrich. Absolute EA (99.9%), and *n*PA (AR) were purchased from S.D. FINE-CHEM Ltd, India. EG (guaranteed reagent, GR), DEG (for synthesis), PEG-400, acetone (GR), IPA (GR), methanol (GR), and 25% ammonia were procured from Merck, India. The chemicals for the syntheses were used as received without any purification. All the syntheses, washings and dilutions were carried out with Millipore water with resistivity 18.2 MΩ cm@25 °C after purging with ultrapure nitrogen gas (99.999% purity) to remove dissolved oxygen from the water.

Preparation

To fabricate the magnetite nanocrystals, an 8.4 mmol portion of FeCl₂·4H₂O and 16.8 mmol FeCl₃·6H₂O (such that Fe³⁺/Fe²⁺ = 2) were dissolved in 35 ml 1 : 1 water–alcohol mixed solvent deaerated by purging with nitrogen gas for 30 min in a 100 ml three-neck round bottom flask. Several alcohols, *ca.* EA, *n*PA, IPA, EG, DEG and PEG-400, were used in this study. The reaction mixture was heated to 80 °C with a hot-plate magnetic stirrer and was maintained at this temperature for ~30 min with continuous stirring and nitrogen purging in a closed setup. Subsequently, the reactor was cooled naturally to 40 °C and was kept constant at this temperature. About 15 ml NH₃ solution was added to the homogeneous mixture in one portion when the reaction mixture turned black (pH ~ 11). Vigorous stirring and the temperature (40 °C) were maintained for 30 more min; the mixture was then allowed to cool to ambient temperature. At this point, the net Fe²⁺ concentration was 168 mM. The settled black precipitate was subjected to repeated alternating magnetic decantation and washing with water to remove impurities; the final washing step was performed with methanol to break down hard agglomerates. The fine powder form of magnetite was obtained by drying the resulting black slurry in a vacuum oven at 60 °C and preserving it in a desiccator for further characterization; the samples are labeled with the corresponding alcohol abbreviations. Magnetite precipitated in water at 40 °C is designated as WA. The magnetite was also precipitated at 80 °C to study the effect of temperature and was labeled with the alcohol abbreviation followed by a number (the precipitation temperature), *e.g.*, EG80 stands for magnetite in ethylene glycol–water solvent at 80 °C.

Instrumental

Transmission electron microscopy, including selected area electron diffraction (SAED) analysis, was used to ascertain the particle shape, size and crystal structure of the synthesized materials using a FEI Tecnai 30 G² S-Twin high resolution HR-TEM operated at 300 kV. The TEM grids were prepared by drop-casting (~15 μl) the nanopowder dispersions onto 400 mesh amorphous-carbon coated copper grids and allowing the solvent to evaporate. The elemental composition of the materials was determined using an EDAX spectrometer (Fischione Instruments, Inc., USA). The crystalline phase and crystal dimensions of the material were determined from the powder XRD patterns recorded with a Bruker D8 Advanced diffractometer using CuKα₁ radiation (λ = 1.5406 Å) in the 10° to 80° 2θ

range with a step size of 0.05° 2θ and a scan speed of 4° min⁻¹. The crystallite size of the powder materials was determined using the Debye–Scherrer expression,¹⁸ given in eqn (2):

$$D_{\text{XRD}} = \frac{0.9\lambda}{\beta_{2\theta} \cos \theta} \quad (2)$$

Standard Harris analysis was performed on the X-ray data of the magnetite powders to estimate the preferred orientation of specific crystal planes and is expressed as the texture coefficient, $C(hkl)$.² Magnetic measurements of the powder specimens were made using VSM (Lakeshore 7305, US) at 300 K.

The specific surface area, pore volume and pore size distribution of the magnetite powders were determined from the N₂ adsorption data following the Brunauer–Emmett–Teller (BET) method at 77 K using Quantachrome NovaWin Instruments (version 10.01) after degassing the powders at 200 °C for 3 h. The particle size (D_{BET}) was also calculated from the BET surface area (S_{SA}) using equation with an assumption that all the particles are spherical and unclustered, where $\rho = 5.18 \text{ g cm}^{-3}$ for magnetite.²

The average particle size of the NP suspensions and the size distribution, charge and colloidal stability of the synthesized magnetite based aqueous nanofluids were determined by the light scattering technique using a Zetasizer Nano-ZS (Malvern Instruments, Malvern, UK). The instrument uses a 4 mW He–Ne laser (λ = 632.6 nm) to illuminate the sample and measures the time dependent fluctuation in the intensity of light scattered from particles in suspension at a fixed scattering angle of 173°. This technique measures the Brownian motion of the NPs in suspension and relates their correlation time to the particle size using the Stokes–Einstein equation:

$$D_{\text{PCS}} = \frac{kT}{3\pi\eta D} \quad (3)$$

where D_{PCS} is the hydrodynamic diameter of the NPs, k is Boltzmann's constant, T is the absolute temperature (K), η is the viscosity (mPa s) and D represents the translational diffusion coefficient (m² s⁻¹). About 10 mg of magnetite powder was dispersed in 10 ml Millipore water by subjecting it to ultrasonication for ~20 min. The size data and the polydispersity index (PDI) were obtained from the correlograms by the cumulant analysis method. A second-order cumulant analysis was performed. The hydrodynamic diameter (Z_{av}) was determined from the first cumulant and the PDI was determined from the second cumulant divided by the square of the first cumulant.³⁰ The surface charge was estimated by measuring the zeta potential converted from the electrophoretic mobility of the dispersion in water at 25 °C using the Smoluchowski formula using Malvern Zetasizer Software v. 7.11. In order to determine the PZC, the pH of the dispersion was adjusted either with aqueous 10⁻³ M NaOH or H₂SO₄. The pH of the well dispersed magnetite fluids was checked just before each ζ-potential measurement.

Thermogravimetry (TG) and differential thermal analysis (DTA) was used to investigate the thermal reactions in the synthesized nanocrystals using a Simultaneous Thermal

Analyzer (STA 449 C, NETZSCH, Perkin-Elmer, US) under ultrapure nitrogen purge. The heating ramp was $10\text{ }^{\circ}\text{C min}^{-1}$ in the 50 to $1000\text{ }^{\circ}\text{C}$ temperature range. The reactivity of magnetite NPs in catalysing the combustion of carbon was investigated by controlled combustion of a 4 mg mixture of Fe_3O_4 catalyst, carbon soot (collected by burning diesel), and α -alumina under dry air atmosphere. The measurements were carried out by applying a sample with a ramp of $10\text{ }^{\circ}\text{C min}^{-1}$ in the 50 to $700\text{ }^{\circ}\text{C}$ range. Standard α -alumina was used as a reference. The sample for soot oxidation was prepared by mixing and grinding carbon, powdered Fe_3O_4 and alumina (average particle size $\sim 450\text{ nm}$, Condea Chemie, Germany) in a weight ratio of 1 : 4 : 5 in an agate mortar. The inert alumina powder was added to prevent any thermal runaways.

Results and discussion

Magnetic nanocrystals were synthesized by the ammonia precipitation technique in different alcohol-water mixed solvents at 40 and $80\text{ }^{\circ}\text{C}$. All the as-synthesized iron oxide powders were typically black in color, indicating the formation of magnetite crystals as the dominant phase. Selected bright-field TEM images, size distribution histograms depicting the mean size and its distribution, and SAED patterns of some representative magnetite specimens prepared in water as well as different alcohol-water solvents are shown in Fig. 1. Magnetite formation follows a crystallization pathway involving nanometer-sized intermediate primary particles that fuse to form the crystalline iron oxide phase, which further grows to spheroidal particles $\sim 10\text{ nm}$ in size as the reaction continues.³¹

Average sizes were determined from the inspection of multiple TEM images of 100 to 120 particles, and these data are presented in Table 1. Relatively large spheroidal particles of *ca.* $12.6 \pm 1.9\text{ nm}$ were produced in water (panel A). When the reaction medium was changed to mixed solvents with mono- or poly-ol alcohols with appreciably lower dielectric constants, more or less polyhedral shaped smaller particles with average sizes in the 8.28 to 10.4 nm range with solvents in the order $\text{EG} < \text{DEG} < n\text{PA} \approx \text{IPA} < \text{PEG} < \text{EA} < \text{WA}$ were obtained. In alcohol-water solvents, the electrostatic attraction between initially precipitated primary particles is relatively low due to the lower dielectric constant of the solution. The possibility that the primary particles will agglomerate and grow is thus drastically reduced. Therefore, monodisperse NPs with narrow size distribution can be easily obtained. In mixed solvents with poly-ols, *e.g.*, EG, DEG and PEG, no such trend was observed. Although the 1 : 1 EG-water mix has the highest dielectric constant (58.95) among the solvents used in this work, next to water, it produced the smallest particles, with average sizes of $8.28 \pm 1.22\text{ nm}$. This is probably due to the presence of di-ol functional groups in this alcohol. High molecular weight poly-ols, *e.g.*, PEG and DEG (please see Fig. S3 in the ESI[†]), with high binding affinities to primary NPs act as surfactants and hinder the growth of particles by steric effects. From the TEM micrographs, it is difficult to comment on the degree of agglomeration among the NPs synthesized from different alcohols. The standard deviation (σ) of the size was a minimum of $\sim 1.3\text{ nm}$ for the NPs

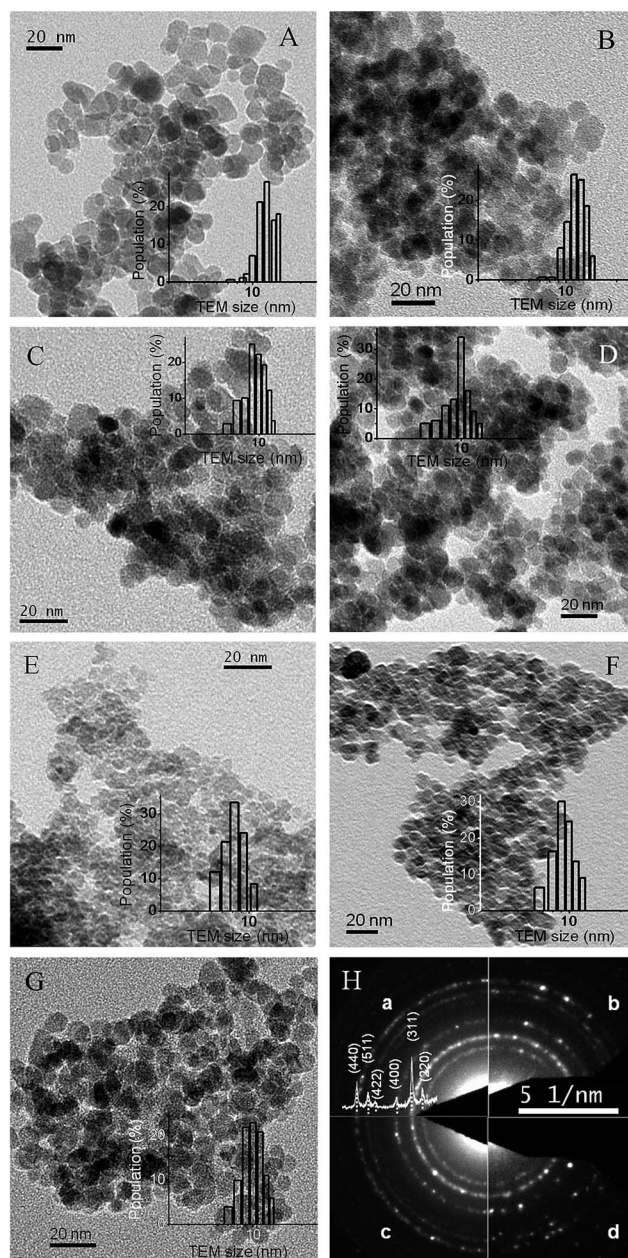


Fig. 1 TEM images of magnetite nanocrystals synthesized at $40\text{ }^{\circ}\text{C}$ in (A) water and different mixed solvents with (B) EA, (C) *n*PA, (D) IPA (E) EG, (F) DEG and (G) PEG. The size distribution histograms of the corresponding nanocrystals for all the specimens are presented as insets to the TEM images. (H) SAED patterns of (a) DEG and its matching X-ray diffraction pattern with the (*hkl*) planes marked, (b) EG, (c) *n*PA, and (d) PEG.

from both EG (size 8.28 nm) and PEG (10.2 nm), followed by 1.53 nm in DEG (9.46 nm), whereas the σ values for the NPs from water (12.6 nm) and EA (10.26 nm) were 1.9 nm and 1.67 nm, respectively. Therefore, it is appropriate to conclude here that we are able to control the polydispersity by controlling the solvent characteristics. The size variation in the magnetite crystals synthesized in different solvents suggests the strong dependence of the crystal growth on the dielectric constant of the precipitating medium. The SAED patterns of DEG, EG, *n*PA, and PEG, given in Fig. 1H, show clear Debye-Scherrer rings for

Table 1 Physical size, crystallite size and surface areal size of magnetite synthesized from mixed solvents with different dielectric constants at different temperatures

Sample/ ϵ (ref. 33)	$D_{\text{TEM}}@40\text{ }^{\circ}\text{C}$ (nm) \pm SD	$D_{\text{XRD}}@40\text{ }^{\circ}\text{C}$ (nm)	$D_{\text{BET}}@40\text{ }^{\circ}\text{C}$ (nm)	$D_{\text{XRD}}@80\text{ }^{\circ}\text{C}$ (nm)
WA/80.2	12.6 ± 1.9	9.87	11.92	12.45
EA/52.4	10.26 ± 1.67	9.72	10.33	11.12
nPA/50.25	9.93 ± 1.45	9.69	13.71	11.86
IPA/50.05	10.03 ± 1.48	9.59	10.31	12.03
EG/58.95	8.28 ± 1.22	7.45	6.34	9.81
DEG/55.95	9.46 ± 1.53	8.31	8.96	10.69
PEG/46.3 (ref. 34)	10.2 ± 1.34	9.37	10.11	11.64

the (220), (311), (400), (422), (511) and (440) planes with corresponding interplanar spacings of 0.2967, 0.2532, 0.2099, 0.1715, 0.1616 and 0.1485 nm, respectively, matching the XRD pattern of DEG (JCPDS card no. 19-0629). In addition, the bright diffraction rings indicate that the NPs are well crystallized. The clustering observed in the TEM micrographs (Fig. 1) is attributed partly to drying artifacts on the TEM grid. The most important contributor to the formation of clusters is the interfacial and magnetic interactions among the NPs and the tendency to decrease the high surface free energy by clustering. The effect of the induction of surface hydration and the electric double layer over the MNP surface due to the mono/poly-ol mediated process on the state of clustering/growth of NPs is investigated by PCS in a later section.

Representative HR-TEM images of selected magnetite specimens with different projections are provided in Fig. 2. Fourier filtering was used to extract the lattice fringe information. The crystals resemble elongated hexagons (panel A), beveled cubes (2D) and two-dimensional projected contours.³² Various projected shapes can result when the NP is viewed along different crystallographic directions.³² Although the particles shown in Fig. 2 are different in shape, all of them are enclosed with three low-energy {100}, {110} and {111} surfaces. Careful examination of the HR images indicates that all the NPs are indeed single crystals; fringes belonging to predominant (111), (220), (311) and (400) planes with corresponding d -spacings of 0.4852, 0.2967, 0.2532 and 0.2099 nm could be identified. Point defects due to missing atoms or local deformation are observed on the nanocrystal surfaces in some instances; these are marked by arrowheads in Fig. 2C. The NPs have no apparent porosity, with well-defined crystalline structures. The NPs synthesized at 80 °C in respective media grew to larger sizes (see Fig. S1 in ESI†).

The elemental compositions of the Fe_3O_4 specimens were determined by EDAX. The peaks characteristic of O and Fe atoms were observed in the EDAX spectra, along with signals from C and Cu; the latter two belong to the carbon coated copper TEM grid (inset of Fig. S1 in the ESI†).

The X-ray profiles of the magnetic products synthesized from mixed solvents with different ' ϵ ' values and temperatures and their calculated texture coefficients are shown in Fig. 3 and S2 of the ESI.† The diffraction patterns for all the powder samples show peaks for magnetite. The position and relative intensity of

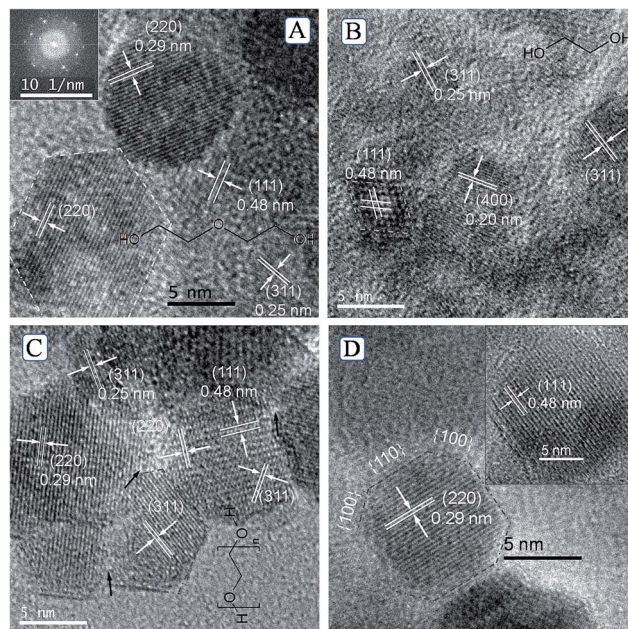


Fig. 2 HR-TEM images of magnetite nanocrystals fabricated in (A) DEG with its fast Fourier transform, (B) EG, (C) PEG, and (D) nPA (inset is another magnified crystal). The corresponding polyol structures are also shown as insets in their respective figures. Point defects in the nanocrystals are marked with black arrowheads in (C).

all diffraction peaks matched well with the characteristic fingerprint reflections of standard Fe_3O_4 with cubic fluorite structure (JCPDS 19-0629) having the space group $\text{Fd}\bar{3}m$ (227). The crystallite size was estimated using the width of the (311) reflection, employing the Debye-Scherrer equation (eqn (2)). The crystal sizes are in the 7 to 10 nm range, and the results are shown in Table 1. The X-ray peaks in the EG/water system are much broader than those in the other solvents. This is obviously because the smallest particles are produced in the EG/water system. In many cases, $D_{\text{XRD}} < D_{\text{TEM}}$, as D_{XRD} calculated employing the Scherrer equation ignores the broadening of the diffraction peaks due to microstrain in the lattice. X-ray often disregards the amorphous layer on the magnetite NP surface.²

The crystallinity indices (CI), as obtained from the XRD patterns of the nanocrystals precipitated at 40 and 80 °C, are in the ~78 to 95% range, indicating reasonably high crystallinity (Table S1†). The CI for WA is 91%; it decreased to ~79% in EG and increased to 95% in the same solvent when the precipitation temperature was increased to 80 °C (Table S1†). The average crystallite size grows and the crystallinity improves with increasing reaction temperature in spite of the decrease in ϵ of the reaction medium at higher temperatures.

Standard Harris analysis of the XRD patterns confirmed that the nanocrystals synthesized from alcohol media have proportionately higher active crystal facets compared to the nanocrystals synthesized from pure aqueous media. The texture coefficient data indicates that aqueous media produced magnetite crystals with minimum exposed active (220) facets. Preferentially grown active {110} and {100} planes with texture coefficient values in the range of 1.1 to 1.3 were obtained in all

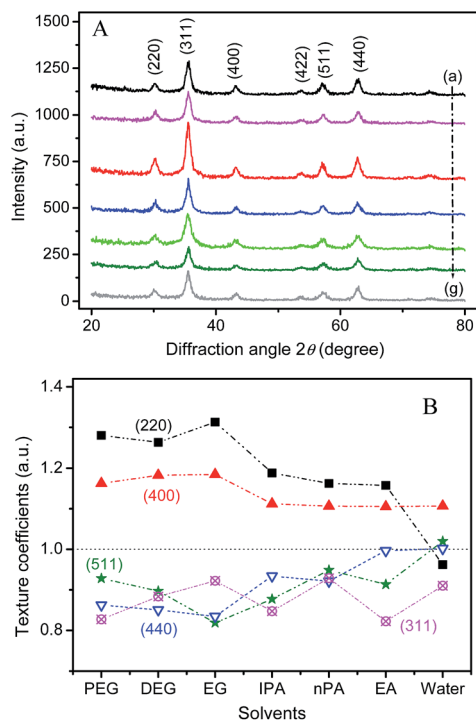


Fig. 3 (A) XRD patterns of magnetite crystals (a) WA, (b) EA, (c) nPA, (d) IPA, (e) EG, (f) DEG, (g) PEG, and (B) calculated texture coefficients.

the alcohol solvents, with the highest being ~ 1.3 in EG, DEG and PEG, by inhibiting the growth of the (311) and (511) crystal facets. We now note that aqueous precipitated magnetite in the presence of PEG shows well developed and predominant $\{100\}$ surfaces (T_C 1.163), as reported earlier.³² Hence, this study opens a ‘conceptual’ possibility of producing nanocrystals in alcohol–water medium with predominant active facets, which may improve the physicochemical properties of the material and allow superior performance.

Fe_3O_4 nanocrystals are ‘soft’ magnetic materials in the sense that they quickly switch magnetization direction once the external magnetic field is reversed. This fact is experimentally shown using VSM in Fig. 4. It is evident that all the specimens showed ferromagnetic behavior at room temperature (~ 300 K), with the hysteresis loops showing saturation magnetization (M_S), remanent magnetization (M_R) and coercivity (H_C); a comparison of the specimens with bulk Fe_3O_4 is given in Table 2.³⁵

The saturation magnetizations achieved are ~ 66 , 68 , and 69 emu g^{-1} in EA, IPA, and nPA respectively, and the M_S values for the remaining samples were clustered at ~ 60 emu g^{-1} of sample.

The M_S values obtained are slightly lower than the reported value for bulk magnetite³⁵ but are sufficient for biomedical applications. This decrease from the bulk value was already reported to be the result of spin canting due to spin frustration and lattice strain in small particles manifested at the surface of the particles, which prevents the co-linear spin arrangement on the A and B sub-lattices of the spinel magnetite (AB_2O_4) structure.^{36–38} This effect would become dominant with decreasing particle size.

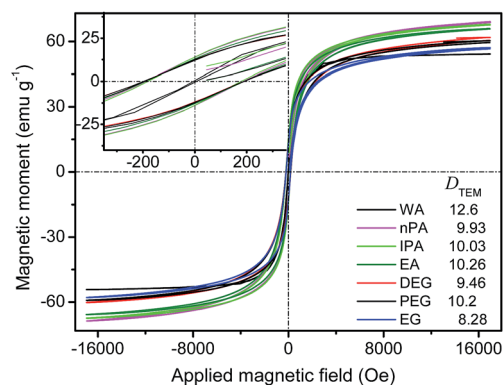


Fig. 4 Room temperature magnetization field studies on the magnetite powders synthesized at 40°C as a function magnetic field (up to 1.7 Tesla). Inset (left top) shows the respective zoomed hysteresis curves.

Table 2 Detailed VSM analysis of magnetite at 300 K

Sample/ ϵ	M_S (emu g^{-1})	M_R (emu g^{-1})	H_C (Oe)
Bulk	84		115–150
WA/80.2	57.1	0.74	3.95
EA/52.4	65.82	13.0	188.2
nPA/50.25	68.79	14.1	187.2
IPA/50.05	67.62	14.2	180.3
DEG/55.95	61.89	12.4	195.5
PEG/46.3	60.33	12.5	197.2
EG/58.95	57.12	12.2	191.5

All the Fe_3O_4 specimens have significant coercivity (H_C , reversed field required to reduce M_R to zero) in the range of 187 to 197 Oe and remnant magnetizations in the range of ~ 12 to 14 emu g^{-1} (inset of Fig. 4) except the pure magnetite produced in water, which shows a negligible coercive field (3.95 Oe) and M_R value (0.74 emu g^{-1}) as well as a smaller M_S value (57 emu g^{-1}). The reported coercive field for bulk magnetite is 115 to 150 Oe. In general, the enhancement in coercivity and reduction in M_S could be due to an increased magnetite interparticle distance concomitant with a weaker dipolar interaction and other surface effects, which can be pronounced under certain conditions in the nano-regime.^{39,40} An alternative explanation for the increase of the coercivity of the NPs produced in alcohols with different polarities is the stronger obstacles when the domains of magnetite attempt to turn under an applied field.⁴¹ When the magnetite NPs are limited and entrenched in the leftover alcohol/glycol, they can be considered as pinned. Since the hysteresis loops of the samples are sensitive to crystal size, they are useful for magnetic grain sizing of natural samples.⁴² High H_C in iron oxides is largely governed by magnetocrystallinity, shape, and magnetostrictive (stress-induced) anisotropy along with the polycrystallinity (multi-domain nature) factor, which further depends on the local magnetic anisotropy and the ferromagnetic exchange energy. The ferromagnetic exchange interaction is reported to determine the magnetic behavior of the smaller crystals.³⁵

High H_C due to polycrystallinity is ruled out in our study, as the crystallite sizes calculated from the X-ray peak broadening

(Scherrer equation) are equal to or smaller than the physical sizes obtained from the TEM measurements (Table 2). Furthermore, we have already established from the HR-TEM images (Fig. 2) that the NPs synthesized from all the solvents are single crystals. Compared to mono-ol solvent systems, the particles from poly-ol systems are relatively smaller, and as the particle size decreases, the remanance decreases, indicating “single domain” behavior in the MNPs.

The BET adsorption–desorption isotherms for all the specimens showed hysteresis loops of type IV by Brunauer's classification, with an apparent hysteresis loop in the range of 0 to 0.89 P/P_0 , indicating the presence of mesopores (data not shown). The pores in the materials are in the mesoporous range (3.6 to 9.5 nm) and are interparticulate in nature. The magnetite products show relatively high surface areas (84 to 183 $\text{m}^2 \text{g}^{-1}$), as expected from their small particle sizes. The magnetite synthesized from alcohol mediated precipitation shows a higher surface area (114 to 183 $\text{m}^2 \text{g}^{-1}$) compared to the aqueous product (84 $\text{m}^2 \text{g}^{-1}$). The size (D_{BET}) estimated from the nitrogen adsorption–desorption isotherms is somewhat larger than the size estimated from TEM (Table 1) for all except the crystals derived from EG, DEG and PEG solvents. Therefore, the particle size and surface area of MNPs can be tuned by changing the dielectric constant of the reaction medium by selecting different alcohols.

The crystalline non-agglomerated dispersible NPs of magnetite obtained by alcohol mediated syntheses are attractive because they are readily dispersible in water using a low energy ultrasonic bath and are able to form transparent colloidal suspensions under ambient conditions. The hydrodynamic size, zeta potential, suspension stability, and optical images of the aqueous suspensions of magnetite nanocrystals (particle concentration 4.3 mM, slightly acidic pH) are illustrated in Fig. 5. The number average size (N_{av}) of 16 to 33 nm of the 40 and 80 °C precipitated powders, with the exception of the water and IPA/water systems, is ~ 2 to 3 times larger than those of the primary particles as observed by TEM (see Fig. 5A and Table S2†). This is possibly due to tetrahedral or hexagonal close-packed assemblies of ~ 10 nm particles in the suspension. The N_{av} is reliable as the PDI values are below 0.3, in most cases, which is indicative of narrow and monodisperse size distribution.⁴³ These aqueous magnetite fluids may find use in various *in vivo* biomedical applications. The colloidal stability of the NPs is closely related to their surface chemistry. The average ζ -values are in the 20.3 to 43 mV range, among which IPA has the least zeta potential and EG has the highest (43 mV) for poly-ol mixed solvent, followed by EA (40.9 mV), which is the highest among the mono-ol solvents (Fig. 5B and Table S2†). The alcohol moieties show slightly acidic behavior when Fe_3O_4 crystals (IEP at pH ~ 6.7) are suspended in them, and the suspension exhibits positive zeta potential due to the positive surface charge over the nanocrystal surfaces. The particle surfaces are positively charged and the strong repulsive forces (electrostatic) among the particles counteract the attractive forces due to magnetic interaction and van der Waals attractive forces and prevent consequent clustering, although the measurements were carried out at their natural pH values (6 to

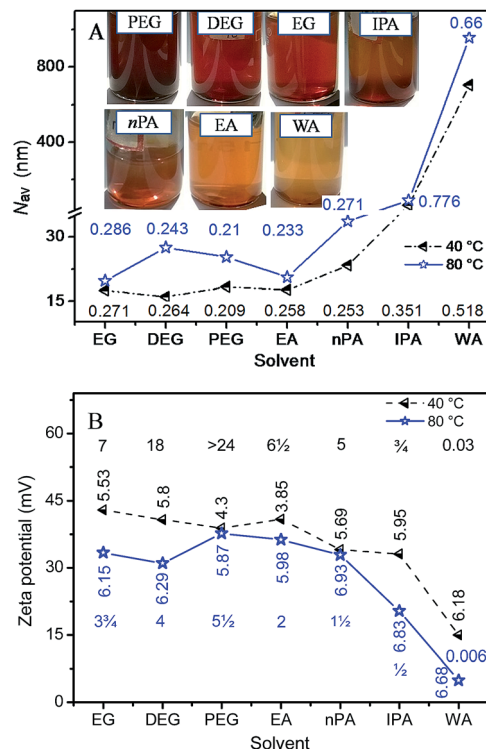


Fig. 5 (A) Hydrodynamic sizes and the corresponding PDI and (B) zeta potential, as well as the stability (horizontal numeric; weeks) of the magnetite suspensions at their natural pH values (vertical numeric), synthesized at 40 and 80 °C in different alcohol–water mixed solvents. Optical images of the freshly prepared dispersions in water are shown as the inset of panel A.

7) where no electrostatic repulsion is expected. The consequent strong electrostatic repulsive forces can be elucidated by analyzing the energy barrier for aggregation between two approaching particles based on DLVO theory,⁷ which can be described as:

$$V_b = -\frac{A\kappa\alpha}{12} + 2\pi\epsilon\alpha\psi^2 \quad (4)$$

where α is the particle diameter, ϵ is the dielectric constant of the solution, and ψ is the surface potential. The effective Hamaker constant A and the Debye–Hückel parameter κ remain constants in our experimental conditions. Therefore, it is evident that the energy barrier V_b largely depends on the dielectric constant of the medium.

It is interesting to note that the products obtained at 40 °C are easily dispersible, and their colloidal stabilities are much higher than those produced at 80 °C (Fig. 5). This is due to the strong positive surface charge as indicated by the high zeta potential at their natural pH values of ~ 6.4 to 6.9 being close to PZC (see Fig. S7 in the ESI†). The narrow size distribution and the corresponding normalized single exponential decay of the self-correlation coefficient for all MNP clusters produced at 40 °C support their monodisperse nature, especially for the polyol based MNPs (Fig. S4†). The EG, DEG, PEG, EA, and nPA dispersions were found to have narrow size distributions, which implies good stability, whereas relatively less stable dispersions

produced broader distributions due to aggregation (in the case of WA and IPA). PEG dispersion (D_{TEM} 10.2 nm) is very stable without any precipitation, even after 6 months of storage. Meanwhile, the IPA slurry, with slightly smaller D_{TEM} size (10.03 nm) and higher CI and PDI as well as the lowest ζ -potential next to water, precipitates completely in 5 days. This suggests that an additional mechanism, *i.e.*, steric effects, in addition to the electrostatic stabilization process (indicated by the ζ -value of ~ 38 mV) is introduced by the PEG chains.²⁹ Similar phenomena were observed with EG and DEG; however, the suspensions were stable for 7 and 18 weeks, respectively, due to the poorer stabilizing efficiency of mono and di-ethylene glycol compared to that of PEG, and their Z_{av} sizes are slightly larger (Table S2[†]). The EA colloids did not sediment over $6\frac{1}{2}$ weeks, probably because of the electrostatic (higher ζ -potential of ~ 40 mV) and steric effects, and this interaction was supported by FTIR (Fig. S3[†]). The PCS size along with the correlation fits and zeta potential data of one of the representative specimens (EA) are given in Fig. 6. A Z_{av} size of ~ 25 nm with a relatively low PDI value of 0.252 is extracted from the good cumulant fit to the auto-correlation function of the intensity fluctuations of scattered photons. The phase plot of this sample is excellent (panel B in Fig. 6).

Magnetite particles with interfacial and even magnetic interactions (due to their small remanence) are also reported to support the clustering process,⁴⁴ which contributes to the

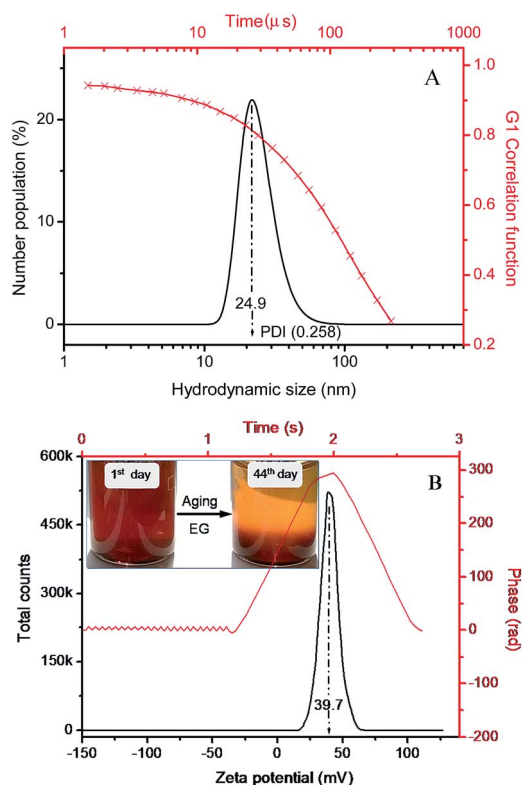


Fig. 6 (A) Hydrodynamic size plot along with the correlation data and (B) zeta potential graph with its phase plot for the EA dispersion in water. The inset is the color gradient formed after incubation of EG for 44 days.

formation of fractal aggregates⁴² with large sediment volumes. With time, when the loose aggregates reach a critical size, the thermal motion cannot hold them in suspension, causing initiation of the sedimentation process. As time elapses, large aggregates drag smaller particles with them and create a significant depletion of nanometer-sized magnetites in the supernatant,⁴⁵ forming a color gradient with a clear colorless fluid zone at the top and a gradual increase in color intensity to the bottom. This phenomenon was observed in all the mono- and poly-ol mediated nanocrystal slurries (optical photographs for EG are shown in the inset of Fig. 6B). As expected, the aqueous suspensions of bare MNPs (WA80 and WA) produced in water medium have the least positive surface charges of 4.9 and 15 mV, respectively, with highly polydisperse natures ($\text{PDI} > 0.5$), and do not show any colloidal stability (precipitated within a couple of hours of suspension). $-\text{OH}_2^+$ ions exist on the surface of the bare NPs at $\text{pH} \sim 7$ in the vicinity of the isoelectric point of synthetic magnetite, and the suspension is normally not stable.⁴⁶ Higher stability of the bare MNP suspension may also be achieved at $\text{pH} > 10$, when ζ almost reaches a plateau in the ζ versus pH profile (Fig. S7[†]).²⁹ This once again supports the fact that the higher ζ -potential in a nanofluid confers greater colloidal stability. The zero charges on the surface of WA, nPA, PEG and EA magnetite were found to be at pH 6.9, 6.46, 6.47 and 6.4, respectively. Although the natural pH of glycol/alcohol mediated MNPs varies slightly from that of the water mediated NPs, the behaviors of their zeta curves are almost the same as the conditions vary from acidic to basic (Fig. S7[†]). This leads to the confirmation that the magnetite MNP surface properties are unaltered, irrespective of the synthetic media.

The increase in particle size with increasing dielectric constant of the precipitating solvent is due to enhanced hydrogen bonding. The roles of the increased precipitation temperature and dielectric constant of the solvents are: (1) the crystallinity and particle size of MNPs increase and the colloidal stability in the aqueous phase decreases; (2) the increased precipitation temperature decreases the density of the surface adsorbed alcoholic moieties, resulting in poorer suspension stability.

Glycol medium produced MNPs with narrow size distribution, as observed from D_{TEM} , which may have helped to produce a stable suspension comparable to those in mono-ol media and pure water at 40 °C. The EG dispersion is almost transparent and remains homogeneous, without any visible precipitation or creaming.

Fig. 7 shows the temperature dependent hydrodynamic properties of the PEG based colloid. The hydrodynamic size of 33.3 nm grew to 38.2 nm at 20 to 35 °C, remained almost constant up to 45 °C, and then decreased back to 33.1 nm when the temperature was further increased to 65 °C; however, interestingly, the N_{av} (number average) of ~ 18 nm remains the same. As expected, the concomitant change in mean count with Z_{av} may be due to the change in the aggregate sizes. The increase in size and mean photon counts up to 45 °C may be due to a slight transformation of the cluster structure from the initial hexagonal shape ($3 \times D_{\text{TEM}}$) to one-shell octahedral close-packed ($4 \times D_{\text{TEM}}$) and back to hexagonal at ~ 65 °C. The poly-ol (PEG, DEG and EG) mediated MNC based colloids are stable, do

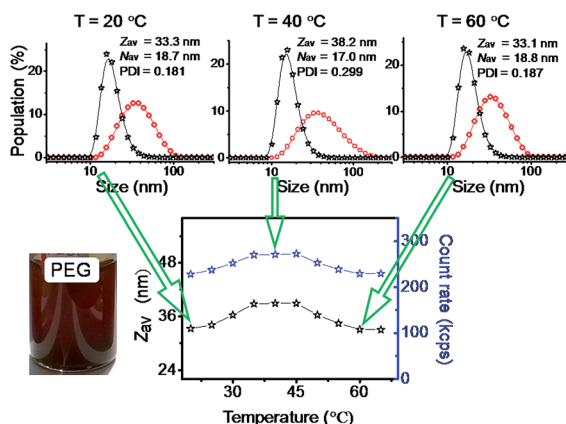


Fig. 7 Temperature dependent PEG agglomerate size in suspension by photon correlation spectroscopic studies. An optical image of the PEG suspension is shown in the inset.

not grow, and precipitate (all data not presented here) over 6–24 weeks as a function of temperature (up to 65 °C). However, these colloids exhibited gradual size growth by 15 to 25% on dilution (up to $\times 10$) due to partial desorption of the chemisorbed poly-ols; hence, they are activated with respect to interaction with other NPs or NPCs.⁴⁷

As anticipated, the DLS data indicated a slight increase in the hydrodynamic size of the particles, with a steadily decreasing count rate for PEG immediately after dilution. A good linear relationship ($R^2 = 0.9983$) was observed between the count rate and the NPs concentration in the range of 10 to 1.25 mM (Fig. S5†).

The presence of organic layers on the surface of the NPs was further confirmed by TG-DTA. The thermogravimetry patterns of magnetite specimens synthesized from mixed solvents are presented in Fig. 8. All the TG profiles show very similar patterns, with three-step decomposition in the temperature range of 50 to 1000 °C.

The aqueous precipitated magnetite presents a simple two stage thermal decomposition at ~ 225 and 330 °C consisting of a total loss of $\sim 6\%$, whereas the total losses are ~ 11.8 , 13.9, and 16.7% for PEG, DEG and EG respectively at temperatures

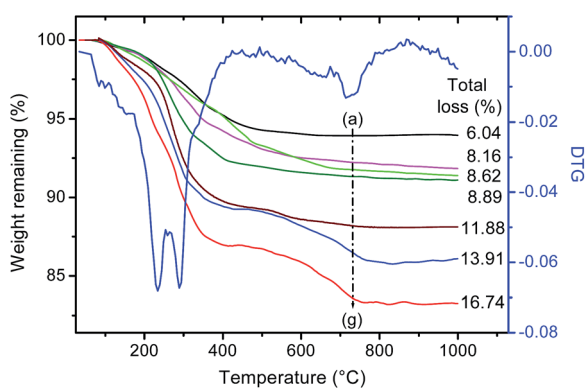


Fig. 8 Thermal analysis patterns of magnetite powders synthesized at 40 °C from a 1 : 1 combination of water with different solvents: (a) WA, (b) *n*PA, (c) EA, (d) IPA, (e) PEG, (f) DEG and (g) EG; DTG of the representative specimen DEG.

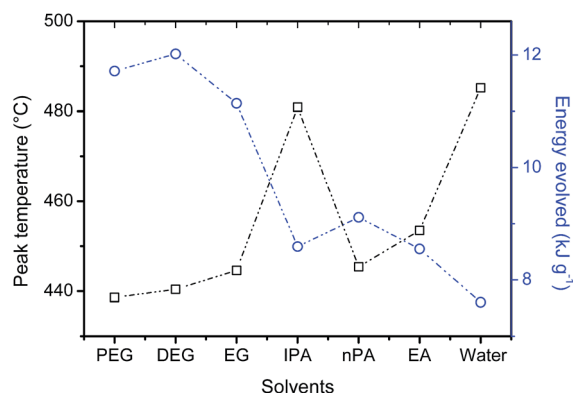


Fig. 9 Differential thermal analysis patterns of magnetite powders synthesized at 40 °C from WA, *n*PA, EA, PEG, DEG, EG, and IPA.

>800 °C. The peak centered at ~ 120 °C is responsible for the removal of structural water from the lattice, followed by an exothermic peak at ~ 250 °C for the removal of unwashed salt from the material along with alcohols attached to the surfaces of the nanocrystals. The last peak for a small loss at ~ 670 °C is due to the combustion of carbon/graphitic products from the decomposition of poly-ols. The weight loss is greater for EG compared to other poly-ols, due to the smaller NPs having higher surface areas available to the adsorbed poly-ol moieties. The TG patterns of *n*PA, EA and IPA have similar losses of $\sim 8.5\%$.

The catalytic activity of the Fe_3O_4 powders was evaluated by measuring the peak combustion temperature (T_p) and the total heat evolved (ΔH) during the Fe_3O_4 catalyzed combustion of carbonaceous diesel soot in excess O_2 ; this is shown in Fig. 9. The catalytic activity of magnetite precipitated in solvent mixtures with different dielectric constants is correlated with the BET surface area and active crystal facets. The poly-ol mediated products (PEG, DEG and EG) showed better activity due to their relatively smaller sizes with abundant active (220) and (400) crystal facets. The figure shows that the catalytic activity, in terms of the total heat evolved from the carbon soot combustion, varies from a minimum of 7.6 kJ g^{-1} for WA to a maximum of 12.0 kJ g^{-1} for DEG. The T_p are, as expected, inversely related with the total heat evolved; the extremes are 485.2 and 438.6 °C for WA and PEG, respectively.

The energies evolved during soot burning were relatively lower at $\sim 9 \text{ kJ g}^{-1}$ for the mono-ol based products, *e.g.*, IPA, *n*PA and EA, possibly due to the lower T_C values for the active (220) and (400) planes (~ 1.2 and 1.1, respectively). In comparison to the T_p of WA, the values decreased by 39.8 and 31.7 °C in *n*PA and EA, respectively, whereas the T_p remained almost unchanged at 481 °C in IPA. Thus, we conclude that the activity of a magnetite material is attributable mainly to the energetics of the reaction on the exposed (220) and (400) crystal facets in addition to the available surfaces.

Conclusions

Magnetite nanocrystals have been synthesized *via* homogeneous precipitation in solvents in media with decreasing ‘*e*’

using 1 : 1 EA, nPA, IPA, EG, DEG and PEG with water at 40 and 80 °C. The presence of alcohol/glycol content (by TG-DTA and FTIR) and the precipitation temperature are vital for the control of the agglomeration, suspension stability, size and crystallinity of the magnetite. IPA magnetite is relatively crystalline (CI ~89%), next to water, with the highest magnetization of ~68 emu g⁻¹. The crystals observed from HRTEM have a mixture of multi-faceted polyhedral shapes, all of which contain abundant undercoordinated atoms located on their edges and corners, serving as extra active sites for the chemical reaction. The PEG, DEG and EG powders showed better catalytic activity due to smaller particles with abundant active (220) and (400) crystal facets. Nanofluids with greater aqueous stability were obtained from relatively lower precipitation temperatures at 40 °C. Furthermore, the monodispersed transparent colloidal suspension of PEG showed stability over a period of 6 months. The hydrodynamic diameter was <20 nm with the temperature trend up to 65 °C. These MNPs and stable colloids open up opportunities for improving existing biomedical/industrial applications and designing novel technologies in the future.

Acknowledgements

The authors are grateful to the Director, Central Glass & Ceramic Research Institute, Kolkata for permission and extending facilities to carry out the above work. Dr Dipten Bhattacharya is acknowledged for the magnetization studies. SJI and MJ acknowledge CSIR and UGC for their fellowships. We thank 12 FYP CSIR Network project ESC-0103 for funding the PCS facility. Staff members of the HR-TEM, XRD, and Central Instrumentation Facility are also acknowledged for their assistance in obtaining data.

Notes and references

- 1 Y. Tian, B. B. Yu, X. Li and K. Li, *J. Mater. Chem.*, 2011, **21**, 2476–2481.
- 2 S. J. Iyengar, M. Joy, C. K. Ghosh, S. Dey, R. K. Kotnala and S. Ghosh, *RSC Adv.*, 2014, **4**, 64919–64929.
- 3 C. Guerrero-Sanchez, M. Rasa and U. S. Schubert, *US Pat.*, US2010/0092419 A1, 2010.
- 4 Y. Li, H. Zhu, H. Gu, H. Dai, Z. Fang, N. J. Weadock, Z. Guo and L. Hu, *J. Mater. Chem. A*, 2013, **1**, 15278–15283.
- 5 Q. Yan, Z. Zhang, Y. Zhang, A. Umar, Z. Guo, D. O'Hare and Q. Wang, *Eur. J. Inorg. Chem.*, 2015, **2015**, 4182–4191.
- 6 A. P. Liu, X. Li, L. H. Duan, G. P. Qin and H. H. Guo, *J. Supercond. Novel Magn.*, 2010, **23**, 967–970.
- 7 L. Gao, W. Li, J. Wang and J. K. Guo, *J. Nanopart. Res.*, 1999, **1**, 349–352.
- 8 D. Ramimoghadam, S. Bagheri and S. B. A. Hamid, *J. Magn. Magn. Mater.*, 2015, **379**, 74–79.
- 9 L. Vékás, D. Bica and O. Marinica, *Rom. Rep. Phys.*, 2006, **58**, 257–267.
- 10 B. Kucuk, N. Ozkan and M. Volkan, *J. Phys. Chem. Solids*, 2013, **74**, 1426–1432.
- 11 T. Usami, K. Kagawa and M. Kawazoe, *JP Pat.*, JP2007130634-A, 2007.
- 12 T. P. Rudy, F. R. Goodson and M. E. Dudley, *US Pat.*, US4881994 A, 1989.
- 13 T. P. Rudy, F. R. Goodson and M. E. Dudley, *US Pat.*, US5688740 A, 1997.
- 14 R. Amutha, M. Muruganandham, G. J. Lee, V. N. Batalova, G. Mokrousov and J. J. Wu, *Adv. Sci. Lett.*, 2011, **4**, 496–500.
- 15 H. I. Chen and H. Y. Chang, *Colloids Surf., A*, 2004, **242**, 61–69.
- 16 X. Wang, Z. Zhao, J. Qu, Z. Wang and J. Qiu, *Cryst. Growth Des.*, 2010, **10**, 2863–2869.
- 17 S. Hamada and E. Matijević, *J. Colloid Interface Sci.*, 1981, **84**, 274–277.
- 18 K. C. Remani and S. Ghosh, *Trans. Indian Ceram. Soc.*, 2009, **68**, 185–188.
- 19 S. Garcia-Jimeno and J. Estelrich, *Colloids Surf., A*, 2013, **420**, 74–81.
- 20 X. Guo and P. Xiao, *J. Eur. Ceram. Soc.*, 2006, **26**, 3383–3391.
- 21 T. S. Sreeremya, K. M. Thulasi, A. Krishnan and S. Ghosh, *Ind. Eng. Chem. Res.*, 2012, **51**, 318–326.
- 22 M. R. Chowdhury, V. Fester, G. Kale and O. Cespedes, *J. Nanopart. Res.*, 2014, **16**, 2412.
- 23 C. Cheng, F. Xu and H. Gu, *New J. Chem.*, 2011, **35**, 1072–1079.
- 24 H. Zhang, H. Lim, J. Wei and C. Wong, *Nanosci. Nanotechnol. Lett.*, 2011, **3**, 155–160.
- 25 J. Zhu, S. Wei, Y. Li, L. Sun, N. Haldolaarachchige, D. P. Young, C. Southworth, A. Khasanov, Z. Luo and Z. Guo, *Macromolecules*, 2011, **44**, 4382–4391.
- 26 Q. He, T. Yuan, S. Wei, N. Haldolaarachchige, Z. Luo, D. P. Young, A. Khasanov and Z. Guo, *Angew. Chem., Int. Ed.*, 2012, **51**, 8842–8845.
- 27 Q. He, T. Yuan, X. Yan, Z. Luo, N. Haldolaarachchige, D. P. Young, S. Wei and Z. Guo, *Chem. Commun.*, 2014, **50**, 201–203.
- 28 M. Erdemoglu and M. Sarikaya, *J. Colloid Interface Sci.*, 2006, **300**, 795–804.
- 29 A. Masoudi, H. R. M. Hosseini, M. A. Shokrgozar, R. Ahmadi and M. A. Oghabian, *Int. J. Pharm.*, 2012, **433**, 129–141.
- 30 K. Helttunen, A. Galán, P. Ballester, J. Bergenholtz and M. Nissinen, *J. Colloid Interface Sci.*, 2016, **464**, 59–65.
- 31 J. Baumgartner, A. Dey, P. H. H. Bomans, C. Le Coadou, P. Fratzl, N. A. J. M. Sommerdijk and D. Faivre, *Nat. Mater.*, 2013, **12**, 310–314.
- 32 C. Liang, S. Huang, W. Zhao, W. Liu, J. Chen, H. Liu and Y. Tong, *New J. Chem.*, 2015, **39**, 2651–2656.
- 33 B. S. Furniss, A. J. Hannaford, V. Rogers, P. W. G. Smith and A. R. Tatchell, *Vogel's Textbook of practical organic chemistry*, English Publisher Book Society, Longman, England, 4th edn, 1978.
- 34 <http://pharmlabs.unc.edu/labs/solubility/structure.htm>, accessed on 10/7/15.
- 35 M. I. Dar and S. A. Shivashankar, *RSC Adv.*, 2014, **4**, 4105–4113.
- 36 *The iron oxides: structure, properties, reactions, occurrences and uses*, ed. R. M. Cornell and U. Schwertmann, Wiley-VCH, Weinheim, 2nd edn, 1996, p. 117.
- 37 J. M. D. Coey, *Phys. Rev. Lett.*, 1971, **27**, 1140–1142.

- 38 F. Bødker, S. Mørup and S. Linderøth, *Phys. Rev. Lett.*, 1994, **72**, 282–285.
- 39 Z. Guo, H. T. Hahn, H. Lin, A. B. Karki and D. P. Young, *J. Appl. Phys.*, 2008, **104**, 014314.
- 40 Z. Guo, S. Park, H. T. Hahn, S. Wei, M. Moldovan, A. B. Karki and D. P. Young, *Appl. Phys. Lett.*, 2007, **90**, 053111.
- 41 M. Wu, Y. Xiong, Z. Peng, N. Jiang, H. Qi and Q. Chen, *Mater. Res. Bull.*, 2004, **39**, 1875–1880.
- 42 S. Ghosh, Ph.D. thesis, Dublin City University, Ireland, 2006.
- 43 S. J. Iyengar, M. Joy, T. Maity, J. Chakraborty, R. K. Kotnala and S. Ghosh, *RSC Adv.*, 2016, **6**, 14393–14402.
- 44 M. R. Gittings and D. A. Saville, *Colloids Surf., A*, 1998, **141**, 111–117.
- 45 J. L. Viota, F. Gonzalez-Caballero, J. D. G. Duran and A. V. Delgado, *J. Colloid Interface Sci.*, 2007, **309**, 135–139.
- 46 M. Mahmoudi, S. Laurent, M. A. Shokrgozar and M. Hosseinkhani, *ACS Nano*, 2011, **5**, 7263–7276.
- 47 J. K. Stolarczyk, S. Ghosh and D. F. Brougham, *Angew. Chem., Int. Ed.*, 2009, **48**, 175–178.